



**HAL**  
open science

# Polypyrrole-metal oxide nanocomposite materials for electro- and photocatalytic water oxidation into oxygen

Daniela Valentina Morales Montecinos

► **To cite this version:**

Daniela Valentina Morales Montecinos. Polypyrrole-metal oxide nanocomposite materials for electro- and photocatalytic water oxidation into oxygen. Inorganic chemistry. Université Grenoble Alpes, 2018. English. NNT: 2018GREAV012 . tel-02645245

**HAL Id: tel-02645245**

**<https://theses.hal.science/tel-02645245>**

Submitted on 29 May 2020

**HAL** is a multi-disciplinary open access archive for the deposit and dissemination of scientific research documents, whether they are published or not. The documents may come from teaching and research institutions in France or abroad, or from public or private research centers.

L'archive ouverte pluridisciplinaire **HAL**, est destinée au dépôt et à la diffusion de documents scientifiques de niveau recherche, publiés ou non, émanant des établissements d'enseignement et de recherche français ou étrangers, des laboratoires publics ou privés.

## THÈSE

Pour obtenir le grade de

### **DOCTEUR DE LA COMMUNAUTÉ UNIVERSITÉ GRENOBLE ALPES**

Spécialité : **Chimie inorganique et bioinorganique**

Arrêté ministériel : 7 août 2006

Présentée par

### **Daniela Valentina MORALES MONTECINOS**

Thèse dirigée par **Marie-Noëlle COLLOMB** et  
Co-dirigée par **Jerôme FORTAGE**

préparée au sein du **Département de Chimie Moléculaire (DCM)**  
dans l'**École Doctorale Chimie et Sciences du Vivant (EDCSV)**

## **Polypyrrole-metal oxide nanocomposite materials for electro- and photocatalytic water oxidation into oxygen**

Thèse soutenue publiquement le **28 mai 2018**,  
devant le jury composé de :

**M. Christophe BUCHER**

Directeur de Recherche CNRS, Ecole Normale Supérieure de Lyon,  
Rapporteur

**M. Cédric TARD**

Chargé de Recherche CNRS, Ecole Polytechnique de Palaiseau,  
Rapporteur

**M. Philippe LAINE**

Directeur de Recherche CNRS, Université Paris Diderot, Examineur

**M. Jean-Claude LEPRETRE**

Professeur à l'Université Grenoble Alpes, Président

**Mme. Marie-Noëlle COLLOMB**

Directrice de Recherche CNRS, Université Grenoble Alpes, Examinatrice

**M. Jérôme FORTAGE**

Chargé de Recherche CNRS, Université Grenoble Alpes, Examineur



## Acknowledgements

---

In my time in DCM-CIRE, there are so many people to thank when I look back. First of all, I thank Serge Cosnier (CNRS Research Director and Director of the “Département de Chimie Moléculaire (DCM)), and Fabrice Thomas (UGA Professor and Director of the group “Chimie Inorganique Rédox” (CIRE)), to give me the permission to do my thesis in DCM and CIRE, and to Becas Chile (Conicyt) “Programa de formación de capital humano avanzado”, Folio N° 72150091 from the Chilean Government for my PhD fellowship, and to Project ECOS-CONICYT exchange program (C13E01) which allowed me to return to Chile twice to attend two congresses and to collaborate closely with the group of Professor Bernabé Rivas at the University of Concepcion (UDEC) and perform TEM NiO<sub>x</sub> analysis.

I thank the members of Jury, Christophe Bucher (CNRS Research Director), Cédric Tard (CNRS Researcher) and Philippe Lainé (CNRS Research Director), for the thesis examination and their attendance and discussion during my PhD defense, and Jean-Claude Leprêtre (UGA Professor) for attending and presiding my PhD defense. I also thank Liliane Guerente (UGA Assistant Professor) and Vincent Artero (CEA Researcher) for accepting to be members of my CST jury during my PhD and for all the great discussions and advices.

I want to thank specially Jean-Claude Moutet (UGA Professor), “my first thesis director”, for accepting me to start the thesis with you, I really appreciate our first year of work, to teach me electrochemistry and all our discussions. I want to thank my PhD supervisors, Marie-Noëlle Collomb (CNRS Research Director) and Jérôme Fortage (CNRS Researcher), without your guidance and support I could not have been achieved in such satisfactory and fruitful way this thesis, thanks for accepting me to continue this thesis with you, to teach me and for all the great scientific discussions, specially for your thesis corrections and all the time that you gave me.

I thank all the members of the laboratory, everybody made in some way a contribution in my formation as a Doctor. I especially thank Veronika Anastasioae (Master 2 student) for her help with the cobalt experiments, it was a pleasure to guide you and work with you; Baptiste Dautreppe (Master 2 student) for the synthesis of the perylene-pyrrole that permits me to perform all the experiments of my last thesis chapter; Selim Sirach (UGA Assistant Engineer) for the synthesis of the pyrrole ammonium and for always helping me to find all kinds of things in the laboratory; and Florian Molton (CNRS Engineer) for always helping me to solve my instrumental problems.

I thank Josiane Arnaud (Biologist and Doctor in CHU Grenoble) and Dominique André (Technician in CHU Grenoble) for the ICPMS analyses, and Jean-Luc Puteaux (CNRS Research Director) and Christine Lancelon-Pin (CNRS Engineer) for SEM and TEM analyses of CoO<sub>x</sub> nanoparticles.

I want to thanks also the Chilean group for TEM analyses of NiO<sub>x</sub> nanoparticles and support me at distance during all this years, Bruno F. Urbano (UDEC Assistant Professor), Julio Sánchez (USACH Assistant Professor), and especially my scientific father Bernabé L. Rivas (UDEC Professor), for encouraging me to follow a PhD, thank you for all your advice and support during all my formation.

I want to thank all my colleagues of my office during all this years: Long, Lianke, Lucy, Robin, Matthew O., Catalina, Suzanne, Martina, Marielle, especially to Matt Stanbury, Jamie, Felix, thanks for all the great conversations and sharing moments.

Finally I want to thank my family, especially my big brother Anibal Morales to encourage me to follow his steps and to my mother Angela Montecinos for being there and always have the necessary words in the days when I didn't have the force to continue, and to my husband Xavier Dessart to give me force and support me during the last step and the most difficult one "the thesis redaction".

# Abbreviations List

HER : Hydrogen evolution reaction

OER: Oxygen evolution reaction

RHE : Reversible hydrogen electrode

NHE : Normal hydrogen electrode

LDH : Layer double hydroxide

TOF : Turnover frequency

Ni-Bi : Nickel borate

FTO : Fluorin tin oxide

ITO : Indium tin oxide

SEM : Scanning electron microscopy

TEM: Transmission electron microscopy

ICP-MS : Inductively coupled plasma mass spectrometry

XAS : X-ray absorption spectroscopy,

XANES: X-ray absorption edge structure

EXAFS : Extended X-ray absorption fine structure

TXRF: Total reflection x-ray fluorescence analysis

XRD : X-ray diffraction

XPS : X-ray photoelectron spectroscopy

EDX : Energy dispersive x-ray spectroscopy

AFM: Atomic force microscopy

UV-Vis : Spectroscopie d'absorption électronique dans l'ultra-violet et le visible

$\epsilon$  : Coefficient d'extinction molaire

EIS : Electrochemical impedance spectroscopy

CPE : Controlled potential electrolysis

LSV : Linear sweep voltammetry

CV : Cyclic Voltammetry

$\eta$ : Overpotential

[Bu<sub>4</sub>N](ClO<sub>4</sub>) : Tetra-*n*-butylammonium perchlorate

CH<sub>3</sub>CN: Acetonitrile

CH<sub>2</sub>Cl<sub>2</sub>: Dichloromethane

## Resumé

Dans le contexte énergétique actuel, l'hydrogène moléculaire ( $H_2$ ) est considéré comme un vecteur d'énergie propre attrayant et une excellente alternative aux combustibles fossiles. Les combustibles fossiles, comme le charbon, le pétrole et le gaz naturel, sont limités et, même si les prévisions d'approvisionnement varient considérablement, il est clair que nos technologies doivent utiliser d'autres sources d'énergie abondantes et idéalement illimitées. Par ailleurs, bien que 1 kg d'hydrogène génère trois fois plus d'énergie que 1 kg d'essence ce qui fait de  $H_2$  le carburant du futur, il n'y a pas de réserve naturelle de  $H_2$  sur terre et il ne peut être obtenu facilement à partir de l'eau et nécessite un apport supplémentaire d'énergie. De nos jours, 95% de l'hydrogène moléculaire est produit à partir de combustibles fossiles par divers procédés industriels (par exemple la gazéification du charbon et le vaporeformage du méthane) qui nécessitent des températures et des pressions élevées, et génèrent du dioxyde de carbone.

Une approche très prometteuse et plus durable consiste à dissocier l'eau en  $O_2$  et  $H_2$  en utilisant uniquement des sources d'énergies renouvelables telles que l'énergie solaire ou l'électricité propre (par exemple à partir de l'énergie éolienne). Néanmoins, la partie oxydante de ce processus, l'oxydation de l'eau en oxygène moléculaire ( $O_2$ ) ou la réaction de dégagement d'oxygène (oxygen evolving reaction ou OER en anglais), est une tâche difficile en raison de sa barrière d'activation élevée, de sa cinétique lente et de sa grande surtension anodique. Par conséquent, de nombreux efforts ont été faits pour développer des électrocatalyseurs efficaces présentant une grande stabilité et une faible surtension d'OER. Depuis le début des années 80, les oxydes métalliques à base de métaux de transition de la première rangée, tels que les très populaires oxyde de nickel ( $NiO_x$ ) et oxyde de cobalt ( $CoO_x$ ), sont apparus comme étant des catalyseurs très prometteurs pour l'oxydation de l'eau en raison de leur abondance relativement élevée sur la croûte terrestre, de leur faible surtension OER et de leur résistance à la corrosion, qui leur confère une grande stabilité dans les conditions opérationnelles. De nombreux travaux ont été consacrés à l'élaboration d'anodes ou de photoanodes utilisant des oxydes métalliques catalytiquement très actifs et très stables. En outre, plusieurs stratégies de synthèse ont été adoptées pour obtenir ces caractéristiques, mais la plus étudiée repose sur le contrôle de la porosité et de la morphologie du film de catalyseurs et de la taille du catalyseur, afin de favoriser le transport d'électrons/de

masse à la surface de l'électrode, pour augmenter la surface électroactive de l'électrode et ainsi améliorer leur performance catalytique vis-à-vis de l'oxydation de l'eau.

Dans ce contexte, ce travail de thèse vise à proposer une approche originale, rarement rapportée dans la littérature, pour développer une anode très efficace pour la réaction d'oxydation de l'eau électrocatalytique à base de nanocomposite oxyde de nickel/cobalt-poly (pyrrole-alkylammonium) (poly1-NiO<sub>x</sub> ou poly1-CoO<sub>x</sub>) préparé par une voie de synthèse facile et tout électrochimique. Cette stratégie a également été étendue à la conception de photoanodes pour l'oxydation de l'eau photocatalytique en combinant ces nanocomposites à un colorant organique robuste de la famille des pérylènes. L'utilisation de nanocomposites pour l'oxydation de l'eau électro-induite fait l'objet de la partie I de ce manuscrit, et l'utilisation de nanocomposites contenant le colorant pérylène pour l'oxydation de l'eau photo-induite fait l'objet de la partie II.

## **Partie I**

**Chapitre 1.** Le premier chapitre présente de manière non exhaustive une étude bibliographique sur les anodes utilisant des oxydes de nickel et des oxydes de cobalt pour l'oxydation électrocatalytique de l'eau. Du fait d'une littérature foisonnante et croissante de façon exponentielle (près de 5 articles par jour sont publiés dans le domaine de la dissociation de l'eau et notamment sur l'oxydation de l'eau), seuls quelques exemples pertinents d'anodes sont discutés à la lumière des stratégies communément employées pour optimiser l'activité des catalyseurs.

L'une des approches les plus utilisées consiste à synthétiser des catalyseurs de petite taille ou des films de catalyseur ayant une morphologie contrôlée en vue d'obtenir des surfaces (électro)actives élevées et par conséquent d'obtenir une activité électrocatalytique OER accrue. Une autre approche vise à résoudre le problème de la faible conductivité électrique des catalyseurs à base de métaux en dopant les films de catalyseur par des ions (par exemple Fe<sup>3+</sup>) ou en associant les catalyseurs à des nanomatériaux conducteurs comme les métaux précieux (Au, Pt ou Pd) et les nanomatériaux de carbone (graphène, nanofils et nanotubes de carbone). A la lumière de ces diverses approches, ce chapitre résume quelques travaux sur la conception d'anodes à base de catalyseurs d'oxyde de nickel et d'oxyde de cobalt. Certains groupes comme ceux de Burke, Noufi, Bockris, Corrigan et Tseung ont été les premiers dans les années 80 à démontrer les potentialités des oxydes de nickel et de cobalt à électrocatalyser l'oxydation de l'eau par dépôt électrochimique à la surface de l'électrode. Depuis ces travaux

pionniers, de nombreuses méthodes, autres que l'électrodéposition, ont été rapportées pour préparer des oxydes de nickel et de cobalt par procédé solvatothermique ou précipitation chimique, qui sont ensuite déposés sur l'électrode par divers procédés tels que le spin coating, le procédé sol-gel, le dépôt par électrospray ou la sérigraphie, pour n'en nommer que quelques-uns. Toutes ces stratégies de synthèse permettent d'obtenir des oxydes métalliques de formes et de tailles contrôlées comme les nanoparticules, les nano-aiguilles, les nano-tiges ou les nano-feuillets. Néanmoins, le dépôt électrochimique reste la méthode la plus simple et la plus utilisée pour préparer des anodes à base de  $\text{NiO}_x$  et  $\text{CoO}_x$ , et le groupe de Nocera montre dans les années 2000 que leur électrodéposition peut être facilitée en utilisant des électrolytes accepteurs de protons (comme les borates ou phosphates). Leur travail a également attiré l'attention sur ces oxydes (i) en fournissant des informations fondamentales sur la structure des oxydes déposés et leur mécanisme d'oxydation de l'eau et (ii) en démontrant que ces électrocatalyseurs peuvent fonctionner efficacement en milieu neutre (pH 7) ou légèrement basique (pH 9,2). Après les travaux de Nocera, de nombreux groupes ont présenté différentes stratégies pour déposer des films d'oxydes métalliques, en particulier le groupe de Spiccia ou Kuznetsov qui utilisent l'électrodécomposition de complexes de nickel ou d'un cluster nickel/molybdène pour préparer des films de  $\text{NiO}_x$  avec une porosité élevée et des performances OER également accrues.

Au vu des nombreux travaux rapportés sur les catalyseurs à base d'oxyde de nickel et d'oxyde de cobalt, quelques tendances émergent pour concevoir des anodes OER efficaces. Dans un premier temps, si l'on compare les activités électrocatalytiques OER de l'oxyde de nickel avec celles de l'oxyde de cobalt, il est clair que  $\text{NiO}_x$  est plus actif que  $\text{CoO}_x$ , notamment lorsque  $\text{NiO}_x$  est dopé avec des sels de Fe en abaissant drastiquement sa surtension pour réaliser l'oxydation de l'eau. En effet, les catalyseurs à double couche d'hydroxyde (layer double hydroxide ou LDH) contenant du fer, comme  $\text{NiFeO}_x$ , qui ont été rapportés en premier par les groupes de Radniecka et Corrigan, sont les électrocatalyseurs les plus efficaces de la littérature pour la réaction d'oxydation de l'eau. D'autre part, l'activité OER des oxydes de nickel et de cobalt, et plus généralement des catalyseurs métalliques, a été améliorée en nanostructurant les films catalytiques sous forme de nanomatériaux 2D tels que des nanofeuillets d'épaisseur atomique pouvant s'empiler sur quelques couches. Cette stratégie augmente le rapport surface-volume et l'exposition des sites actifs métalliques pour réagir avec l'eau ou les anions hydroxydes, et accélère le transport de masse de l'oxygène libéré et des sels de l'électrolyte à la surface de l'électrode. En fin, comme il a été évoqué plus haut, en

vue d'améliorer la conductivité électrique du matériau catalytique, différentes stratégies de préparation des anodes ont été rapportées comme par exemple l'introduction de nanomatériaux conducteurs (par exemple des nanotubes de carbone ou des oxydes de graphène réduit, rapporté par l'équipe de Song) entre l'oxyde métallique et l'électrode ou le dépôt de nanoréseaux bien organisés d'oxyde métallique directement sur l'électrode (par exemple des réseaux de nanoparticules de  $\text{NiFeO}_x$  alignés sur une électrode de carbone vitreux, développé par l'équipe de Shao). Ces approches assurent un bon contact électrique entre le catalyseur et l'électrode, et une grande surface électroactive, augmentent ainsi les cinétiques de transfert d'électrons au sein du matériau et accélérant la réaction catalytique d'oxydation de l'eau.

Bien que de nombreuses avancées aient été réalisées ces dernières années dans la conception de films catalytiques inorganiques nanostructurés à base d'oxydes de métaux de transition de la première rangée (Ni, Co, Fe), le développement de catalyseurs avec une grande stabilité et une performance OER élevée reste un grand défi et un certain nombre de verrous scientifiques sont encore à lever. En conclusion, certaines orientations générales sont proposées en vue d'améliorer les performances OER des anodes utilisant des catalyseurs inorganiques du type oxyde métallique.

**Chapitre 2.** Ce chapitre est consacré à la préparation électrochimique et à l'étude de nanocomposites d'oxyde de nickel-poly(pyrrole-alkylammonium) ( $\text{poly1-NiO}_x$ ) pour l'élaboration d'anodes hautement efficaces pour l'oxydation de l'eau electrocatalytique. Le nanocomposite  $\text{poly1-NiO}_x$  a été facilement synthétisé par une procédure entièrement électrochimique. Les nanoparticules de nickel métallique ( $\text{Ni}^0$ ) ont été électrodéposées dans un film de poly(pyrrole-ammonium) cationique ( $\text{poly1}$ ), préalablement électropolymérisé sur des électrodes de carbone vitreux ou d'ITO (*i.e.* Indium Tin Oxide), par réduction d'un complexe anionique nickel-oxalate dans un tampon borate aqueux à pH 6. Les nanoparticules de  $\text{Ni}^0$  ont ensuite été électro-oxydées en oxyde de nickel ( $\text{NiO}_x$ ) dans un tampon aqueux borate à pH 9.2. Les propriétés physiques, chimiques et électrocatalytiques du matériau nanostructuré  $\text{poly1-NiO}_x$  ont alors été évaluées par spectrométrie de masse à plasma induit (ICP-MS), microscopie à force atomique (AFM) et microscopie électronique à transmission (TEM) couplées à diverses techniques électrochimiques et comparées à celles de  $\text{NiO}_x$  directement déposé sur une électrode nue (sans polymère) par la même procédure électrochimique. De telles caractérisations mettent clairement en évidence le rôle bénéfique de la matrice de polypyrrole pour générer des particules de  $\text{NiO}_x$  de taille nanométrique (21

nm) et non agglomérées. En raison de la petite taille des nanoparticules de NiO<sub>x</sub> et de la nanostructuration importante du film composite poly1-NiO<sub>x</sub> déposé sur la surface de l'électrode, ce matériau présente des performances électrocatalytiques très élevées en solution faiblement basique (pH 9,2) et même en solution alcaline (pH 14) avec des activités massiques et des fréquences de cycle catalytique (TOF) respectivement de 1,12 A mg<sup>-1</sup> et 0,17 s<sup>-1</sup> à la surtension de 0,61 V à pH 9,2 et de 1,28 A mg<sup>-1</sup> et 0,19 s<sup>-1</sup> à la surtension de 0,35 V à pH 14. Ces performances placent l'électrode à base de poly1-NiO<sub>x</sub> parmi les meilleures anodes à base d'oxyde de nickel rapportées dans la littérature pour OER et sans dopage par des ions de fer.

**Chapitre 3.** Ce chapitre vise à démontrer que la stratégie originale présentée au chapitre II, fondée sur l'utilisation de nanocomposites d'oxyde métallique-polypyrrole, peut être étendue à d'autres métaux de transition de la première rangée tel que le cobalt. Ce chapitre décrit donc la synthèse et l'étude de nanocomposites d'oxyde de cobalt-poly(pyrrole-alkylammonium) (poly1-CoO<sub>x</sub>) pour des anodes efficaces pour l'oxydation de l'eau. En suivant la même stratégie décrite dans le chapitre précédent, les nanoparticules de cobalt (Co<sup>0</sup>) ont été déposées par électrolyse dans le film de poly(pyrrole-ammonium) cationique (poly1) initialement déposé sur des électrodes de carbone ou d'ITO, par réduction d'un complexe cobalt-oxalate anionique. Contrairement à l'oxyde de nickel, les nanoparticules de Co<sup>0</sup> sont ensuite oxydées à l'air en oxyde de cobalt (CoO<sub>x</sub>) en trempant l'électrode dans un tampon aqueux de borate à pH 9.2 non dégazé. De manière similaire, les propriétés physiques, chimiques et électrocatalytiques du matériau poly1-CoO<sub>x</sub> nanostructuré ont été évaluées par ICP-MS, AFM, TEM et par microscopie électronique à balayage (MEB), couplées à diverses techniques électrochimiques, puis comparées à celles de CoO<sub>x</sub> directement déposé sur une électrode nue. Les caractérisations par microscopie révèlent des tailles de particules d'oxyde de cobalt similaires et nanométriques (31 nm) à la fois pour le dépôt direct de CoO<sub>x</sub> et le nanocomposite poly1-CoO<sub>x</sub>, mais dans le cas du nanocomposite les nanoparticules ne sont pas agglomérées et sont parfaitement dispersées dans poly1, démontrant ainsi une fois de plus le rôle bénéfique de la matrice polymère dans la nanostructuration du matériau. Le nanocomposite poly1-CoO<sub>x</sub> présente des performances électro-catalytiques très élevées dans une solution à pHs 9.2 et 14 avec des activités massives et des valeurs de TOF respectivement de 2.75 A mg<sup>-1</sup> et 0.41 s<sup>-1</sup> à une surtension de 0.61 V à pH 9.2 et de 4.58 A mg<sup>-1</sup> et 0.69 s<sup>-1</sup> à une surtension de 0.35 V à pH 14. De plus, le nanocomposite poly1-CoO<sub>x</sub> montre une bonne stabilité en maintenant un courant catalytique élevé de plus de 7 mA cm<sup>-2</sup> au cours d'une

électrolyse de 2h à pH 9.2 et avec une surtension de 0.71 V. L'anode poly1-CoO<sub>x</sub> présente des performances électrocatalytiques supérieures à celles d'une simple anode CoO<sub>x</sub>, mais aussi à celles de poly1-NiO<sub>x</sub> décrite dans le Chapitre 2 et de poly1-IrO<sub>x</sub> précédemment développée dans le groupe. L'oxyde de cobalt étant connu pour être un catalyseur actif à pH 7, le nanocomposite poly1-CoO<sub>x</sub> ouvre la voie pour le développement d'anodes originales et robustes, fabriquées uniquement à partir d'éléments abondants et très actives en milieu neutre pour l'oxydation de l'eau. Cette anode nanocomposite se situe donc parmi les meilleures anodes à base d'oxyde de cobalt rapportées dans la littérature.

## **Partie II.**

**Chapitre 1.** La construction de dispositifs photoélectrochimiques pour la dissociation de l'eau est un domaine de recherche qui ne cesse de croître. Les cellules photoélectrochimiques de dissociation de l'eau associent une photoanode pour la réaction d'oxydation de l'eau (OER) et une photocathode pour la réduction des protons libérés lors de l'oxydation en H<sub>2</sub> (HER). La construction de tels dispositifs reste au stade de la recherche exploratoire et les photoélectrodes, photoanodes et photocathodes sont souvent optimisées séparément et étudiées avec une simple contre-électrode en platine nécessitant l'apport d'électricité pour fonctionner.

De nombreuses recherches sont consacrées au développement de photoélectrodes uniquement à base de matériaux semi-conducteurs (SCs), mais elles rencontrent la difficulté d'avoir un SC capable d'absorber efficacement la lumière visible et un niveau d'énergie suffisant pour catalyser l'OER pour les photoanodes et HER pour les photocathodes. Une stratégie pour améliorer l'efficacité de ces PECs à base de SC consiste à découpler les fonctions d'absorption de lumière et catalytiques de l'électrode, en couplant aux SCs un catalyseur OER pour les photoanodes ou HER dans le cas des photocathodes, généralement à base de nanoparticules d'(oxyde) métallique. Une autre stratégie consiste à adsorber un colorant moléculaire ou photosensibilisateur (PS) sur la surface du SC pour étendre l'absorption dans le visible, et également de le coupler à un catalyseur, généralement à base de métal, pour promouvoir la réaction OER (ou HER). Cette approche moléculaire de construction de cellules PEC (ou dye-sensitized-PEC (DS-PEC)) pour la dissociation de l'eau est un domaine de recherche émergent inspiré par la technologie des cellules photovoltaïques (cellules solaires sensibilisées aux colorants (DS-SC)). Les catalyseurs OER ou HER sont soit des nanoparticules d'(oxydes) de métaux, soit des complexes de métaux de transition moléculaires liés ou co-adsorbés avec le PS.

Actuellement, seulement une dizaine de photoanodes "hybrides" associant un photosensibilisateur (PS) moléculaire à un catalyseur d'oxyde métallique ont été publiées. Ces photoanodes couplent les bénéfices d'une grande stabilité des catalyseurs inorganiques comparés aux catalyseurs moléculaires aux excellentes propriétés de PS moléculaire pour absorber la lumière visible.

Ce chapitre bibliographique résume ces études relativement récentes. Ces photoanodes "hybrides" sont constituées d'une électrode transparente semi-conductrice (SC) (Indium Thin Oxide (ITO) ou Fluoride Thin oxide (FTO)) qui peut être recouverte ou non d'un autre SC de type n tels que  $\text{TiO}_2$ ,  $\text{SnO}_2$  ou  $\text{WO}_3$  sur lesquels sont co-adsorbés, généralement en monocouche, un chromophore moléculaire ainsi que des nanoparticules d'oxyde métallique ( $\text{IrO}_x$ ,  $\text{CoO}_x$ ,  $\text{Ni}_{0.5}\text{Co}_{0.5}\text{O}_x$  ou  $\text{Co}_3\text{O}_4$ ) déposées par voie chimique ou co-adsorbées. Des dérivés du ruthenium-tris-bipyridine ou des colorants organiques incluant l'heptazine, des pérylènes, un polymère  $\pi$  conjugué de type naphthalène, ou des porphyrines base libre ont été employés comme PS.

L'absorption de la lumière par la molécule de PS conduit à un état excité, suivi d'une injection rapide de l'électron dans la bande de conduction (CB) du SC nanostructuré ( $\text{TiO}_2$ ,  $\text{SnO}_2$  ou  $\text{WO}_3$ ), conduisant à l'oxydation du PS. En l'absence d'une photocathode pour la réduction de l'eau par exemple, l'application d'un bias à la photoanode DS-PEC est nécessaire pour récupérer les électrons générés dans la CB du SC. Si la durée de vie de cet état à charges séparées est suffisamment longue, un transfert d'électrons du catalyseur au colorant oxydé se produit. Puisque l'oxydation de l'eau nécessite quatre électrons, le catalyseur doit accumuler quatre trous pour oxyder l'eau. L'oxydation catalytique de l'eau est généralement trop lente pour concurrencer efficacement le transfert d'électrons retour, ce qui explique les rendements quantiques faibles pour la dissociation de l'eau.

En effet, si les photoanodes hybrides publiées sont actives en milieu neutre ou faiblement acide, démontrant leur potentiel pour la réaction OER, elles sont peu stables et présentent des photocourants assez faibles ( $150\text{-}200 \mu\text{A cm}^{-2}$  pour les dérivés du pérylène et  $<20 \mu\text{A cm}^{-2}$  pour les autres exemples). La faible densité de photocourant a été principalement attribuée à la cinétique rapide du transfert d'électrons retour (recombinaison des charges) d'échelle de temps de l'ordre de la centaine de microsecondes, qui entre en compétition avec l'oxydation catalytique lente de l'eau (de l'ordre de la milliseconde) et la cinétique lente de transfert d'électrons entre le PS et le catalyseur inorganique.

Pour améliorer l'efficacité de ces PECs d'oxydation de l'eau, le défi consiste toujours à éviter les réactions de recombinaison des charges et également à accélérer la réaction d'oxydation de l'eau. Enfin, il convient de souligner que dans ces exemples de PECs, la quantité de PS et de catalyseurs d'oxydes métalliques déposée à la surface des électrodes est faible et mal contrôlée. Il sera ainsi très intéressant d'explorer de nouvelles méthodes de fabrication et de dépôt à la surface des électrodes de photosensibilisateurs / nanoparticules d'oxyde métallique et d'évaluer l'effet de l'augmentation de la quantité de matériaux et de la structuration du film sur l'intensité du photocourant. C'est ce que nous proposons de réaliser dans le chapitre suivant.

**Chapitre 2.** Ce chapitre se focalise sur le développement de nouvelles photoanodes hydrides et leur utilisation pour l'oxydation photo-induite de l'eau. Sur la base des résultats déjà acquis dans les chapitres précédents (Partie I), le but de ce travail était d'introduire un chromophore moléculaire dans nos matériaux d'électrode nanocomposites d'oxyde de nickel ou de cobalt-poly pyrrole afin d'obtenir l'oxydation de l'eau par voie photo-induite. Pour s'affranchir de l'utilisation de métaux nobles rares et coûteux, nous avons utilisé un photosensibilisateur de la famille du pérylène diimide (PDI). Bien que cette famille soit encore peu explorée pour l'oxydation ou la réduction de l'eau par voie photocatalytique, de telles molécules organiques sont très prometteuses pour ce type de réactions. En effet, les dérivés du pérylène présentent toutes les propriétés requises pour de telles applications: i) robustesse dans l'eau tant à l'état fondamental qu'à l'état excité et photostabilité élevée, ii) forte absorption dans le visible avec un coefficient d'extinction molaire très élevé, iii) propriétés photophysiques et électrochimiques adéquates. En effet, les pérylènes présentent un fort potentiel d'oxydation, permettant l'activation de nombreux oxydes métalliques et de catalyseurs moléculaires. De plus, ils sont constitués uniquement d'éléments abondants et leur structure est facile à fonctionnaliser par différents substituants permettant d'ajuster leurs potentiels redox et d'introduire des groupes électropolymérisables tels que le pyrrole.

Notre stratégie a été de synthétiser un dérivé pérylène avec deux substituants pyrroles électropolymérisables et quatre groupes tert-butylphénoxy encombrants (noté **PyrPDI**) selon une procédure précédemment publiée. La présence des groupements tert-butylphénoxy attracteurs d'électrons donne un potentiel d'oxydation d'environ +1 V par rapport à Ag/AgNO<sub>3</sub> (soit +1,3 V vs Ag/AgCl) suffisamment positif pour oxyder les nanoparticules d'oxyde de nickel ou de cobalt. De plus, ces substituants améliorent la solubilité dans les solvants organiques, facilitant ainsi l'étape de polymérisation. Puisque ce dérivé de pérylène est neutre,

la stratégie employée dans l'étude décrite dans ce chapitre a été de le copolymériser avec le monomère cationique ammonium pyrrole **1** afin d'avoir un film de polypyrrole chargé positivement. Ceci a permis l'introduction de nanoparticules métalliques de nickel ou cobalt par la même stratégie que celle déjà utilisée dans les deux précédents Chapitres 2 et 3 de la Partie I.

Dans ce chapitre, les propriétés électrochimiques et spectroscopiques de **PyrPDI** sont tout d'abord décrites, puis la fabrication des électrodes modifiées correspondantes est présentée. Des photoanodes hybrides associant un chromophore de pérylène et un oxyde de nickel ou de cobalt comme catalyseurs d'oxydation de l'eau ont ensuite été élaborées. Le dérivé **PyrPDI** neutre a été copolymérisé avec le monomère **1** cationique. La charge positive apportée par les unités d'ammonium a permis l'incorporation de particules de NiO<sub>x</sub> et CoO<sub>x</sub> dans les films poly**1**/**PyrPDI** déposés à la surface des électrodes de carbone sans détérioration significative du colorant pérylène. La présence de MO<sub>x</sub> dans les films a été confirmée par des mesures électrochimiques. Les charges de Ni et Co ont également été estimées par des expériences d'ICP-MS et pour la même charge de dépôt (4 mC), la quantité de Ni et de Co déposée correspond à environ 80-83% de celle déposée dans les films C/poly**1** sans pérylène (voir Partie I, Chapitres 2 et 3).

Avec ces photoanodes de C/poly**1**/**PyrPDI**-MO<sub>x</sub>, un photocourant très élevé jusqu'à 750  $\mu\text{A cm}^{-2}$  avec l'oxyde de nickel et jusqu'à 375  $\mu\text{A cm}^{-2}$  avec l'oxyde de cobalt ont été mesurés sous éclairage visible ( $\lambda = 400 - 700 \text{ nm}$ ) à une surtension modérée de  $\eta = +0,3 \text{ V}$  ( $E = + 0,8 \text{ V vs Ag/AgCl}$ ) avec une relativement bonne stabilité dans le temps. Ces valeurs de densité de photocourant dépassent largement celles atteintes par des photoanodes "hybrides" similaires combinant un colorant organique et un oxyde métallique comme catalyseur (voir Partie I, Chapitre 1). Cela peut être dû à la plus grande quantité de colorant et de catalyseur déposée à la surface de l'électrode (non limitée à une seule monocouche). Par ailleurs, la nanostructuration de nos matériaux peut également conduire à un photocourant plus important. En outre, la matrice polymère (film de polypyrrole) peut jouer un rôle favorable pour maintenir l'intégrité des nanoparticules d'oxyde métallique empêchant leur corrosion et ainsi améliorant la stabilité des photoanodes.

Quoi qu'il en soit, d'autres expériences doivent être effectuées pour confirmer l'activité catalytique pour l'oxydation de l'eau par la détection de l'oxygène libéré par chromatographie en phase gazeuse et électrode de Clark. Une photolyse plus longue sera également nécessaire pour évaluer la stabilité et mesurer le rendement faradique de la formation d'oxygène. Par

ailleurs, des caractérisations supplémentaires de ces nouveaux matériaux photoactifs nanocomposites doivent être réalisées par différentes méthodes complémentaires, telles que l'ICP-MS, l'AFM, le MEB couplé à la spectroscopie à rayons X dispersive (EDX), la Spectroscopie Photoélectronique par rayons X (XPS), et la Microscopie Electronique à Transmission à Haute Résolution (HR-TEM) afin d'évaluer la morphologie, la composition chimique, l'état d'oxydation des métaux et la taille des nanoparticules.

Enfin, les photoanodes décrites dans ce chapitre nécessitent une optimisation supplémentaire, par exemple en étudiant l'effet de l'épaisseur du film et de la charge en colorant (rapport **PyrPDI/1**) ainsi que la quantité d'oxyde métallique sur l'activité photocatalytique. L'introduction d'un semi-conducteur tel que le  $\text{TiO}_2$  déposé sur la surface ITO (ou FTO) sera également importante pour concevoir une DS-PEC qui pourront fonctionner avec un potentiel moins positif.

## Table of Contents

General Introduction .....	1
----------------------------	---

### **PART I : Anodes for water oxidation based on nickel and cobalt oxide oxygen-evolving catalyst.....5**

#### *PART I : CHAPTER 1: Anodes based on nickel and cobalt oxides for electrocatalytic water oxidation: A Bibliographic Study.....7*

1. Hydrogen production <i>via</i> water splitting reaction .....	11
2. Nickel Oxide as Electrocatalytic Material for Water Oxidation.....	15
3. Cobalt Oxide as Electrocatalytic Material for Water Oxidation.....	44
References.....	47

#### *PART I : CHAPTER 2: Nickel Oxide-Polypyrrole Nanocomposite Electrode Materials for Electrocatalytic Water Oxidation.....53*

1. Introduction.....	57
2. Results and discussion .....	58
2.1. Electrosynthesis and Electrocharacterization of Nickel Oxide and Poly(pyrrole-alkylammonium)-Nickel Oxide Nanocomposite Electrode Materials .....	58
2.2. Characterization of Nickel Oxide and Poly(pyrrole-alkylammonium)-Nickel Oxide Nanocomposite Electrode Materials by AFM and TEM Microscopies.....	67
2.3. Electrocatalytic performance of Nickel Oxide and Poly(pyrrole-alkylammonium)-Nickel Oxide Nanocomposite Electrodes.....	69
3. Conclusion.....	79
References.....	80

#### *PART I : CHAPTER 3 : Cobalt Oxide-Polypyrrole Nanocomposite Electrode Materials for Electrocatalytic Water Oxidation.....83*

1. Introduction.....	87
2. Results and discussion .....	88

2.1. Electrosynthesis and Electrocharacterization of Cobalt Oxide and Poly(pyrrole-alkylammonium)-Cobalt Oxide Nanocomposite Electrode Materials .....	88
2.2. Characterization of Cobalt Oxide and Poly(pyrrole-alkylammonium)-Cobalt Oxide Nanocomposite Electrode Materials by AFM and TEM Microscopies.....	94
2.3. Electrocatalytic performance of Cobalt Oxide and Poly(pyrrole-alkylammonium)-Cobalt Oxide Nanocomposite Electrodes.....	97
3. Conclusion.....	103
References.....	104

**PART II : Hybrid Photoanodes for Water Oxidation Based on a Molecular Photosensitizer and a Metal Oxide Oxygen-Evolving Catalyst.....105**

*PART II : CHAPTER 1 : Hybrid Photoanodes for Water Oxidation: a Bibliographic Study.....107*

1. Introduction.....	111
2. Hybrid Photoanodes with a Ru-tris-Bipyridine Derivatives as Photosensitizer.....	113
3. Hybrid Photoanodes with an Organic Chromophore.....	117
3.1. Heptazine Chromophore .....	117
3.2. Perylene Chromophore.....	118
3.3. $\pi$ -Conjugated Polymer Naphtalene Based Chromophore... ..	123
3.4. Porphyrin Free Base Chromophore.....	124
4. Conclusion.....	126
References.....	127

*PART II: CHAPTER 2 : Hybrid Photoanodes Based on Nickel or Cobalt Oxide-Polypyrrole nanocomposite Electrode Materials and a Perylene Organic Dye for Photocatalytic Water Oxidation.....129*

1. Introduction.....	133
2. Results and Discussion.....	134
2.1. Electrochemical and Spectroscopic Properties of <b>PyrPDI</b> .....	134

2.2. Electropolymerization of <b>PyrPDI</b> and Electrochemical Behaviour of the Resulting Films .....	136
2.3. Preparation of Hybrid C or ITO/poly <b>1/PyrPDI</b> -MO <sub>x</sub> photoanodes.....	139
2.3.1. Electropolymerization of <b>PyrPDI</b> and <b>1</b> , and the Electrochemical Behaviour of the Corresponding poly <b>1/PyrPDI</b> Modified Electrodes.....	140
2.3.2. Electrogeneration Of Nickel or Cobalt Nanoparticles into poly <b>1/PyrPDI</b> Copolymer.....	143
2.3.3. Photoelectrochemical Activity for Water Oxidation with C/poly <b>1/PyrPDI</b> -MO <sub>x</sub> Photoanodes (M=Ni or Co).....	147
3. Conclusion.....	150
References.....	152
<i>General Conclusion and Perspectives.....</i>	<i>153</i>
<i>Experimental Section.....</i>	<i>157</i>
1. Chemicals and Reagents.....	160
2. Electrodes, Electrochemical Cells and Instrumentation.....	160
3. Preparation of the Nanocomposite Film Modified Electrodes.....	161
3.1. Electrosynthesis of Poly(pyrrole-alkylammonium) Film Modified Electrodes .....	161
3.2. Electrodeposition of Metallic Nanoparticles (M <sup>0</sup> ) and Electrooxidation into Metal Oxide MO <sub>x</sub> (M=Ni or Co).....	163
3.3. Electrodeposition of poly <b>1/PyrPDI</b> -MO <sub>x</sub> Nanocomposite.....	164
4. Determination of M contents (q) on Electrodes by Inductively Coupled Plasma Mass Spectrometry (ICP-MS).....	164
5. Determination of the Average Number of Electron Consumed per Nickel Deposited on Electrodes.....	165
6. Capacitance Measurements.....	165
7. Calculation of Mass Activity and Turnover Frequency (TOF).....	166
8. Tafel Plot.....	167
9. Atomic Force Microscopy (AFM) Observation.....	167
10. Transmission Electron Microscopy (TEM) Observation and Selected Area Electron Diffraction (SAED).....	168
11. Selected Area Electron Microscopy (SAED) Analysis for Nickel.....	168
12. Scanning Electron Microscopy (SEM) Analysis for Cobalt.....	169
13. Irradiation Lamp for Photoelectrolysis.....	170
References.....	171

## General introduction

In the actual energy context, molecular hydrogen ( $H_2$ ) is considered as an attractive clean energy carrier and an excellent alternative to fossil fuels. Fossil fuels, as coal, oil and natural gas, are limited and, even though supply predictions vary significantly, it is clear that we must have technologies utilizing alternative sources of energy that are abundant and ideally unlimited. Although 1 kg of hydrogen generates three times more energy than 1 kg of gasoline which makes  $H_2$  the fuel of the future, there is no natural reserve of  $H_2$  on earth and it cannot be obtained for free from water and needs additional energy to be produced. Nowadays, 95% of molecular hydrogen is produced from fossil fuels through industrial processes (*e.g.* coal gasification and steam reforming of methane), which require high temperature, high pressure and generate carbon dioxide.

A very promising and more sustainable approach is to split water into  $O_2$  and  $H_2$  using only renewable energy sources as solar energy or clean electricity (*e.g.* from wind power). Nevertheless, the oxidative part of this process, water oxidation to molecular oxygen ( $O_2$ ) or oxygen evolving reaction (OER), is a challenging task due to its high activation barrier, its slow electrode kinetic and its large anodic overpotential. Hence, many efforts have been done to develop efficient electrocatalysts displaying long-term stability and a low OER overpotential. Since the beginning of 80's, metal oxides based on first-row transition metals, such as the very popular nickel oxide ( $NiO_x$ ) and cobalt oxide ( $CoO_x$ ), appeared as very promising OER catalysts due to their relative high earth abundance, their low OER overpotential and their corrosion resistance, conferring a great stability under operational conditions. Numerous works have been devoted to implement anodes or photoanodes for water oxidation using metal oxides with high catalytic activity and high stability. Besides, several preparation strategies have been adopted, but the most investigated relies on the control of the porosity and morphology of catalyst' film and of the size of nanoparticles of catalyst, in view to promote the electron/mass transport at the electrode surface, to increase the electroactive surface area of the electrode and thus to enhance their OER catalytic performance.

In this context, this thesis work aims at proposing an original approach, which has been rarely reported in literature, to develop very efficient anodes for electrocatalytic water oxidation reaction based on nanocomposite materials in which nickel oxide or cobalt oxide nanoparticles are inserted in a positively charged poly(pyrrole-alkylammonium) film (denoted

poly1). These nanocomposite materials are prepared by an easy all-electrochemical synthesis at the surface of an electrode. This strategy has also been extended to the design of photoanodes for photocatalytic water oxidation by combining these nanocomposite materials with a robust organic dye of the perylene family.

The first part of this manuscript is devoted to nanocomposites for electro-induced OER. The first chapter presents a bibliographic study on the development of anodes based on nickel and cobalt oxides for electrocatalytic water oxidation. Some relevant examples of anodes are discussed in the light of the general guidelines often used in literature to optimize the activity of catalysts. In conclusion, some general strategies are provided in view to further improve the OER performance of the anodes.

The second chapter of this part is devoted to the electrochemical preparation and the study of nickel oxide-poly(pyrrole-alkylammonium) nanocomposites (poly1-NiO<sub>x</sub>) for the elaboration of highly efficient anode for OER. The poly1-NiO<sub>x</sub> nanocomposite material has been characterized by various electrochemical and physico-chemical techniques. The electrocatalytic properties of this material toward water oxidation in mildly basic (pH 9.2) and basic (pH > 13) conditions is also evaluated and compared with those of a NiO<sub>x</sub> film directly electrodeposited on a naked electrode. Finally, we have performed a careful comparison of the electrocatalytic OER performance of these electrodes at pHs 9.2 and above 13 to that of some nickel-based electrodes previously reported at similar pHs.

Chapter III aims at demonstrating that the original strategy presented in Chapter II, based on the use of nickel oxide/polypyrrole nanocomposite, can be extended to other first-row transition metals as cobalt. So this chapter describes a similar study with cobalt oxides as water oxidation catalyst.

The second part of this manuscript deals with the use of nanocomposites containing the perylene dye for light-driven OER. The part starts with a bibliographic chapter which summarizes the few examples of “hydride” photoanodes for light-driven water oxidation already published, combining a molecular photosensitizer and a metal oxide catalyst.

In the chapter II, the results concerning the development of new hybrid photoanodes combining a perylene diimine chromophore and nickel or cobalt oxide as water oxidation catalyst are described. The strategy explored was to copolymerize the cationic ammonium pyrrole monomer and a neutral perylene diimine derivative having pyrrole substituents and to

use this positively charged copolymer to introduce metal oxide nanoparticles. Finally, the photoelectrochemical activity for water oxidation of these hydride photoanodes based on photoactive nanocomposite materials has been investigated by the measure of photocurrents under visible light irradiation.

**ANODES FOR WATER OXIDATION BASED ON  
NICKEL AND COBALT OXIDE OXYGEN-  
EVOLVING CATALYST**



Anodes based on nickel and cobalt oxides for  
electrocatalytic water oxidation: A Bibliographic Study



## Index

1. Hydrogen Production <i>via</i> Water Splitting. ....	11
2. Nickel Oxide as Electrocatalytic Material for Water Oxidation.....	15
3. Cobalt Oxide as Electrocatalytic Material for Water Oxidation .....	25
4. Conclusions .....	44
References .....	47



## 1 - Hydrogen production *via* water splitting reaction

In the actual energy context, molecular hydrogen ( $H_2$ ) is considered as an attractive clean energy carrier and an excellent alternative to fossil fuels. Fossil fuels, as coal, oil and natural gas, are limited and, although supply predictions vary significantly, it is clear that we must have technologies to utilize alternative sources of energy that are abundant and ideally unlimited.  $H_2$  is proposed as a solution to the energy problem for several reasons: (1) hydrogen is one of the most plentiful elements on the earth and is one of the constituent elements of water; (2)  $H_2$  has a high energy density ( $120 \text{ MJ kg}^{-1}$ ) and 1 kg of hydrogen generates three times more energy than 1 kg of gasoline (energy density of  $44.4 \text{ MJ kg}^{-1}$ ); (3) the combination of molecular hydrogen and oxygen ( $O_2$ ) in a fuel cell produces heat and electricity; (4) the only byproduct of the combination of  $H_2$  and  $O_2$  is water, while burning fossil fuels generates  $CO_2$ , a greenhouse gas; (5) prototype cars powered by fuel cell can use directly  $H_2$ . However, there is no natural reserve of  $H_2$  on earth and it cannot be obtained for free from water and requires additional energy to be produced. Therefore molecular hydrogen is not an alternative fuel, but a promising energy carrier.<sup>1</sup> The challenge is then to produce it at a large scale and with an attractive cost, without using fossil fuels.

Today, 95% of molecular hydrogen is produced from fossil fuels through various industrial processes (*e.g.* coal gasification and steam reforming of methane), which require high temperature, high pressure and generate carbon dioxide. A very promising and more sustainable approach is to split water into  $O_2$  and  $H_2$  using only renewable energy sources as solar energy or clean electricity (*e.g.* from wind power).<sup>1,2</sup> Indeed, this approach is largely in exploiting carbon-neutral technologies, such as wind, tidal, nuclear, and solar.<sup>3</sup> Light-driven water splitting reaction, which is one of the most seducing approaches to produced  $H_2$  since it could stem from an almost inexhaustible source of energy, will be presented and discussed in part II of the manuscript.

Electro-induced water splitting, also called electrolysis of water, is mature technology known for around 200 years,<sup>4</sup> but only 4% of  $H_2$  worldwide is produced by this process due to its expensive cost. According to a brief essay of de Levie,<sup>5</sup> the phenomenon of water splitting was first reported in 1789 by two Dutchmen, van Trootswijk and Deiman,<sup>6</sup> following by Pearson<sup>7</sup> in 1797 and Nicholson<sup>8</sup> in 1800. Afterwards, in 1874 Jules Verne wrote in his fiction's novel "The Mysterious Island" through one of the main protagonists Cyrus Smith: "*I believe that water will one day be employed as fuel, that hydrogen and oxygen which*

constitute it, used singly or together, will furnish an inexhaustible source of heat and light, of an intensity of which coal is not capable.... Water will be the coal of the future". By 1902, more than 400 industrial electrolyzers were in operation to produce H<sub>2</sub> and the latter was widely used in combination with carbon monoxide (mixture called "town gas" or "water gas"), to heat and light homes and streets, confirming the visionary writings of Jules Verne.<sup>9</sup>

The water splitting is an arduous reaction, clearly endergonic ( $\Delta G^0 > 0$ ), that can be used to store energy in the chemical bond of hydrogen: <sup>10</sup>



Water splitting consist of two half reactions, hydrogen and oxygen evolution reactions (eqs 2 and 3), respectively denoted HER and OER, which can be investigated separately. Among both reactions, OER remains the bottleneck of water splitting since it involves four electron transfers coupled to protons transfers and the formation of the O-O bond. Consequently, OER requires a large anodic overpotential and displays a high activation barrier and slow electrode kinetics.



Although many metal complexes have been developed to catalyze this reaction inspired from the natural Oxygen Evolving Center (OEC) of photosystem II in plants,<sup>11,12</sup> metal oxides (MO<sub>x</sub>) with high oxidation states remain one of the most promising electrocatalysts in terms of catalytic efficiency and stability. Indeed, many efforts are thus turned towards developing inorganic catalysts which are stable and highly active for OER (by lowering its activation barrier), in view to be deposited on conducting electrodes to implement anodes. Among those, noble metal oxide as RuO<sub>2</sub> and IrO<sub>2</sub> are known to be among the best OER catalysts in acidic and alkaline solutions due their low overpotential and high catalytic current.<sup>13</sup> However, these catalysts suffer from instability through corrosion under anodic potential and contain costly and rare metals that are not compatible with large-scale H<sub>2</sub> production. In view to their substitution, many metal oxides based on more earth abundant first-row transition metals (*e.g.* Mn,<sup>14-24</sup> Fe,<sup>25-30</sup> Co<sup>31-56</sup> and Ni<sup>57-71</sup>) have been investigated under various oxide forms such as perovskite (ABO<sub>3</sub>; A = alkaline and/or rare-earth metals, B = transition metals), spinel (A'B<sub>2</sub>O<sub>4</sub>; A' = alkaline-earth and/or transition metals, B' = group 13 elements and/or

transition metals) and oxyhydroxide (M(O)(OH); M = transition metals), and have shown very promising electrocatalytic performances.<sup>72,13,73–77</sup>

The interest of the scientific community for the hydrogen production *via* the water splitting reaction is growing so much that the number of articles related to this issue exponentially increases since 2005, achieving more than 2040 articles only for 2017, which corresponds to 5-6 publications per day (Figure 1). In spite of the fact that it is a tedious and arduous task to give an exhaustive overview of all molecular and inorganic catalysts developed for water splitting reaction, and especially for OER, several groups have published more or less comprehensive reviews on different aspects of the issue.

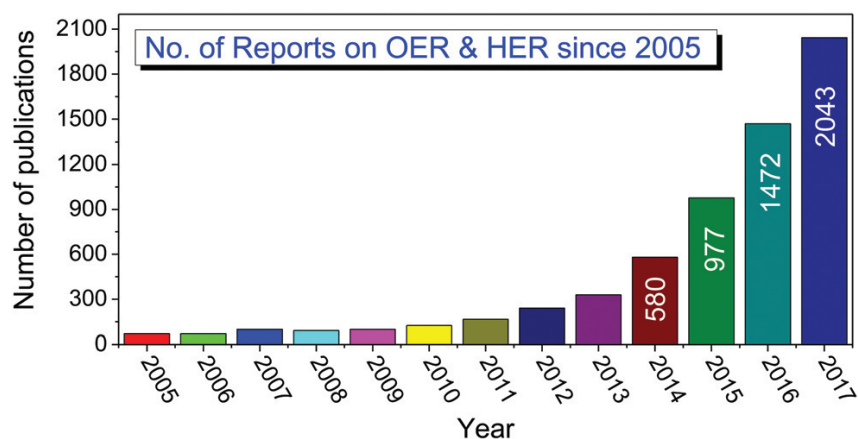


**Figure 1.** Histogramm of the number of articles dedicated to oxygen and hydrogen evolving reaction (OER and HER respectively) since 2005 (Reproduced from Ref<sup>78</sup>, with the permission from the Royal Society of Chemistry, Copyright 2018).

The groups of Åkermark and Brudvig reviewed molecular catalysts for water oxidation to achieve artificial photosynthesis using Ru, Ir, Mn, Cu, Fe and Co.<sup>11,12</sup> The group of Verpoort reported earth-abundant metal complexes for water oxidation, and tried to highlight the link between homogeneous and heterogeneous catalysts, *i.e.* the conversion of molecular catalysts during catalysis into nanoparticles of metal oxides or hydroxides, known to be robust OER catalysts.<sup>79</sup> Recent reviews dealing with inorganic OER catalysts based on abundant first row-transition metals, especially Mn, Fe, Co and Ni, have been reported by the groups of Galán-Mascarós,<sup>74</sup> Wang<sup>76</sup> and Müller.<sup>75</sup> The group of Spiccia also reviewed molecular and inorganic OER catalysts using Mn, Fe, Co, Ni and Cu, and their application for photoelectrochemical devices towards light-driven water splitting.<sup>73</sup> Otherwise, the groups of Xu and Chen reviewed the recent development and perspectives of electrocatalysts for OER composed of metal oxides and their various forms, such as perovskite, spinel and layer double hydroxide (LDH) families, of non-oxide catalysts as metal chalcogenides (sulfides, selenides, tellurides), metal pnictides (nitrides, phosphides) and organometallics, and of metal-free

compounds as carbon nanotubes and graphene doped by N, O and S.<sup>13</sup> Finally, the groups of Boettcher<sup>80</sup> and Dai<sup>81</sup> discussed within short reviews about the activity trend and the design principles of oxides and (oxy)hydroxides of Ni and Co (the most investigated inorganic catalysts for OER), and the effect of Fe impurities on their OER activity.

In the light of the large number of publications and reviews about inorganic electrocatalysts for water oxidation, it is vital to estimate their catalytic activity and to classify them in function of their performance. The main activity parameters used for the evaluation of OER catalysts are, to name a few, OER overpotential at a defined current density (or catalytic current density at a defined overpotential), stability over time of catalyst at a constant potential or current density, mass activity (*i.e.* catalytic current per mass of metal) and turnover frequency (TOF) at a defined overpotential, faradaic yield and Tafel slope value.<sup>78</sup> Basically, a good OER catalyst present a low overpotential at 10 mA cm<sup>-2</sup> (below 0.4 V), a high stability (sustained OER activity beyond 10 hours), high values of mass activity and TOF (*e.g.* above 1.0 A mg<sup>-1</sup> and 1.0 s<sup>-1</sup> respectively), a high faradaic yield towards OER close to 100% and a low Tafel slope (below 60 mV dec<sup>-1</sup>, correlated to high kinetics of catalysis).

In view of the activity parameters mentioned above, the anodes based on nickel and cobalt oxides are among the most investigated electrodes for OER owing to their high stability in alkaline conditions and their high catalytic activity, especially when they are doped with iron salts. For these reasons, we decided to use nickel and cobalt oxides for demonstrating the great potentialities of our approach to build anodes and photoanodes for OER, that consists in employing nanostructured composite materials in which metal oxide nanoparticles are dispersed within poly(pyrrole-alkylammonium). The latter polymer matrix allows electrogenerating small and non-agglomerated nanoparticles of metal oxides, conferring a great nanostructuring of material, a high electroactive surface area and thus a high catalytic performance. These new materials will be presented in the Chapters 2 and 3 of Part I for the implementation of anodes and in the Chapter 2 of Part II for photoanodes.

The next sections of this chapter will be then focused only on nickel oxide and cobalt oxide based anodes for OER. These sections do not list exhaustively all the anodes of the literature using nickel and cobalt oxides, but presents only the more significant examples.

## 2 - Nickel Oxide as Electrocatalytic Material for Water Oxidation

Nickel hydroxide and oxyhydroxide present one of the most studied redox systems in electrochemistry, due to their practical utilization in technologic areas like alkaline batteries and electrolysis cells.<sup>72</sup> For instance, Ni(OH)<sub>2</sub> was widely used as a cathode in Ni-Cd and Ni-Metal Hydride batteries. In the last century, it was discovered that nickel oxides have a good electrocatalytic activity toward OER in alkaline solution.<sup>81</sup> In fact, nickel is an earth-abundant first row transition metal with good ductility and high corrosion resistance in aqueous alkaline media and low cost, which make them an attractive material for OER. It is now well-recognized that nickel and cobalt oxides and their mixed oxides exhibit very promising electrocatalytic properties for the electrochemical oxidation of water, and nickel and its alloys are a good alternative to replace the benchmark inorganic catalysts as IrO<sub>2</sub> and RuO<sub>2</sub> for water electrolysis, even if their overpotential for OER is often higher than that of IrO<sub>2</sub> and RuO<sub>2</sub>.

There are different methods to prepare hydroxide electrodes, *i.e.* Ni(OH)<sub>2</sub>, by chemical or physical methods as sol-gel processes, hydrothermal synthesis, chemical precipitation, vacuum evaporation, mechanical grinding, pyrogenation, electrostatic spray deposition and electron beam deposition, sputtering and vapour deposition techniques.<sup>82</sup> Besides, there are different ways to obtain thin layers of Ni(OH)<sub>2</sub> film, as by chemical co-precipitation by alternate immersion in Ni(SO<sub>4</sub>)<sub>2</sub> or Ni(NO<sub>3</sub>)<sub>2</sub> solutions, or in mixtures of nitrates or sulfates of other metals in alkaline solution.<sup>83</sup> The most used and simple method is electrochemical deposition by potentiostatic, galvanostatic, potentiodynamic or pulse techniques, where the conductive material is coated with a metal oxide or hydroxides anodically or cathodically. With the electrochemical deposition technique, it is possible to have a control of the physical and chemical properties of the surface nanostructure of the metal oxide film, changing deposition parameters as current density and the concentration of nickel salt in solution. It is also possible to obtain various morphologies as nanoparticles, nanoneedles and nanorods.<sup>82-83</sup>

The redox properties of nickel oxides are highly influenced by the nature of the oxide (structure of oxide, doping agents, etc...) and the manner of its preparation. For instance, the deposition of Ni(OH)<sub>2</sub> films, which is often performed from Ni(NO<sub>3</sub>)<sub>2</sub>, occurs in that case by the direct or indirect reduction of nitrate ion to either nitrous acid, hydroxylamine or nitrite

ion. In all cases, the generated hydroxyl ion promotes the formation of  $\alpha$ -Ni(OH)<sub>2</sub> or  $\beta$ -Ni(OH)<sub>2</sub> according to the equation (4).



Ni(OH)<sub>2</sub> can also be prepared by cyclic voltammetry in presence of Ni<sup>2+</sup> and OH<sup>-</sup> ions in an aqueous buffer solution. Under these conditions, the process may occur at anodic potentials following the equations (5) and (6).



Besides, the redox properties of nickel oxides/hydroxides can be strongly influenced by the experimental conditions of electrodeposition such as the nature of the electrolyte, the nature of the electrode or the applied potential. For instance, the group of Lyons demonstrated that sweep rate, during an electrodeposition of Ni(OH)<sub>2</sub> through cyclic voltammetry, can significantly affect the composition of deposited oxide films.<sup>84</sup> The Figure 2 displays redox signatures of nickel oxide films electrodeposited *via* 30 cycles at various sweep rates. They showed that the  $\alpha$ -Ni<sup>II</sup>(OH)<sub>2</sub>/ $\gamma$ -Ni<sup>III/IV</sup>O(OH) redox transition (according to the Bode's diagram, see below) is observed with a relative fast sweep rate of 50 mV s<sup>-1</sup>, while at slower rate of 10-20 mV s<sup>-1</sup> cyclic voltammograms exhibit a mixture of  $\alpha$ -Ni<sup>II</sup>(OH)<sub>2</sub>/ $\gamma$ -Ni<sup>III/IV</sup>O(OH) and  $\beta$ -Ni<sup>II</sup>(OH)<sub>2</sub>/ $\beta$ -Ni<sup>III</sup>O(OH). This difference in the oxide composition was ascribed to a dehydration of the oxides occurring at slow sweep rate (*i.e.* at long experimental timescale) favouring the formation of  $\beta$ -Ni<sup>II</sup>(OH)<sub>2</sub>.

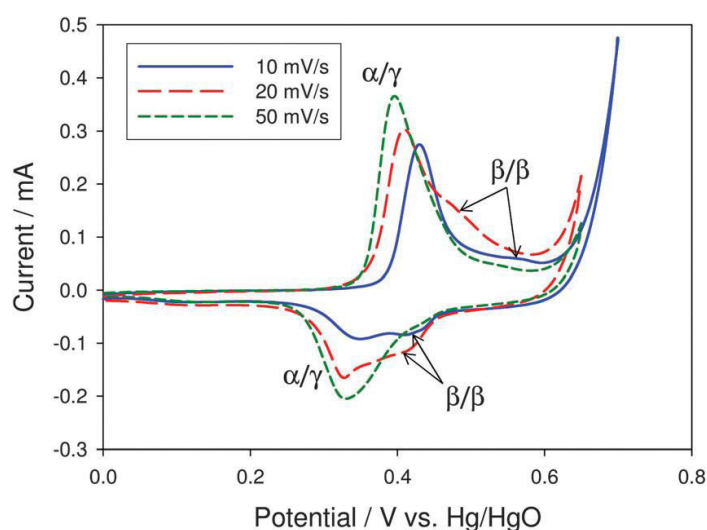
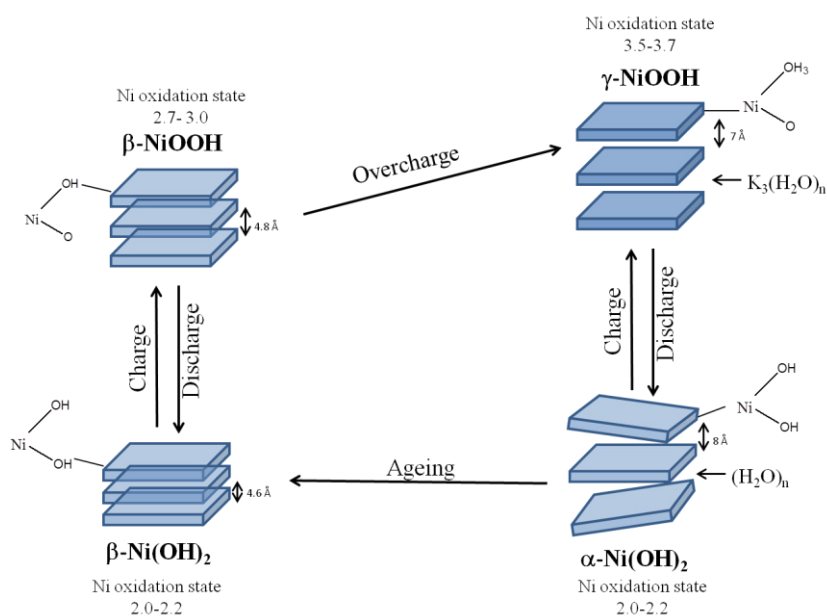
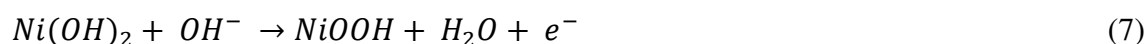


**Figure 2.** Cyclic voltammograms recorded in 1.0 M NaOH at 40 mV s<sup>-1</sup> for Au electrode modified with nickel hydroxide films deposited using 30 growth cycles performed at a sweep rate of 10, 20 and 50

$\text{mV s}^{-1}$  (reproduced from ref <sup>84</sup> with the permission from the Royal Society of Chemistry, Copyright 2013).

Basically, according to the Bode's diagram (Scheme 1), nickel oxide can be represented by four phases,  $\alpha\text{-Ni}^{\text{II}}(\text{OH})_2$ ,  $\beta\text{-Ni}^{\text{II}}(\text{OH})_2$ ,  $\beta\text{-Ni}^{\text{III}}\text{O}(\text{OH})$  and  $\gamma\text{-Ni}^{\text{III/IV}}\text{O}(\text{OH})$ , and their nature and structure will depend on the method of preparation, degree of hydration, concentration of defects, etc.... Scheme 1 presents for each phase the oxidation state of nickel, the distances between the average crystallographic plans and the schematic organization of the plans. It is important to mention that Bode cycle is specific for electrodeposited nickel hydroxides. In Scheme 1 are presented two main different redox transitions,  $\beta/\beta$  and  $\alpha/\gamma$ . The reduced (discharged)  $\text{Ni}(\text{OH})_2$  film can exist as the anhydrous  $\beta\text{-Ni}(\text{OH})_2$  phase, or as the hydrated  $\alpha\text{-Ni}(\text{OH})_2$  phase.  $\beta\text{-Ni}(\text{OH})_2$  can be oxidized to the  $\beta\text{-NiO}(\text{OH})$  phase, meanwhile  $\alpha\text{-Ni}(\text{OH})_2$  can be converted to  $\gamma\text{-NiO}(\text{OH})$  phase. Finally, upon ageing in concentrated alkaline solution the  $\alpha\text{-Ni}(\text{OH})_2$  phase dehydrates and recrystallizes as  $\beta\text{-Ni}(\text{OH})_2$ , meanwhile under overcharging at very anodic potentials  $\beta\text{-NiO}(\text{OH})$  can be transformed to  $\gamma\text{-NiO}(\text{OH})$  phase.<sup>82</sup> So, the redox transition process of  $\text{Ni}(\text{OH})_2/\text{NiO}(\text{OH})$  (Eq. 7) recorded by cyclic voltammetry can give an idea about the nature of OER active sites deposited on the electrode surface.



**Scheme 1.** Bode's schematic representation for the cycle of  $\text{Ni}^{\text{II}}/\text{Ni}^{\text{III/IV}}$  redox transition in nickel hydroxide layers (Adapted from Ref <sup>83</sup>).

Different groups of research prepared OER catalysts based on nickel oxide using the different electrochemical techniques mentioned above. To name some of them,<sup>85</sup> the group of Nocera

studied a catalyst of nickel-borate (Ni-B<sub>i</sub>) for oxygen evolution at near-neutral pH 9.2. They electrodeposited nickel oxyhydroxide (*i.e.* NiO(OH)) from Ni<sup>2+</sup> in a borate buffer solution pH 9.2 by cyclic voltammetry on glassy carbon of 0.07 cm<sup>2</sup>. From the charge integration of the anodic peak of Ni(OH)<sub>2</sub>/NiO(OH), the surface density was determined to be approximately 5 Ni atoms/25 Å<sup>2</sup>, corresponding to a monolayer coverage of catalyst with an integrated charge of ~ 300 μC cm<sup>-2</sup>. The authors demonstrated that film formation and catalysis do not occur in absence of B<sub>i</sub> electrolyte, suggesting that the presence of a proton-accepting electrolyte is important for facilitating the film electrodeposition and the catalytic oxygen evolution. Ni-B<sub>i</sub> exhibits an interesting catalytic performance of 1 mA cm<sup>-2</sup> at overpotential of ~425 mV at pH 9.2, along with quantitative faradaic yield for OER and a high stability under electrocatalytic conditions with no corrosion in water. In order to study the morphology of the catalytic material, thicker films of Ni-B<sub>i</sub> were prepared on fluorine tin oxide (FTO) electrodes (thickness of 3-4 μm) passing 10 C cm<sup>-2</sup> at 1.3 V *vs.* NHE. The scanning electron microscopy (SEM) and powder X-ray diffraction (XRD) of Ni-B<sub>i</sub> showed its amorphous nature. From the elemental analysis of the dry film, its composition was determined to be Ni<sup>III</sup>O(OH)<sub>2/3</sub>(H<sub>2</sub>BO<sub>3</sub>)<sub>1/3</sub>•1.5 H<sub>2</sub>O, which is undoubtedly quite different from that of the wet catalyst under operational conditions. This confirms that the catalytic material is composed of nickel oxyhydroxide associated with borate anions. To further characterize its catalytic activity, a Tafel Plot was performed on FTO/Ni-B<sub>i</sub> with current densities between 1 mA cm<sup>-2</sup> and 7 μA cm<sup>-2</sup> giving a slope of ~59 mV dec<sup>-1</sup>. It is important to mention that, for obtaining reproducible values of Tafel slope, the anode underwent a preelectrolysis over 12h at a current density of ~1 mA cm<sup>-2</sup>. Conversely, electrodes with freshly prepared Ni-B<sub>i</sub> without preconditioning exhibit Tafel slopes around 120 mV dec<sup>-1</sup>, while nickel oxide based anodes of literature present values between 40 and 80 mV dec<sup>-1</sup>. Finally the electrodeposited film shows a high stability to cathodic bias after 100 scans by cycling voltammetry, suggesting that the Ni-B<sub>i</sub> catalyst film may also present O<sub>2</sub> reduction activity.

In a following work,<sup>86</sup> Nocera and coworkers showed that the catalytic performance of Na-B<sub>i</sub> can be significantly improved by an anodic activation of the film *via* an electrolysis at 1.1 V *vs* NHE in a borate buffered aqueous solution at pH 9.2, inducing a change of structure and oxidation state of catalyst. To have a clearer insight on the nature of Na-B<sub>i</sub> film after its anodization and during OER catalysis, the authors studied these changes by in situ X-ray absorption spectroscopy (XAS), such as in situ X-ray absorption near-edge structure (XANES) and extended X-ray absorption fine structure (EXAFS). The XANES

measurements reveal that nickel within anodized films displays an average oxidation state of +3.6, ascribe to a  $\gamma$ -NiO(OH) phase with a large proportion of Ni<sup>IV</sup>, while the Ni oxidation state in nonactivated films is 3.16 corresponding to  $\beta$ -NiO(OH) which essentially contains Ni<sup>III</sup>. The average of Ni oxidation state within activated and nonactivated films was also confirmed by coulometric titration coupled to ICPMS measurements (Inductively Coupled Plasma Mass Spectrometry). From the structural parameters extracted from EXAFS data of anodized films, the authors proposed that Ni<sup>IV</sup> atoms are connected by bis-oxo/hydroxo bridges within sheets of edge-sharing NiO<sub>6</sub> octahedra highly ordered, as usually observed in  $\gamma$ -NiO(OH), with a domain size of *c.a.* 2 nm (Figure 3). Otherwise, the EXAFS measurements on the nonactivated Na-B<sub>i</sub> film reveal a similar oxidic nature of the metal center and a Jahn-Teller distortion in its coordination sphere, characteristic of a low spin d<sup>7</sup> Ni<sup>III</sup> that is found in the  $\beta$ -NiO(OH) phase. This study clearly demonstrates that the increase of activity of Na-B<sub>i</sub> film after its anodization is correlated to the conversion of  $\beta$ -NiO(OH) to  $\gamma$ -NiO(OH) and that the  $\gamma$  phase is more active towards OER than the  $\beta$  phase, contradicting the long-held notion that the catalytic performance of  $\beta$ -NiO(OH) is superior to that of  $\gamma$ -NiO(OH).

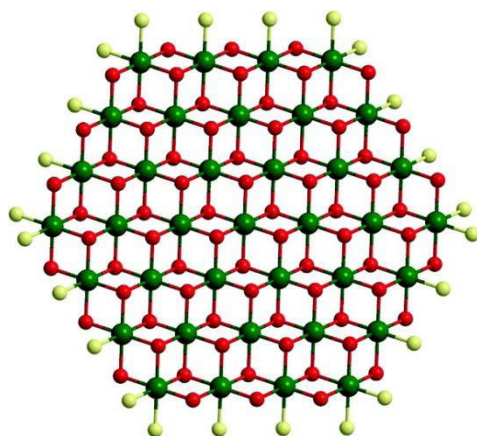


**Figure 3.** Simplified hexagonal cluster model of Ni-B<sub>i</sub> with an average domain size between 2 and 3 nm. Ni ions are shown in green, bridging oxo/hydroxo ligands are shown in red, and nonbridging oxygen ligands, which may include water, hydroxide, or borate, are shown in pale green (reproduced from ref<sup>86</sup>, with the permission from the American Chemical Society, Copyright 2012).

The group of Spiccia<sup>59</sup> also studied nickel oxide films (denoted NiO<sub>x</sub>) obtained through the electro-decomposition of nickel complexes in borate buffer. The authors prepared uniform films of NiO<sub>x</sub> particles from a Ni(II) diamine complex as [Ni(en)<sub>3</sub>]Cl<sub>2</sub> (denoted NiO<sub>x</sub>-en, where en = 1,2-diaminoethane), by electrochemical deposition on glassy carbon (C) or FTO electrodes at a constant applied potential of 1.1 V vs Ag/AgCl at pH 9.2 in a 0.1 M borate buffer (NaB<sub>i</sub>) solution. Its OER catalytic activity was then compared with that of NiO<sub>x</sub> films

obtained from the electro-decomposition of  $[\text{Ni}(\text{H}_2\text{O})_6]^{2+}$  and  $[\text{Ni}(\text{NH}_3)_6]^{2+}$  complexes (respectively denoted  $\text{NiO}_x\text{-aqua}$  and  $\text{NiO}_x\text{-NH}_3$ ) performed under similar conditions.  $\text{NiO}_x\text{-en}$  displayed a stable catalytic current of  $1.8 \text{ mA cm}^{-2}$  over a long period of 6h at pH 9.2 and 1.1 V vs Ag/AgCl (*i.e.* at overpotential of 0.61 V), while  $\text{NiO}_x\text{-aqua}$  and  $\text{NiO}_x\text{-NH}_3$  only produced  $1.2 \text{ mA cm}^{-2}$  at the same overpotential. Note that the difference of catalytic performance between these films are not due to a difference of nickel mass deposited on electrode since almost the same amount of nickel was deposited, *c.a.*  $0.28 \text{ } \mu\text{mol cm}^{-2}$  (determined by ICPMS). From these ICPMS data, the TOF value was also estimated to be  $0.015 \text{ s}^{-1}$  per deposited Ni center for  $\text{NiO}_x\text{-en}$ , which is slightly superior to that of  $\text{NiO}_x\text{-aqua}$  ( $0.011 \text{ s}^{-1}$ ).

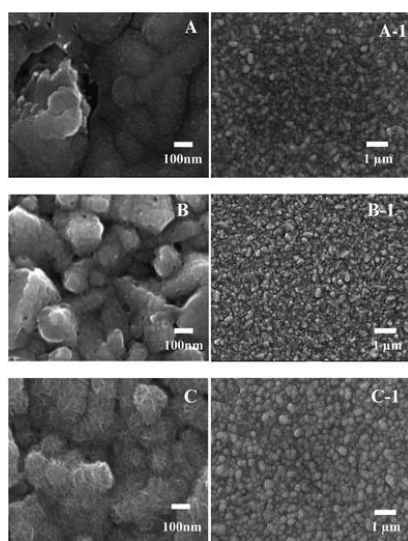


**Figure 4.** High (left side) and low (right side) magnification SEM images of  $\text{NiO}_x\text{-aqua}$  (A, A-1),  $\text{NiO}_x\text{-NH}_3$  (B, B-1) and  $\text{NiO}_x\text{-en}$  (C, C-1) films deposited on FTO electrode. (reproduced from ref <sup>59</sup>, with the permission from the Royal Society of Chemistry, Copyright 2013).

The highest catalytic performance of  $\text{NiO}_x\text{-en}$  film compared to that of  $\text{NiO}_x\text{-aqua}$  and  $\text{NiO}_x\text{-NH}_3$  was ascribed to the great difference in morphology between these films, as supported by SEM and capacitance measurements. SEM images of the  $\text{NiO}_x\text{-en}$  film show homogeneous dendritic features with particles size between 300 and 350 nm (Figure 4). By contrast, SEM images of  $\text{NiO}_x\text{-NH}_3$  and  $\text{NiO}_x\text{-aqua}$  present a similar morphology of packed particles of size between 250 and 500 nm, heterogeneously deposited with numerous pinholes. So,  $\text{NiO}_x\text{-en}$  film possesses higher electroactive surface area than  $\text{NiO}_x\text{-NH}_3$  and  $\text{NiO}_x\text{-aqua}$ , explaining the highest catalytic activity of  $\text{NiO}_x\text{-en}$  towards OER. Besides, the great catalytic performance of  $\text{NiO}_x\text{-en}$  was attributed to the presence of  $\gamma\text{-NiO}(\text{OH})$  in the film, as supported by XANES and EXAFS measurements, confirming the previous observation of Nocera's group (see above).

Due to the fact that molecular complexes were proved to be good precursors for deposition of catalysts based on metal oxides films, the group of Spiccia<sup>60</sup> in a following work obtained  $\text{NiO}_x$  particles *via* electro-decomposition on the surface of C and FTO electrodes of three other macrocyclic nickel(II) amine complexes,  $[\text{Ni}(\text{tacn})(\text{OH}_2)_3]^{2+}$ ,  $[\text{Ni}(\text{tacn})_2]^{2+}$  (tacn = 1,4,7-triazacyclononane), and  $[\text{Ni}(\text{cyclen})(\text{OH})_2]^{2+}$  (cyclen = 1,4,8,11-tetraazacyclotetradecane), at pH 9.2 and 12.9 from buffered solutions with  $\text{NaB}_i$  and  $\text{NaOH}$ , respectively. The films were deposited using 1.0 mM of each Ni(II) complexes by CPE (Constant potential electrolysis) at 1.1 V vs. Ag/AgCl in 0.1 M  $\text{NaB}_i$  buffer, and at 0.75 V vs. Ag/AgCl for 0.1 M  $\text{NaOH}$

solution. Films deposited from  $[\text{Ni}(\text{tacn})(\text{OH}_2)_3]^{2+}$ ,  $[\text{Ni}(\text{tacn})_2]^{2+}$ ,  $[\text{Ni}(\text{OH}_2)_6]^{2+}$  and  $[\text{Ni}(\text{cyclen})(\text{OH})_2]^{2+}$  with  $\text{NaB}_i$  buffer are abbreviated as tacn-Bi, SWtacn-Bi,  $\text{NiO}_x$ -aqua and cyclen-Bi, meanwhile the film deposited from  $[\text{Ni}(\text{tacn})_2]^{2+}$  in  $\text{NaOH}$  electrolyte is abbreviated as SWtacn-OH.

The linear sweep voltammograms (LSV) of all  $\text{NiO}_x$  films studied herein at pH 9.2 (0.6 M  $\text{NaB}_i$ ) display similar catalytic OER activities (Figure 5).<sup>60</sup> Applying a CPE of 1.10V,

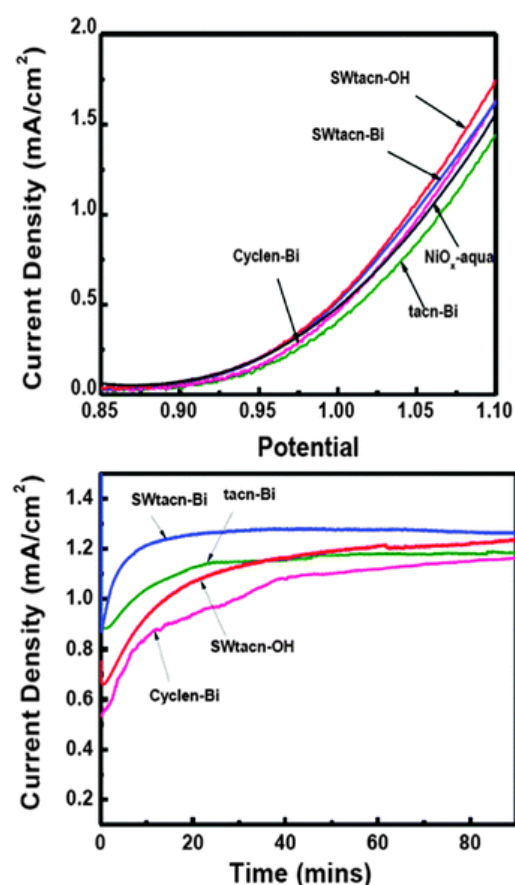


**Figure 5.** LSVs of  $\text{NiO}_x$  films deposited on FTO electrode obtained from the  $\text{Ni}^{\text{II}}$  complexes of this study (scan rate  $1 \text{ mV s}^{-1}$ ) (top) and the corresponding CPEs performed at  $1.10 \text{ V vs Ag/AgCl}$  (bottom) in  $0.6 \text{ M NaB}_i$  buffer (pH 9.2) (reproduced from ref <sup>60</sup>, with the permission from the Royal Society of Chemistry, Copyright 2013).

depositions of  $\text{Ni} \sim 0.26 \mu\text{mol cm}^{-2}$  were realized (determined by ICPMS) for the  $\text{NiO}_x$  films derived from the four complexes in  $\text{NaB}_i$  Buffer (pH 9.2) and the latter films have presented almost identical catalytic performances of  $1.2\text{-}1.3 \text{ mA cm}^{-2}$  at a  $\eta$  of  $0.6 \text{ V}$ , with a Faradaic efficiency of the film of  $90\%$  after  $2 \text{ h}$  of operation. During approximately  $4 \text{ h}$  of electrolysis, similar values were obtained in the previous work. The complexes deposited in buffer  $\text{NaB}_i$  and  $\text{NaOH}$  electrolyte were also studied in  $0.1 \text{ M NaOH}$  electrolyte by LSV showing an onset potential of  $0.63 \text{ V vs. Ag/AgCl}$  ( $\eta \sim 0.37 \text{ V}$ ). The CPE at  $0.75 \text{ V}$  ( $\eta = 0.49 \text{ V}$ ) for the  $\text{NiO}_x$  film in  $\text{NaOH}$  buffer produces a current density of  $1.5\text{-}1.6 \text{ mA cm}^{-2}$  at pH 12.9, running during  $2 \text{ hours}$ . An increase of pH increases the catalytic activity and the onset of catalysis. The catalytic activity was studied also by Tafel plot in  $\text{NaB}_i$  electrolyte, slopes between  $100$  and  $110 \text{ mV dec}^{-1}$  were obtained for all films. The SEM characterization of all films shows homogeneous deposition with well-defined grain boundaries. SWtacn-Bi and SWtacn-OH films present a similar morphology. New SEM images were recorded after  $30 \text{ min}$  of CPE in  $\text{NaB}_i$  solution and the films exhibit no changes in morphology. X-ray (EDS) analyses for SWtacn-Bi and SWtacn-OH show a similar elemental composition but it was found some  $\text{Na}^+$  ions in SWtacn-OH film, meanwhile films deposited in  $\text{NaB}_i$  do not. However the  $\text{Na}^+$  ions do not affect the catalytic activity. Profilometry

measurements were performed to estimate the film thickness. With a charge of  $50 \text{ mC cm}^{-2}$  for the deposition of  $\text{NiO}_x$  films, it was found an average thickness of 0.12, 0.11 and  $0.13 \mu\text{m}$  for SWtacn-Bi, tacn-Bi and cyclen-Bi respectively; whereas a thicker film ( $0.20 \pm 0.02 \mu\text{m}$ ) was obtained for SWtacn-OH. The IR spectra of  $[\text{Ni}(\text{tacn})_2]^{2+}$  and SWtacn-Bi films confirm the deposition of  $\text{NiO}(\text{OH})$  films. Finally the Raman spectrum of SWtacn-Bi supports the presence of  $\gamma\text{-NiO}(\text{OH})$  phase in the  $\text{NiO}_x$  film.

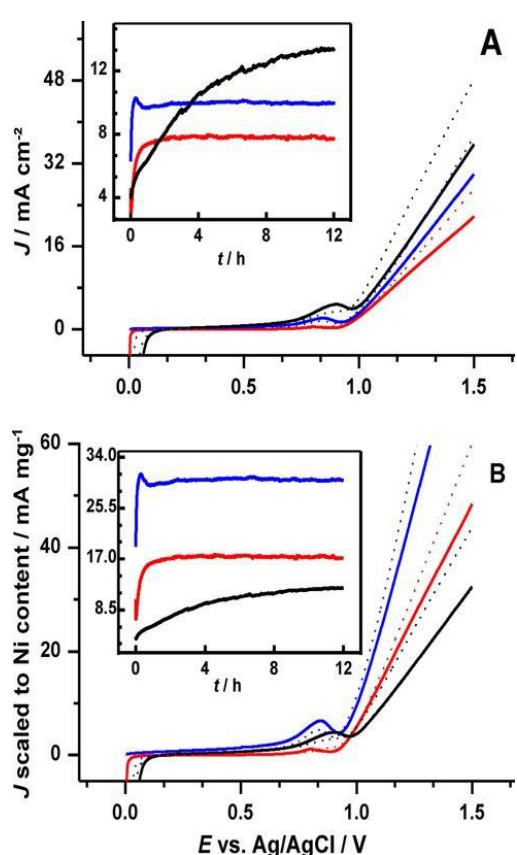


**Figure 6.** LSVs of (A) fresh NiO-MB (red line), NiO-NP (black line), NiO-NP1 (blue line), anodized NiO-MB (dashed red line), anodized NiO-NP (dashed black line), and NiO-NP1 (dashed blue line) films in 0.60 M  $\text{NaB}_4$  buffer (pH 9.2; scan rate of  $20 \text{ mV s}^{-1}$ ). Inset shows CPEs of 12h for NiO-MB, NiO-NP and NiO-NP1 films in 0.60 M  $\text{NaB}_4$  buffer at 1.10 V vs. Ag/AgCl ( $\eta = 0.62 \text{ V}$ ). (B) Data of (A) scaled against Ni content of each film. (reproduced from ref <sup>87</sup>, with the permission from Wiley, Copyright 2015).

Finally the group of Spiccia<sup>87</sup> studied screen-printed nickel oxide on FTO electrode for water oxidation. They synthesized NiO-MB microballs ( $0.45 \text{ mg cm}^{-2}$  of Ni content) with spherical morphology ( $3 \mu\text{m}$  diameter) by thermolysis method and compared the activity with commercial NiO-NP nanoparticles ( $1.1 \text{ mg cm}^{-2}$  of Ni content). NiO-NP ( $14.4 \text{ mA cm}^{-2}$  at  $\eta$  of 0.62V) presents higher catalytic activity than NiO-MB ( $6.4 \text{ mA cm}^{-2}$  at  $\eta$  of 0.62V), but if the current density is scaled to Ni content (*i.e.* mass activity in  $\text{mA mg}^{-2}$ ), NiO-NP ( $12.5 \text{ mA mg}^{-2}$  at a  $\eta$  of 0.62V) displays lower performance than NiO-MB ( $15.2 \text{ mA mg}^{-2}$  at  $\eta$  of 0.62V) (Figure 6). This behavior could be ascribed to the fact that NiO-MB is more porous than NiO-NP, and then the Ni centers are more accessible for water oxidation and the mass transport of water substrate and  $\text{O}_2$  released is promoted. Otherwise, catalytic current density is improved by 12h of anodization in borate buffer at  $\eta$  of 0.62 V.

The morphology of the NiO films was studied by TEM and SEM. The SEM images show differences in morphology of the  $\text{NiO}_x$  films. NiO-MB film looks like thin flakes with a lacelike fine structure; meanwhile NiO-NP film is an agglomeration of nanoparticles (diameter  $\sim 25 \text{ nm}$ ). SEM images after 12h of operation show some corrosion for NiO-MB film and no changes for

NiO-NP film which confirms the mechanical and chemical stability of NiO-NP. According to the XRD patterns and high-resolution transmission electron microscopy (TEM), a cubic NiO phase predominates within fresh NiO-MB and NiO-NP films. Besides, after 12h of anodization, no bulk phase transformation is observed in the crystalline structure of NiO-MB and NiO-NP as supported by XANES, EXAFS and, XRD. Nevertheless, analyses by X-ray photoelectron spectroscopy (XPS) reveal that a thin layer of nickel oxyhydroxide is generated at the surface of nanoparticles (NiO-NP) and microballs (NiO-MB) after anodization, explaining the increase of catalytic activity following a long CPE at 1.1 V *vs* Ag/AgCl. Electrochemical impedance spectroscopy (EIS) confirms a significant change of Ni oxidation state induced by the generation of NiO(OH) phase in the NiO-MB and NiO-NP films after anodization, and also a strong decrease in the  $R_{tr}$  resistance of all films (related to the recombination of charge carriers at the surface traps), which correlate well with the higher catalytic current densities observed in LSV and CPE following the anodization of NiO<sub>x</sub> films.

Kuznetsov et al.<sup>88</sup> prepared NiO<sub>x</sub> electrodes from an original bimetallic Ni-Mo alkoxide precursor, the complex  $[\text{Ni}_2\text{Mo}_2\text{O}_4(\text{OCH}_3)_8(\text{CH}_3\text{OH})_2(\text{DMF})_2]$  (denoted Ni<sub>2</sub>Mo<sub>2</sub>; where DMF is N,N-dimethylformamide, Figure 7). Ni<sub>2</sub>Mo<sub>2</sub> was first drop-casted in a methanol solution on

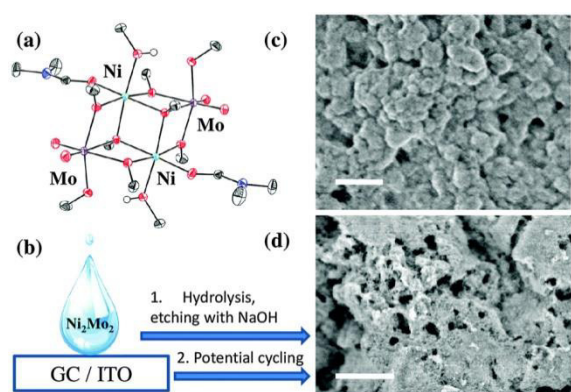


**Figure 7.** (a) ORTEP representation of Ni<sub>2</sub>Mo<sub>2</sub> (H atoms are omitted except those of hydroxo groups); (b) Scheme of the OER electrode preparation procedure. FE-SEM images of (c) the as-deposited Ni<sub>2</sub>Mo<sub>2</sub> sample and (d) the catalyst film after preconditioning and 30 min electrolysis in 1 M NaOH at 2 mA cm<sup>-2</sup> (scale bar: 500 nm) (reproduced from ref<sup>88</sup>, with the permission from the Royal Society of Chemistry, Copyright 2016).

various electrodes (glassy carbon (GC), pyrolytic carbon (PC) and indium tin oxide (ITO)), dried in air, hydrolyzed with subsequent addition of water and 1 M NaOH solution, dried in air again, and it finally underwent a potential cycling in 1 M NaOH buffer between 1 and 1.75 V *vs* RHE ensuring the conversion of Ni(OH)<sub>2</sub> to NiO(OH). This procedure allowed easily preparing highly porous NiO<sub>x</sub> materials, with foam-like structure (as observed by field-emission scanning electron microscopy (FE-SEM), Figure 7(d)), displaying high electrochemically active surface area (ECSA) of  $64 \pm 50 \text{ cm}^2$  along with

a very high roughness factor (ratio of ECSA to geometrical surface area) of  $900 \pm 700$ , which is among the highest values reported for electrodeposited OER catalysts.<sup>89,90</sup> Note that Mo was washing out as molybdate from the catalytic material since it was not observed by XPS

and EDX into the deposited NiO<sub>x</sub> film. Consequently, this high specific surface area coupled to a high catalyst loading (between 1.4 and 1.7 mg cm<sup>-2</sup>) confer high electrocatalytic activity for water oxidation at basic and near neutral pHs. At pH 13.6 (1 M NaOH), NiO<sub>x</sub>/PC electrode exhibits a low overpotential of 0.32 V at 10 mA cm<sup>-2</sup>, a low Tafel slope of 41 mV dec<sup>-1</sup> and an excellent stability over 6 h by maintaining a constant potential of 1.58 V vs RHE at applied current density of 10 mA cm<sup>-2</sup>. At pH 9.2 (0.1 M NaB<sub>4</sub>O<sub>7</sub>), which is a more suitable buffer for light-driven water splitting devices, the catalytic activity of NiO<sub>x</sub>/PC is also interesting with  $\eta$  of 0.55 V at 10 mA cm<sup>-2</sup> and a long stability over 8h by a galvanostatic experiment at 10 mA cm<sup>-2</sup> while maintaining a constant potential at 1.83 V vs RHE. An easy approach to access to anodes coated with highly porous nickel oxide and along with high catalytic performance make this material a very attractive alternative to implement efficient and cheap electrolyzers and photoelectrochemical cells devoted to water splitting.

Takanabe and co-authors<sup>91</sup> demonstrate that it is possible to boost the OER performance of a nickel oxide anode by a simple electrochemical activation. This method consists in electrochemically cycling a NiO<sub>x</sub> electrode (using a Ni foam as conducting electrode) between 1.0 and 1.8 V vs RHE in 1.5 M carbonate or phosphate electrolyte (containing K or Cs) at basic pH (9.4 < pH < 12.2) and under temperature superior to 55°C. This protocol allows restructuring the NiO<sub>x</sub> surface, generating a thick layer (> 1 μm) and forming an active stable NiO(OH) phase, which could weakly bound alkali-metal cations and water (hydrate form) in its three-dimensional structure. The electrochemically activate (ECA) NiO<sub>x</sub> electrode reached a current of 10 mA at potential below 1.40 V vs. RHE ( $\eta$  < 0.17 V) at a temperature superior to 75 °C and at pH 10.5 with good stability over 24 h of electrolysis. The prepared activated electrode present higher OER performance than the state of art NiFeO<sub>x</sub> electrode under similar conditions (see below).

The groups of Radniecka<sup>92</sup> and Corrigan<sup>93</sup> were the first to report the positive effect of the intentional or involuntary introduction of iron within nickel oxide films on the electrocatalytic water oxidation. Since these pioneer works, many groups have been interested in developing mixed nickel/iron oxides (NiFeO<sub>x</sub>), also called layer double hydroxide (LDH), which is among the best OER electrocatalysts of literature. We won't provide in this chapter an overview of the development of mixed nickel/iron oxides devoted to OER, since it is somewhat out of the scope of this manuscript. However we can quote some groups that work on the design of these mixed metal oxides. Several groups, such as those of Bell,<sup>61,27</sup>

Boettcher<sup>94,95,58,80</sup> and Strasser<sup>96</sup>, who have performed in-depth investigations of NiFeO<sub>x</sub> material and tried to rationalize the fundamental role of iron salts incorporated inside the nickel oxide in its high OER performance. In parallel to these works, other groups like those of Hu,<sup>97</sup> Fattakhova-Rohlfing,<sup>98,99</sup> Yan,<sup>100</sup> Shao<sup>101</sup> and Cao,<sup>102</sup> to name a few, explored different strategies to improve the OER performance of these LDHs by controlling either their composition (*e.g.* varying the content of cation inside the layered structure), the catalyst size (*e.g.* with nanocrystals), or the catalyst shape (*e.g.* with nanolayers, nanoplatelet arrays, interconnected nanoribbons). Many efforts have to be done to further improve the catalytic activity of this LDH, but among all OER catalysts reported since few years, mixed NiFeO<sub>x</sub> with its high activity (low OER overpotential and low Tafel slope) and its high stability under electrocatalysis conditions, is the most promising.

### 3 - Cobalt Oxide as Electrocatalytic Material for Water

#### Oxidation

As nickel oxide, cobalt oxide has also been extensively studied to promote electrocatalytic water oxidation reaction. The OER activity of cobalt oxide is known since the end of the 60's *via* an US patent of Suzuki and co-workers,<sup>103</sup> and was investigated in detail only at the beginning of the 80's by the groups of Shafirovich,<sup>104</sup> Burke,<sup>105</sup> Bockris,<sup>106,107</sup> Noufi<sup>108</sup> and Tseung.<sup>109,110</sup> Since these pioneer works, few studies appeared in the 90's but cobalt oxide and more generally OER catalysts based on cobalt materials knew a renewed interest in 2008 with the works of Nocera and co-workers.<sup>31</sup> They reported an efficient inorganic cobalt OER catalyst electrodeposited from Co<sup>2+</sup> ions in phosphate buffer, which opened the way of the use of OER electrocatalysts devoid of rare metals at neutral and near neutral pH (9.2) in appropriate buffer solution (see below). Cobalt oxides developed for OER in literature are amorphous or crystalline of spinel type (Co<sub>3</sub>O<sub>4</sub>, NiCo<sub>2</sub>O<sub>4</sub>, LiCoO<sub>2</sub>), perovskite type (LaCoO<sub>3</sub>, SrCoO<sub>3</sub>) or layered (oxy)hydroxides.<sup>111</sup> Besides, various methods have been employed to prepare cobalt-based catalysts as spin coating, sol-gel process, radio frequency sputtering, spray pyrolysis, chemical vapour deposition, pulsed layer deposition and electrodeposition.<sup>112</sup> As mentioned for nickel oxide, electrodeposition has many advantages since it can be carried out under ambient and soft conditions (*e.g.* room temperature and near neutral pH) and allows a fine control of the purity, the growth process, the morphology and the inner structure of the deposited oxide film.

In the early 90's, Tseung and Jiang<sup>113</sup> used this versatile electrochemical approach to deposit cobalt hydroxide on electrodes and to study their electrocatalytic activity for H<sub>2</sub> and O<sub>2</sub> evolution reaction in 7 N KOH at room temperature. Cobalt hydroxide was electrodeposited on nickel electrode by galvanostatic electrolysis at 20 mA cm<sup>-2</sup> in presence of bubbling oxygen. For a Co loading of 93 mg cm<sup>-2</sup>, the cell displayed at room temperature low overpotentials of 0.39 and 0.34 V for OER and HER respectively at a current density of 1 A cm<sup>-2</sup> (Figure 18). At 80°C, the overpotentials required to operate at 1 A cm<sup>-2</sup>, significantly decreased until 0.285 and 0.264 V for OER and HER respectively. The Tafel slopes of 56 mV dec<sup>-1</sup> obtained with a cobalt electrode polarized during 0.5 h and of 62 mV dec<sup>-1</sup> after a polarization of 20 h, indicate that the OER takes place on the surface of cobalt oxide film. Otherwise, the authors demonstrated that the electrochemical efficiency in alkaline solution is proportional to the Co loading between 23-132 mg cm<sup>-2</sup>. The high performance of these

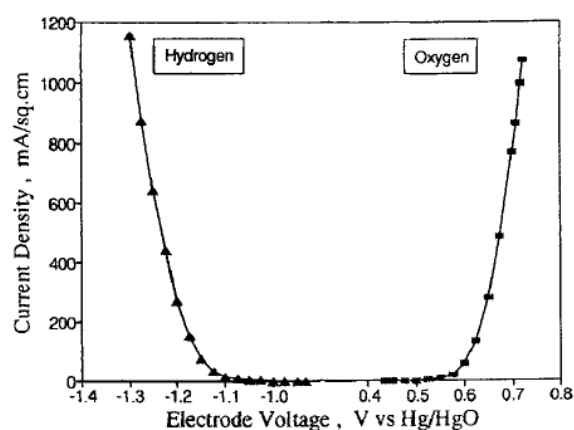


**Figure 18.** LSV curves for H<sub>2</sub> and O<sub>2</sub> evolution on a cobalt electrode (Co loading of 93 mg cm<sup>-2</sup>) in 7N KOH buffered electrolyte at room temperature (not IR-corrected) (reproduced from ref<sup>113</sup>, with the permission from the Society for solid-state and electrochemical science and technology, Copyright 1991).

cobalt electrodes was attributed to their unique porous structure characterized by an interlaced network of fine and coarse pores (observed by SEM) which confers a high surface area and a very high electrical conductivity of the electrodes. Finally, the electrochemical performance of Co electrodes in this study has been improved (*i.e.* the OER and HER overpotentials have been reduced) by activating the electrodes *via* the deposition of nickel cobalt sulfide material by reduction of nickel and cobalt chloride with NaS in water.

In the end of 90's, Castro et al.<sup>114</sup> also reported the preparation of cobalt oxide based electrodes by electrodeposition on different substrates: Ni, Pt, Fe and vitreous carbon disc electrodes in alkaline solution. Two types of electrodes (I and II) were implemented from two different electrochemical methods from alkaline solution (1 M NaOH, pH 14) containing 0.05 M Co(NO<sub>3</sub>)<sub>2</sub>•6H<sub>2</sub>O and 0.5 M NaNO<sub>3</sub>. For the electrodes I, cobalt oxide was deposited by potentiostatic electrolysis at 0.5 V vs Hg/HgO during 60 min, whose the structure was assigned to Co<sub>3</sub>O<sub>4</sub> spinel type, according to the voltammograms of Co deposit which displays

two redox processes,  $\text{Co}_3\text{O}_4/\text{CoO}(\text{OH})$  and  $\text{CoO}(\text{OH})/\text{CoO}_2$ , respectively at 0.222 and 0.562 V vs Hg/HgO (Figure 19(a)). For the electrodes II, cobalt oxide was deposited by potentiodynamic electrodeposition (*i.e.* repetitive triangular potential scans, RTPS) only on Ni substrate sweeping between -0.1 and 0.7 V vs Hg/HgO during 60 min, resulting in a deposit with the electrochemical signature of  $\text{Ni}_x\text{Co}_{3-x}\text{O}_4$  in which some Co have been substituted by Ni (closed to the  $\text{NiCo}_2\text{O}_4$  form; Figure 19(b)). The electrodeposited cobalt oxide films present higher OER current density in comparison with that of the corresponding bare substrates (Figure 19). The cobalt electrodes also displayed long-term stability under electrocatalytic conditions, losing less than 10% of its OER activity after 24h of exposure to air or to 1M NaOH solution. A Tafel slope of  $40 \text{ mV dec}^{-1}$  was determined at low overpotential ( $< 0.7 \text{ V}$ ) for both types of electrodes, demonstrating that electrodes I and II share similar mechanistic pathways for OER whose the rate determining step was ascribed to the second electron transfer step.

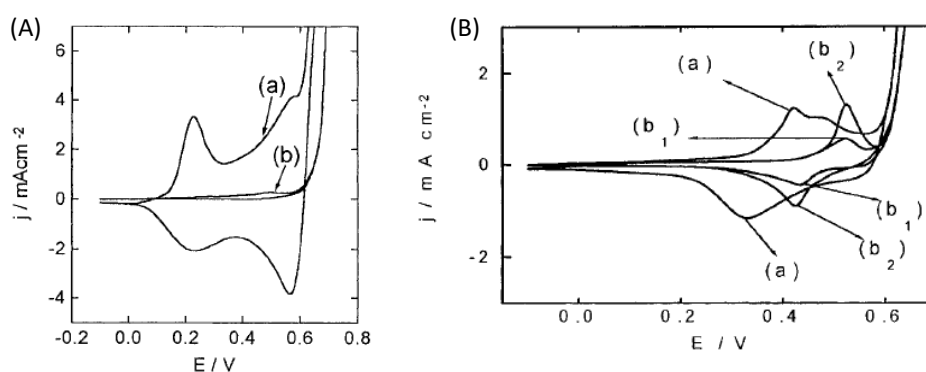
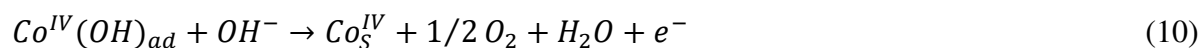


**Figure 19.** (A) Cyclic voltammograms of electrode I on Ni substrate (a) and of a bare Ni substrate (b) in 1 M NaOH (scan rate  $10 \text{ mV s}^{-1}$  and electrode rotation rate 2000 rpm). (B) Cyclic voltammograms of electrode II on Ni substrate (a) and of a bare Ni substrate at different RTPS times of 5 min ( $b_1$ ) and 60 min ( $b_2$ ) (scan rate  $50 \text{ mV s}^{-1}$  and electrode rotation rate 2000 rpm) (reproduced from ref <sup>114</sup>, with the permission from Springer, Copyright 1998).

Electrochemical impedance spectroscopy (denoted EIS) performed on both electrodes reveals that cobalt oxide at the electrode surface is already oxidized, before  $\text{O}_2$  evolution, to  $\text{Co}^{\text{IV}}$  for the electrodes I and to  $\text{Co}^{\text{IV}}/\text{Ni}^{\text{IV}}$  for the electrodes II, as it was observed in their corresponding voltammograms (Figure 19). In addition, EIS exhibited only one capacitive contribution related to OER, whose the capacitive time constant was related to the potential dependent of the surface concentration of only one intermediate state, that would be OH or O adsorbed species (*i.e.*  $\text{Co}^{\text{IV}}(\text{OH})_{\text{ad}}$ ). From the experimental data, the authors finally proposed a possible mechanism through a series of reversible steps (8 and 9) yielding the  $\text{Co}^{\text{IV}}(\text{OH})_{\text{ad}}$  species at the surface of the oxide, that can undergo a charge transfer coupled to an  $\text{OH}^-$

adsorption to evolve oxygen (10). The latter path was designated as the rate determining step of the mechanism, explaining the impedance data and the Tafel slope value of  $40 \text{ mV dec}^{-1}$ .



In 2002, the group of Casella<sup>115</sup> were among the first group to investigate the deposition of cobalt oxide on conducting electrode for OER and the oxidation of organic compounds, *via* the electrodecomposition of a cobalt complex as precursor. The authors prepared cobalt oxide based electrodes (glassy carbon) by potentiostatic electrolysis at constant potential at *ca.* 0.5 V *vs* SCE during 1 h or by cyclic voltammetry between 0.4 and 1.1 V (Figure 20(a)) in alkaline solution (30 mM NaOH, pH 12.5) and in presence of 6 mM CoCl<sub>2</sub> and 30 mM sodium citrate. The cobalt content deposited on glassy carbon by potentiostatic method was estimated to be between 3 and 18 nmol cm<sup>-2</sup>, and it increases with more anodic applied potentials. Basically, during the electrodeposition of cobalt oxide, cobalt(II) citrate complex is oxidized into Co<sup>III</sup> and Co<sup>IV</sup> oxide species which are insoluble at pH 12.5 and deposit on electrode. Although the OER catalytic activity of this cobalt oxide is not impressive at pH 12.5 with a catalytic current density lower than 1 mA cm<sup>-2</sup> at 0.7 V *vs* SCE (corresponding to an overpotential of 0.45 V), this study provides a clear insight on the redox behavior of cobalt oxide film in alkaline solution. The cobalt oxide film electrodeposited was characterized by cyclic voltammetry and independently of the electrodeposition method, three redox waves were observed and assigned to the following redox couples: Co(OH)<sub>2</sub>/Co<sub>2</sub>O<sub>3</sub> at 0.08 V *vs* SCE (Ia/Ic), Co<sub>2</sub>O<sub>3</sub>/CoOOH at 0.3 V (IIa/IIc) and CoOOH/CoO<sub>2</sub> at 0.55 V (IIIa/IIIc, Figure 20(b)). The authors demonstrated that increasing concentrations of NaNO<sub>3</sub>, K<sub>2</sub>SO<sub>4</sub> and Na<sub>3</sub>PO<sub>4</sub> inactive electrolytes inhibit the redox processes of cobalt oxide film and also its OER performance.

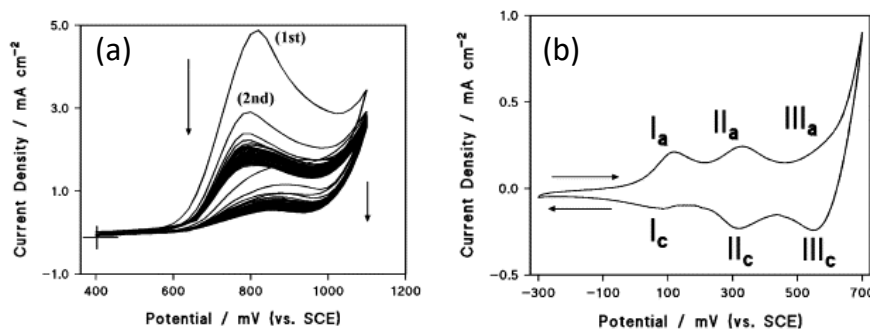


**Figure 20.** a) Consecutive cyclic voltammograms of cobalt oxide film growth on glassy carbon electrode in a 30 mM NaOH electrolyte in presence of 30 mM sodium citrate and 3 mM  $\text{CoCl}_2$  (scan rate  $50 \text{ mV s}^{-1}$ ). b) Cyclic voltammograms (30<sup>th</sup> cycle) of cobalt oxide film on glassy carbon electrode in a 30 mM NaOH electrolyte (scan rate  $50 \text{ mV s}^{-1}$ ) (reproduced from ref <sup>115</sup>, with the permission from Elsevier, Copyright 2002).

In 2008, the group of Nocera<sup>31</sup> opened a new area of exploration for the development of inorganic catalyst easy prepared and based on earth abundant elements with a significant OER catalytic activity at neutral pH. They reported an in situ formation of cobalt catalyst for OER prepared by cyclic voltammetry between 0 and 1.4 V vs NHE or by a potentiostatic electrolysis at 1.29 V on ITO (or FTO) electrode using a neutral phosphate buffer (KPi) containing 0.5 mM  $\text{Co}^{2+}$  salts. Indeed, the cyclic voltammogram of 0.5 mM  $\text{Co}(\text{NO}_3)_2$  solution in KPi at pH 7 shows an anodic wave at 1.13 V vs NHE and the onset of a significant OER catalytic wave at 1.23 V (Figure 21(a)), assigned to a dark coating of cobalt catalyst on ITO.

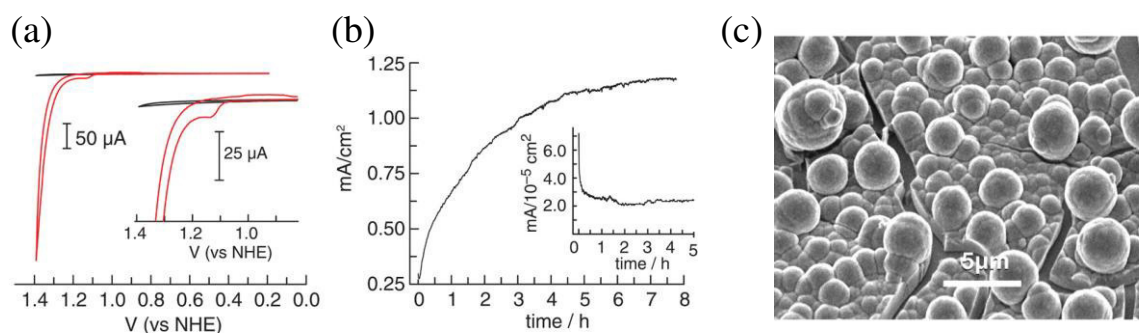


**Figure 21.** a) Cyclic voltammograms on ITO electrode in 0.1 M KPi electrolyte at pH 7 with no  $\text{Co}^{2+}$  ion (black line) and with 0.5 mM  $\text{Co}^{2+}$  (red line). b) Current density in function of time during an electrolysis at 1.29 V vs NHE on ITO electrode in 0.1 M KPi electrolyte at pH 7 in presence of 0.5 mM  $\text{Co}^{2+}$ . (Inset) Current density profile in absence of  $\text{Co}^{2+}$  under similar experimental conditions. c) SEM image of the electrodeposited cobalt film on ITO electrode after  $30 \text{ C cm}^{-2}$  were passed in 0.1 M KPi electrolyte at pH 7 in presence of 0.5 mM  $\text{Co}^{2+}$  (reproduced from ref <sup>116</sup>, with the permission from American Association for the Advancement of Science, Copyright 2008).

A long electrolysis at 1.29 V was then performed in KPi during 7-8 h without stirring, and after that, a strong catalytic current density over  $1 \text{ mA cm}^{-2}$  was observed, which confirmed

the cobalt deposit on electrode (Figure 21(b)). The maximum OER activity was obtained with a film of *ca.* 2  $\mu\text{m}$  of thickness prepared by potentiostatic electrodeposition. The cobalt catalyst film was characterized by SEM exhibiting coalesced particles inside the film and individual microparticles on the surface of the film (Figure 21(c)).

X-ray diffraction coupled to EDX and XPS analyzes on electrodeposited catalyst film displayed amorphous cobalt oxide or hydroxide with no crystalline phase formation, containing phosphate anions along with a stoichiometric ratio of 2:1:1 for Co:P:K. A Faradaic efficiency closed to 100% and  $^{31}\text{P}$  NMR analyzes showed that the KPi electrolyte is not decomposed after a consistent electrolysis of 45 C demonstrating its robustness under these experimental conditions, and that the cobalt film cleanly oxidizes  $\text{H}_2\text{O}$  to  $\text{O}_2$  at pH 7. The electrodeposited cobalt film presents significant catalytic performance with a current density of  $1 \text{ mA cm}^{-2}$  at an overpotential of 0.41 V. The study of Tafel plot at various pHs between 5 and 8 revealed a Nernstian behavior of the cobalt film involving a series of reversible oxidations coupled to deprotonations (or proton-coupled electron transfers, PCET) before the rate determining step of  $\text{O}_2$  evolution, whose deprotonation could be ensured by  $\text{HPO}_4^{2-}$  anions. Finally the authors proposed that the KPi promotes the in situ catalyst formation through the interaction between phosphate and  $\text{Co}^{3+}$ . Basically, due to this specific interaction, cobalt catalyst film can be self-repaired during electro-induced  $\text{O}_2$  evolution, proceeding *via* a dynamic equilibrium between the water soluble  $\text{Co}^{2+}\text{-HPO}_4^{2-}$  and the insoluble  $\text{Co}^{3+}\text{-HPO}_4^{2-}$  that deposits on electrode.<sup>117</sup> This self-repair mechanism confers a great stability on the OER catalyst as it was observed in the natural oxygen evolving center, a cluster of manganese and calcium, operating in the photosynthesis of green plant.

Nocera and co-workers<sup>118</sup> also investigated the effect of phosphate (Pi) and of other proton-accepting electrolytes as methylphosphate (MePi) and borate (Bi) (at pH 7.0, 8.0 and 9.2, respectively) on the electrodeposition of cobalt-based catalysts on ITO electrode and their catalytic activity for water oxidation. The authors showed that the electrolyte is a key factor for the catalyst formation and to obtain a catalytic activity with appreciable current density and selectivity for water oxidation. In absence of a proton-accepting electrolyte, the catalyst formation is inhibited and its OER performance diminishes over time along with a deterioration of catalyst. As their previous study,<sup>31</sup> an active catalyst film was generated on ITO with desired thickness by an anodic single scan of 0.5 mM  $\text{Co}^{2+}$  solution in Pi, MePi and Bi, or by controlled potential electrolysis at 1.3 V *vs.* NHE. X-ray diffraction and TEM analysis revealed an amorphous nature with no crystalline features in the cobalt oxide films

and an active unit of dimension inferior to 5 nm. Co-MePi catalyst reaches a current density of  $1.5 \text{ mA cm}^{-2}$  after 2h of electrocatalysis,  $2.3 \text{ mA cm}^{-2}$  after 10 min for Co-Bi, and  $1 \text{ mA cm}^{-2}$  after 1h for Co-Pi. Tafel plots demonstrate that Co-MePi and Co-Bi present similar catalytic activity than that of Co-Pi. The faradaic efficiency for the catalysts was determined *via* bulk electrolysis, obtaining  $98 \pm 5\%$  and  $104 \pm 5\%$  for MePi and Bi, respectively. In conclusion, an electrodeposition of an ultrathin layer of cobalt oxide film can be obtained by rapid oxidation of  $\text{Co}^{2+}$  in solution on a several substrates with a large surface area and a complicated geometry such as those of nanostructured semiconductors, which would be of great interest for the implementation of photoelectrochemical cell devoted to water splitting reaction.

The group of Nocera<sup>119</sup> carried their work on the Co-Pi catalyst performing in-depth study on its structure and valency by in situ X-ray spectroscopy. The Co-Pi prepared by electrodeposition has been obtained with two different thickness: in a thick Co-Pi film synthesized by applying a potential of 1.25 V *vs* NHE, an average cluster nuclearity of  $\sim 40\text{-}50 \text{ nmol Co ions cm}^{-2}$  was obtained, meanwhile in a thin film deposited at 1.1 V, a lower nuclearity of  $\sim 3 \text{ nmol Co ions cm}^{-2}$  was achieved. EXAFS characterizations confirmed the presence of bis-oxo/hydroxo-bridged Co subunits inside higher nuclearity clusters in Co-Pi. EXAFS data of Co-Pi of the two samples was compared with the data of Co oxide compounds, and it was proposed a model where the Co oxo/hydroxo clusters have the same structure found in extended planes of cobaltates,  $\text{CoO}(\text{OH})$ , and Co-Pi clusters are composed of edge-sharing  $\text{CoO}_6$  octahedra with molecular dimensions (Figure 22). This molecular cobaltate cluster (MCC) can accommodate N values for the nearest Co-Co neighbor vector higher than 4. XANES characterization indicated the Co valence is higher than 3 when water oxidation is catalyzed at 1.25 V *vs* NHE for both Co-Pi samples. The significant activity suggests that the molecular dimensions of the Co-Pi clusters are may be essential for catalysis and raises the possibility to synthesize mixed-metal oxide clusters with improved catalytic performance. Indeed, Co ions can be replaced for one or more alternative metals as Mn, Ni or Ru, changing the oxidation state *versus* the potential profile or the M-O bond strengths altering the catalysis rate in view to access more efficient catalyst.

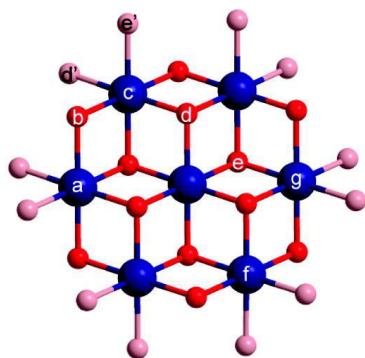


**Figure 22.** Edge-sharing molecular cobaltate cluster (MCC) model for Co-Pi surface. Bridging oxo/hydroxo ligands are in red and non bridging oxygen ligands (*i.e.* water, hydroxide, phosphate) are in pink (reproduced from ref <sup>119</sup>, with the permission from the American Chemical Society, Copyright 2010).

The group of Stahl<sup>120</sup> developed original fluoride cobalt catalyst films for electrochemical oxidation of water under non-alkaline conditions. The authors speculated that fluoride cobalt species could be good OER catalysts since fluorocobaltate(III) are known to evolve O<sub>2</sub> and HF from water and F<sup>-</sup> anions, which are oxidatively robust, could play the role of acidic buffer in water (HF, pK<sub>a</sub> = 3.17), offering the possibility to perform OER under acidic conditions. The catalyst film was generated on FTO electrode applying a constant potential of 1.48 V *vs.* NHE at pH 3.5 of F<sup>-</sup>-buffered solution containing 1 mM CoSO<sub>4</sub>. Cyclic voltammogram of the electrodeposited fluoride cobalt film in a fresh F<sup>-</sup> (0.1 M) buffer devoid of cobalt salt displayed a strong OER catalytic wave around 1.6 V *vs.*

NHE (Figure 23A), that gradually diminished after a prolonged electrolysis in 1.0 M fluoride buffer due to the dissolution of the catalytic material. The fluoride cobalt deposit could be more stable and more active during electrocatalysis by adding a low concentration of Co<sup>2+</sup> (*i.e.* 0.1-1 mM) in the electrolyte along with 1 M fluoride (Figure 23B). Under these experimental conditions, a stable oxygen evolution was obtained with a faradaic yield of O<sub>2</sub> superior to 95%. The current passed is directly proportional to the concentration of fluoride or cobalt salt, less current passes at lower concentration of F<sup>-</sup> or Co<sup>2+</sup>. SEM characterization showed a layer of fused spheroidal nodules (Figure 23C), and XPS analysis indicated the presence of cobalt, oxygen and fluorine with a ratio CoO<sub>6.3±0.4</sub>F<sub>0.29±0.04</sub> and CoO<sub>6.7±0.3</sub>F<sub>0.37±0.14</sub> for a sample deposited from 0.1 and 1.0 M F<sup>-</sup>, respectively. Besides, XPS data are consistent with a hydrated cobalt oxohydroxide containing Co<sup>2+</sup> and Co<sup>3+</sup>, which also suggests a mixture of oxides (CoO and Co<sub>3</sub>O<sub>4</sub>). Tafel plot of fluoride cobalt film was performed on fluoride and phosphate (Pi) electrolytes at 0.1 and 1.0 M. At 1.0 M F<sup>-</sup>, a linear Tafel-like correlation was observed, whereas at 1.0 M Pi a marked decrease of current density and nonlinear correlation were obtained, highlighting the importance of the buffer nature and its concentration on the OER performance of the film. In conclusion, fluoride buffer has been proven to be an effective proton-accepting electrolyte for in situ formation of cobalt catalyst on electrode and for electrocatalytic water oxidation reaction at lower pH than those previously reported on literature for cobalt-oxide catalyst presenting an advantage for (photo)electrolysis cells where proton reduction and fuel-forming reactions will be easier at low pH.

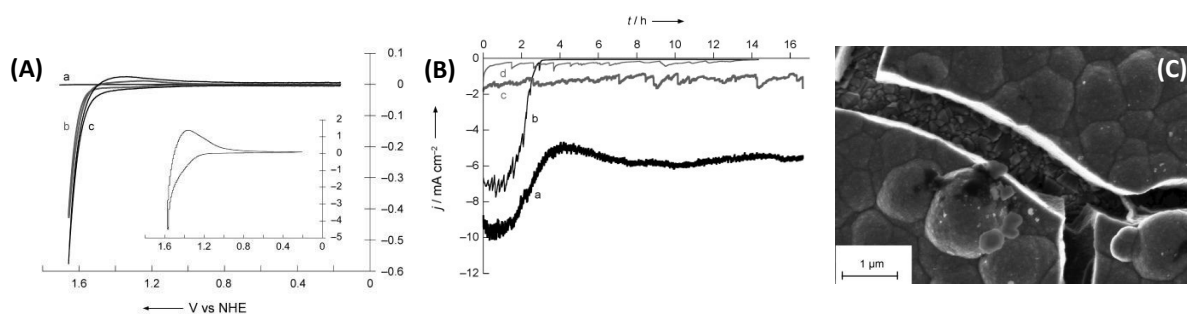


**Figure 23.** (A) Cyclic voltammograms recorded at pH 3.5 with solutions of  $\text{CoSO}_4$  (1 mM) and KF (0.1 M and 1.0 M, scans b and c, respectively) or with a KF (0.1 M) solution without cobalt salt (scan a). Inset: Cyclic voltammogram of an electrodeposited fluoride cobalt on FTO electrode recorded at pH 3.5 in a fresh KF (0.1 M) solution without  $\text{CoSO}_4$ . (B) Potentiostatic electrolysis performed with an electrodeposited fluoride cobalt electrode at 1.6 V vs NHE in an electrolyte containing 1.0 M KF with and without 1 mM  $\text{CoSO}_4$  (traces a and b, respectively), and 0.1 M KF with and without 1 mM  $\text{CoSO}_4$  (traces c and d, respectively). The initial pH was 3.7 and cobalt catalyst was deposited on FTO electrode. (C) SEM image of the fluoride cobalt film deposited on FTO with 0.5 M KF (reproduced from ref<sup>120</sup>, with the permission from Wiley, Copyright 2010)

In a consecutive work, Stahl and coworkers<sup>121</sup> undertook a meticulous and complex mechanistic investigation of water oxidation electrocatalyzed by cobalt oxide-based material in aqueous solution with different buffer electrolytes with pHs between 0 and 14. The authors mentioned in first place that cobalt based electrocatalysts reported in literature commonly follow three distinct behaviors in function of pH of the solution: with a pH above 5.5, cobalt catalyst films are stable and long electrolysis with stable catalytic current density could be performed without need of additional  $\text{Co}^{2+}$  salt in electrolyte; at pHs between 3 and 5.5, the cobalt oxide films are in dynamic equilibrium between  $\text{Co}^{2+}$  salts soluble in electrolyte and insoluble  $\text{CoO}_x$  deposited on electrode; at a pH below 3,  $\text{CoO}_x$  is soluble in electrolyte and heterogeneous coating is absent at the surface of electrode during OER electrolysis. Based on these observations, Stahl and coworkers<sup>121</sup> carried out different Tafel plots of cobalt oxide electrodes with various electrolytes and at various pHs (Table 1). The examination of the Tafel data reveals two different regimes for catalytic activity. Above pH 4.0, cobalt oxide electrodes possess a low Tafel slope of 50-70  $\text{mV dec}^{-1}$  independent of pH and electrolyte nature, which is coherent with the OER activity of heterogeneous  $\text{CoO}_x$  catalysts. At pH 2.0 and below,  $\text{CoO}_x$  films deposited on electrode quickly dissolve and exhibit high values of Tafel slope above 110  $\text{mV dec}^{-1}$ . At the intermediate pH 3.4 in 0.1 M fluoride buffer, the two regimes are observed with two different Tafel slopes of 60 and 113  $\text{mV dec}^{-1}$  respectively at low and high overpotential, indicating a change at this pH in the nature of catalyst (heterogeneous vs homogeneous) and the rate-determining step of OER.

**Table 1.** Tafel plots performed in different buffer electrolytes for electrochemical water oxidation catalyzed by cobalt material.\*

pH	Electrolyte composition	Catalyst Formation and/or Composition	Tafel Slope (mV dec <sup>-1</sup> )
14	1 M NaOH	ex-situ/Co free solution	61
13	0.1 M NaOH	ex-situ/Co free solution	54
7	1 M phosphate	in-situ/Co free solution	70
7	0.1 M phosphate	in-situ/Co free solution	65
6.3	1 M TfNH <sub>2</sub>	in-situ/Co free solution	56
6.3	0.1 M TfNH <sub>2</sub>	in-situ/Co free solution	55
4.8	0.1 M HFPO <sub>3</sub> <sup>-</sup>	in-situ/[Co]= 1 mM	67
3.4	0.1 M fluoride	in-situ/[Co]= 1 mM	60 (Low $\eta$ )
3.4	1 M fluoride	in-situ/[Co]= 1 mM	113 (High $\eta$ )
2.1	0.1 M sulfate	No film/[Co]= 1 mM	113
2	1 M phosphate	No film/[Co]= 1 mM	112
2	0.1 M phosphate	No film/[Co]= 1 mM	113
1	1 M BF <sub>4</sub> <sup>-</sup>	No film/[Co]= 1 mM	137
1	0.1 M BF <sub>4</sub> <sup>-</sup>	No film/[Co]= 1 mM	118
0.3	1 M sulfate	No film/[Co]= 1 mM	135
1	1 M BF <sub>4</sub> <sup>-</sup>	Control/[Co]= 0	529

\*CoO<sub>x</sub> films formed in situ were then electrolyzed in the same electrolyte buffer, either with or without cobalt solution. Films formed ex-situ were prepared by Noufi's<sup>122</sup> method in 0.1 M F at pH 3.4 and at current densities greater than the break in the slope with 0.1 M fluoride, where the CoO<sub>x</sub> is unstable.

Stahl and coworkers<sup>121</sup> also performed cyclic voltammograms of CoO<sub>x</sub> deposited on FTO at various pHs and electrolytes (Figure 24(A)), whose the number and the potential value of the redox processes are pH-dependent. Above pH 8.0, two redox couples are observed, while at pHs 3.0-8.0, only one redox couple appears below the OER catalytic wave. Note that at pH *ca.* 3.0 and below, only the catalytic wave along with a broad cathodic peak is present in the cyclic voltammograms and no heterogeneous coating appears on electrode. The midpoint potentials of quasi-reversible redox processes (*i.e.* their half-wave potentials) and the catalytic waves were plotted in function of pH values to build a Pourbaix diagram that matches well with a Pourbaix diagram derived from literature free energies of formation for cobalt aquo/hydroxide/oxide species (Figure 24(B)). The correlation between both diagrams allows assigning all redox processes observed in the previous cyclic voltammograms recorded at various pHs (Figure 24(A)), giving precious information on the in-situ electroformation of CoO<sub>x</sub> from Co<sup>2+</sup> salts and on the nature of active forms of CoO<sub>x</sub> during OER. This electrochemical study was completed by an EPR analysis that characterized only the paramagnetic species of the CoO<sub>x</sub> based electrodes, such the Co<sup>II</sup> and Co<sup>IV</sup> salts. The EPR investigation confirmed the assignment of the redox couples recorded in the cyclic voltammograms and indicated that, during OER process, several Co<sup>IV</sup> sites are generated

within the catalyst stemming from various coordination spheres of cobalt and/or the formation of an oxygen-centered radical.

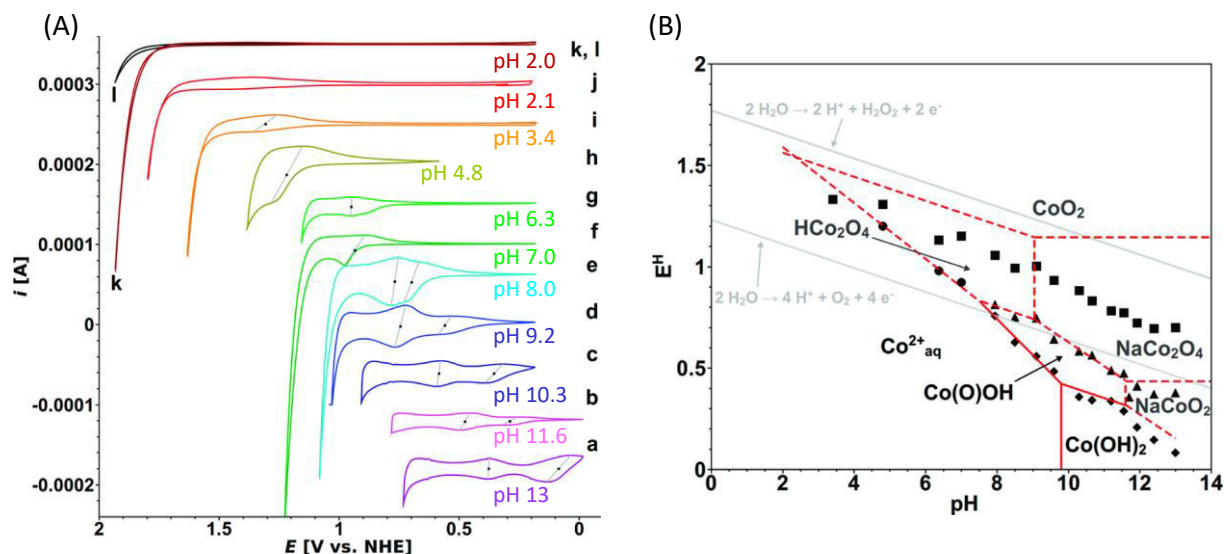


**Figure 24.** (A) Cyclic voltammograms (CVs) of  $\text{CoO}_x$  deposited on FTO electrodes realized at  $1 \text{ mV s}^{-1}$  in buffering electrolyte at indicated pH: (a) pH 13 hydroxide, (b) pH 11.6 vanadate, (c) pH 10.3 carbonate, (d) pH 9.2 borate, (e) pH 8.0 methylphosphonate, (f) pH 7.0 phosphate, (g) pH 6.3 trifluoromethylsulfonamide (vertical scale reduced 10x) and (h) pH 4.8 fluorophosphate. CVs recorded in electrolyte of  $0.5 \text{ mM CoSO}_4$  at indicated pH: (i) pH 3.4 fluoride, (j) pH 2.1 phosphate, (k) pH 2.0 sulfate and (l) pH 2.0 blank without  $\text{Co}^{2+}$  salt. Black dots mark the midpoints of the quasi-reversible redox processes. Potentials are referenced *versus* NHE and currents are vertically offset for visibility. (B) Pourbaix diagram showing the pH/potential characteristics of the precatalytic features evident in CVs, shown in A, obtained from  $\text{CoO}_x$  in diverse buffering electrolytes. Symbols denote the following redox features:  $\blacksquare$ , potential at which the catalytic wave in the CV is equal in magnitude to the anodic prefeature;  $\blacklozenge$ , position of the midpoint potential for the first quasi-reversible wave;  $\blacktriangle$ , position of the midpoint potential for the second quasi-reversible wave; and  $\bullet$ , position of the midpoint potential in cases where only a single prefeature is observed. Solid red lines show the pH/potential equilibria of soluble and insoluble cobalt oxide and hydroxide species shown in black with  $[\text{Co}^{2+}] = 10^{-7} \text{ M}$  from data in ref<sup>123</sup> dashed lines indicate equilibria for species shown in gray calculated from experimental data (reproduced from ref<sup>121</sup>, with the permission from the American Chemical Society, Copyright 2011).

From all characterizations cited above, Stahl and coworkers<sup>121</sup> proposed a layered structure model for cobalt oxide catalysts and a set of mechanism for electrochemical water oxidation in acid, neutral and alkaline electrolytes with electrodeposited  $\text{CoO}_x$  films, also with homogeneous cobalt electrocatalyst for water oxidation reaction (Figure 25). The authors claimed that a layered double hydroxide (LDH) structure for the  $\text{CoO}_x$  films is quite consistent with their pH dependence of their quasi-reversible curves in cyclic voltammograms, giving a Pourbaix diagram for a family of cobalt-based layered materials very similar to the classic Pourbaix diagram of cobalt (Figure 24). Below pH 3, production of  $\text{H}_2\text{O}_2$  by homogeneous catalyst is observed, above pH 3 a  $\text{CoO}_x$  film is formed from the aqueous solution of  $\text{Co}^{2+}$  in buffering electrolyte by applying an oxidizing potential to the

anode. Previously reported XRD analyses on  $\text{CoO}_x$  indicated that the crystallite size of cobalt oxides remains between 10-100 Å. From these XRD data, Stahl and coworkers proposed that the amorphous bulk films of  $\text{CoO}_x$  are composed of a mix of polydisperse and oligomeric stacked layers of cobaltate, resulting in a three-dimensional layered double-hydroxide structure.

The Tafel data listed in Table 1 show that  $\text{CoO}_x$  materials present the same Tafel slope from middle acid to strong alkaline conditions, thus follow the same OER mechanism, or a similar one (Figure 25(A)). At pH 3-4, the increase of Tafel slope indicates the limit between heterogeneous cobalt oxide catalysts and homogeneous cobalt catalyst. At high value of Tafel slope, the oxygen production decreases and the cobalt film detaches from the electrode during long electrolysis. As illustrated in the Pourbaix diagram (Figure 24(B)), from pH ~8.0-9.5 the oxidation of aqueous  $\text{Co}^{\text{II}}$  produces a heterogeneous  $\text{Co}^{\text{III}}(\text{O})\text{OH}$  species corresponding to a  $3\text{H}^+/\text{e}^-$  process (**1**→**2**→**3** in Figure 25(A)). Under mildly acidic to neutral conditions (*i.e.* pH ~3-8), the  $\text{Co}(\text{O})\text{OH}$  species is thermodynamically unstable, hence the oxidation of  $\text{Co}^{\text{II}}$  affords deposition of  $\text{Co}^{\text{III/IV}}$  species (**4** in Figure 25(A)), process associated with a  $7\text{H}^+/3\text{e}^-$  trend. Meanwhile under basic conditions (pH ~10-12), the oxidation of the heterogeneous  $\text{Co}^{\text{II}}(\text{OH})_2$  (**2**) follows a stepwise process (**2**→**3**→**4** in Figure 25(A)) with low oxidation potentials. Hence the species **4** is deprotonated and the formation mechanism of  $\text{CoO}_x$  at oxidizing potentials suggests a “self-healing” nature. Tafel plots at pH ~ 3.5-14 present a similar Tafel slope of ~ 60  $\text{mV dec}^{-1}$ , that is associated with multistep electrochemical processes whose the mechanism would involve one electrochemical pre-equilibrium step preceding a rate-limiting chemical step. According to this mechanism, pre-equilibrium oxidation of **4** achieves a reactive  $\text{CoO}_2$ -type intermediate **5** which can undergo the rate-limiting O-O bond formation (Figure 25(A)).

Below pH 3,  $\text{CoO}_x$  deposit is not observed on electrode and a Tafel slope of ~ 120  $\text{mV dec}^{-1}$  was determined, corresponding to a mechanism with a rate-limiting one-electron transfer without electrochemical pre-equilibria. The Pourbaix diagram of cobalt at pH below 3 is coherent with a non redox adsorption/deprotonation equilibrium, **1**  $\rightleftharpoons$  **2** (step 1 in Figure 25(B)). Oxidation of  $\text{Co}^{\text{II}}$  (steps 2) corresponds to the rate-limiting one-electron process. Under acidic conditions, the absence of base to withdraw protons after oxidation of  $\text{Co}(\text{O})\text{OH}$  intermediate (**3**) inhibits the formation of  $\text{Co}^{\text{III/IV}}$  oxide. Instead, oxidation of **3** produces  $\text{Co}^{\text{IV}}$  species (**7** in Figure 25(B)) which dissolves from the electrode surface. Then oxygen evolution occurs through the generation and subsequent disproportionation of  $\text{H}_2\text{O}_2$  (step 8).

In summary, the electrokinetic studies highlighted the existence of two possible interrelated OER mechanisms occurring respectively at pHs below and above 3.5.

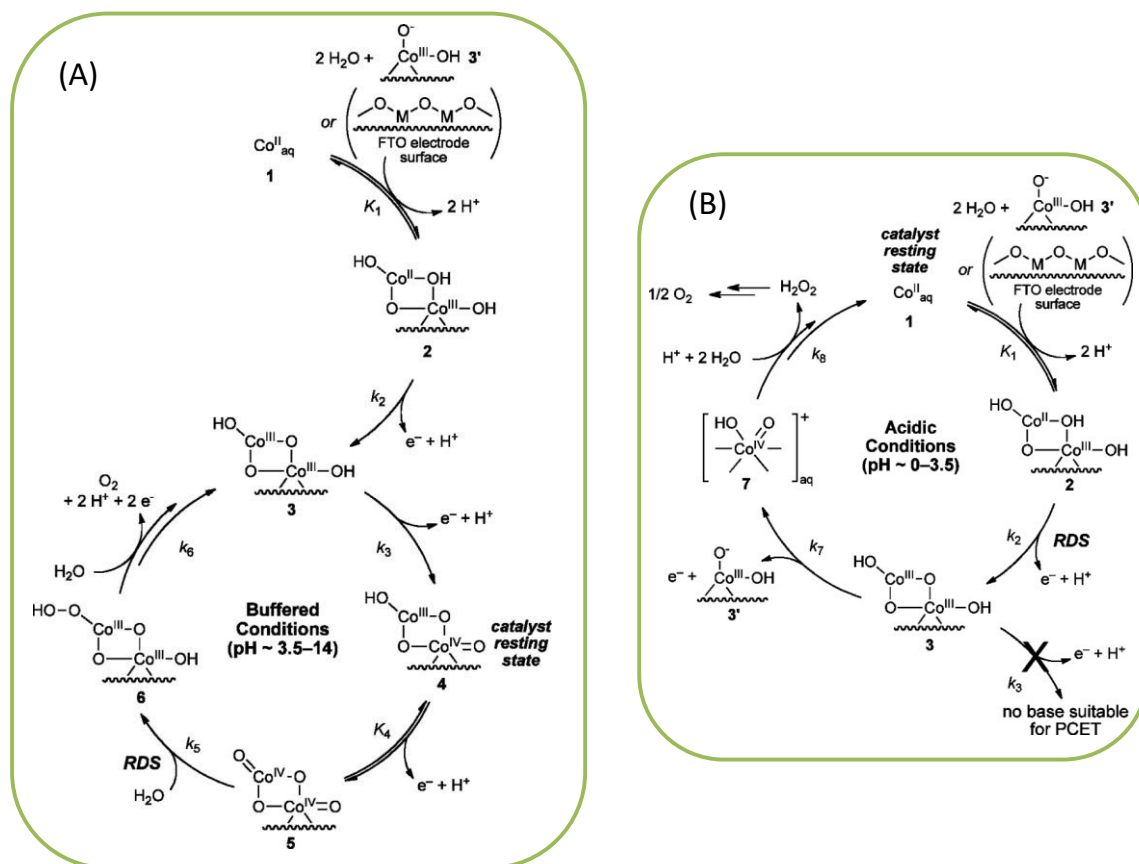


**Figure 25.** (A) Deposition of  $\text{CoO}_x$  and  $\text{CoO}_x$ -catalyzed water oxidation under mildly-acidic to basic conditions with buffering electrolytes. (B) Deposition of  $\text{CoO}_x$  and  $\text{CoO}_x$ -catalyzed water oxidation under acidic conditions with buffering electrolytes. Cobalt oxide intermediates shown are shorthand for adsorbed sites on the electrode surface or a layered double-hydroxide material. Oxo species are depicted schematically and may have significant O-centered radical character and/or a bond order lower than 2. Step 6 is a composite of several rapid reactions that take place after the rate-limiting step (or rate-determining step, RDS) (reproduced from ref <sup>121</sup>, with the permission from the American Chemical Society, Copyright 2011).

Cyclic voltammetry and electron paramagnetic resonance (EPR) spectroscopy allowed the identification of cobalt salts and their oxidation states inside  $\text{CoO}_x$  films at various pHs and electrochemical potentials, and also the oxidation states of the intermediates involved in the OER mechanism. The pH dependence of the electrochemical features recorded in voltammograms provided a basis to build a Pourbaix diagram that mirrors a Pourbaix diagram derived from thermodynamic free energies of formation for various heterogeneous cobalt catalysts. This study, considered in its entirety, provided a basis for understanding the structure, the stability and catalytic activity of heterogeneous cobalt electrocatalysts devoted to OER.

The group of Sun<sup>48</sup> reported a cobalt-phosphorous (Co-P) film as highly efficient bifunctional catalyst for overall water splitting. Co-P films are electrodeposited on copper foils by slowly scanning 15 times between -0.3 and -1.0 V vs Ag/AgCl (scan rate 5 mV s<sup>-1</sup>) in an aqueous solution containing 50 mM CoSO<sub>4</sub>, 0.5 M NaH<sub>2</sub>PO<sub>2</sub> and 0.1 M NaOAc. This electrochemical way allows easily preparing cobalt-phosphorous films with Co and P contents of 2.52 and 0.19 mg cm<sup>-2</sup> respectively, corresponding to a Co/P molar ratio of 6.98. Co-P films showed remarkable catalytic performance for HER and OER in alkaline media (1 M KOH), with a current density of 10 mA cm<sup>-2</sup> at low overpotentials of -94 and 345 mV, and low Tafel slopes of 42 and 47 mV dec<sup>-1</sup>, for HER and OER, respectively. Indeed, the Co-P film is among the best HER catalysts of literature at pH 14, surpassing the catalytic performance of the benchmark Pt-C cathode, since it can produce a catalytic current density of 1 A cm<sup>-2</sup> within a low overpotential of -227 mV cm<sup>-2</sup> and it also displays a long-term stability by maintaining a strong catalytic current after a potentiostatic electrolysis at  $\eta$  of -107 mV during 24 h (Figure 26(a-b)). The Co-P film also competes with the more efficient OER catalysts of literature, especially with IrO<sub>2</sub>. Co-P film is able to reach high catalytic current densities as 10, 100 and 500 mA cm<sup>-2</sup> with low overpotentials as 345, 413 and 463 mV respectively, and exhibits a great stability under long electrolysis over 24 h at  $\eta$  of 345 mV (Figure 26(c-d)). When Co-P film is used as electrocatalytic material for the cathode and the anode within an electrolyzer, the performance of the latter was proven to be superior to that of electrolyzer using the benchmark Pt-C/IrO<sub>2</sub> couple, and the Co-P/Co-P couple presented a faradaic efficiency of 100% for the water splitting reaction.

In view to understand the high OER and HER activities of Co-P, the as-prepared film on copper foil were first characterized by SEM and XPS. SEM images revealed a rough film of cobalt material covering all the electrode with a thickness of 1-3  $\mu$ m and displaying no crystalline particles or aggregates (Figure 26(e)). XPS analysis indicates that the as-prepared film contains a mixture of metallic cobalt, cobalt phosphide and cobalt phosphate. After HER electrocatalysis, SEM and XPS analysis were newly performed on a post-HER Co-P film revealing that the morphology did not change (Figure 26(f)) but the composition of Co-P evolved to a simple mixture of metallic cobalt and cobalt phosphide known to be efficient HER catalysts; cobalt phosphate being dissolved in solution under cathodic conditions. After OER electrocatalysis, SEM and XPS on a post-OER Co-P film indicated a new morphology with large nanoparticle aggregates (Figure 26(g)) along with a partial oxidation of Co-P to Co<sub>3</sub>O<sub>4</sub> and cobalt phosphate, which are among the best OER cobalt-based catalysts.

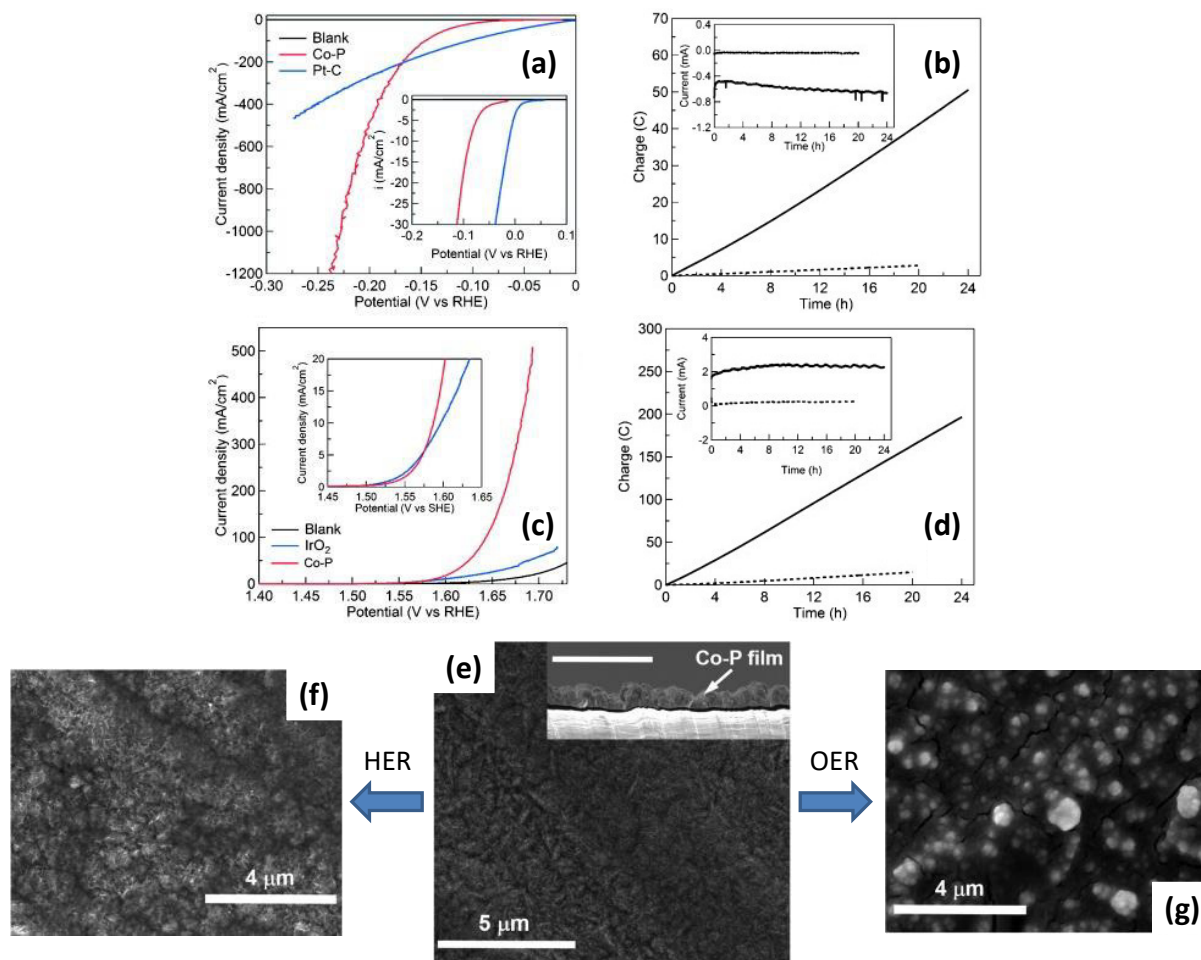


**Figure 26.** (a) LSV curves of Co-P (red), Pt-C (blue) and blank Cu foil (black) in 1 M KOH at a scan rate  $2 \text{ mV s}^{-1}$  and rotating rate of 2000 rpm (Inset: expanded region around the onsets of the LSV curves). (b) Long-term potentiostatic electrolysis of Co-P (solid) and blank Cu foil (dotted) in 1 M KOH at overpotential of  $-107 \text{ mV}$  (Inset: the corresponding current in function of time of Co-P (bottom trace) and blank Cu foil (top trace) during electrolysis at  $\eta -107 \text{ mV}$ ). (c) LSV curves of Co-P (red),  $\text{IrO}_2$  (blue) and blank Cu foil (black) in 1 M KOH at a scan rate  $2 \text{ mV s}^{-1}$  and rotating rate of 2000 rpm (Inset: expanded region around the onsets of the LSV curves). (d) Long-term potentiostatic electrolysis of Co-P (solid) and blank Cu foil (dotted) in 1 M KOH at overpotential of  $343 \text{ mV}$  (Inset: the corresponding current in function of time of Co-P (solid) and blank Cu foil (dotted) during electrolysis at  $\eta 343 \text{ mV}$ ). SEM images of (e) an as-prepared Co-P film (Inset: Cross section of a Co-P film; scale bar is  $5 \mu\text{m}$ ), (f) a Co-P film after a HER electrolysis of 2h at  $\eta -107 \text{ mV}$  and (g) a Co-P film after an OER electrolysis of 2h at  $\eta 343 \text{ mV}$  (reproduced from ref 48, with the permission from Wiley, Copyright 2015).

Sun and coworkers succeeded to prepare by an easy way a cobalt phosphorus film that can be directly utilized as catalysts for anode and cathode with great efficiency, high robustness and 100 % faradaic yield. The high catalytic performance has been correlated to the good roughness and porosity of Co-P and to its adequate composition which is optimized to afford high HER and OER activities at the cathode and the anode.

A large number of heterogeneous cobalt based catalysts has been investigated for water oxidation and most of them possess a specific cobalt local environment with an octahedral geometry ( $O_h$ ), as it was observed by the group of Nocera<sup>119</sup> (see above) for the amorphous Co-Pi. In spite of the fact that the coordination sphere and the electronic structure of the metal within the catalyst have a strong influence on its OER activity, there is no systematic work studying the correlation between the local Co coordination and the water oxidation performance. The group of Kang<sup>124</sup> explored the coordination of cobalt phosphate catalysts toward efficient water oxidation to better understand the catalytic activity of cobalt-based materials. Four cobalt catalysts were investigated,  $Na_2CoP_2O_7$ ,  $NaCoPO_4$ ,  $Li_2CoP_2O_7$  and  $LiCoPO_4$ , presenting various cobalt- and phosphate-coordination groups. These catalysts were synthesized using conventional solid-state methods (*i.e.* solvothermal methods), then spin-coated on ITO electrode *via* an aqueous mixture of catalyst and neutralized Nafion® and dried at 80°C. All these catalysts have crystalline structures with different local cobalt coordination including octahedral ( $NaCoPO_4$  and  $LiCoPO_4$ ), mix of octahedral and trigonal bipyramidal ( $Li_2CoP_2O_7$ ), and tetrahedral ( $Na_2CoP_2O_7$ ) geometries. Among these catalysts,  $Na_2CoP_2O_7$  exhibits high structural stability with a distorted tetrahedral geometry for cobalt (Figure 27(a)) and a higher catalytic activity than that of the amorphous Co-Pi catalyst under neutral conditions. The distorted cobalt geometry was analyzed by DFT calculations which suggested that the former would be induced by the reorganization of pyrophosphate ligand, where water molecules can bind, resulting in a low overpotential of  $\sim 0.42$  eV. Otherwise, characterizations by CV, HR-TEM, XPS, XANES, STEM-EDX and EPR confirm the catalytic and structural stability of  $Na_2CoP_2O_7$  catalyst. The catalytic water oxidation properties of  $Na_2CoP_2O_7$  catalyst was studied by cyclic voltammetry (100 scans between 0.7-1.5 V *vs* NHE) in a sodium phosphate buffer at pH 7, reaching a current density of 2.62 mA  $cm^{-2}$  at 1.44 V *vs.* NHE (Figure 27b). Long-term stability tests performed on  $Na_2CoP_2O_7$  catalyst demonstrated a highly stable catalytic current after 500 scans or 12h of bulk electrolysis at 1.4 V *vs* NHE (Figure 27c).

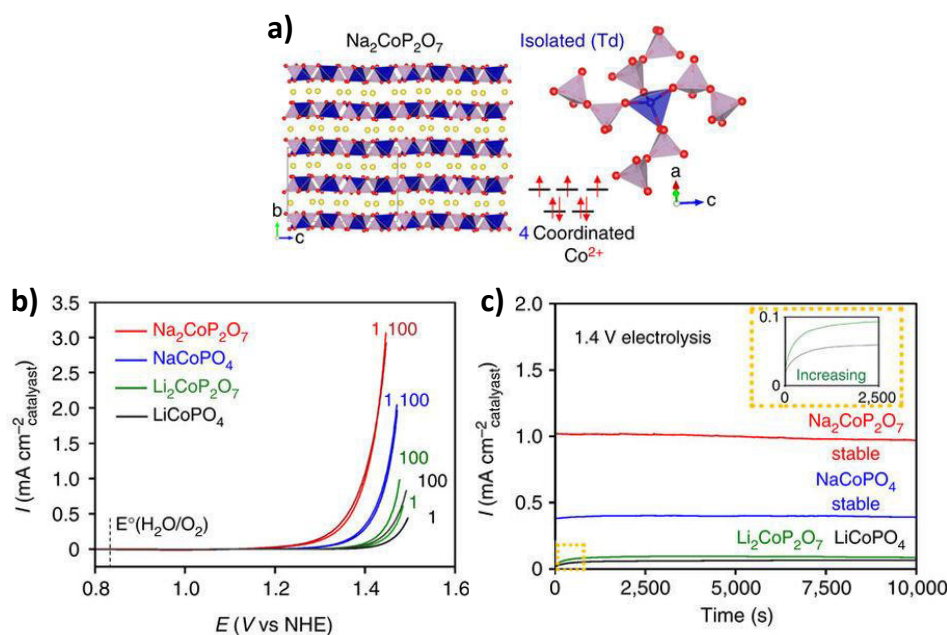


**Figure 27.** (a) Crystal structure and cobalt crystal field of  $\text{Na}_2\text{CoP}_2\text{O}_7$  catalyst. The cobalt atoms, phosphate units and Na atoms are depicted in blue, grey and yellow respectively. (b) Cyclic voltammograms (CVs) of  $\text{Na}_2\text{CoP}_2\text{O}_7$ ,  $\text{Li}_2\text{CoP}_2\text{O}_7$ ,  $\text{NaCoPO}_4$  and  $\text{LiCoPO}_4$  after the 1<sup>st</sup> and 100<sup>th</sup> cycle from 0.7 to 1.5 V vs NHE. The thermodynamic potential for OER at pH 7.0 is positioned at 0.816 V vs NHE. (c) Potentiostatic electrolysis at 1.4 V vs NHE with  $\text{Na}_2\text{CoP}_2\text{O}_7$ ,  $\text{Li}_2\text{CoP}_2\text{O}_7$ ,  $\text{NaCoPO}_4$  and  $\text{LiCoPO}_4$  catalyst. Electrochemical measurements were performed with cobalt catalysts deposited on ITO electrode in sodium phosphate buffer (pH 7.0) (reproduced from ref <sup>124</sup>, with the permission from Macmillan, Copyright 2015).

A Faradaic efficiency of 100 % was calculated for  $\text{Na}_2\text{CoP}_2\text{O}_7$  catalyst attesting its selectivity towards OER. Besides, a Tafel slope of 82 mV  $\text{dec}^{-1}$  was obtained from the 100<sup>th</sup> scan. The Tafel slope value is far from  $2.3\text{RTF}^{-1}$ , indicating that before the rate determining step (RDS) there is a one electron transfer step, most probably due to a limitation in ion or electron transport inside the film of  $\text{Na}_2\text{CoP}_2\text{O}_7$ . Examination of OER kinetic of  $\text{Na}_2\text{CoP}_2\text{O}_7$  catalyst by variation of pH and phosphate concentration of electrolyte indicated that the reaction rate follows approximately an inverse first-order dependence on the proton activity, meanwhile no dependence of the phosphate buffer strength was found. Based on pH dependence and Tafel slope, the authors postulated an equilibrium step involving one-proton/one-electron transfer before RDS. Considering  $\text{Co}^{4+} = \text{O}$  formation could be the RDS of  $\text{Na}_2\text{CoP}_2\text{O}_7$  catalyst according to DFT calculations, the  $\text{Co}^{2+}/\text{Co}^{3+}$  equilibrium could take place before this RDS. Kang and coworkers opened the way for the development of new and efficient OER catalysts using polyanion cobalt-based materials and established a new paradigm by correlating the tetrahedral cobalt geometry to its high OER catalytic activity.

Another strategy to improve the OER performance of cobalt oxide-based catalysts is to deposit them in thin layers on conducting substrates with a high surface area, such as carbon nanowire,<sup>125</sup> graphene<sup>126</sup> and reduced graphene oxide (rGO),<sup>127</sup> thus increasing the exposure of active cobalt atoms to water substrates (or OH<sup>-</sup> anions) to evolve oxygen. In this framework, Song and coworkers<sup>128</sup> reported very recently a synthesis of ultrathin Co<sub>3</sub>O<sub>4</sub>/rGO nanocomposite by one-pot hydrothermal strategy, with an improved surface activity toward OER in comparison with a ultrathin Co<sub>3</sub>O<sub>4</sub> 2D nanosheets, Co<sub>3</sub>O<sub>4</sub>/1D carbon nanotubes (CNTs) and Co<sub>3</sub>O<sub>4</sub>/0D carbon spheres (CS) in alkaline conditions. Characterization by Raman spectrum and XRD demonstrated that the GO is reduced to rGO after hydrothermal reaction, presenting functional groups of -OH and -COOH under hydrothermal conditions. XPS analysis on Co<sub>3</sub>O<sub>4</sub>/rGO showed the presence of C, O and Co elements in the nanocomposite. From XPS data, the atomic Co<sup>2+</sup>/Co<sup>3+</sup> ratio was calculated to be 1.4 for Co<sub>3</sub>O<sub>4</sub>/rGO nanocomposite which is higher than that of 1.2 for Co<sub>3</sub>O<sub>4</sub> nanosheets. Higher Co<sup>2+</sup>/Co<sup>3+</sup> ratio indicates a higher Co<sup>2+</sup> content in the ultrathin Co<sub>3</sub>O<sub>4</sub>/rGO and thus more oxygen vacancies that is often associated with high OER performance. SEM characterization of Co<sub>3</sub>O<sub>4</sub>/rGO nanocomposite showed a structure of flower-like with smooth surface (Figure 28(a)). In addition, the surface of Co<sub>3</sub>O<sub>4</sub>/rGO is fluffy and rougher, with more staggered holes or folds, than that of ultrathin Co<sub>3</sub>O<sub>4</sub> nanosheets. This difference in morphology observed by SEM between both nanocomposites corresponds to a higher specific surface area of Co<sub>3</sub>O<sub>4</sub>/rGO, which was also confirmed by Brunauer-Emmett-Teller (BET) analysis with surface area of 30.68, 74.94, 110.65 and 133.52 m<sup>2</sup> g<sup>-1</sup> for ultrathin Co<sub>3</sub>O<sub>4</sub> nanosheets, Co<sub>3</sub>O<sub>4</sub>/CS, Co<sub>3</sub>O<sub>4</sub>/CNTs and Co<sub>3</sub>O<sub>4</sub>/rGO nanocomposites, respectively. To assess the OER electrocatalytic performance of Co<sub>3</sub>O<sub>4</sub> nanosheets, Co<sub>3</sub>O<sub>4</sub>/CS, Co<sub>3</sub>O<sub>4</sub>/CNTs and Co<sub>3</sub>O<sub>4</sub>/rGO nanocomposite, these cobalt-based materials were dispersed in ethanol with Nafion® and drop casted on carbon fiber paper before drying (mass loading of 0.2 mg cm<sup>-2</sup>). Among the series of studied catalysts, the ultrathin Co<sub>3</sub>O<sub>4</sub>/rGO displayed the best OER activity with a low overpotential of 290 mV at 10 mA cm<sup>-2</sup> (Figure 28(b)), a high and stable catalytic current density above 10 mA cm<sup>-2</sup> during a potentiostatic electrolysis of 10 h and a small value of Tafel slope of 68 mA dec<sup>-1</sup> (Figure 28(c)) in 1 M KOH electrolyte. The low Tafel slope for Co<sub>3</sub>O<sub>4</sub>/rGO nanocomposite suggests a most favorable OER kinetic reaction, due to rGO which improves the efficiency of charge transfer and the surface active area of the nanocomposite. The electrochemical impedance spectroscopy (EIS) analysis also confirmed that Co<sub>3</sub>O<sub>4</sub>/rGO has better conductivity with lower liquid resistance (R<sub>L</sub>) and charge transfer resistance (R<sub>CT</sub>) than Co<sub>3</sub>O<sub>4</sub> nanosheets, Co<sub>3</sub>O<sub>4</sub>/CS and Co<sub>3</sub>O<sub>4</sub>/CNTs. The group of Song

offers a new strategy to improve the OER performance of cobalt oxide-based catalysts, *via* the use of nanocarbon composite, to design highly efficient and stable anodes for water splitting application.

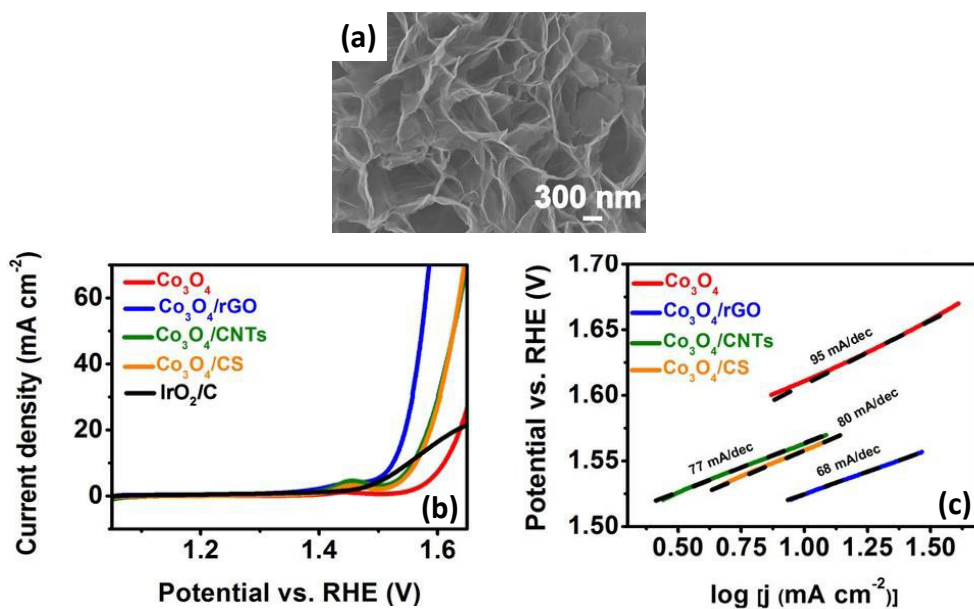


**Figure 28.** (a) SEM images of  $\text{Co}_3\text{O}_4/\text{rGO}$  nanocomposite. (b) LSV curves of  $\text{Co}_3\text{O}_4$  nanosheets (red),  $\text{Co}_3\text{O}_4/\text{rGO}$  (blue),  $\text{Co}_3\text{O}_4/\text{CNTs}$  (green),  $\text{Co}_3\text{O}_4/\text{CS}$  (orange) and  $\text{IrO}_2/\text{C}$  (black) (scan rate  $5 \text{ mV s}^{-1}$ ). (c) Tafel plots of  $\text{Co}_3\text{O}_4$  nanosheets (red),  $\text{Co}_3\text{O}_4/\text{rGO}$  (blue),  $\text{Co}_3\text{O}_4/\text{CNTs}$  (green) and  $\text{Co}_3\text{O}_4/\text{CS}$  (orange). Electrochemical measurements were performed with cobalt/nanocarbon composite catalysts deposited on carbon-fiber paper electrode in 1 M KOH buffer (pH 14.0) (reproduced from ref <sup>128</sup>, with the permission from Wiley, Copyright 2017).

## 4 – Conclusion

Water splitting reaction performed within an electrolyzer remains one of the simplest and most economical ways to produce molecular hydrogen ( $H_2$ ), as alternative of fossil fuels. Nevertheless, its oxidative part, water oxidation to molecular oxygen ( $O_2$ ) or oxygen evolving reaction (OER), is a challenging task due to its high activation barrier, its slow electrode kinetic and its large anodic overpotential. Thus, it is still essential to develop efficient electrocatalysts displaying long-term stability and a low OER overpotential. Since the early 80's, many electrocatalysts using transition-metal oxide, as nickel oxide and cobalt oxide, under various forms, as perovskite, spinel and layer double hydroxide, have been largely investigated for OER following two main guidelines. One guideline consists in developing various synthesis strategies to obtain catalysts of small size or catalyst films with a controlled morphology in view to afford high active surface areas and hence a high OER electrocatalytic activity. Another guideline aims to get rid of the problem of low electrical conductivity of metal based catalysts by ions doping (*e.g.*  $Fe^{3+}$ ) to the catalyst film or by the association of catalysts with a conducting nanomaterial as precious metals (Au, Pt or Pd) and carbon materials (graphene, carbon nanowires and nanotubes).

In the light of these guidelines, this chapter summarized some works on the design of anodes devoted to water oxidation reaction and based on nickel oxide and cobalt oxide catalysts. Some groups like those of Burke, Noufi, Bockris, Corrigan and Tseung, to name a few, were the first in the 80's to demonstrate the potentialities of nickel and cobalt oxides to electrocatalyse water oxidation reaction by electrochemically depositing them on the surface of electrode. Since these pioneer works, many methods, other than electrodeposition, have been reported to prepare nickel and cobalt oxide by solvothermal process or chemical precipitation, which are then deposited on electrode by various processes as spin coating, dropcasting, sol-gel process, electrospray deposition or screen printing, to name a few. All these synthetic strategies allow obtaining metal oxides with controlled forms and sizes as nanoparticles, nanoneedles, nanorods or nanosheets. Nevertheless, electrochemical deposition remains the simplest and the most used method to prepare  $NiO_x$  and  $CoO_x$  based anodes for OER, and the group of Nocera shows in the 2000's that their electrodeposition can be facilitated by using proton-accepting electrolytes (with borate or phosphate salt). Their work has also drawn significant attention to  $NiO_x$  and  $CoO_x$  (i) by providing fundamental insight into the structure of deposited oxides and their OER mechanism, and (ii) by demonstrating

that these electrocatalysts can operate efficiently in neutral (pH 7) or mildly basic media (pH 9.2). After the Nocera's work, many groups reported different strategies to deposit films of metal oxides, especially the group of Spiccia or Kuznetsov which uses the electrodecomposition of nickel complexes or a nickel/molybdenum cluster to prepare NiO<sub>x</sub> films with a high porosity and high OER performance.

Considering the numerous works reported on nickel oxide and cobalt oxide based catalysts, few trends are emerging to design efficient OER anodes. At first glance, if we compare the OER electrocatalytic activities of nickel oxide with those of cobalt oxide, it is clear that NiO<sub>x</sub> is more active than CoO<sub>x</sub>, particularly when NiO<sub>x</sub> is doped with Fe salts by drastically lowering its OER overpotential. Indeed, the mixed layer double hydroxide (LDH) catalysts containing iron, as NiFeO<sub>x</sub> that was first reported by the groups of Radniecka and Corrigan, are the most efficient electrocatalysts of literature for water oxidation reaction. Secondly, the OER activity of NiO<sub>x</sub> and CoO<sub>x</sub>, and more generally of metal-based catalysts, has been improved by nanostructuring the catalytic films in the form of 2D nanomaterials such as nanosheets with a thickness on the atomic scale which can stack on a few layers. This strategy increases the surface-to-volume ratio and the exposure of metal active sites to react with water or hydroxide anions, and accelerates the mass transport of electrolyte salts at the electrode surface, reactants and also of O<sub>2</sub> released. Thirdly, in view to improve the electrical conductivity of the catalytic material, different strategies to prepare anodes have been reported such as for instance the introduction of conducting nanomaterials (*e.g.* carbon nanotube or reduced graphene oxide, see above the work of Song<sup>128</sup>) between the metal oxide and the electrode or the deposition of well-organized nanoarrays of metal oxide directly on electrode (*e.g.* nanoplatelet arrays of NiFeO<sub>x</sub> aligned on glassy carbon electrode, developed by Shao<sup>101</sup>). These approaches ensure a good electrical contact between the catalyst and the electrode and a great electroactive surface area, and thus increase the kinetics of electron transfer and catalytic water oxidation.

Although a great deal of advances has been achieved in recent years in the design of nanostructured inorganic catalyst films based on first-row transition metal oxides (Ni, Co, Fe) of anodes devoted to OER, development of catalysts with a great stability and a high OER performance remains a great challenge and some scientific barriers still need to be raised. To possess the latter features, the catalysts' performance would be improved by:<sup>76</sup>

- (a) Controlling the morphology: An innovative design and synthesis of unique nanostructures has to be developed to increase the specific surface area to expose the catalytic active sites, also, shorten the path for charge/mass transport, and enhancing the conductivity.
- (b) Operating in appropriate media: The OER activity will depend on the pH media. In literature most of OER catalysts of transition metal oxides and hydroxides are investigated in alkaline media. Water oxidation in alkaline media requires 30% KOH electrolyte and high temperature causing high energy consumption, high corrosion and high maintenance costs. OER catalysis in neutral media can resolve these problems.
- (c) Improving stability: Some carbon nanomaterials have been used in combination with metal oxide to enhance the OER performance, but these material can undergo carbon corrosion under working conditions and their electrochemical oxidation produces CO or CO<sub>2</sub> at high potentials (standard potential of 0.297 V *vs* NHE), which decreases the reactive surface area by carbon dissolution and also results in the agglomeration of catalyst. Developing electrocatalysts devoid of carbon supports would be desirable to obtain anode with a great stability.
- (d) Studying OER mechanism: The role of the ion doping (*e.g.* Fe) in the enhancement of the OER activity of the metal oxides mixture is still unclear and under debate. Some groups hypothesized that the better catalytic performance of the metal hydroxides/oxides mixture (NiFeO<sub>x</sub> or CoFeO<sub>x</sub>) over the single-metal oxides (NiO<sub>x</sub> or CoO<sub>x</sub>) is due to a change of electronic structure or increase of electrical conductivity by the introduction of other ions. By contrast, some groups like those of Bell and Boettcher claimed in the case of the NiFeO<sub>x</sub> that FeO<sub>x</sub> is the active sites in the mixed LDH since it is much more active towards OER than NiO<sub>x</sub>. Nevertheless, due to its poor intrinsic electrical conductivity, FeO<sub>x</sub> needs the environment of NiO<sub>x</sub> to ensure a good conductivity of the material and a good catalytic activity. Better understand the interaction of metals inside mixed LDHs will provide guidance to design novel OER catalysts.

## REFERENCES

- (1) Armaroli, N.; Balzani, V. *ChemSusChem* **2011**, *4* (1), 21–36.
- (2) Walter, M. G.; Warren, E. L.; McKone, J. R.; Boettcher, S. W.; Mi, Q.; Santori, E. A.; Lewis, N. S. *Chem. Rev. (Washington, DC, United States)* **2010**, *110* (11), 6446–6473.
- (3) Woolerton, T. W.; Sheard, S.; Chaudhary, Y. S.; Armstrong, F. A. *Energy Environ. Sci.* **2012**, *5*, 7470–7490.
- (4) Santos, D. M. F.; Sequeira, C. A. C.; Figueiredo, J. L. *Quim. Nova* **2013**, *36* (8), 1176–1193.
- (5) de Levie, R. *J. Electroanal. Chem.* **1999**, *476*, 92–93.
- (6) Paets van Troostwijk, A.; Deiman, J. R. *Obs. Phys.* **1789**, *35*, 369.
- (7) Pearson, G. *Phil. Trans.* **1797**, *87*, 142.
- (8) Nicholson W., N. *J. Nat. Phil. Chem. Arts* **1800**, *4*, 179.
- (9) Kreuter, W.; Hofmann, H. *Int. J. Hydrogen Energy* **1998**, *23* (8), 661–666.
- (10) Grewe, T.; Meggouh, M.; Tüysüz, H. *Chem. - An Asian J.* **2016**, *11* (1), 22–42.
- (11) Kärkäs, M. D.; Verho, O.; Johnston, E. V.; Åkermark, B. *Chem. Rev.* **2014**, *114*, 11863–12001.
- (12) Blakemore, J. D.; Crabtree, R. H.; Brudvig, G. W. *Chem. Rev.* **2015**, *115* (23), 12974–13005.
- (13) Suen, N.-T.; Hung, S.-F.; Quan, Q.; Zhang, N.; Xu, Y.-J.; Chen, H. M. *Chem. Soc. Rev.* **2017**, *46* (2), 337–365.
- (14) Indra, A.; Menezes, P. W.; Zaharieva, I.; Baktash, E.; Pfrommer, J.; Schwarze, M.; Dau, H.; Driess, M. *Angew. Chem., Int. Ed.* **2013**, *52* (50), 13206–13210.
- (15) González-Flores, D.; Zaharieva, I.; Heidkamp, J.; Chernev, P.; Martínez-Moreno, E.; Pasquini, C.; Mohammadi, M. R.; Klingan, K.; Gernet, U.; Fischer, A.; Dau, H. *ChemSusChem* **2016**, *9* (4), 379–387.
- (16) Huynh, M.; Bediako, D. K.; Nocera, D. G. *J. Am. Chem. Soc.* **2014**, *136* (16), 6002–6010.
- (17) Hocking, R. K.; Malaeb, R.; Gates, W. P.; Patti, A. F.; Chang, S. L. Y.; Devlin, G.; MacFarlane, D. R.; Spiccia, L. *ChemCatChem* **2014**, *6* (7), 2028–2038.
- (18) Hocking, R. K.; King, H. J.; Hesson, A.; Bonke, S. A.; Johannessen, B.; Fekete, M.; Spiccia, L.; Chang, S. L. Y. *Aust. J. Chem.* **2015**, *68* (11), 1715–1722.
- (19) Huynh, M.; Shi, C.; Billinge, S. J. L.; Nocera, D. G. *J. Am. Chem. Soc.* **2015**, *137* (47), 14887–14904.
- (20) Liu, G.; Hall, J.; Nasiri, N.; Gengenbach, T.; Spiccia, L.; Cheah, M. H.; Tricoli, A. *ChemSusChem* **2015**, *8* (24), 4162–4171.
- (21) Kurz, P. In *Solar Energy for Fuels*; Tüysüz, H., Chan, C. K., Eds.; Springer International Publishing: Cham, 2016; pp 49–72.
- (22) Najafpour, M. M.; Hosseini, S. M. *Dalt. Trans.* **2016**, *45* (42), 16948–16954.
- (23) Najafpour, M. M.; Renger, G.; Hołyńska, M.; Moghaddam, A. N.; Aro, E.-M.; Carpentier, R.; Nishihara, H.; Eaton-Rye, J. J.; Shen, J.-R.; Allakhverdiev, S. I. *Chem. Rev.* **2016**, *116* (5), 2886–2936.
- (24) Lee, S. Y.; González-Flores, D.; Ohms, J.; Trost, T.; Dau, H.; Zaharieva, I.; Kurz, P. *ChemSusChem* **2014**, *7* (12), 3442–3451.
- (25) Smith, R. D. L.; Prévot, M. S.; Fagan, R. D.; Zhang, Z.; Sedach, P. A.; Siu, M. K. J.; Trudel, S.; Berlinguette, C. P. *Science (80-. )* **2013**, *340* (6128), 60–63.
- (26) Kurzman, J. A.; Dettelbach, K. E.; Martinolich, A. J.; Berlinguette, C. P.; Neilson, J. R. *Chem. Mater.* **2015**, *27* (9), 3462–3470.
- (27) Friebel, D.; Louie, M. W.; Bajdich, M.; Sanwald, K. E.; Cai, Y.; Wise, A. M.; Cheng,

- M.-J.; Sokaras, D.; Weng, T.-C.; Alonso-Mori, R.; Davis, R. C.; Bargar, J. R.; Nørskov, J. K.; Nilsson, A.; Bell, A. T. *J. Am. Chem. Soc.* **2015**, *137* (3), 1305–1313.
- (28) Zou, S.; Burke, M. S.; Kast, M. G.; Fan, J.; Danilovic, N.; Boettcher, S. W. *Chem. Mater.* **2015**, *27* (23), 8011–8020.
- (29) Chowdhury, D. R.; Spiccia, L.; Amritphale, S. S.; Paul, A.; Singh, A. *J. Mater. Chem. A* **2016**, *4* (10), 3655–3660.
- (30) Fan, K.; Ji, Y.; Zou, H.; Zhang, J.; Zhu, B.; Chen, H.; Daniel, Q.; Luo, Y.; Yu, J.; Sun, L. *Angew. Chem., Int. Ed.* **2017**, *56* (12), 3289–3293.
- (31) Kanan, M. W.; Nocera, D. G. *Science*. **2008**, *321* (5892), 1072–1075.
- (32) Kanan, M. W.; Surendranath, Y.; Nocera, D. G. *Chem. Soc. Rev.* **2009**, *38* (1), 109–114.
- (33) Surendranath, Y.; Dinca, M.; Nocera, D. G. *J. Am. Chem. Soc.* **2009**, *131* (7), 2615–2620.
- (34) Kanan, M. W.; Yano, J.; Surendranath, Y.; Dinca, M.; Yachandra, V. K.; Nocera, D. G. *J. Am. Chem. Soc.* **2010**, *132* (39), 13692–13701.
- (35) Esswein, A. J.; Surendranath, Y.; Reece, S. Y.; Nocera, D. G. *Energy Environ. Sci.* **2011**, *4* (2), 499–504.
- (36) Surendranath, Y.; Lutterman, D. A.; Liu, Y.; Nocera, D. G. **2012**.
- (37) Cobo, S.; Heidkamp, J.; Jacques, P.-A.; Fize, J.; Fourmond, V.; Guetaz, L.; Jousset, B.; Ivanova, V.; Dau, H.; Palacin, S.; Fontecave, M.; Artero, V. *Nat. Mater.* **2012**, *11* (9), 802–807.
- (38) Blakemore, J. D.; Gray, H. B.; Winkler, J. R.; Müller, A. M. *ACS Catal.* **2013**, *3* (11), 2497–2500.
- (39) Farrow, C. L.; Bediako, D. K.; Surendranath, Y.; Nocera, D. G.; Billinge, S. J. L. *J. Am. Chem. Soc.* **2013**, *135* (17), 6403–6406.
- (40) Bediako, D. K.; Costentin, C.; Jones, E. C.; Nocera, D. G.; Savéant, J.-M. *J. Am. Chem. Soc.* **2013**, *135* (28), 10492–10502.
- (41) Smith, R. D. L.; Prévot, M. S.; Fagan, R. D.; Trudel, S.; Berlinguette, C. P. *J. Am. Chem. Soc.* **2013**, *135* (31), 11580–11586.
- (42) Bonke, S. A.; Wiechen, M.; Hocking, R. K.; Fang, X. Y.; Lupton, D. W.; Macfarlane, D. R.; Spiccia, L. *ChemSusChem* **2015**, *8* (8), 1394–1403.
- (43) Zhu, J.; Lambert, F.; Policar, C.; Mavre, F.; Limoges, B. *J. Mater. Chem. A* **2015**, *3* (31), 16190–16197.
- (44) González-Flores, D.; Sánchez, I.; Zaharieva, I.; Klingan, K.; Heidkamp, J.; Chernev, P.; Menezes, P. W.; Driess, M.; Dau, H.; Montero, M. L. *Angew. Chemie - Int. Ed.* **2015**, *54* (8), 2472–2476.
- (45) Menezes, P. W.; Indra, A.; González-Flores, D.; Sahraie, N. R.; Zaharieva, I.; Schwarze, M.; Strasser, P.; Dau, H.; Driess, M. *ACS Catal.* **2015**, *5* (4), 2017–2027.
- (46) Bergmann, A.; Martinez-Moreno, E.; Teschner, D.; Chernev, P.; Gliech, M.; De Araújo, J. F.; Reier, T.; Dau, H.; Strasser, P. *Nat. Commun.* **2015**, *6*, 1–9.
- (47) Risch, M.; Ringleb, F.; Kohlhoff, M.; Bogdanoff, P.; Chernev, P.; Zaharieva, I.; Dau, H. *Energy Environ. Sci.* **2015**, *8* (2), 661–674.
- (48) Jiang, N.; You, B.; Sheng, M.; Sun, Y. *Angew. Chem., Int. Ed.* **2015**, *54* (21), 6251–6254.
- (49) Najafpour, M. M.; Hosseini, S. M.; Tavahodi, M.; Ghobadi, M. Z. *Int. J. Hydrog. Energy* **2016**, *41* (31), 13469–13475.
- (50) Liu, G.; Karuturi, S. K.; Simonov, A. N.; Fekete, M.; Chen, H.; Nasiri, N.; Le, N. H.; Reddy Narangari, P.; Lysevych, M.; Gengenbach, T. R.; Lowe, A.; Tan, H. H.; Jagadish, C.; Spiccia, L.; Tricoli, A. *Adv. Energy Mater.* **2016**, 1–9.
- (51) Bediako, D. K.; Ullman, A. M.; Nocera, D. G. In *Solar Energy for Fuels*; Tüysüz, H.,

- Chan, C. K., Eds.; Springer International Publishing: Cham, 2016; pp 173–213.
- (52) Chen, H.; Gao, Y.; Sun, L. *ChemCatChem* **2016**, *8* (17), 2757–2760.
- (53) Costentin, C.; Porter, T. R.; Savéant, J.-M. *J. Am. Chem. Soc.* **2016**, *138* (17), 5615–5622.
- (54) King, H. J.; Bonke, S. A.; Chang, S. L. Y.; Spiccia, L.; Johannessen, B.; Hocking, R. K. *ChemCatChem* **2017**, *9* (3), 511–521.
- (55) Huynh, M.; Ozel, T.; Liu, C.; Lau, E. C.; Nocera, D. G. *Chem. Sci.* **2017**, *8* (7), 4779–4794.
- (56) Daniel, Q.; Ambre, R. B.; Zhang, B.; Philippe, B.; Chen, H.; Li, F.; Fan, K.; Ahmadi, S.; Rensmo, H.; Sun, L. *ACS Catal.* **2017**, *7* (2), 1143–1149.
- (57) Dinca, M.; Surendranath, Y.; Nocera, D. G. *Proc. Natl. Acad. Sci.* **2010**, *107* (23), 10337–10341.
- (58) Trotochaud, L.; Ranney, J. K.; Williams, K. N.; Boettcher, S. W. *J. Am. Chem. Soc.* **2012**, *134* (41), 17253–17261.
- (59) Singh, A.; Chang, S. L. Y.; Hocking, R. K.; Bach, U.; Spiccia, L. *Energy Environ. Sci.* **2013**, *6* (2), 579–586.
- (60) Singh, A.; Chang, S. L. Y.; Hocking, R. K.; Bach, U.; Spiccia, L. *Catal. Sci. Technol.* **2013**, *3* (7), 1725.
- (61) Louie, M. W.; Bell, A. T. *J. Am. Chem. Soc.* **2013**, *135* (33), 12329–12337.
- (62) Bediako, D. K.; Surendranath, Y.; Nocera, D. G. *J. Am. Chem. Soc.* **2013**, *135* (9), 3662–3674.
- (63) Stern, L.-A.; Hu, X. *Faraday Discuss.* **2014**, *176*, 363–379.
- (64) Singh, A.; Fekete, M.; Gengenbach, T.; Simonov, A. N.; Hocking, R. K.; Chang, S. L. Y.; Rothmann, M.; Powar, S.; Fu, D. C.; Hu, Z.; Wu, Q.; Cheng, Y. B.; Bach, U.; Spiccia, L. *ChemSusChem* **2015**, *8* (24), 4266–4274.
- (65) McCrory, C. C. L.; Jung, S.; Ferrer, I. M.; Chatman, S. M.; Peters, J. C.; Jaramillo, T. F. *J. Am. Chem. Soc.* **2015**, *137* (13), 4347–4357.
- (66) Görlin, M.; Chernev, P.; Ferreira de Araújo, J.; Reier, T.; Dresp, S.; Paul, B.; Krähnert, R.; Dau, H.; Strasser, P. *J. Am. Chem. Soc.* **2016**, *138* (17), 5603–5614.
- (67) Smith, R. D. L.; Sherbo, R. S.; Dettelbach, K. E.; Berlinguette, C. P. *Chem. Mater.* **2016**, *28* (16), 5635–5642.
- (68) Fan, K.; Chen, H.; Ji, Y.; Huang, H.; Claesson, P. M.; Daniel, Q.; Philippe, B.; Rensmo, H.; Li, F.; Luo, Y.; Sun, L. *Nat. Commun.* **2016**, *7*, 11981.
- (69) Najafpour, M. M.; Moghaddam, N. J. *New J. Chem.* **2017**, *41* (5), 1909–1913.
- (70) Li, N.; Bediako, D. K.; Hadt, R. G.; Hayes, D.; Kempa, T. J.; von Cube, F.; Bell, D. C.; Chen, L. X.; Nocera, D. G. *Proc. Natl. Acad. Sci.* **2017**, *114* (7), 1486–1491.
- (71) Görlin, M.; Ferreira de Araújo, J.; Schmies, H.; Bernsmeier, D.; Dresp, S.; Gliech, M.; Jusys, Z.; Chernev, P.; Kraehnert, R.; Dau, H.; Strasser, P. *J. Am. Chem. Soc.* **2017**, *139* (5), 2070–2082.
- (72) Doyle, R. L.; Godwin, I. J.; Brandon, M. P.; Lyons, M. E. G. *Phys. Chem. Chem. Phys.* **2013**, *15* (33), 13737–13783.
- (73) Singh, A.; Spiccia, L. *Coord. Chem. Rev.* **2013**, *257* (17–18), 2607–2622.
- (74) Galán-Mascarós, J. R. *ChemElectroChem* **2015**, *2* (1), 37–50.
- (75) Hunter, B. M.; Gray, H. B.; Müller, A. M. *Chem. Rev.* **2016**, *116* (22), 14120–14136.
- (76) Han, L.; Dong, S.; Wang, E. *Adv. Mater.* **2016**, *28* (42), 9266–9291.
- (77) Bonke, S. A.; Bond, A. M.; Spiccia, L.; Simonov, A. N. *J. Am. Chem. Soc.* **2016**, *138* (49), 16095–16104.
- (78) S, A.; Ede, S. R. R.; Kannimuthu, K.; Sam Sankar, S.; Sangeetha, K.; Pitchiah, E. K.; Kundu, S. *Energy Environ. Sci.* **2018**, 1–90.
- (79) Asraf, M. A.; Younus, H. A.; Yusubov, M.; Verpoort, F. *Catal. Sci. Technol.* **2015**, *5*

- (11), 4901–4925.
- (80) Burke, M. S.; Enman, L. J.; Batchellor, A. S.; Zou, S.; Boettcher, S. W. *Chem. Mater.* **2015**, *27* (22), 7549–7558.
- (81) Gong, M.; Dai, H. *Nano Res.* **2015**, *8* (1), 23–39.
- (82) Lyons, M. E. G.; Brandon, M. P. *Int. J. Electrochem. Sci.* **2008**, *3* (12), 1386–1424.
- (83) Wehrens-Dijksma, M.; Notten, P. H. L. *Electrochim. Acta* **2006**, *51* (18), 3609–3621.
- (84) Lyons, M. E. G.; Cakara, A.; O'Brien, P.; Godwin, I.; Doyle, R. L. *Int. J. Electrochem. Sci.* **2012**, *7* (12), 11768–11795.
- (85) Dinca, M.; Surendranath, Y.; Nocera, D. G. *Proc. Natl. Acad. Sci. U. S. A.* **2010**, *107* (23), 10337–10341.
- (86) Bediako, D. K.; Lassalle-Kaiser, B.; Surendranath, Y.; Yano, J.; Yachandra, V. K.; Nocera, D. G. *J. Am. Chem. Soc.* **2012**, *134* (15), 6801–6809.
- (87) Singh, A.; Fekete, M.; Gengenbach, T.; Simonov, A. N.; Hocking, R. K.; Chang, S. L. Y.; Rothmann, M.; Powar, S.; Fu, D.; Hu, Z.; Wu, Q.; Cheng, Y. B.; Bach, U.; Spiccia, L. *ChemSusChem* **2015**, *8* (24), 4266–4274.
- (88) Kuznetsov, D. A.; Konev, D. V.; Komarova, N. S.; Ionov, A. M.; Mozhchil, R. N.; Fedyanin, I. V. *Chem. Commun.* **2016**, *52* (59), 9255–9258.
- (89) McCrory, C. C. L.; Jung, S.; Ferrer, I. M.; Chatman, S. M.; Peters, J. C.; Jaramillo, T. F. *J. Am. Chem. Soc.* **2015**, *137* (13), 4347–4357.
- (90) McCrory, C. C. L.; Jung, S.; Peters, J. C.; Jaramillo, T. F. *J. Am. Chem. Soc.* **2013**, *135* (45), 16977–16987.
- (91) Shinagawa, T.; Garcia-Esparza, A. T.; Takanabe, K. *Sci. Rep.* **2015**, *5* (1), 13801.
- (92) Młynarek, G.; Paszkiewicz, M.; Radniecka, A. *J. Appl. Electrochem.* **1984**, *14* (2), 145–149.
- (93) Corrigan, D. A. *J. Electrochem. Soc.* **1987**, *134* (2), 377–384.
- (94) Smith, A. M.; Trotochaud, L.; Burke, M. S.; Boettcher, S. W. *Chem. Commun.* **2015**, *51* (25), 5261–5263.
- (95) Trotochaud, L.; Young, S. L.; Ranney, J. K.; Boettcher, S. W. *J. Am. Chem. Soc.* **2014**, *136*, 6744.
- (96) Görlin, M.; Gliech, M.; De Araújo, J. F.; Dresch, S.; Bergmann, A.; Strasser, P. *Catal. Today* **2016**, *262*, 65–73.
- (97) Song, F.; Hu, X. *Nat. Commun.* **2014**, *5*, 4477.
- (98) Fominykh, Ksenia; Feckl, Johann M.; Sicklinger, Johannes; Doblinger Markus; Bocklein Sebastien; Ziegler Jurgen; Peter, Laurence; Rathousky, Jiri; Scheidt, Ernst-Wilhelm; Bein, Thomas; Fattakhova-Rohlfing, D. *Ad. Funct. Mater* **2014**, *24*, 3123–3129.
- (99) Fominykh, K.; Chernev, P.; Zaharieva, I.; Sicklinger, J.; Stefanic, G.; Döblinger, M.; Müller, A.; Pokharel, A.; Böcklein, S.; Scheu, C.; Bein, T.; Fattakhova-Rohlfing, D. *ACS Nano* **2015**, *9* (5), 5180–5188.
- (100) Weng, B.; Xu, F.; Wang, C.; Meng, W.; Grice, C. R.; Yan, Y. *Energy Environ. Sci.* **2017**, *10* (1), 121–128.
- (101) Li, Z.; Shao, M.; An, H.; Wang, Z.; Xu, S.; Wei, M.; Evans, D. G.; Duan, X. *Chem. Sci.* **2015**, *6* (11), 6624–6631.
- (102) Zhang, W.; Wu, Y.; Qi, J.; Chen, M.; Cao, R. *Adv. Energy Mater.* **2017**, *7* (9), in Press, DOI:10.1002/aenm.201602547.
- (103) Suzuki, O.; Takahashi, M.; Fukunaga, T.; Kuboyama, J. US Patent, 1968.
- (104) Shafirovich, V. Y.; Strelets, V. V. *Nouv. J. Chim.* **1978**, *2* (3), 199–201.
- (105) Burke, L. D.; Lyons, M. E.; Murphy, O. J. *J. Electroanal. Chem. Interfacial Electrochem.* **1982**, *132*, 247–261.
- (106) Bockris, J. O.; Otagawa, T. *J. Phys. Chem.* **1983**, *87* (15), 2960–2971.

- (107) Brockis, J. O.; Otagawa, T. *J. Electrochem. Soc.* **1984**, *131* (2), 290–302.
- (108) Chen, Y.-W. D.; Noufi, R. N. *J. Electrochem. Soc.* **1984**, *131* (6), 1447.
- (109) Rasiyah, P.; Tseung, A. C. C. *J. Electrochem. Soc.* **1983**, *130* (2), 365–368.
- (110) Rasiyah, P.; Tseung, A. C. C. *J. Electrochem. Soc.* **1984**, *131* (4), 803–808.
- (111) Gardner, G.; Al-Sharab, J.; Danilovic, N.; Go, Y. B.; Ayers, K.; Greenblatt, M.; Charles Dismukes, G. *Energy Environ. Sci.* **2016**, *9* (1), 184–192.
- (112) Suryanto, B. H. R.; Lu, X.; Chan, H. M.; Zhao, C. *RSC Adv.* **2013**, *3* (43), 20936.
- (113) Jiang, S. P.; Tseung, A. C. C. *J. Electrochem. Soc.* **1991**, *138* (5), 1216–1222.
- (114) Castro, E. B.; Gervasi, C. A.; Vilche, J. R. *J. Appl. Electrochem.* **1998**, *28*, 835–841.
- (115) Casella, Inocenzo G.; Gatta, M. *J. Electroanal. Chem.* **2002**, *534*, 31–38.
- (116) Kanan, M. W.; Nocera, D. G. *Science (80-. )*. **2008**, *321* (5892), 1072–1075.
- (117) Surendranath, Y.; Lutterman, D. A.; Liu, Y.; Nocera, D. G. *J. Am. Chem. Soc.* **2012**, *134* (14), 6326–6336.
- (118) Surendranath, Y.; Dinc, M.; Nocera, D. G. **2009**, No. 8, 2615–2620.
- (119) Kanan, M. W.; Yano, J.; Surendranath, Y.; Dinca, M.; Yachandra, V. K.; Nocera, D. G. *J. Am. Chem. Soc.* **2010**, *132* (39), 13692–13701.
- (120) Gerken, J. B.; Landis, E. C.; Hamers, R. J.; Stahl, S. S. *ChemSusChem* **2010**, *3* (10), 1176–1179.
- (121) Gerken, J. B.; McAlpin, J. G.; Chen, J. Y. C.; Rigsby, M. L.; Casey, W. H.; Britt, R. D.; Stahl, S. S. *J. Am. Chem. Soc.* **2011**, *133* (36), 14431–14442.
- (122) Noufi, R. *J. Electrochem. Soc.* **1983**, *130* (10), 2126–2128.
- (123) Deltombe, E. Pourbaix, M. *In Atlas D'Equilibres Electrochimiques*; Ed. Gauthier-Villars: Paris, France, 1963.
- (124) Kim, H.; Park, J.; Park, I.; Jin, K.; Jerng, S. E.; Kim, S. H.; Nam, K. T.; Kang, K. *Nat. Commun.* **2015**, *6*, 1–11.
- (125) Ma, T. Y.; Dai, S.; Jaroniec, M.; Qiao, S. Z. *J. Am. Chem. Soc.* **2014**, *136* (39), 13925–13931.
- (126) Zhao, Y.; Chen, S.; Sun, B.; Su, D.; Haung, X.; Liu, H.; Yan, Y.; Sun, K.; Wang, G. *Sci. Rep.* **2015**, *5*, 7629.
- (127) Liang, Y.; Li, Y.; Wang, H.; Zhou, J.; Wang, J.; Regier, T.; Dai, H. *Nat. Mater.* **2011**, *10*, 780–786.
- (128) Chen, Y.; Hu, J.; Diao, H.; Luo, W.; Song, Y. F. *Chem. - A Eur. J.* **2017**, *23* (16), 4010–4016.



**Nickel Oxide-Polypyrrole Nanocomposite Electrode  
Materials for Electrocatalytic Water Oxidation**



---

**INDEX**

1 – Introduction .....	57
2 – Results and discussion.....	58
2.1 – Electrosynthesis and Electrocharacterization of Nickel Oxide and Poly(pyrrrole-alkylammonium)-Nickel Oxide Nanocomposite Electrode Materials. ....	58
2.2 – Characterization of Nickel Oxide and Poly(pyrrrole-alkylammonium)-Nickel Oxide Nanocomposite Electrode Materials by AFM and TEM Microscopies.....	67
2.3 – Electrocatalytic performance of Nickel Oxide and Poly(pyrrrole-alkylammonium)-Nickel Oxide Nanocomposite Electrodes.....	69
3. Conclusion.....	79
References .....	80



## 1 - Introduction

As we saw in the previous chapter of this manuscript, a very attractive approach to produce molecular hydrogen, one of the best alternatives to fossil fuels, is to perform water splitting reaction *via* an electrochemical way. However, the oxidative part of this process, oxygen evolving reaction (OER) through water oxidation, remains an arduous reaction since it displays high activation barrier and large anodic overpotential. Since the early 80's, numerous works aimed at developing electrocatalysts for OER based on metal oxides that tend to lower its activation barrier and exhibit a great stability during a long-term electrolysis and a low OER overpotential. Among these electrocatalysts, the most extensively studied are nickel oxyhydroxide (Ni(O)(OH), also denoted herein nickel oxide or NiO<sub>x</sub>) and nickel hydroxide (Ni(OH)<sub>2</sub>) because of their large use in supercapacitors, alkaline batteries and electrolysis cells,<sup>1</sup> and their long term corrosion resistance and high electrocatalytic activity towards OER. It has been shown that the catalytic performances of NiO<sub>x</sub> can be significantly enhanced by the introduction of iron ions within the structure of the oxide, leading to a decrease of its OER overpotential of at least 200 mV.<sup>2-5</sup> Another way to improve the electrocatalytic performance of NiO<sub>x</sub> and more generally of metal oxide deposited on electrodes, is to control the porosity and morphology of the films and/or to decrease the size of metal oxide particles, which allow promoting the electron/mass transport at the electrode surface, increasing the electroactive surface area of the electrode and thus enhancing the accessibility of catalytic active sites towards water substrate. To this end, several physical and chemical methods have already been employed to deposit nickel oxide on conducting electrodes,<sup>1, 6-7</sup> as solvothermal, electrochemical or sol-gel deposition, in order to obtain various forms and morphologies like hollow spheres,<sup>8</sup> microballs,<sup>9</sup> nanoplates,<sup>8</sup> nanosheets<sup>10</sup> or very small nanocrystals.<sup>11</sup>

Herein, we propose an “all electrochemical” strategy to prepare highly nanostructured nickel oxide anodes very active for OER based on a nanocomposite material deposited on an electrode surface. This material is composed of NiO<sub>x</sub> nanoparticles entrapped into a poly(pyrrole-alkyl ammonium) matrix (denoted poly**1**, where **1** is the pyrrole-ammonium monomer, Scheme S1 in the Supporting Information). By contrast to the usual oxidation process employed for the electrodeposition of nickel oxide films at an electrode surface, the approach used here consists in first inducing the electroprecipitation of Ni<sup>0</sup> nanoparticles into the poly**1** film and then to generate *in-situ* NiO<sub>x</sub> by electro-oxidation of Ni<sup>0</sup>. A rather similar strategy was previously employed in our group to build iridium oxide-polypyrrole

nanocomposite anodes very efficient for OER, displaying 2 nm nanoparticles of IrO<sub>x</sub> dispersed within the polymer matrix.<sup>12</sup>

The poly1-NiO<sub>x</sub> nanocomposite material has been characterized by various electrochemical techniques, and also by inductively coupled plasma mass spectroscopy (ICP-MS), atomic force microscopy (AFM), transmission electron microscopy (TEM) and selected area electron diffraction (SAED). The electrocatalytic properties of this material toward water oxidation in mildly neutral and basic conditions have been also evaluated and compared with those of a NiO<sub>x</sub> film directly deposited on a naked electrode by the same electrochemical procedure. Finally, we have performed a careful comparison of the electrocatalytic OER performance of these electrodes in near neutral and basic conditions to that of some nickel-based electrodes previously reported at similar pHs.

## 2 - Results and discussion

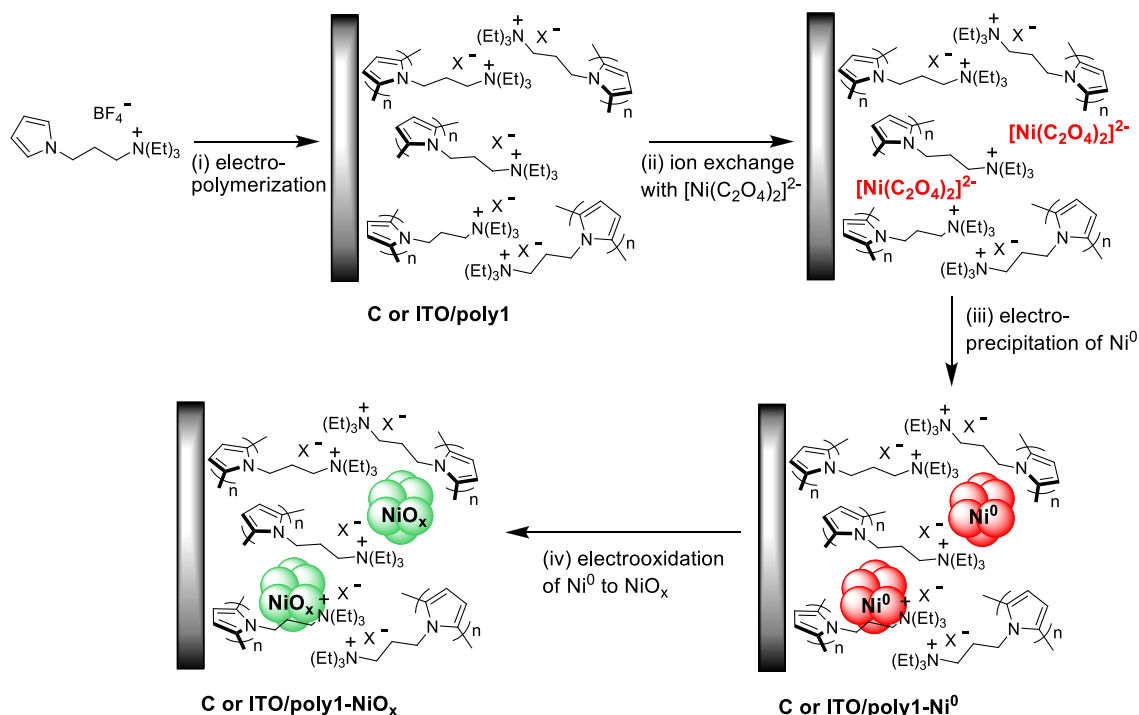
### *2.1 - Electrosynthesis and Electrocharacterization of Nickel Oxide and Poly(pyrrole-alkylammonium)-Nickel Oxide Nanocomposite Electrode Materials.*

Deposition of metallic oxide on electrodes, specially nickel oxide, has been performed *via* several physical and chemical methods<sup>1</sup> but the simplest and the more versatile one is the electrochemical technique.<sup>7</sup> Nickel oxide is generally electrodeposited anodically either by galvanostatic, potentiostatic or potentiodynamic (*i.e.* cyclic voltammetry) experiments<sup>1</sup> from a basic aqueous solution of nickel salt or nickel complexes in presence of borate buffer at pH 9.2. The resulting bulk NiO<sub>x</sub> films are known to be efficient and low-cost OER electrocatalyst in alkaline conditions with overpotentials lower than 0.47 V for a current density of 10 mA cm<sup>-2</sup>.<sup>13-14</sup> In view of developing structured, active and stable anodes for OER as mentioned in introduction, we synthesized by an all electrochemical procedure nanocomposite electrode materials composed of NiO<sub>x</sub> particles entrapped into a poly(pyrrole-alkylammonium) thin film coated onto C or ITO electrodes. This strategy based on the electroprecipitation of catalyst particles into a functionalized polypyrrole film was previously reported by Noufi<sup>15</sup>, Yoneyama<sup>16</sup> and also by our group with various metals and employed as electrocatalytic materials for several reactions.<sup>12, 17-23</sup> Indeed, in our group, metallic (oxide) nanoparticles dispersed into a poly(pyrrole-alkylammonium) film were electrogenerated either by reduction or by oxidation of the corresponding metallic salts leading to Pd<sup>0</sup>,<sup>18</sup> Rh<sup>0</sup>,<sup>18</sup> Ni<sup>0</sup>,<sup>17</sup> and MoS<sub>x</sub><sup>22-</sup>

<sup>23</sup> for hydrogenation of various organic substrates and water reduction, or to ruthenium<sup>19</sup> and iridium<sup>21, 37</sup> oxides for the oxidation of arsenite and water.

Here, the C or ITO/poly1-NiO<sub>x</sub> modified electrodes were prepared following a four step electrochemical procedure depicted in Scheme 1. The poly1 electrodes were first easily obtained by electropolymerization of the pyrrole ammonium monomer **1** (4 mM) at a controlled-oxidation potential of +0.95 V vs Ag/AgNO<sub>3</sub> for C and 1.1 V for ITO in acetonitrile (Scheme 1 and Figure 1). The surface coverage in ammonium units  $\Gamma_N^+$  (mol cm<sup>-2</sup>), *i.e.* the quantity of pyrrole units deposited on C and ITO electrodes (0.071 and 0.5 cm<sup>2</sup>, respectively), was quantified electrochemically by integration of the polypyrrole reversible wave (see the Supporting Information).  $\Gamma_N^+$  values ranging from 1.1 × 10<sup>-7</sup> to 1.3 × 10<sup>-7</sup> mol cm<sup>-2</sup> for C electrodes and 4.5 × 10<sup>-7</sup> to 5.5 × 10<sup>-7</sup> mol cm<sup>-2</sup> for ITO electrodes were obtained when 4 and 28 mC of anodic charge was used for the polymerization of **1** on the C and ITO electrodes respectively (Figure 2).

**Scheme 1.** General Strategy for the Electrosynthesis of Poly(Pyrrole-alkylammonium)/NiO<sub>x</sub> Composite Film Modified Electrodes<sup>a</sup>



<sup>a</sup>(i) Formation of poly1 by oxidative electropolymerization of monomer **1** (4 mM) at  $E_{app} = +0.95$  V vs Ag/AgNO<sub>3</sub> in CH<sub>3</sub>CN, 0.1 M [Bu<sub>4</sub>N]ClO<sub>4</sub>; (ii) incorporation of  $[\text{Ni}(\text{C}_2\text{O}_4)_2]^{2-}$  into poly1 upon soaking during 1h in an aqueous solution (pH 6) of 1 mM NiSO<sub>4</sub>, 5 mM NaC<sub>2</sub>O<sub>4</sub>, 0.1 M Na<sub>2</sub>SO<sub>4</sub> and 0.1 M H<sub>3</sub>BO<sub>3</sub>; (iii) electroprecipitation of Ni<sup>0</sup> within poly1 at  $E_{app} = -1.4$  V vs Ag/AgCl in the previously mentioned aqueous solution of nickel oxalate; (iv) electrooxidation of Ni<sup>0</sup> to NiO<sub>x</sub> by repeated cyclic voltammetry scans between 0 and +1.2 V vs Ag/AgCl in an aqueous solution (pH 9.2) of 0.1 M H<sub>3</sub>BO<sub>3</sub> and 0.05 M NaOH.

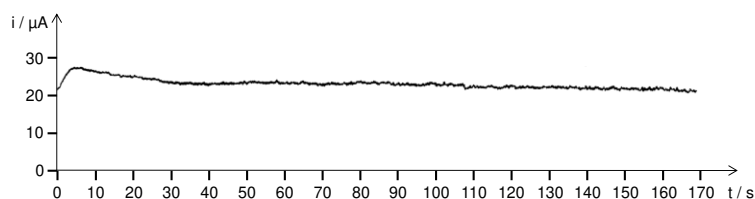


**Figure 1.** Deposition of a poly $\mathbf{1}$  film on a C disc electrode (3 mm diameter), charge passed 4.0 mC at +0.95 V vs Ag/AgNO<sub>3</sub> in a 4.0 mM solution of  $\mathbf{1}$  in CH<sub>3</sub>CN with 0.1 M [Bu<sub>4</sub>N]ClO<sub>4</sub>.

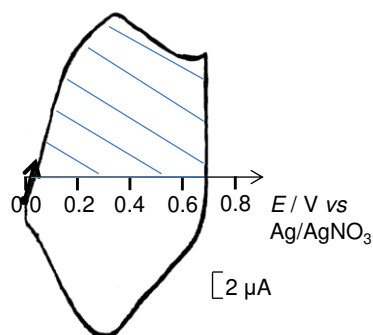


**Figure 2.** Three successive scans between 0 and +0.7 V of the C/poly $\mathbf{1}$  modified electrode ( $\Gamma_{\text{N}^+} = 1.2 \times 10^{-7} \text{ mol cm}^{-2}$ ) in CH<sub>3</sub>CN with 0.1 M [Bu<sub>4</sub>N]ClO<sub>4</sub>; scan rate of 10 mV s<sup>-1</sup>.

Using the excellent ion-exchange properties of the cationic polymeric film poly $\mathbf{1}$ , this film was then loaded with the anionic nickel oxalate complex,  $[\text{Ni}(\text{C}_2\text{O}_4)_2]^{2-}$  generated *in situ* from an aqueous borate buffer (0.1 M) solution at pH 6 containing 1 mM of NiSO<sub>4</sub> and 5 mM NaC<sub>2</sub>O<sub>4</sub>. According to previous studies, in such conditions, the di-anionic  $[\text{Ni}(\text{C}_2\text{O}_4)_2]^{2-}$  complex is the largely predominate species present in solution compared to Ni(C<sub>2</sub>O<sub>4</sub>) and  $[\text{Ni}(\text{C}_2\text{O}_4)_3]^{4-}$ .<sup>17</sup> The large concentration in the negatively charged  $[\text{Ni}(\text{C}_2\text{O}_4)_2]^{2-}$  complex allows ensuring a good loading of nickel into the cationic pyrrole-alkylammonium polymer film. In a third step, an efficient incorporation of Ni<sup>0</sup> particles inside the poly $\mathbf{1}$  film was achieved by electroreduction of the  $[\text{Ni}(\text{C}_2\text{O}_4)_2]^{2-}$  loaded in the film at a controlled-potential of -1.4 V vs Ag/AgCl by maintaining the electrode in the nickel oxalate solution. For this electroreduction, only about 80-90 seconds was required to pass 4 mc of cathodic charge (Figure 3). This approach was already used by our group to prepare C/polypyrrole-alkylammonium-Ni<sup>0</sup> nanocomposite electrode materials for electrocatalytic hydrogenation of ketones and enones.<sup>17</sup> For comparative studies, a similar Ni<sup>0</sup> electrodeposition was performed on naked C electrodes in the nickel oxalate aqueous borate buffer solution (pH 6) using also a cathodic charge of 4 mC. In this case, the deposition, requiring only 60 seconds, is even faster (Figure 3). The optimum cathodic potential of -1.4 V for Ni<sup>0</sup> electrodeposition was

determined from cyclic voltammetry experiments carried out with naked C and C/poly1 electrodes as shown in Figure 4.

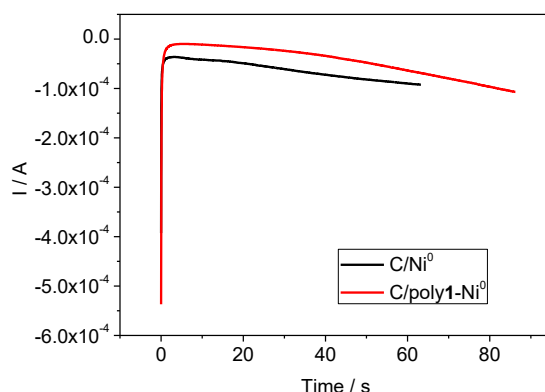


**Figure 3.** Nickel deposition ( $E_{appl} = -1.4$  V,  $Q_{deposition} = 4$  mC) on C ( $\Gamma_{Ni} = 1.2 \times 10^{-8}$  mol  $cm^{-2}$ ) and C/poly1 ( $\Gamma_{N^+} = 1.2 \times 10^{-7}$  mol  $cm^{-2}$ ,  $\Gamma_{Ni} = 3.3 \times 10^{-8}$  mol  $cm^{-2}$ ) electrodes (3 mm of diameter) in 1 mM NiSO<sub>4</sub>, 5 mM Na<sub>2</sub>C<sub>2</sub>O<sub>4</sub>, 0.1 M Na<sub>2</sub>SO<sub>4</sub>, 0.1 M H<sub>3</sub>BO<sub>3</sub>.

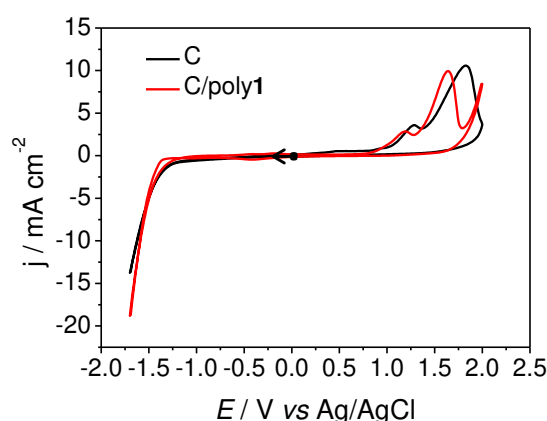


**Figure 4.** Cyclic voltammetry recorded at C (black line) and C/poly1 ( $\Gamma_{N^+} = 1.1 \times 10^{-7}$  mol  $cm^{-2}$ ) (red line) electrodes (3 mm of diameter) in an aqueous solution (pH 6) of 1 mM NiSO<sub>4</sub>, 5 mM NaC<sub>2</sub>O<sub>4</sub>, 0.1 M Na<sub>2</sub>SO<sub>4</sub> and 0.1 M H<sub>3</sub>BO<sub>3</sub>; The C/poly1 electrode was dipped in the aforementioned aqueous solution during 1h before the cyclic voltammetry experiment.

The electroactivity of the nickel oxalate solution is characterized by an irreversible cathodic reduction process observed below -1.25 V which is ascribed to the reduction of Ni<sup>2+</sup> (coordinated to oxalate) to Ni<sup>0</sup> leading to its deposition on C and C/poly1 electrodes and to the concomitant electrocatalytic reduction of protons to H<sub>2</sub> through the Ni<sup>0</sup> deposited.<sup>17</sup> On the reverse scan, in the anodic part, two successive irreversible redox processes are observed at +1.28 and +1.82 V for C (+1.19 and +1.64 V for C/poly1) which are respectively attributed to the oxidation of oxalate anions and the reoxidation of Ni<sup>0</sup> deposited at the electrode surface to Ni<sup>2+</sup> leading to its dissolution.<sup>17</sup> It can be noticed that the charge involved in this stripping wave between +1.3 and +2.0 V does not allow for estimating the quantity of nickel deposited

on C/poly1 and naked C electrodes. Indeed, the polypyrrole film is known to protect metallic particles from dissolution,<sup>17, 24-25</sup> and besides the dissolution of Ni<sup>0</sup> deposited on the surface of naked C electrodes is often incomplete due to passivation phenomena.<sup>17</sup> The precise determination of nickel loaded on electrodes was thus performed by ICP-MS experiments after the electrogeneration of NiO<sub>x</sub> from Ni<sup>0</sup> (see below). Finally, in the last step, the nickel oxide (*i.e.* Ni(O)(OH), denoted NiO<sub>x</sub>), is generated by oxidation of Ni<sup>0</sup> by scanning the C/poly1-Ni<sup>0</sup> or C/Ni<sup>0</sup> modified electrodes in an aqueous borate buffer at pH 9.2 over the 0 to +1.2 V potential range for 50 consecutive cycles (scan rate 50 mV s<sup>-1</sup>) (Figure 5, Scheme 1).

The formation of NiO<sub>x</sub> is evidenced by the progressive growth of the well-known Ni<sup>II</sup>(OH)<sub>2</sub>/Ni<sup>III</sup>(O)(OH) redox process<sup>1</sup> with an anodic peak and a cathodic peak respectively located at +0.88 and +0.60 V for C/poly1-NiO<sub>x</sub> and at +0.80 and +0.67 V for C/NiO<sub>x</sub> (Figure 5A, B). More cycles do not lead to a significant increase of the Ni<sup>II</sup>(OH)<sub>2</sub>/Ni<sup>III</sup>(O)(OH) redox process. Note that the first scan of the C/poly1-Ni<sup>0</sup> modified electrode shows two broad anodic processes around +0.7 and +1.0 V corresponding respectively to the oxidation and the overoxidation of the polypyrrole. Consequently, after the first scan from 0 to +1.2 V, the conductivity of polypyrrole is fully destroyed owing to its complete overoxidation. Thus, at this stage, the overoxidized poly1 plays only the role of matrix and the conductivity of the film is ensured by the nickel catalyst. Otherwise, upon scanning from 0 to +1.2 V, a concomitant growing catalytic current is observed above +0.95 V for both C/poly1-Ni<sup>0</sup> and C/Ni<sup>0</sup> electrodes (Figure 5). This process is ascribed to the catalytic oxidation of water to O<sub>2</sub>, concomitantly to the formation of the NiO<sub>x</sub> species (potentially the β-Ni<sup>III</sup>(O)(OH) and/or γ-Ni<sup>IV</sup>(O)(OH) phases<sup>1, 26-27</sup>) from Ni<sup>0</sup> which occurs at the same potential. Indeed, as shown in Figure 6(A), the NiO<sub>x</sub> formation is not observed by successive scans between 0 and +0.95 V of a C/poly1-Ni<sup>0</sup> electrode and only the polypyrrole oxidation and overoxidation are observable on the first scan. The NiO<sub>x</sub> formation is only effective by scanning up to +1.20 V as shown by the appearance and the progressive increase of the characteristic Ni<sup>II</sup>(OH)<sub>2</sub>/Ni<sup>III</sup>(O)(OH) redox process<sup>1</sup> (Figure 6(B)). The growth of the NiO<sub>x</sub> redox process is stopped (Figure 6(C)), if the oxidation potential of further scans is restricted to +0.95 V, confirming the need to sweep above +0.95 V to generate NiO<sub>x</sub>. Basically, the sequential three-electrons oxidation of Ni<sup>0</sup> to Ni<sup>3+</sup> that takes place above +0.95 V is followed by the formation of nickel(III) oxy-hydroxide species (Ni<sup>III</sup>(O)(OH)) in basic medium.<sup>28</sup> The overall reaction for the NiO<sub>x</sub> formation can be schematically displayed as:



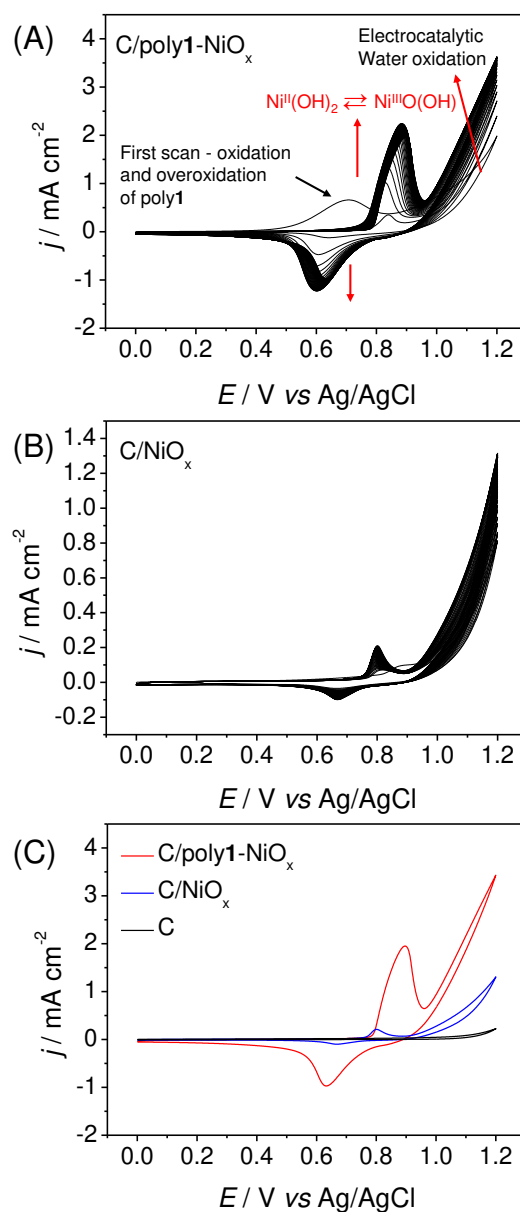


**Figure 5.** Electro-induced generation of NiO<sub>x</sub> from Ni<sup>0</sup> by repeated cyclic voltammetry (CV) scans (50 scans; scan rate of 50 mV s<sup>-1</sup>) in an aqueous 0.1 M borate buffer solution (pH 9.2) at (A) C/poly1-Ni<sup>0</sup> electrode ( $\Gamma_{\text{N}^+} = 1.1 \times 10^{-7} \text{ mol cm}^{-2}$ ,  $\Gamma_{\text{Ni}} = 3.3 \times 10^{-8} \text{ mol cm}^{-2}$ ), (B) C/Ni<sup>0</sup> electrode ( $\Gamma_{\text{Ni}} = 1.2 \times 10^{-8} \text{ mol cm}^{-2}$ ) and (C) overlay of 50<sup>th</sup> scans of the C/poly1-Ni<sup>0</sup> (red) and C/Ni<sup>0</sup> (blue) electrodes (in black, the electroactivity of a naked C electrode of 3 mm diameter).

The loading of nickel (*i.e.* the surface coverage of Ni, denoted  $\Gamma_{\text{Ni}}$ ) on the C/poly1 and C electrodes and their associated Ni deposition yield were quantified by ICP-MS after complete dissolution of the poly1-NiO<sub>x</sub> and NiO<sub>x</sub> films in acidic aqueous solution (5 mL) containing HNO<sub>3</sub> (0.45 M) (Table 1, see the Experimental Section). The complete dissolution of the film is verified by the disappearance of the Ni<sup>II</sup>(OH)<sub>2</sub>/Ni<sup>III</sup>(O)(OH) redox couple in the cyclic voltammograms after film dissolution. With a charge of 4 mC passed for nickel deposition, the Ni loading on the C/poly1 and C electrodes was estimated to be  $3.32 \times 10^{-8} (\pm 0.19 \times 10^{-8})$

and  $1.19 \times 10^{-8}$  ( $\pm 0.03 \times 10^{-8}$ ) mol cm<sup>-2</sup> respectively corresponding to deposition yields of 11.4 and 4.1%, respectively. Thus, for the same quantity of charge (4 mC), the amount of Ni<sup>0</sup> deposited on the C/poly1 film is 2.8 times greater than that deposited on the naked C electrode. The ratio of nickel incorporated within the poly1 film was also calculated considering that the di-anionic [Ni(C<sub>2</sub>O<sub>4</sub>)<sub>2</sub>]<sup>2-</sup> complex should be bound to two ammonium units during the Ni loading in the film. For an incorporation ratio of nickel of 100%, the  $\Gamma_{\text{Ni}}/\Gamma_{\text{N}^+}$  ratio should be equal to 0.5. For the C/poly1-NiO<sub>x</sub> electrodes, the average surface coverage values of Ni and poly1 was determined to be respectively  $\Gamma_{\text{Ni}} = 3.32 \times 10^{-8}$  mol cm<sup>-2</sup> and  $\Gamma_{\text{N}^+} = 1.2 \times 10^{-7}$  mol cm<sup>-2</sup> which corresponds to an average  $\Gamma_{\text{Ni}}/\Gamma_{\text{N}^+}$  ratio of 0.28 and thus to an incorporation ratio of nickel of 56%. A similar incorporation ratio was previously obtained by our group for incorporation of the [MoS<sub>4</sub>]<sup>2-</sup> complex within poly(pyrrole-alkylammonium) films.<sup>23</sup>

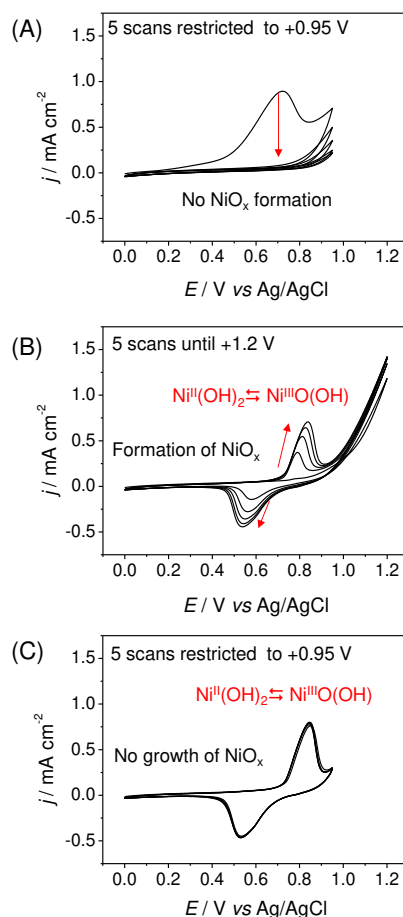


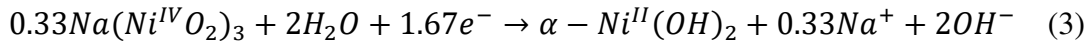
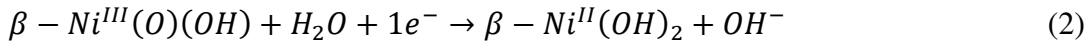
**Figure 6.** Cyclic voltammograms recorded at a C/poly1-Ni<sup>0</sup> ( $\Gamma_{\text{N}^+} = 1.1 \times 10^{-7}$  mol cm<sup>-2</sup>,  $\Gamma_{\text{Ni}} = 3.2 \times 10^{-8}$  mol cm<sup>-2</sup>) electrode (3 mm of diameter) in an aqueous 0.1 M borate buffer solution (pH 9.2), scan rate of 50 mV s<sup>-1</sup>: (A) 5 successive scans between 0 and +0.95 V vs Ag/AgCl, followed by (B) 5 scans between 0 and +1.2 V and then by (C) 5 scans between 0 and +0.95 V.

**Table 1.** Loading and deposition yield of nickel on C/poly1 and C electrodes, along with their coulometric titration.<sup>a</sup>

Electrode	Charge for Ni <sup>0</sup> deposition (mC)	Ni loading <sup>b</sup> (nmol cm <sup>-2</sup> )	Deposition yield of Ni <sup>0</sup> (%)	Film discharge to Ni <sup>II</sup> (OH) <sub>2</sub> <sup>c</sup> (μC)	no. of e <sup>-</sup> consumed per Ni
C/poly1-NiO <sub>x</sub>	4	33.2 ± 1.9	11.4 ± 0.7	251.0 ± 10.1	1.11 ± 0.11
C/NiO <sub>x</sub>	4	11.9 ± 0.3	4.1 ± 0.1	14.0 ± 0.7	0.17 ± 0.01

<sup>a</sup>Measurements performed on three independent electrodes for C/poly1-NiO<sub>x</sub> and C/NiO<sub>x</sub>. <sup>b</sup>Determined by ICP-MS for an electrode surface of 0.071 cm<sup>2</sup>. <sup>c</sup>Charge used for reducing the NiO<sub>x</sub> films (*i.e.* C/poly1-NiO<sub>x</sub> and C/NiO<sub>x</sub> initially anodized at 0.95 V vs Ag/AgCl) to the Ni<sup>II</sup> state.

The average number of electron consumed per nickel within C/poly1-NiO<sub>x</sub> and C/NiO<sub>x</sub> electrodes was estimated from the ratio of the charge used to reduce NiO<sub>x</sub> into Ni<sup>II</sup>(OH)<sub>2</sub>, to the nickel content on electrode (Table 1 and see the Experimental Section). A value of 1.11 was determined for C/poly1-NiO<sub>x</sub>, while a significantly lower value of 0.17 was obtained for C/NiO<sub>x</sub>. According to the schematic Bode representation,<sup>1, 27, 29</sup> the oxidation state of nickel within C/poly1-NiO<sub>x</sub> lies between two limit states, the β-Ni<sup>III</sup>(O)(OH) and γ-Ni<sup>IV</sup>(O)(OH) phases. It was also previously established by Corrigan et al<sup>30</sup> that the β-Ni<sup>II</sup>(OH)<sub>2</sub>/β-Ni<sup>III</sup>(O)(OH) transition requires a transfer of 1 electron while the α-Ni<sup>II</sup>(OH)<sub>2</sub>/γ-Ni<sup>IV</sup>(O)(OH) transition needs 1.67 electrons, as depicted respectively in equations (2) and (3). Note that γ-Ni<sup>IV</sup>(O)(OH) phase can be also referred to Na(Ni<sup>IV</sup>O<sub>2</sub>)<sub>3</sub> phase.<sup>30</sup>



Consequently, from the value of 1.11, it could be inferred that NiO<sub>x</sub> electrogenerated in the C/poly1 electrode is mainly a β-Ni<sup>III</sup>(O)(OH) phase which was commonly considered as the most active phase towards water oxidation.<sup>29, 31-34</sup> However, the question “which of the β or γ phases is the most efficient” is still a matter of debate<sup>35</sup> and some recent articles<sup>26, 36</sup> have concluded that the γ-Ni<sup>IV</sup>(O)(OH) phase is a better catalyst than a β-Ni<sup>III</sup>(O)(OH) phase. Otherwise, the average number of electron consumed per Ni could be related to the ratio of the number of effective catalytically active sites to the theoretical number of active sites.<sup>11</sup> While all Ni sites present on C/poly1-NiO<sub>x</sub> electrode are accessible for catalysis, less than 17 % of sites are active for C/NiO<sub>x</sub>. The greater accessibility of Ni sites on C/poly1-NiO<sub>x</sub> is most probably ascribed to a better nanostructuring of material owing to the polypyrrole matrix.

To get another clue of the better nanostructuring of the poly1-NiO<sub>x</sub> nanocomposite material, the relative capacitance of C/poly1-NiO<sub>x</sub> and C/NiO<sub>x</sub> electrodes, which is correlated to the

electrochemically active surface area of the electrode,<sup>13, 33, 37</sup> were determined from the slope of the plot of the current density *versus* scan rate at 0 V (Figure 7). Indeed, the capacitive current measured in non-Faradaic potential region is assumed to be due to double-layer charging and can be measured from cyclic voltammograms at various scan rates (Figures 7A and 7B). As shown in Figure 7C, C/poly1-NiO<sub>x</sub> exhibits a 1.4-fold higher capacitance (93.2 and -109.2  $\mu\text{F cm}^{-2}$  for anodic and cathodic capacitances respectively) than C/NiO<sub>x</sub> (63.6 and -79.6  $\mu\text{F cm}^{-2}$  for anodic and cathodic capacitances respectively).

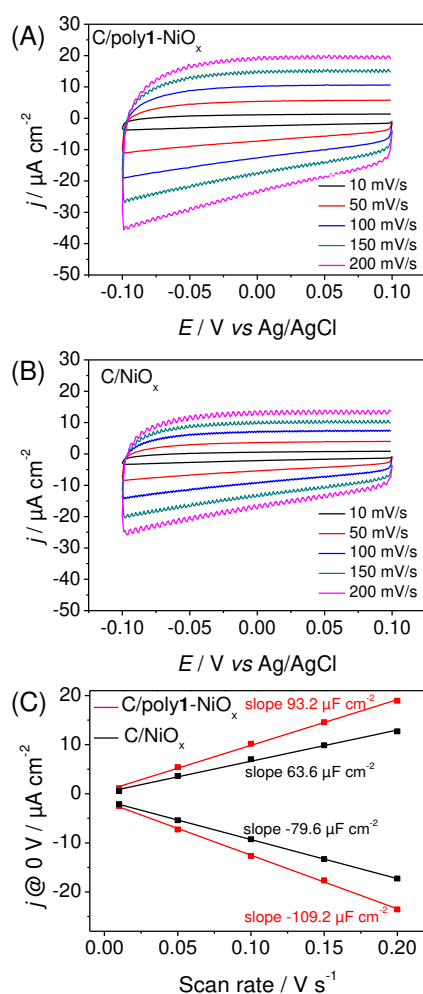


**Figure 7.** Electrochemical double-layer capacitance measurements: Cyclic voltammograms recorded at the (A) C/poly1-NiO<sub>x</sub> ( $\Gamma_{\text{N}^+} = 1.2 \times 10^{-7} \text{ mol cm}^{-2}$ ,  $\Gamma_{\text{Ni}} = 3.3 \times 10^{-8} \text{ mol cm}^{-2}$ ) and (B) C/NiO<sub>x</sub> ( $\Gamma_{\text{Ni}} = 1.2 \times 10^{-8} \text{ mol cm}^{-2}$ ) electrodes (3 mm of diameter) in an aqueous 0.1 M borate buffer solution (pH 9.2); the scans were recorded between -0.10 and +0.10 V vs Ag/AgCl with the scan rate of 10, 50, 100, 150 and 200  $\text{mV s}^{-1}$ . (C) The cathodic and anodic current densities at 0 V vs Ag/AgCl plotted as function of scan rate for the C/poly1-NiO<sub>x</sub> (red) and C/NiO<sub>x</sub> (black) electrodes.

This confirms that the C/poly1-NiO<sub>x</sub> electrode has a higher electroactive surface than the C/NiO<sub>x</sub> electrode. The capacitance values determined from cyclic voltammograms are not absolute values and should be used with great care when they are compared to other catalytic

OER electrodes of literature.<sup>11, 33</sup> Indeed, these relative capacitance values should be only used for the estimation of the electroactive area of electrodes displaying the same type of materials within the same study. Nevertheless, it is interesting to note that similar capacitance values (between 64 and 94  $\mu\text{F cm}^{-2}$ ) were obtained by Spiccia et coll.<sup>38</sup> for  $\text{NiO}_x$  films deposited on C electrodes from various molecular nickel complexes dissolved in aqueous borate buffer.

## 2.2 – Characterization of Nickel Oxide and Poly(pyrrole-alkylammonium)-Nickel Oxide Nanocomposite Electrode Materials by AFM and TEM Microscopies.

Atomic force microscopy (AFM) measurements in peak force mode were performed on ITO/poly1- $\text{NiO}_x$  and ITO/ $\text{NiO}_x$  electrodes in view to identify and compare the surface morphology of both electrodes (Figure 8).

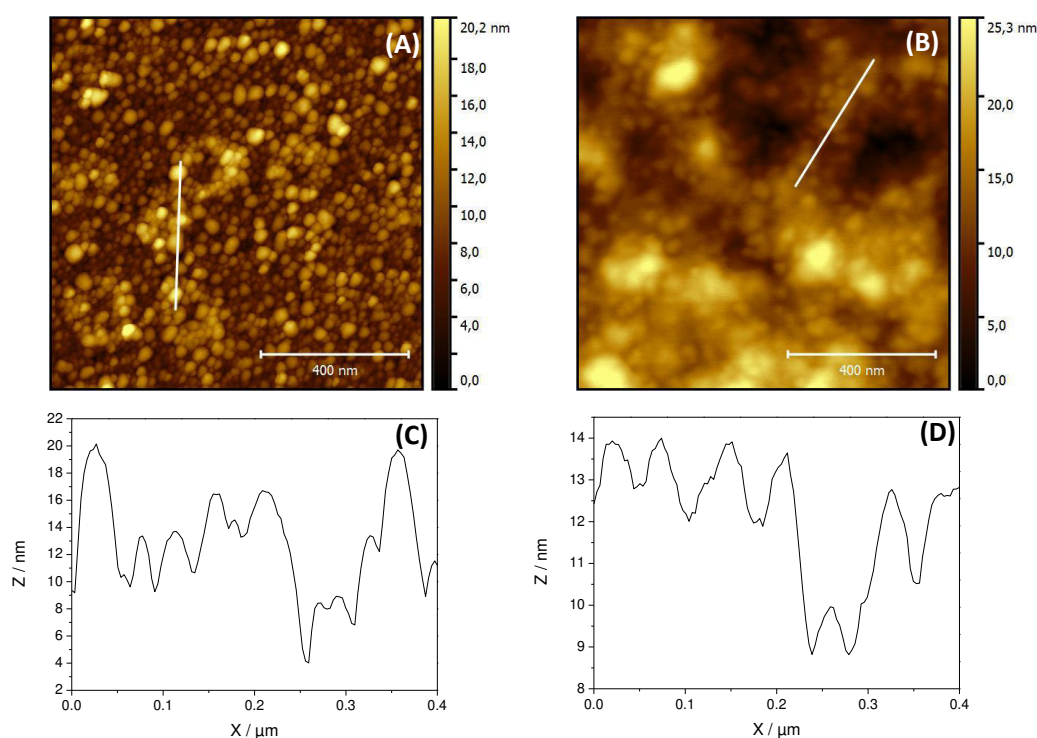


**Figure 8.** AFM images in peak force mode of (A) ITO coated with  $\text{NiO}_x$  (28 mC used for deposition of  $\text{Ni}^0$ ); (B) ITO coated with poly1- $\text{NiO}_x$  nanocomposite (28 mC used for deposition of poly1 and for subsequent deposition of  $\text{Ni}^0$ ); (C) and (D) exhibit section analysis of ITO/ $\text{NiO}_x$  and ITO/poly1- $\text{NiO}_x$  shown respectively in (A) and (B).

The electrodes (ITO surface of  $0.5 \text{ cm}^2$ ) were prepared with a charge of 28 mC for both the poly1 and  $\text{Ni}^0$  deposition in view to obtain a charge density of  $56 \text{ mC cm}^{-2}$ , similar to that used for the preparation of the C/poly1- $\text{NiO}_x$  and C/ $\text{NiO}_x$  electrodes (4 mC for a C electrode

surface of  $0.071 \text{ cm}^2$ ). From AFM images, a homogenous granular topography along with well-defined grain boundaries were observed for ITO/ $\text{NiO}_x$  with a root-mean square (r.m.s.) roughness of 2.9 nm (Figure 8 (A)), while an ill-defined nodular topography (as cauliflower) was obtained with ITO/poly1- $\text{NiO}_x$  with a close r.m.s. roughness of 4.8 nm (Figure 8 (B)). Cauliflower topology is typical for electrodeposited polypyrrole film<sup>12, 18</sup> and, since the  $\text{NiO}_x$  particles are embedded into the polymer matrix, it was difficult to measure their size within the nanocomposite from AFM measurements. Conversely, the  $\text{NiO}_x$  particles size on the surface of the ITO/ $\text{NiO}_x$  electrode was roughly estimated to be  $47 \pm 21 \text{ nm}$  from the section analysis of its AFM image (Figure 5(C)). At first glance, the employment of a nickel oxalate complex (with or without polymer matrix) seems to be a good strategy to prepare well-nanostructured and homogeneous  $\text{NiO}_x$  films.

In view to determine precisely the  $\text{NiO}_x$  particles size deposited inside the film and directly on ITO, the poly1- $\text{NiO}_x$  and  $\text{NiO}_x$  materials were peeled off from the ITO plates and deposited on carbon-coated copper grids for transmission electron microscopy (TEM) analyses (Figure 9). TEM image clearly reveals big  $\text{NiO}_x$  nanoparticles for the ITO/ $\text{NiO}_x$  electrode with an average particle size of  $99.9 \pm 42.5 \text{ nm}$  associated with a larger size distribution (Figure 9 (A)). This average size obtained from TEM images is greater than that obtained from AFM images. This difference of particle sizes could be explained by the fact that (i) AFM measurements provide a view of the surface of the film while TEM measurements display the internal and superficial nature of the film and (ii) there is potentially a gradient of particle size within the nanocomposite film (*i.e.* bigger particles inside the film and smaller particles at its surface). By contrast, TEM image of  $\text{NiO}_x$  trapped in poly1 film shows a percolated network of smaller nanoparticles of  $21.0 \pm 3.6 \text{ nm}$  with a very narrow particle size distribution (Figure 9 (B)). We have previously demonstrated the possibility to achieve very small metallic nanoparticles, as  $\text{IrO}_x$  or  $\text{RuO}_x$ , within positively-charged polypyrrole film.<sup>12, 19</sup> TEM images unambiguously illustrate the finer nanostructure of poly1- $\text{NiO}_x$  material compared to that of the bare  $\text{NiO}_x$ . In addition, the SAED pattern recorded from poly1- $\text{NiO}_x$  indicates that the particles within polypyrrole are crystalline and randomly oriented. The indexing of the punctuated diffraction rings confirms that the metal oxide generated within the poly1 film is indeed nickel oxide (see the Experimental Section).<sup>39-40</sup> To sum up, the use of polypyrrole films as template for nickel deposition and  $\text{NiO}_x$  formation allows obtaining  $\text{NiO}_x$  films with a high nanostructuring by avoiding agglomeration of particles and a high crystallinity.

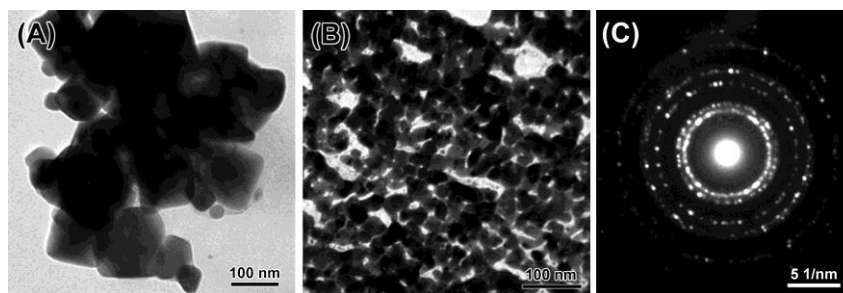


**Figure 9.** TEM images (scale bar: 100 nm) of (A) NiO<sub>x</sub> (28 mC used for Ni<sup>0</sup> deposition on ITO) and (B) poly1-NiO<sub>x</sub> nanocomposite (28 mC used for deposition of poly1 and for subsequent deposition of Ni<sup>0</sup> on ITO) scratched off from an ITO plate and deposited on a carbon-coated Cu-grid. (C) SAED pattern of NiO<sub>x</sub> nanoparticles within the poly1-NiO<sub>x</sub> nanocomposite shown in (B). Analyses performed in Chile by Mr. Ricardo Oliva.

### ***2.3 - Electrocatalytic performance of Nickel Oxide and Poly(pyrrole-alkylammonium)-Nickel Oxide Nanocomposite Electrodes.***

The electrocatalytic activity of C/poly1-NiO<sub>x</sub> and C/NiO<sub>x</sub> electrodes have been evaluated in a conventional three-electrode cell by linear sweep voltammetry at pH 9.2 as well as at more basic pHs of 13 and 14 (Figure 10). Tables 2 and 3 summarize the catalytic OER performances of these electrodes and those of some nickel-based electrodes reported in the literature at similar pHs. The design of catalysts able to operate at nearly neutral pH is of high importance in view to use natural water sources but also to develop photoelectrochemical cells for light-driven water splitting that couple a catalyst and a molecular photosensitizer, this later being often poorly stable in strongly basic solution.<sup>41</sup> The two figures of merit usually measured for an electrocatalyst working at pH 9.2 are the catalytic current density ( $j$ ) at overpotential ( $\eta$ ) of +0.61 V (corresponding to +1.1 V vs Ag/AgCl at pH 9.2) and the overpotential to reach the catalytic current density of 1 mA cm<sup>-2</sup>. For C/poly1-NiO<sub>x</sub>, the  $j$  value at +0.61 V and the  $\eta$  value at 1 mA cm<sup>-2</sup> are respectively 2.17 mA cm<sup>-2</sup> and +0.51 V, while for C/NiO<sub>x</sub> these values are 0.66 mA cm<sup>-2</sup> and +0.67 V, respectively (Table 2). The higher  $j$  value and lower  $\eta$  value of C/poly1-NiO<sub>x</sub> compared to those of C/NiO<sub>x</sub> can be attributed to the greater amount of NiO<sub>x</sub> deposited on electrode owing to the presence of polypyrrole film, but also to the greater nanostructuration of the NiO<sub>x</sub> particles within the poly1 matrix as observed in TEM images (*vide supra*). Regarding the significant difference in the particle size and in the mass loading of NiO<sub>x</sub> within C/poly1-NiO<sub>x</sub> and C/NiO<sub>x</sub> electrodes, the catalytic activity of C/poly1-NiO<sub>x</sub> is expected to be five or six-fold higher than that of C/NiO<sub>x</sub>. However, the catalytic current density at an overpotential of +0.61 V with C/poly1-NiO<sub>x</sub> is only 3.3 times higher than that of C/NiO<sub>x</sub> (Table 2). This weaker difference in term of

catalytic activity between both electrodes could be ascribed to a more difficult mass transport (*i.e.* transport of water and OH<sup>-</sup> anions into the nanocomposite and release of O<sub>2</sub> outside the nanocomposite) within the polypyrrole film which limits the electrocatalytic performances of C/poly1-NiO<sub>x</sub>.

In spite of a hypothetical slow mass transport, the catalytic current density at an overpotential of +0.61 V for C/poly1-NiO<sub>x</sub> is quite significant at pH 9.2 and higher than those reported by Spiccia et coll.<sup>38, 42</sup> with analogous NiO<sub>x</sub> based electrodes prepared by anodic electrodeposition of nickel(II) amine complexes ( $j$  at +0.61 V in the range 1.2 and 1.3 mA cm<sup>-2</sup>, Table 2). The higher catalytic current of C/poly1-NiO<sub>x</sub> can be ascribed to the smaller NiO<sub>x</sub> particles (average size of 21 nm, *vide supra*) than those deposited on Spiccia's electrodes (particle size between 300 and 350 nm), improving the accessibility of Ni sites to the water (or OH<sup>-</sup>) substrate. The same group<sup>9</sup> succeeded in improving the efficiency of their electrodes towards water oxidation in term of  $j$  value by increasing the amount of NiO<sub>x</sub> deposited on electrode (*i.e.* mass loading between 330 and 1100 μg cm<sup>-2</sup>) *via* screen-printing method, that uses inks of NiO<sub>x</sub> microballs (NiO<sub>x</sub>-MB) and nanoparticles (NiO<sub>x</sub>-NP and NiO<sub>x</sub>-NP1) (Table 2). A greater Ni mass loading on electrode generates thicker films of NiO<sub>x</sub> with a larger electrocatalytic surface area beneficial for the catalytic performance. Nevertheless, a thicker NiO<sub>x</sub> film could also hinder the mass transport of OH<sup>-</sup> and O<sub>2</sub> and usually displays a strong electrical resistance.<sup>9,43,44</sup> Consequently the mass activity (catalytic current (A) per milligram of Ni) and the turnover frequency (denoted TOF) of the FTO/NiO<sub>x</sub>-MB, FTO/NiO<sub>x</sub>-NP and FTO/NiO<sub>x</sub>-NP1 electrodes lying respectively between 0.013 and 0.027 A mg<sup>-1</sup> at  $\eta$  value of 0.61 V and between 0.002 and 0.005 s<sup>-1</sup> at 0.52 V, are very low (Table 2). By comparison, the mass activity and the TOF values at an overpotential of 0.61 V of the electrodes described in this work are clearly superior and are among the highest values of the literature for a NiO<sub>x</sub>-based anode operating at pH 9.2, with respectively 1.12 A mg<sup>-1</sup> and 0.17 s<sup>-1</sup> for C/poly1-NiO<sub>x</sub>, and 0.95 A mg<sup>-1</sup> and 0.14 s<sup>-1</sup> for C/NiO<sub>x</sub> (Table 2). Note that, at an overpotential of 0.52 V, our electrodes with TOF values of 0.075 and 0.060 s<sup>-1</sup> respectively for C/poly1-NiO<sub>x</sub> and C/NiO<sub>x</sub>, are also much more active than the FTO/NiO<sub>x</sub>-MB, FTO/NiO<sub>x</sub>-NP and FTO/NiO<sub>x</sub>-NP1 electrodes.<sup>9</sup>

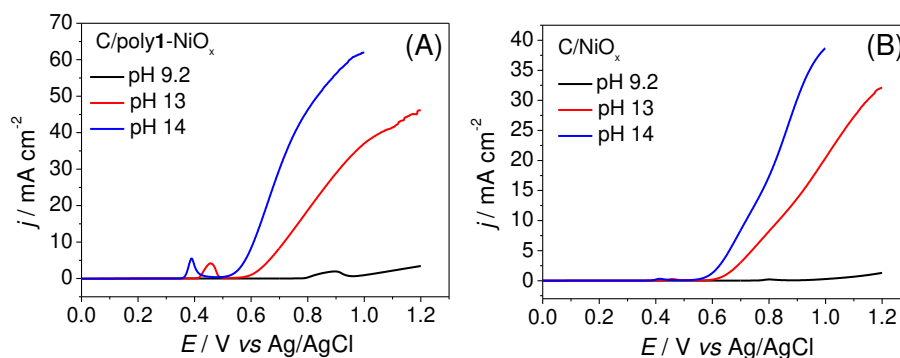


**Figure 10.** Linear sweep voltammograms recorded at (A) C/poly1-NiO<sub>x</sub> ( $\Gamma_{\text{Ni}^+} = 1.1 \times 10^{-7} \text{ mol cm}^{-2}$ ,  $\Gamma_{\text{Ni}} = 3.3 \times 10^{-8} \text{ mol cm}^{-2}$ ) and (B) C/NiO<sub>x</sub> ( $\Gamma_{\text{Ni}} = 1.2 \times 10^{-8} \text{ mol cm}^{-2}$ ) electrodes (3 mm of diameter) in an aqueous solution at pH 9.2 (0.1 M H<sub>3</sub>BO<sub>3</sub> and 0.05 M NaOH), 13 (0.1 M KOH) and 14 (1.0 M KOH); Scan rate of 50 mV s<sup>-1</sup>.

Only NiFeO<sub>x</sub> deposited on C electrode by Strasser et coll.<sup>45</sup> outperforms the electrodes prepared in this work at pH 9.2 with a lower  $\eta$  value of 0.37 V at 1 mA cm<sup>-2</sup> along with a high mass activity of 1.9 A mg<sup>-1</sup> and a high TOF value of 0.29 s<sup>-1</sup> at an overpotential of 0.40 V (Table 2). The mixed NiFe oxide, published first by Radniecka et coll.<sup>2</sup> and Corrigan et coll.<sup>3</sup> in the 80s, is among the best OER electrocatalysts of the literature and it was postulated by Boettcher et coll.<sup>4</sup> and Bell et coll.<sup>5</sup> that iron is the catalytically active site within this mixed oxide, NiO<sub>x</sub> only offering to FeO<sub>x</sub> an electrically conductive framework with a high surface area that reveals the real catalytic activity of FeO<sub>x</sub>. Indeed Boettcher et coll.<sup>23,74</sup> demonstrated that FeO<sub>x</sub> is much more active than NiO<sub>x</sub> towards OER when very thin films of metallic oxide are deposited on electrode, but thicker films of FeO<sub>x</sub> suffer from a very low electrical conductivity which limits their electrocatalytic performance.

It can also be noted that Nocera et coll.<sup>46</sup> reported a quite efficient electrode with very low overpotential of 0.425 V at 1 mA cm<sup>-2</sup> at pH 9.2. Such high catalytic activity would be assigned to the deposition of a very thin NiO<sub>x</sub> film on electrode, close to a monolayer of catalyst, conferring a high electrical conductivity and promoting the mass transport, as mentioned above (Table 2). Otherwise, Hu et coll.<sup>47</sup> published also an interesting approach to build nanostructured Ni-based anode with high porosity *via* the use of a scaffold of SiO<sub>2</sub>. Basically, silica was co-electrodeposited with nickel on stainless steel electrode and then removed under basic condition leading to a porous NiO<sub>x</sub> film with an average particle size of 50 nm. Although this electrode exhibits good catalytic performance with  $\eta$  value of +0.45 V at 1 mA cm<sup>-2</sup>, the mass activity at the overpotential of 0.61 V of 0.021 A mg<sup>-1</sup> is still significantly inferior to those of C/poly1-NiO<sub>x</sub> and C/NiO<sub>x</sub> (Table 2).

**Table 2.** OER performances of C/poly1-NiO<sub>x</sub> and C/NiO<sub>x</sub> prepared in this work compared to those of NiO<sub>x</sub> catalysts of literature at pH 9.2.

Catalyst/electrode	$j$ (mA cm <sup>-2</sup> ) @ $\eta$ (V)	$\eta$ (V) @ $j$ (mA cm <sup>-2</sup> )	Ni mass loading ( $\mu\text{g cm}^{-2}$ )	mass activity (A mg <sup>-1</sup> ) @ $\eta$ (V)	TOF <sub>min</sub> (s <sup>-1</sup> ) @ $\eta$ (V)	Author <sup>ref</sup>
pH 9.2 with 0.1 M H <sub>3</sub> BO <sub>3</sub> + NaOH or KOH						
C/poly1-NiO <sub>x</sub>	2.17@0.61	0.51@1	1.9	1.12@0.61	0.17@0.61	This work
C/NiO <sub>x</sub>	0.66@0.61	0.67@1	0.7	0.95@0.61	0.14@0.61	This work
C/NiO <sub>x</sub>	1.2@0.61	-	15.8	0.076 <sup>a</sup> @0.61	0.015@0.61	Spiccia <sup>38</sup>
FTO/NiO <sub>x</sub>	1.3@0.60	-	15.3	0.085 <sup>a</sup> @0.60	-	Spiccia <sup>42</sup>
FTO/MB-NiO <sub>x</sub>	6.8@0.61	-	450	0.015 <sup>a</sup> @0.61	0.003@0.52	Spiccia <sup>9</sup>
FTO/NP-NiO <sub>x</sub>	14.4@0.61	-	1100	0.013 <sup>a</sup> @0.61	0.002@0.52	Spiccia <sup>9</sup>
FTO/NP1-NiO <sub>x</sub>	8.8@0.61	-	330	0.027 <sup>a</sup> @0.61	0.005-@0.52	Spiccia <sup>9</sup>
C/NiO <sub>x</sub>	-	0.425@1	0.2	-	-	Nocera <sup>46</sup>
SS/SiO <sub>2</sub> -NiO <sub>x</sub>	7.5@0.61	0.45@1	353	0.021 <sup>a</sup> @0.61	-	Hu <sup>47</sup>
C/Ni <sub>0.62</sub> Fe <sub>0.38</sub> O <sub>x</sub>	-	0.37@1	2.0 <sup>b</sup>	1.9@0.40	0.29@0.40	Strasser <sup>45</sup>

<sup>a</sup>Data non calculated by the authors but estimated herein from the current density ( $j$ ) at defined overpotentials ( $\eta$ ) and the mass loading of Ni given in the article. <sup>b</sup>Mass loading of Ni and Fe. MB and NP mean respectively MicroBall and NanoParticle. C, SS and FTO mean respectively glassy Carbon, Stainless Steel and Fluorine Tin Oxyde.

The stability of C/poly1-NiO<sub>x</sub> and C/NiO<sub>x</sub> electrodes during electrolysis at pH 9.2 was evaluated by chronoamperometry measurements over a period of 6 h at an applied potential of +1.2 V vs Ag/AgCl under stirring in order to decrease the resistance due to the mass transport and thus to improve the catalytic performance of the electrode (Figure 11 and Figure S2 in the Experimental Section). The catalytic current density of the C/poly1-NiO<sub>x</sub> electrode is high (*c.a.* 7 mA cm<sup>-2</sup>) and very stable within the first hour (Figure 11), while that of C/NiO<sub>x</sub> electrode gradually decreases from 4.65 to 0.44 mA cm<sup>-2</sup> in 45 minutes, reaching a value similar to that of a bare carbon electrode (0.56 mA cm<sup>-2</sup>). This clearly indicates that C/poly1-NiO<sub>x</sub> is more efficient than C/NiO<sub>x</sub> with an initial 1.5-fold higher catalytic current and much more stable. The instability of the C/NiO<sub>x</sub> electrode could be attributed to the gradual release of nickel oxide from the electrode surface, which does not occur on C/poly1-NiO<sub>x</sub> since the NiO<sub>x</sub> particles are embedded into the polymer matrix. Nevertheless, after 1 h of electrolysis (Figure S2 in the Experimental Section), the current density of the C/poly1-NiO<sub>x</sub> electrode

gradually decreases until  $0.65 \text{ mA cm}^{-2}$  at 2h35 and then slowly until  $0.23 \text{ mA cm}^{-2}$  after 6h, exhibiting a OER catalytic activity close to that of a simple carbon electrode. This loss of activity is due to the progressive detachment of the polymer film caused by the oxygen bubbling during electrolysis. Conversely, the current density of the C/NiO<sub>x</sub> electrode increases slightly after 1h of electrolysis to reach a pseudo plateau at  $0.87 \text{ mA cm}^{-2}$  after 6h (Figure S2 in the Experimental Section).

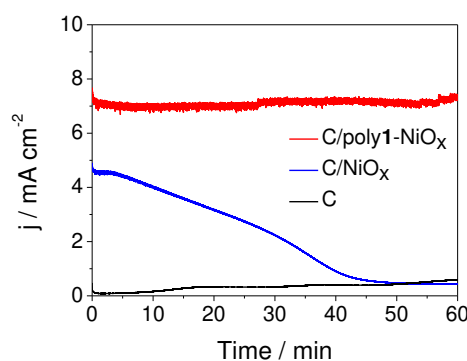
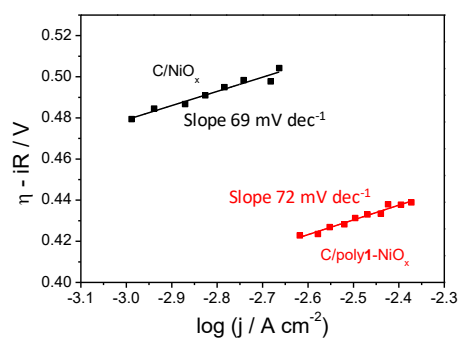


**Figure 11.** Chronoamperograms recorded at C/poly1-NiO<sub>x</sub> ( $\Gamma_{\text{N}^+} = 1.1 \times 10^{-7} \text{ mol cm}^{-2}$ ,  $\Gamma_{\text{Ni}} = 3.3 \times 10^{-8} \text{ mol cm}^{-2}$ ) (red), C/NiO<sub>x</sub> ( $\Gamma_{\text{Ni}} = 1.2 \times 10^{-8} \text{ mol cm}^{-2}$ ) (blue) and bare C (black) electrodes (3 mm of diameter) in a stirred 0.1 M aqueous borate buffer solution (pH 9.2), at constant potential of +1.2 V vs Ag/AgCl.

Tafel analysis was carried out by stepwise chronoamperometry (see the Experimental section) at pH 9.2 on C/poly1-NiO<sub>x</sub> and C/NiO<sub>x</sub> electrodes in order to gain some mechanistic information, through the Tafel slope, about the rate determining step for OER (Figure 12). The Tafel slopes calculated for C/poly1-NiO<sub>x</sub> and C/NiO<sub>x</sub> of 72 and 69 mV per decade respectively are almost identical, showing that the same catalytic mechanism occurs within both electrodes. A similar Tafel slope was previously reported with a Ni-based anode<sup>47</sup> operating at pH 9.2 and these slope values are closed to the predicted value of  $60 \text{ mV dec}^{-1}$ , which suggests that the rate determining step leading to O<sub>2</sub> evolution is a chemical reaction subsequent to the first electron transfer step.<sup>1</sup> The Tafel analysis also confirms that C/poly1-NiO<sub>x</sub> electrodes operate efficiently at lower overpotential than the C/NiO<sub>x</sub> electrodes.

**Figure 12.** Tafel plot recorded at a C/poly1-NiO<sub>x</sub> ( $\Gamma_{\text{N}^+} = 1.2 \times 10^{-7} \text{ mol cm}^{-2}$ ,  $\Gamma_{\text{Ni}} = 3.3 \times 10^{-8} \text{ mol cm}^{-2}$ ) (red) and C/NiO<sub>x</sub> ( $\Gamma_{\text{Ni}} = 1.2 \times 10^{-8} \text{ mol cm}^{-2}$ ) (black) electrodes (3 mm of diameter) in 0.1 M aqueous borate buffer solution (pH 9.2).



The electrocatalytic activity of the C/poly1-NiO<sub>x</sub> and C/NiO<sub>x</sub> electrodes was also investigated at pHs 13 and 14 (Figures 10, 13 and 14), since the most common commercial electrolyzers operate in strongly alkaline media and most of the metallic catalysts for OER based on non precious and earth-abundant elements are studied in basic conditions in order to avoid the corrosion of metal.<sup>4, 48</sup> At these basic pHs, the onset potential for OER and the Ni<sup>II</sup>(OH)<sub>2</sub>/Ni<sup>III</sup>(O)(OH) redox process recorded at C/poly1-NiO<sub>x</sub> and C/NiO<sub>x</sub> by linear sweep voltammetry (Figure 10) are cathodically shifted compared to the values measured at pH 9.2, which is a classical behavior for a nickel-based electrode studied at various basic pH.<sup>42, 45</sup> The figures of merit for an electro-catalyst operating at basic pH are the catalytic  $j$  value at  $\eta$  of 0.30 and 0.35 V (respectively corresponding to 0.56 and 0.61 V *vs* Ag/AgCl at pH 13 and 0.51 and 0.56 V *vs* Ag/AgCl at pH 14) and the overpotential at the  $j$  value of 10 mA cm<sup>-2</sup>. These figures of merit stem from the works of Weber et coll.<sup>49-50</sup> and Jaramillo et coll.<sup>14, 51</sup> who have proposed that an integrated solar water-splitting device, under 1 sun of illumination with a quantum yield of energy conversion (solar-to-fuels) of 10 %, should work with a current density per geometric area of 10 mA cm<sup>-2</sup> and a global overpotential inferior to 0.45 V. In addition, considering an overpotential of 0.45 V for the water-splitting reaction, Jaramillo et coll.<sup>14</sup> have estimated that the cathode in charge of HER should operate at  $\eta$  value of 0.10 V and thus the anode devoted to OER should work at 0.35 V. This explains why most of the electrocatalytic activities of anodes published in recent years are referenced at overpotential of 0.35 V or at a closer value of 0.30 V.

At pH 13 (Table 3), the C/poly1-NiO<sub>x</sub> anode displays interesting catalytic performances with  $j$  values of 1.75 and 0.25 mA cm<sup>-2</sup> at 0.35 V and 0.30 V respectively and a  $\eta$  value of 0.45 V at 10 mA cm<sup>-2</sup>, while C/NiO<sub>x</sub> seems again less active with  $j$  values of 0.39 and 0.07 mA cm<sup>-2</sup> at 0.35 V and 0.30 V respectively and a  $\eta$  value of 0.57 V at 10 mA cm<sup>-2</sup>. Similarly to what has been observed at pH 9.2, C/poly1-NiO<sub>x</sub> exhibits at pH 13 very high mass activity and TOF values at an overpotential of 0.35 V with 0.90 A mg<sup>-1</sup> and 0.14 s<sup>-1</sup> respectively. However, at pHs 13 and 14, the C/poly1-NiO<sub>x</sub> and C/NiO<sub>x</sub> electrodes lose their activity after only few CV successive scans by cyclic voltammetry between 0 and 1.2 V *vs* Ag/AgCl (Figures 13 and 14). This poor stability in strong basic conditions can be directly correlated to the detachment of the film of poly1-NiO<sub>x</sub> or NiO<sub>x</sub> induced by the strong oxygen bubbling as the consequence of their high catalytic performances. Nevertheless, the first scan recorded at the C/poly1-NiO<sub>x</sub> and C/NiO<sub>x</sub> electrodes at pHs 13 and 14 is sufficient to evaluate their real catalytic activity

and thus their potentiality towards OER in very basic conditions. At pH 13, the C/poly1-NiO<sub>x</sub> and C/NiO<sub>x</sub> electrodes have disclosed catalytic activities substantially superior to that of most of literature anodes using nickel oxide or ruthenium oxide. For comparison, we reported in Table 3 the performances of the anodes of the groups of Yan,<sup>8</sup> Liu<sup>52</sup> and Bell<sup>33</sup>. Among these groups, Yan et coll.<sup>8</sup> published the most efficient anode based on a well nanostructured  $\alpha$ -Ni(OH)<sub>2</sub> in the form of a hollow sphere (average diameter of 1.8  $\mu\text{m}$ ), actually made by numerous nanosheets. Although the overpotential obtained with this electrode is low (0.33 V at 10 mA cm<sup>-2</sup>) owing to its great nanostructuring and high Ni mass loading (200  $\mu\text{g cm}^{-2}$ ), its mass activity and TOF values at 0.35 V with only 0.15 A mg<sup>-1</sup> and 0.036 s<sup>-1</sup>, remain below those of the C/poly1-NiO<sub>x</sub> and C/NiO<sub>x</sub> electrodes. As for the nearly neutral conditions, only the mixed Ni/Fe oxides deposited on either gold, glassy carbon or ITO electrode, possess higher catalytic performances than those of our NiO<sub>x</sub> based electrodes at pH 13.<sup>33, 45, 52-53</sup> For instance, the C/Ni<sub>0.62</sub>Fe<sub>0.38</sub>O<sub>x</sub> electrode of Strasser et coll.<sup>45</sup> presents a low overpotential of 0.33 V at 10 mA cm<sup>-2</sup> only with a weak mass loading of 2  $\mu\text{g cm}^{-2}$  (comparable to the value of 1.9  $\mu\text{g cm}^{-2}$  obtained with C/poly1-NiO<sub>x</sub>), and mass activity and TOF values higher of one order than those of C/poly1-NiO<sub>x</sub> with 1.31 A mg<sup>-1</sup> and 0.20 s<sup>-1</sup> respectively at a  $\eta$  value of 0.30 V (Table 3). The iridium oxide-based nanocomposite using the same polypyrrole alkylammonium previously reported<sup>12</sup> by our group (*i.e.* C/poly1-IrO<sub>x</sub>) is also efficient at pH 13. The small particles size of IrO<sub>x</sub> (between 1 and 2 nm) and their well distribution within the poly1 film have participated for obtaining a relatively low overpotential for OER (0.42 V at 10 mA cm<sup>-2</sup>) and a high catalytic activity at 0.35 V with a  $j$  value of 4.4 mA cm<sup>-2</sup> and TOF of 0.32 s<sup>-1</sup>, which are *ca.* 2.4-fold higher than those of the C/poly1-NiO<sub>x</sub> electrode measured at pH 13 (Table 3). The greater electrocatalytic performance of C/poly1-IrO<sub>x</sub> over C/poly1-NiO<sub>x</sub> could be mainly ascribed to the large size difference between the nanoparticles of IrO<sub>x</sub> (*ca.* 1.5 nm) and NiO<sub>x</sub> (*ca.* 21.0 nm) that impacts the real surface area of the electrode and thus the accessibility of catalytic sites with respect to water or OH<sup>-</sup> (*vide supra*).

At pH 14, the C/poly1-NiO<sub>x</sub> electrode presents a higher electrocatalytic activity than at pH 13 with  $j$  values of 2.49 mA cm<sup>-2</sup> at 0.35 V and 0.52 mA cm<sup>-2</sup> at 0.30 V, and a lower overpotential of 0.41 V at 10 mA cm<sup>-2</sup> (Table 3). Its mass activity and TOF values are also slightly higher at pH 14 at an overpotential of +0.35 V (*i.e.* 1.28 A mg<sup>-2</sup> and 0.19 s<sup>-1</sup>) and these values double at 0.30 V compared to those at pH 13 (*i.e.* 0.27 A mg<sup>-2</sup> and 0.04 s<sup>-1</sup>). Surprisingly, the performance of the simple C/NiO<sub>x</sub> electrode decreases at pH 14 compared to that at pH 13, most probably due to a poor mass transport of OH<sup>-</sup> anions within the NiO<sub>x</sub> film

that hinders the oxidation reaction. For instance, the C/poly1-NiO<sub>x</sub> electrode surpasses the C/NiO<sub>x</sub> electrode of Jaramillo et al<sup>54</sup> that exhibits catalytic current density of 1.77 mA cm<sup>-2</sup> at 0.35 V and an overpotential of 0.43 V at 10 mA cm<sup>-2</sup> (Table 3). In addition, although several anodes composed of nickel deposited on either glassy carbon electrode,<sup>55</sup> pyrolytic graphite (HOPG) electrode<sup>56</sup> or carbon fiber paper (CFP),<sup>57</sup> display higher catalytic performances than C/poly1-NiO<sub>x</sub> in terms of *j* and *η* values owing to a high Ni mass loading at the surface of the electrode, they are also associated with a poor mass activity or very low TOF values (Table 3). An efficient nickel-based electrode towards OER was reported by the group of Boettcher,<sup>58</sup> this latter being easily fabricated by spin coating a solution of nickel nitrate on a mixed Au-Ti electrode followed by a thermal decomposition of the nitrate anions. This Au-Ti/NiO<sub>x</sub> anode displayed a quite high catalytic activity at an overpotential of 0.3 V (1.01 mA cm<sup>-2</sup>, 0.896 A mg<sup>-1</sup> and 0.17 s<sup>-1</sup>) with a low amount of nickel deposited on electrode (1.1 μg cm<sup>-2</sup>).

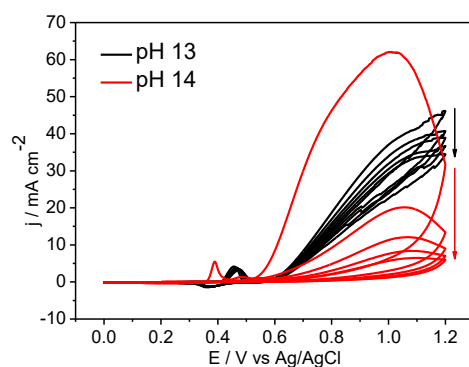


**Figure 13.** Cyclic voltammograms recorded at a C/poly1-NiO<sub>x</sub> ( $\Gamma_{\text{N}^+} = 1.1 \times 10^{-7} \text{ mol cm}^{-2}$ ,  $\Gamma_{\text{Ni}} = 3.3 \times 10^{-8} \text{ mol cm}^{-2}$ ) electrode (3 mm of diameter) in an aqueous solution at pH 13 (black, 0.1 M KOH) and 14 (red, 1.0 M KOH); Scan rate of 50 mV s<sup>-1</sup>.

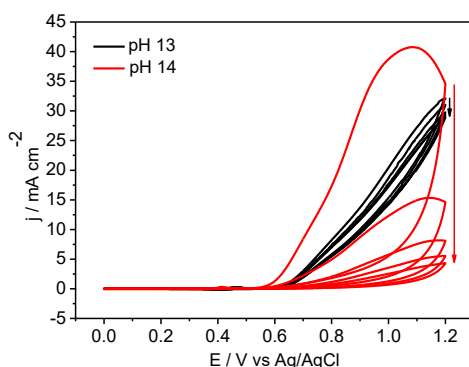


**Figure 14.** Cyclic voltammograms recorded at a C/NiO<sub>x</sub> ( $\Gamma_{\text{Ni}} = 1.2 \times 10^{-8} \text{ mol cm}^{-2}$ ) electrode (3 mm of diameter) in an aqueous solution at pH 13 (black, 0.1 M KOH) and 14 (red, 1.0 M KOH); Scan rate of 50 mV s<sup>-1</sup>.

**Table 3.** OER performances of C/poly1-NiO<sub>x</sub> and C/NiO<sub>x</sub> prepared in this work compared to those of Ni based catalysts of literature and classical IrO<sub>2</sub> and RuO<sub>2</sub> catalysts at pH 13 and 14.

Catalyst/electrode	$j$ (mA cm <sup>-2</sup> ) @ $\eta$ (V)	$\eta$ (V) @ $j$ (mA cm <sup>-2</sup> )	Ni mass loading ( $\mu\text{g cm}^{-2}$ )	mass activity (A mg <sup>-1</sup> ) @ $\eta$ (V)	TOF <sub>min</sub> (s <sup>-1</sup> ) @ $\eta$ (V)	Author <sup>ref</sup>
pH 13 with 0.1M NaOH or KOH						
C/poly1-NiO <sub>x</sub>	1.75@0.35	0.45@10	1.9	0.90@0.35	0.14@0.35	This work
C/poly1-NiO <sub>x</sub>	0.25@0.30		1.9	0.13@0.30	0.020@0.30	This work
C/NiO <sub>x</sub>	0.39@0.35	0.57@10	0.7	0.55@0.35	0.08@0.35	This work
C/NiO <sub>x</sub>	0.07@0.30		0.7	0.10@0.30	0.015@0.30	This work
C/ $\alpha$ Ni(OH) <sub>2</sub> -HS	0.26@0.35	0.331@10	200	0.15@0.35	0.036@0.35	Yan <sup>8</sup>
C/ $\beta$ Ni(OH) <sub>2</sub> -PL	0.03@0.35	0.444@10	200	0.013@0.35	0.003@0.35	Yan <sup>8</sup>
C/ $\alpha$ Ni(OH) <sub>2</sub>		0.42@10	200			Liu <sup>52</sup>
Au/NiO <sub>x</sub>	0.20@0.30	0.47@10	0.06		0.008@0.30	Bell <sup>33</sup>
Au/Ni <sub>0.6</sub> Fe <sub>0.4</sub> O <sub>x</sub>	20.0@0.30	0.27@10	0.06 <sup>b</sup>		0.45@0.30	Bell <sup>33</sup>
C/Ni <sub>0.62</sub> Fe <sub>0.38</sub> O <sub>x</sub>		0.33@10	2.0 <sup>b</sup>	1.31@0.30	0.20@0.30	Strasser <sup>45</sup>
ITO/Ni <sub>0.88</sub> Fe <sub>0.12</sub> O <sub>x</sub>	10@0.30	0.30@10	25 <sup>b</sup>	0.40 <sup>a</sup> @0.30		Buriak <sup>53</sup>
C/Ni <sub>0.88</sub> Fe <sub>0.12</sub> O <sub>x</sub> - $\alpha$ Ni(OH) <sub>2</sub>		0.34@10	200 <sup>b</sup>			Liu <sup>52</sup>
C/poly1-IrO <sub>x</sub>	4.4@0.35	0.42@10	6.9 <sup>b</sup>	0.64@0.35	0.32@0.35	Moutet <sup>12</sup>
C/poly1-IrO <sub>x</sub>	1.1@0.30		6.9 <sup>b</sup>	0.16@0.30	0.08@0.30	Moutet <sup>12</sup>
C/RuO <sub>2</sub>	0.23@0.35	0.387@10	200 <sup>b</sup>	0.030@0.35	0.010@0.35	Yan <sup>8</sup>
pH 14 with 1M NaOH or KOH						
C/poly1-NiO <sub>x</sub>	2.49@0.35	0.41@10	1.9	1.28@0.35	0.19@0.35	This work
C/poly1-NiO <sub>x</sub>	0.52@0.30		1.9	0.27@0.30	0.04@0.30	This work
C/NiO <sub>x</sub>	0.30@0.35	0.51@10	0.7	0.43@0.35	0.07@0.35	This work
C/NiO <sub>x</sub>	0.10@0.30		0.7	0.14@0.30	0.02@0.30	This work
C/NiO <sub>x</sub>	1.77@0.35	0.43@10	800	0.002 <sup>a</sup> @0.35		Jaramillo <sup>54</sup>
C/ $\alpha$ Ni(OH) <sub>2</sub>	10@0.30	0.30@10	142	0.07 <sup>a</sup> @0.30		Hu <sup>55</sup>
C/NiO <sub>x</sub>		0.331@10	142	0.07 <sup>a</sup> @0.33		Hu <sup>55</sup>
Au-Ti/NiO <sub>x</sub>	1.01@0.30		1.1	0.896@0.30	0.17@0.30	Boettcher <sup>58</sup>
HOPG/NiO <sub>x</sub>		0.37@10	444	0.023 <sup>a</sup> @0.37	0.0006@0.3	Muller <sup>56</sup>
CFP/NiO <sub>x</sub> -NiS		0.37@10	200	0.050 <sup>a</sup> @0.37		Peng <sup>57</sup>
Au-Ti/Ni <sub>0.9</sub> Fe <sub>0.1</sub> O <sub>x</sub>	1.24@0.30		1.2 <sup>b</sup>	1.065@0.30	0.21@0.30	Boettcher <sup>58</sup>

C/NS-NiFeO <sub>x</sub>	166.3@0.35	0.302@10	70 <sup>b</sup>	2.38 <sup>a</sup> @0.35	0.11@0.30	Hu <sup>10</sup>
C/NPL-NiFeO <sub>x</sub>		0.38@10	160 <sup>b</sup>			Wei <sup>59</sup>
Nifo/rGO-NiFeO <sub>x</sub>		0.206@10	250 <sup>b</sup>		0.98@0.30	Yang <sup>60</sup>
C/N <sub>a0.08</sub> Ni <sub>0.9</sub> Fe <sub>0.1</sub> O <sub>2</sub>	62.1@0.35	0.26@10	130 <sup>b</sup>	0.48 <sup>a</sup> @0.35		Yan <sup>61</sup>
HOPG/[Ni <sub>0.78</sub> Fe <sub>0.22</sub> (OH) <sub>2</sub> ](NO <sub>3</sub> ) <sub>y</sub> (OH) <sub>0.22-y</sub> .nH <sub>2</sub> O		0.28@10	444 <sup>b</sup>		0.013@0.30	Muller <sup>56</sup>
C/Ni <sub>0.82</sub> Fe <sub>0.18</sub> O <sub>x</sub>		0.24@10	3.8 <sup>b</sup>		8.7@0.33	Cao <sup>62</sup>
C/NiCoO <sub>2</sub>	2.25@0.35	0.39@10	800 <sup>b</sup>	0.003 <sup>a</sup> @0.35		Jaramillo <sup>54</sup>
C/NS-NiCoO <sub>x</sub>	22.78@0.35	0.334@10	70 <sup>b</sup>	0.33 <sup>a</sup> @0.35	0.01@0.30	Hu <sup>10</sup>
Au-Ti/Ni <sub>0.75</sub> Co <sub>0.25</sub> O <sub>x</sub>	0.47@0.30		1.0 <sup>b</sup>	0.452@0.30	0.089@0.30	Boettcher <sup>58</sup>
C/NiMoO <sub>x</sub>		0.32@10	320 <sup>b</sup>	0.031 <sup>a</sup> @0.32		Kuznetsov <sup>41</sup>
Au-Ti/IrO <sub>2</sub>	0.063@0.30		4.1 <sup>b</sup>	0.015@0.30	0.0089@0.3	Boettcher <sup>58</sup>
C/IrO <sub>2</sub>	2.23@0.35	0.38@10	800 <sup>b</sup>	0.003 <sup>a</sup> @0.35		Jaramillo <sup>54</sup>
C/IrO <sub>2</sub>		0.49@10	160 <sup>b</sup>			Wei <sup>59</sup>
C/IrO <sub>2</sub>		0.338@10	210 <sup>b</sup>	0.047 <sup>a</sup> @0.34	0.01@0.30	Hu <sup>10</sup>
C/RuO <sub>2</sub>	3.63@0.35	0.38@10	800 <sup>b</sup>	0.005 <sup>a</sup> @0.35		Jaramillo <sup>54</sup>
C/RuO <sub>2</sub>		0.35@10	130 <sup>b</sup>	0.077 <sup>a</sup> @0.35		Yan <sup>61</sup>

<sup>a</sup>Data non calculated by the authors but estimated herein from the current density (*j*) at defined overpotentials ( $\eta$ ) and the mass loading of Ni given in the article. <sup>b</sup>Mass loading of Ni and Fe (or Mo, Co, Ir, Ru). HS, PL, NPL, rGO and NS mean respectively Hollow Sphere, NanoPlate, NanoPLatelets, reduced Graphene Oxide and NanoSheet. C, ITO, HOPG, CFP and Nifo mean respectively glassy Carbon, Indium Tin Oxide, Highly Ordered Pyrolytic Graphite, Carbon Fiber Paper and Nickel foam.

The great performance of this electrode at pH 14 has been correlated to the fact that all Ni atoms in the film are electroactive and the catalytic water oxidation takes place within all the three-dimensional layered structure of Ni(OH)<sub>2</sub>/NiOOH, and not only at the active sites on the surface of the film. Otherwise, whereas the NiFeO<sub>x</sub>-based anodes<sup>10, 56, 58-62</sup> show once again a higher catalytic activity than C/poly1-NiO<sub>x</sub> at pH 14, the anodes using mixed NiCoO<sub>x</sub><sup>10, 54, 58</sup> or NiMoO<sub>x</sub><sup>41</sup> materials known to be also efficient electrodes for OER are less active than C/poly1-NiO<sub>x</sub>. Note that slightly higher mass activity and TOF values (*i.e.* 0.452 A mg<sup>-1</sup> and 0.089 s<sup>-1</sup> at 0.3 V) were observed with the Au-Ti/Ni<sub>0.75</sub>Co<sub>0.25</sub>O<sub>x</sub> anode of Boettcher et coll.<sup>58</sup> Interestingly, C/poly1-NiO<sub>x</sub> electrode also displays a greater catalytic activity compared to that of anodes based on IrO<sub>2</sub> or RuO<sub>2</sub> which are commonly considered as benchmark electrocatalysts for water oxidation due their high catalytic performances in acidic and basic

media (Table 3). This confirms that the use of polymer matrix to design metallic anodes is a good strategy to obtain highly structured and very active electrodes for water oxidation.

### 3 - Conclusion

We report a very efficient OER anode based on a nickel oxide-poly(pyrrole-alkylammonium) nanocomposite prepared by an easy all-electrochemical synthesis. As observed by AFM and TEM, this composite features a great nanostructuring along with small crystalline NiO<sub>x</sub> particles of 21 nm dispersed in the polymer film, which confers a high electroactive surface area and thus high electrocatalytic performances. These nickel oxide particles entrapped within the polypyrrole film, whose nature has been determined by coulometric titration to be  $\beta$ -Ni<sup>III</sup>(O)(OH), exhibits exceptional mass activity and TOF values for OER at pH 9.2 of 1.12 A mg<sup>-1</sup> and 0.17 s<sup>-1</sup> at an overpotential of 0.61 V. Under basic conditions at pH 14, the nickel oxide-polypyrrole nanocomposite electrode, present high mass activity and TOF values of 1.28 A mg<sup>-1</sup> and 0.19 s<sup>-1</sup> at an overpotential of 0.35 V, outperforms the nickel-based anodes of the literature (undoped by Fe) and those using precious metal oxides, such as RuO<sub>2</sub> and IrO<sub>2</sub>. In addition, the nickel oxide electrogenerated into polypyrrole-alkylammonium films appeared also more efficient than the nickel oxide film electrogenerated on a naked electrode surface by the same electrochemical procedure, highlighting the beneficial role of the polypyrrole matrix in generating small NiO<sub>x</sub> particles with high activity. This very promising way to elaborate nanocomposite material paves the way for the design of new anodes very active for OER by using other earth abundant metals, as cobalt, manganese and iron. This all electrochemical method of preparation offers great potentialities to prepare mixed metal oxide nanoparticles more efficient for OER such as NiFeO<sub>x</sub>, but also to develop photoanodes by the introduction of a molecular photosensitizer within the polymer matrix in view to implement photoelectrochemical cells for light-driven water splitting reaction.

## References

- (1) Doyle, R. L.; Godwin, I. J.; Brandon, M. P.; Lyons, M. E. G., *PhysChemChemPhys* **2013**, 15 (33), 13737-13783.
- (2) Młynarek, G.; Paszkiewicz, M.; Radniecka, A., *J. Appl. Electrochem.* **1984**, 14 (2), 145-149.
- (3) Corrigan, D. A., *J. Electrochem. Soc.* **1987**, 134 (2), 377-384.
- (4) Burke, M. S.; Enman, L. J.; Batchellor, A. S.; Zou, S.; Boettcher, S. W., *Chem. Mater.* **2015**, 27 (22), 7549-7558.
- (5) Friebel, D.; Louie, M. W.; Bajdich, M.; Sanwald, K. E.; Cai, Y.; Wise, A. M.; Cheng, M.-J.; Sokaras, D.; Weng, T.-C.; Alonso-Mori, R.; Davis, R. C.; Bargar, J. R.; Nørskov, J. K.; Nilsson, A.; Bell, A. T., *J. Am. Chem. Soc.* **2015**, 137 (3), 1305-1313.
- (6) Han, L.; Dong, S.; Wang, E., *Adv. Mater.* **2016**, 28 (42), 9266-9291.
- (7) Roger, I.; Symes, M. D., *J. Mater. Chem. A* **2016**, 4 (18), 6724-6741.
- (8) Gao, M.; Sheng, W.; Zhuang, Z.; Fang, Q.; Gu, S.; Jiang, J.; Yan, Y., *J. Am. Chem. Soc.* **2014**, 136 (19), 7077-7084.
- (9) Singh, A.; Fekete, M.; Gengenbach, T.; Simonov, A. N.; Hocking, R. K.; Chang, S. L. Y.; Rothmann, M.; Powar, S.; Fu, D. C.; Hu, Z.; Wu, Q.; Cheng, Y. B.; Bach, U.; Spiccia, L., *ChemSusChem* **2015**, 8 (24), 4266-4274.
- (10) Song, F.; Hu, X., *Nat. Commun.* **2014**, 5, 4477.
- (11) Fominykh, K.; Chernev, P.; Zaharieva, I.; Sicklinger, J.; Stefanic, G.; Döblinger, M.; Müller, A.; Pokharel, A.; Böcklein, S.; Scheu, C.; Bein, T.; Fattakhova-Rohlfing, D., *ACS Nano* **2015**, 9 (5), 5180-5188.
- (12) Lattach, Y.; Rivera, J. F.; Bamine, T.; Deronzier, A.; Moutet, J.-C., *ACS Appl. Mater. Interfaces* **2014**, 6 (15), 12852-12859.
- (13) McCrory, C. C. L.; Jung, S.; Peters, J. C.; Jaramillo, T. F., *J. Am. Chem. Soc.* **2013**, 135 (45), 16977-16987.
- (14) McCrory, C. C. L.; Jung, S.; Ferrer, I. M.; Chatman, S. M.; Peters, J. C.; Jaramillo, T. F., *J. Am. Chem. Soc.* **2015**, 137 (13), 4347-4357.
- (15) Noufi, R., *J. Electrochem. Soc.* **1983**, 130 (10), 2126-2128.
- (16) Yoneyama, H.; Shoji, Y.; Kawai, K., *Chem. Lett.* **1989**, (6), 1067-1070.
- (17) Zouaoui, A.; Stephan, O.; Ourari, A.; Moutet, J. C., *Electrochim. Acta* **2000**, 46 (1), 49-58.
- (18) De Oliveira, I. M. F.; Moutet, J. C.; Hamarhibault, S., *J. Mater. Chem.* **1992**, 2 (2), 167-173.
- (19) Rivera, J. F.; Bucher, C.; Saint-Aman, E.; Rivas, B. L.; Aguirre, M. D.; Sanchez, J.; Pignot-Paintrand, I.; Moutet, J. C., *Appl. Catal., B* **2013**, 129, 130-136.
- (20) Rivera, J. F.; Pignot-Paintrand, I.; Pereira, E.; Rivas, B. L.; Moutet, J. C., *Electrochim. Acta* **2013**, 110, 465-473.
- (21) Zouaoui, A.; Stephan, O.; Carrier, M.; Moutet, J. C., *J. Electroanal. Chem.* **1999**, 474 (2), 113-122.
- (22) Lattach, Y.; Fortage, J.; Deronzier, A.; Moutet, J.-C., *ACS Appl. Mater. Interfaces* **2015**, 7 (8), 4476-4480.
- (23) Lattach, Y.; Deronzier, A.; Moutet, J.-C., *ACS Appl. Mater. Interfaces* **2015**, 7 (29), 15866-15875.
- (24) Singh, R. N.; Malviya, M.; Chartier, P., *J. New Mat. Electrochem. Systems* **2007**, 10 (3), 181-186.
- (25) Cong, H. N.; El Abbassi, K.; Chartier, P., *Electrochem. Solid State Lett.* **2000**, 3 (4), 192-195.

- (26) Bediako, D. K.; Lassalle-Kaiser, B.; Surendranath, Y.; Yano, J.; Yachandra, V. K.; Nocera, D. G., *J. Am. Chem. Soc.* **2012**, 134 (15), 6801-6809.
- (27) Bode, H.; Dehmelt, K.; Witte, J., *Electrochim. Acta* **1966**, 11 (8), 1079-1081.
- (28) Tench, D.; Warren, L. F., *J. Electrochem. Soc.* **1983**, 130 (4), 869-872.
- (29) Wehrens-Dijksma, M.; Notten, P. H. L., *Electrochim. Acta* **2006**, 51 (18), 3609-3621.
- (30) Corrigan, D. A.; Knight, S. L., *J. Electrochem. Soc.* **1989**, 136 (3), 613-619.
- (31) Lu, P. W. T.; Srinivasan, S., *J. Electrochem. Soc.* **1978**, 125 (9), 1416-1422.
- (32) Lyons, M. E. G.; Brandon, M. P., *Int. J. Electrochem. Sci.* **2008**, 3 (12), 1386-1424.
- (33) Louie, M. W.; Bell, A. T., *J. Am. Chem. Soc.* **2013**, 135 (33), 12329-12337.
- (34) Godwin, I. J.; Lyons, M. E. G., *Electrochem. Commun.* **2013**, 32, 39-42.
- (35) Singh, A.; Spiccia, L., *Coord. Chem. Rev.* **2013**, 257 (17-18), 2607-2622.
- (36) Trotochaud, L.; Young, S. L.; Ranney, J. K.; Boettcher, S. W., *J. Am. Chem. Soc.* **2014**, 136 (18), 6744-6753.
- (37) Trasatti, S.; Petrii, O. A., *Pure Appl. Chem.* **1991**, 63 (5), 711-734.
- (38) Singh, A.; Chang, S. L. Y.; Hocking, R. K.; Bach, U.; Spiccia, L., *Energy Environ. Sci.* **2013**, 6 (2), 579-586.
- (39) Long, H.; Shi, T.; Hu, H.; Jiang, S.; Xi, S.; Tang, Z., *Scientific reports* **2014**, 4, 7413.
- (40) Wang, Z.; Kale, G. M.; Yuan, Q.; Ghadiri, M., *RSC Advances* **2012**, 2 (26), 9993-9997.
- (41) Kuznetsov, D. A.; Konev, D. V.; Komarova, N. y. S.; Ionov, A. M.; Mozhchil, R. N.; Fedyanin, I. V., *Chem. Commun.* **2016**, 52 (59), 9255-9258.
- (42) Singh, A.; Chang, S. L. Y.; Hocking, R. K.; Bach, U.; Spiccia, L., *Catal. Sci. Technol.* **2013**, 3 (7), 1725-1732.
- (43) Yeo, B. S.; Bell, A. T., *J. Phys. Chem. C* **2012**, 116 (15), 8394-8400.
- (44) Dyer, C. K., *J. Electrochem. Soc.* **1985**, 132 (1), 64-67.
- (45) Görlin, M.; Glied, M.; de Araújo, J. F.; Dresch, S.; Bergmann, A.; Strasser, P., *Catal. Today* **2016**, 262, 65-73.
- (46) Dinca, M.; Surendranath, Y.; Nocera, D. G., *Proc. Natl. Acad. Sci. U. S. A.* **2010**, 107 (23), 10337-10341.
- (47) Wu, L.-K.; Hu, J.-M.; Zhang, J.-Q.; Cao, C.-N., *J. Mater. Chem. A* **2013**, 1 (41), 12885-12892.
- (48) Li, X.; Walsh, F. C.; Pletcher, D., *PhysChemChemPhys* **2011**, 13 (3), 1162-1167.
- (49) Weber, M. F.; Dignam, M. J., *J. Electrochem. Soc.* **1984**, 131 (6), 1258-1265.
- (50) Weber, M. F.; Dignam, M. J., *Int. J. Hydrogen Energy* **1986**, 11 (4), 225-232.
- (51) Seitz, L. C.; Chen, Z.; Forman, A. J.; Pinaud, B. A.; Benck, J. D.; Jaramillo, T. F., *ChemSusChem* **2014**, 7 (5), 1372-1385.
- (52) Chen, H.; Yan, J.; Wu, H.; Zhang, Y.; Liu, S., *J. Power Sources* **2016**, 324, 499-508.
- (53) Bau, J. A.; Lubner, E. J.; Buriak, J. M., *ACS Appl. Mater. Interfaces* **2015**, 7 (35), 19755-19763.
- (54) Jung, S.; McCrory, C. C. L.; Ferrer, I. M.; Peters, J. C.; Jaramillo, T. F., *J. Mater. Chem. A* **2016**, 4 (8), 3068-3076.
- (55) Stern, L.-A.; Hu, X., *Faraday Discuss.* **2014**, 176 (0), 363-379.
- (56) Hunter, B. M.; Blakemore, J. D.; Deimund, M.; Gray, H. B.; Winkler, J. R.; Müller, A. M., *J. Am. Chem. Soc.* **2014**, 136 (38), 13118-13121.
- (57) Gao, M.; Yang, L.; Dai, B.; Guo, X.; Liu, Z.; Peng, B., *J. Solid State Electrochem.* **2016**, 20 (10), 2737-2747.
- (58) Trotochaud, L.; Ranney, J. K.; Williams, K. N.; Boettcher, S. W., *J. Am. Chem. Soc.* **2012**, 134 (41), 17253-17261.
- (59) Li, Z.; Shao, M.; An, H.; Wang, Z.; Xu, S.; Wei, M.; Evans, D. G.; Duan, X., *Chem. Sci.* **2015**, 6 (11), 6624-6631.

- (60) Long, X.; Li, J.; Xiao, S.; Yan, K.; Wang, Z.; Chen, H.; Yang, S., *Angew. Chem., Int. Ed.* **2014**, 53 (29), 7584-7588.
- (61) Weng, B.; Xu, F.; Wang, C.; Meng, W.; Grice, C. R.; Yan, Y., *Energy Environ. Sci.* **2017**, 10 (1), 121-128.
- (62) Zhang, W.; Wu, Y.; Qi, J.; Chen, M.; Cao, R., *Adv. Energy Mater.* **2017**, 7 (9), 1602547.

**Cobalt Oxide-Polypyrrole Nanocomposite Electrode  
Materials for Electrocatalytic Water Oxidation**



---

**INDEX**

1 – Introduction .....	87
2 – Results and discussion.....	88
2.1 – Electrosynthesis and Electrocharacterization of Cobalt Oxide and Poly(pyrrole-alkylammonium)-Cobalt Oxide Nanocomposite Electrode Materials.....	88
2.2 – Characterization of Cobalt Oxide and Poly(pyrrole-alkylammonium)-Cobalt Oxide Nanocomposite Electrode Materials by AFM and TEM Microscopies .....	94
2.3 – Electrocatalytic performance of Cobalt Oxide and Poly(pyrrole-alkylammonium)-Cobalt Oxide Nanocomposite Electrodes .....	97
3. Conclusion.....	103
References .....	104



## 1 - Introduction

As we introduced in the Part I: Chapter 1, cobalt oxide or  $\text{CoO}_x$  has been identified as a possible catalyst for water oxidation in the late 60's<sup>1</sup> and was intensively studied since the early 80s by numerous groups.<sup>2-11</sup> Otherwise,  $\text{CoO}_x$  knew a renewed interest in 2008 owing to the work of Nocera and co-workers<sup>10</sup> demonstrating that proton-accepting electrolyte can facilitate their electrodeposition on electrode and that an OER electrocatalyst based on earth abundant metal can be very active in neutral or in mildly basic solution. Among the OER catalysts based on first-row transition metal, metal oxides using Ni, Fe and Co have been front-runners essentially due to their low overpotentials, close to that of noble metal oxides as  $\text{IrO}_x$  or  $\text{RuO}_x$ . Various forms of cobalt oxide have been investigated for OER such as amorphous oxides, spinel-type ( $\text{Co}_3\text{O}_4$ ,  $\text{MCo}_2\text{O}_4$ ,  $\text{CoM}_2\text{O}_4$  and  $\text{MCoO}_2$ ), perovskite-type ( $\text{MCoO}_3$ ) and layered oxyhydroxides.<sup>12</sup> Besides  $\text{CoO}_x$  can be deposited on electrode *via* different methods as spin coating, sol-gel process and electrochemical deposition to name a few.<sup>13</sup>

Inspired by our work described in Part I: Chapter 2 consisting in designing nickel oxide/polypyrrole nanocomposite for anode, we extend our strategy to cobalt oxide to prepare nanostructured electrodes very active for OER based on the same nanocomposite material. As previously described for  $\text{NiO}_x$ , the  $\text{CoO}_x$  nanoparticles are entrapped into a poly(pyrrole-alkyl ammonium) matrix (denoted poly**1**, where **1** is the monomer (3-pyrrole-1-yl-propyl)-triethylammonium tetrafluoroborate, Scheme 1) that was initially electrodeposited at an electrode surface of glassy carbon (denoted C) or ITO. Our strategy here to deposit  $\text{CoO}_x$  consists in electroprecipitating  $\text{Co}^0$  nanoparticles by reduction of an anionic cobalt oxalate complex into the poly**1** film, this later being previously deposited onto C or ITO electrodes by electropolymerization of **1**. The cobalt oxide nanoparticles were then *in-situ* generated by air oxidation of the  $\text{Co}^0$  nanoparticles in the composite. A similar strategy was also employed in our group to prepare iridium oxide-polypyrrole nanocomposite anodes displaying high OER activity.<sup>14</sup>

The poly**1**- $\text{CoO}_x$  nanocomposite material was characterized by various electrochemical techniques (cyclic voltammetry, linear sweep voltammetry, Tafel plot), and also by inductively coupled plasma mass spectroscopy (ICP-MS), atomic force microscopy (AFM), scanning electron microscopy (SEM) and transmission electron microscopy (TEM). The physical and electrocatalytic properties of this nanocomposite material toward water oxidation

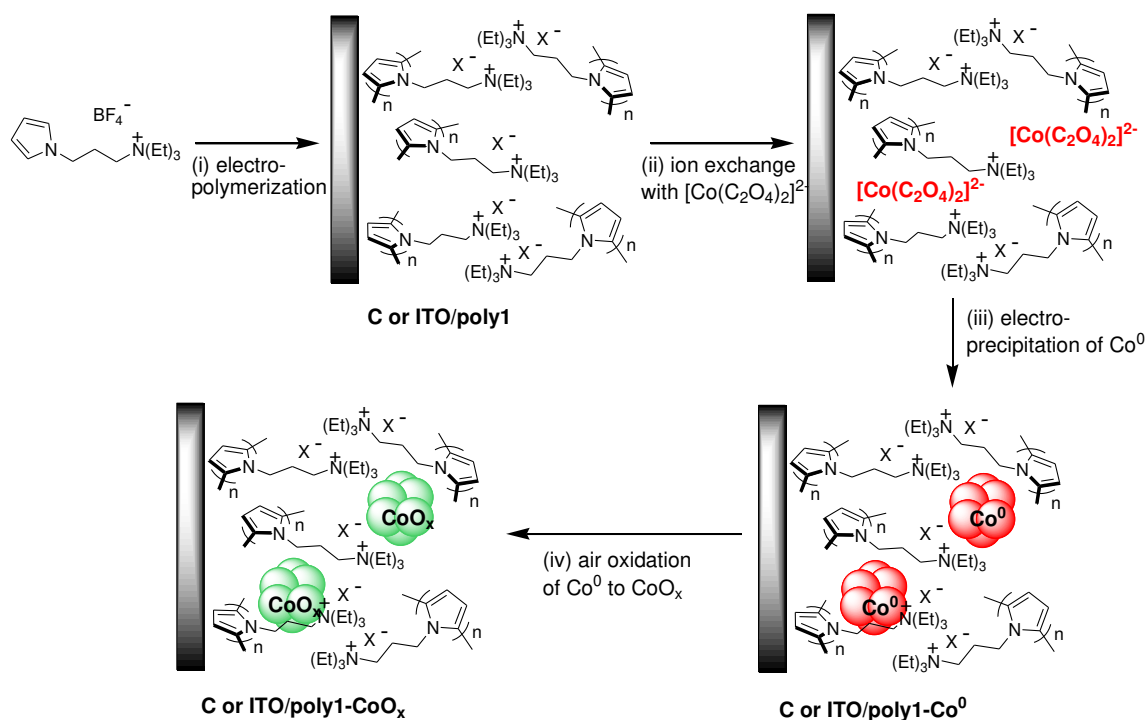
in mildly basic (pH 9.2) and basic (pHs 13 and 14) conditions were also evaluated and compared with those of  $\text{CoO}_x$  film directly deposited on a naked electrode by the same electrochemical procedure to highlight the beneficial role of the poly1 matrix in generating non-agglomerated  $\text{CoO}_x$  particles with higher OER activity.

## 2 - Results and discussion

### 2.1 - *Electrosynthesis and Electrocharacterization of Cobalt Oxide and Poly(pyrrole-alkylammonium)-Cobalt Oxide Nanocomposite Electrode Materials.*

In this work, we synthesized by an electrochemical procedure nanocomposite electrode materials composed of  $\text{CoO}_x$  particles entrapped into a poly(pyrrole-alkylammonium) thin film coated onto C or ITO electrodes. A three-step electrochemical procedure is used here to prepare the C or ITO/poly1- $\text{CoO}_x$  modified electrodes depicted in Scheme 1. The C/poly1 electrodes were first prepared by electropolymerization of the pyrrole ammonium monomer **1** (4 mM) at a controlled-oxidation potential of +0.95 V vs Ag/AgNO<sub>3</sub> in acetonitrile (Scheme 1 and Figure 1, Part I: Chapter 2). The surface coverage in ammonium units  $\Gamma_{\text{N}^+}$  (mol cm<sup>-2</sup>), *i.e.* the quantity of pyrrole units deposited on C electrode (0.071 cm<sup>2</sup>), was quantified electrochemically by integration of the polypyrrole reversible wave (Figure 2, Part I: Chapter 2).  $\Gamma_{\text{N}^+}$  values ranging from  $1.10 \times 10^{-7}$  to  $1.30 \times 10^{-7}$  mol cm<sup>-2</sup> were obtained when a 4 mC anodic charge was used for the polymerization of **1**.

Because the cationic polymeric film poly1 has an excellent ion-exchange properties, this film was used like matrix, and was loaded with the anionic cobalt oxalate complex,  $[\text{Co}(\text{C}_2\text{O}_4)_2]^{2-}$  generated *in situ* from an aqueous borate buffer (0.1 M) solution at pH 6 containing 4 mM of  $\text{CoSO}_4$  and 20 mM  $\text{NaC}_2\text{O}_4$ . In a third step, an efficient generation of  $\text{Co}^0$  particles inside a poly1 film was achieved by electroreduction of the  $[\text{Co}(\text{C}_2\text{O}_4)_2]^{2-}$  loaded in the film at a controlled-potential of -1.3 V vs Ag/AgCl in the cobalt oxalate solution. Indeed, about 130 seconds are required for a cathodic charge deposition of 4 mC (Figure 1). For comparative studies, a similar  $\text{Co}^0$  electrodeposition was performed on naked C electrodes in the cobalt oxalate aqueous borate buffer solution (pH 6) using also a cathodic charge of 4 mC. In this case, the deposition is slower and it requires around 170 seconds (see Figure 1).

**Scheme 1.** General Strategy for the Electrosynthesis of Poly(Pyrrrole-alkylammonium)/CoO<sub>x</sub> Composite Film Modified Electrodes<sup>a</sup>

<sup>a</sup>(i) Formation of poly**1** by oxidative electropolymerization of monomer **1** (4 mM) at  $E_{\text{app}} = +0.95$  V vs Ag/AgNO<sub>3</sub> in CH<sub>3</sub>CN, 0.1 M [Bu<sub>4</sub>N]ClO<sub>4</sub>; (ii) incorporation of  $[\text{Co}(\text{C}_2\text{O}_4)_2]^{2-}$  into poly**1** upon soaking during 1h in an aqueous solution (pH 6) of 4 mM CoSO<sub>4</sub>, 20 mM NaC<sub>2</sub>O<sub>4</sub>, 0.1 M Na<sub>2</sub>SO<sub>4</sub> and 0.1 M H<sub>3</sub>BO<sub>3</sub>; (iii) electroprecipitation of Co<sup>0</sup> within poly**1** at  $E_{\text{app}} = -1.3$  V vs Ag/AgCl in the previously mentioned aqueous solution of cobalt oxalate; (iv) air oxidation of Co<sup>0</sup> to CoO<sub>x</sub> in an aqueous solution (pH 9.2) of 0.1 M H<sub>3</sub>BO<sub>3</sub> and 0.05 M NaOH.

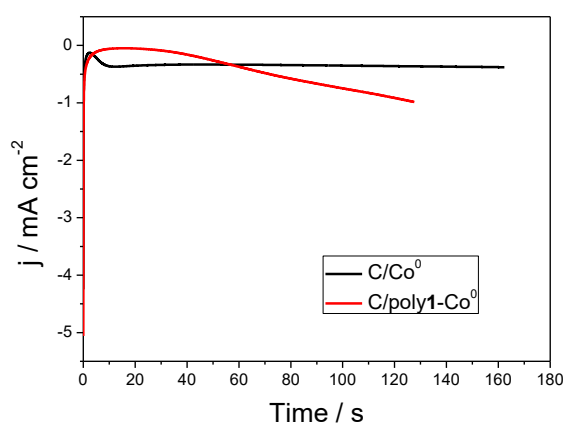


**Figure 1.** Cobalt deposition ( $E_{\text{appl}} = -1.3$  V,  $Q_{\text{deposition}} = 4$  mC) on C ( $\Gamma_{\text{Co}} = 5.32 \times 10^{-8}$  mol cm<sup>-2</sup>) and C/poly**1** ( $\Gamma_{\text{N}^+} = 1.2 \times 10^{-7}$  mol cm<sup>-2</sup>,  $\Gamma_{\text{Co}} = 1.82 \times 10^{-8}$  mol cm<sup>-2</sup>) electrodes (3 mm of diameter) in 4 mM CoSO<sub>4</sub>, 20 mM Na<sub>2</sub>C<sub>2</sub>O<sub>4</sub>, 0.1 M Na<sub>2</sub>SO<sub>4</sub>, 0.1 M H<sub>3</sub>BO<sub>3</sub>.

The optimum cathodic potential of  $-1.3$  V for  $\text{Co}^0$  electrodeposition was determined from cyclic voltammetry experiments as shown in Figure 2 which was carried out with naked C and C/poly1 electrodes. The electroactivity of the cobalt oxalate solution is characterized by an irreversible cathodic reduction process observed below  $-1.0$  V which is ascribed to the reduction of  $\text{Co}^{2+}$  (coordinated to oxalate) to  $\text{Co}^0$  leading its deposition on C and C/poly1 electrodes and to the concomitant electrocatalytic reduction of protons to  $\text{H}_2$  through the  $\text{Co}^0$  deposit.<sup>15</sup> On the reverse scan, in the anodic part, one irreversible redox process is observed at  $-0.5$  V for C/poly1- $\text{Co}^0$  ( $-0.4$  V for C/ $\text{Co}^0$ ) which is attributed to the reoxidation of  $\text{Co}^0$  deposited at the electrode surface to  $\text{Co}^{2+}$  leading to its dissolution.<sup>16</sup> It can be noticed that the charge involved in this stripping wave between  $-1.5$  and  $+0.4$  V does not allow for estimating the quantity of cobalt deposited on C/poly1 and naked C electrodes. As evoked in the previous chapter, the polypyrrole film is known to protect metallic particles from dissolution, and besides the dissolution of  $\text{Co}^0$  deposited on the surface of naked C electrodes is often incomplete due to passivation phenomena.<sup>15</sup> The precise determination of cobalt loaded on electrodes was thus performed by ICP-MS experiments after the formation of  $\text{CoO}_x$  from  $\text{Co}^0$  (see below).

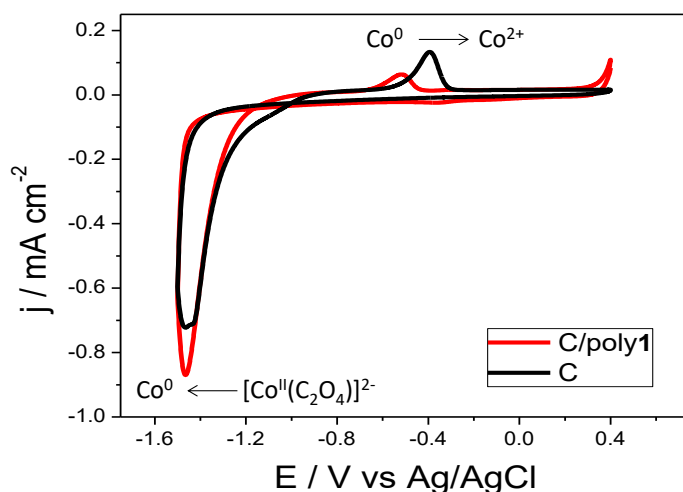


**Figure 2.** Cyclic voltammetry recorded at C (black line) and C/poly1 ( $\Gamma_N^+ = 1.2 \times 10^{-7} \text{ mol cm}^{-2}$ ) (red line) electrodes (3 mm of diameter) in an aqueous solution (pH 6) of 4 mM  $\text{CoSO}_4$ , 20 mM  $\text{NaC}_2\text{O}_4$ , 0.1 M  $\text{Na}_2\text{SO}_4$  and 0.1 M  $\text{H}_3\text{BO}_3$ ; The C/poly1 electrode was dipped in the aforementioned aqueous solution during 1h before the cyclic voltammetry experiment.

Finally, the last step is the oxidation of  $\text{Co}^0$  to the cobalt oxide. The cobalt oxide is probably generated by oxidation of  $\text{Co}^0$  with  $\text{O}_2$  in contact with the air. A small part of the cobalt oxide could be also formed by scanning the C/poly1- $\text{Co}^0$  or C/ $\text{Co}^0$  modified electrodes in an aqueous borate buffer at pH 9.2 between 0 and  $+1.2$  V for 5 consecutive cycles (scan rate 50

$\text{mV s}^{-1}$ ) (Figure 3, scheme 1). The formation of  $\text{CoO}_x$  on  $\text{C/poly1}$  is not easy to observed because the progressive growth of  $\text{Co}^{\text{II}}(\text{OH})/\text{Co}^{\text{III}}(\text{O})(\text{OH})$  redox process is very small, with an anodic peak and a cathodic peak respectively located at +0.58 and +0.54 V for  $\text{C/poly1-CoO}_x$  (Figure 3 (A, B)) and at +0.57 and +0.41 V for  $\text{C/CoO}_x$  for which the redox process is more obvious (Figure 3(C)). The weak magnitude of the redox process may be due to the small amount of cobalt loaded in the polymer film, as it can be seen from the ICP-MS analysis. More cycles do not lead to a significant increase of the  $\text{Co}^{\text{II}}(\text{OH})_2/\text{Co}^{\text{III}}(\text{O})(\text{OH})$  redox process.

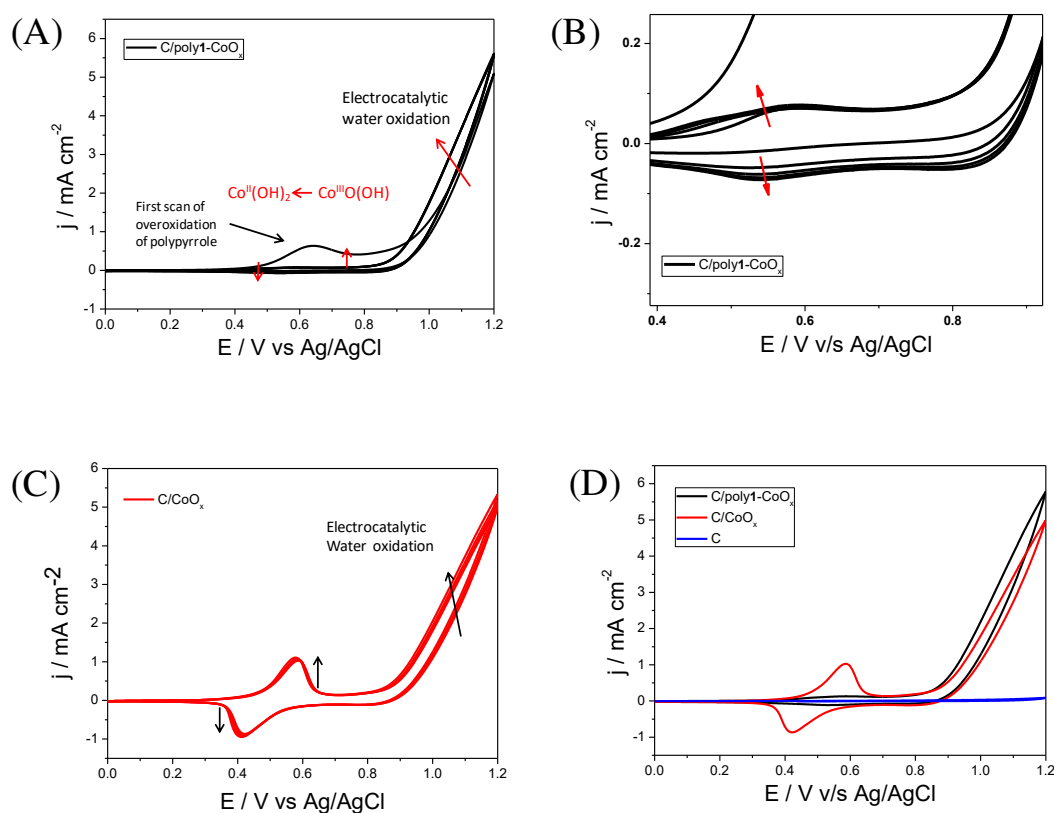


**Figure 3.** Electro-induced generation of  $\text{CoO}_x$  from  $\text{Co}^0$  by repeated cyclic voltammetry (CV) scans (5 scans; scan rate of  $50 \text{ mV s}^{-1}$ ) in an aqueous solution (pH 9.2) of  $0.1 \text{ M H}_3\text{BO}_3$  and  $0.05 \text{ M NaOH}$  at a (A)  $\text{C/poly1-CoO}_x$  electrode ( $\Gamma_{\text{N}^+} = 1.2 \times 10^{-7} \text{ mol cm}^{-2}$ ,  $\Gamma_{\text{Co}} = 2.29 \times 10^{-8} \text{ mol cm}^{-2}$ ) (5 consecutive scans), (B) zoom for  $\text{Co}^{\text{II}}(\text{OH})/\text{Co}^{\text{III}}(\text{O})(\text{OH})$  redox process, and at a (C)  $\text{C/CoO}_x$  electrode ( $\Gamma_{\text{Co}} = 6.33 \times 10^{-8} \text{ mol cm}^{-2}$ ), and (D) overlay of 5<sup>th</sup> scans of the  $\text{C/poly1-CoO}_x$  (black) and  $\text{C/CoO}_x$  (red) electrodes (in blue, the electroactivity of a naked C electrode of 3 mm diameter).

According to the Pourbaix diagram (Figure 4) for cobalt in aqueous solution, the oxidation of  $\text{Co}^0$  to  $\text{Co}^{\text{II}}(\text{OH})_2$  by  $\text{O}_2$  is possible at pH 9.2 since the oxidation potential of  $\text{O}_2$  is at  $-0.45 \text{ V}$  vs NHE ( $-0.65 \text{ V}$  vs Ag/AgCl) and the oxidation potential of  $\text{Co}^0$  is at  $-0.5 \text{ V}$  vs NHE ( $-0.75 \text{ V}$  vs Ag/AgCl) at this basic pH.

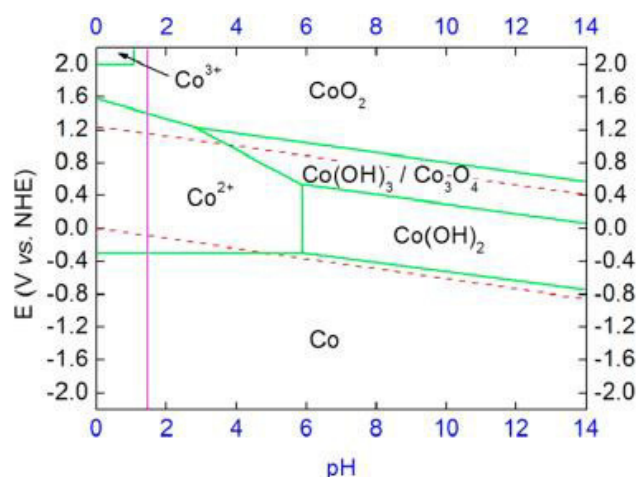


**Figure 4.** Diagram of Pourbaix for cobalt in aqueous solution. Green lines represent the borders of thermodynamic stability of the various species. Dissolved species are considered as having an activity of 1. Red dashed lines mark the region of water stability, the lower line corresponding to the hydrogen evolution reaction and the upper line to the oxygen evolution reaction. The vertical magenta line is drawn at  $\text{pH} = 1.6$  as a guide to the eye.<sup>17</sup>

The first scan of the C/poly1-CoO<sub>x</sub> modified electrode in Figure 3(A) shows one broad anodic process around +0.64 V corresponding respectively to the oxidation and the overoxidation of polypyrrole. Consequently, after the first scan from 0 to +1.2 V, the conductivity of polypyrrole is fully destroyed owing to its complete overoxidation, as we previously observed for C/poly1-Ni<sup>0</sup>.<sup>18</sup> Thus, at this stage, the overoxidized poly1 plays only the role of matrix and the conductivity of the film is ensured by the cobalt catalyst. We can also see the current density ( $j$ ) for the C/poly1-CoO<sub>x</sub> electrode is bigger than for C/CoO<sub>x</sub> electrode, with 5.77 mA cm<sup>-2</sup> versus 4.98 mA cm<sup>-2</sup>, respectively.

With a charge of 4 mC passed for cobalt deposition, the Co loading on the C/poly1 and C electrodes was estimated to be  $2.29 (\pm 0.82) \times 10^{-8}$  and  $6.33 (\pm 1.78) \times 10^{-8}$  mol cm<sup>-2</sup> respectively corresponding to deposition yields of 21.6 and 8% respectively. Thus, for the same quantity of charge (4 mC), the amount of Co<sup>0</sup> deposited on the C/poly1 film is 2.76 times smaller than that deposited on the naked C electrode. The ratio of cobalt incorporated within the poly1 film was also calculated considering that the di-anionic  $[\text{Co}(\text{C}_2\text{O}_4)_2]^{2-}$  complex should be bound to two ammonium units during the Co loading in the film. For an incorporation ratio of cobalt of 100%, the  $\Gamma_{\text{Co}}/\Gamma_{\text{N}^+}$  ratio should be equal to 0.5. For the C/poly1-CoO<sub>x</sub> electrodes, the average surface coverage values of Co and poly1 was determined to be respectively  $\Gamma_{\text{Co}} = 2.29 \times 10^{-8}$  mol cm<sup>-2</sup> and  $\Gamma_{\text{N}^+} = 1.2 \times 10^{-7}$  mol cm<sup>-2</sup> which corresponds to an average  $\Gamma_{\text{Co}}/\Gamma_{\text{N}^+}$  ratio of 0.2 and thus to an incorporation ratio of cobalt of 40%.

To get a clue of the better nanostructuration of the poly1-CoO<sub>x</sub> nanocomposite material, the relative capacitance of C/poly1-CoO<sub>x</sub> and C/CoO<sub>x</sub> electrodes, which is correlated to the electrochemically active surface area of the electrode,<sup>19</sup> were determined from the slope of the plot of the current density *versus* scan rate at 0 V (Figure 5).

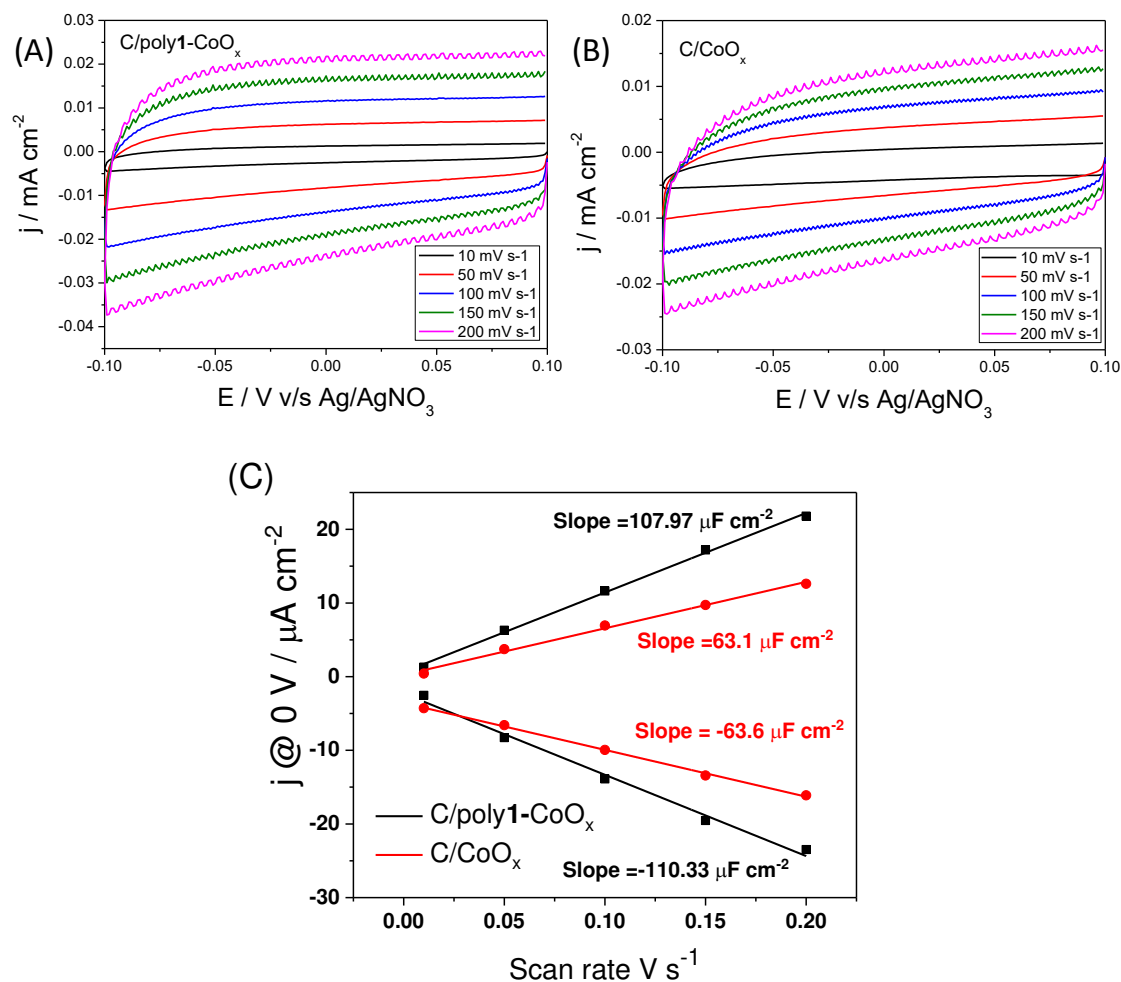


**Figure 5.** Cyclic voltammograms recorded at the (A) C/poly1-CoO<sub>x</sub> ( $\Gamma_{\text{N}^+} = 1.2 \times 10^{-7} \text{ mol cm}^{-2}$ ,  $\Gamma_{\text{Co}} = 2.29 \times 10^{-8} \text{ mol cm}^{-2}$ ) and (B) C/CoO<sub>x</sub> ( $\Gamma_{\text{Co}} = 6.33 \times 10^{-8} \text{ mol cm}^{-2}$ ) electrodes (3 mm of diameter) in an aqueous solution (pH 9.2) of 0.1 M H<sub>3</sub>BO<sub>3</sub> and 0.05 M NaOH; the scans were recorded between -0.10 and 0.10 V vs Ag/AgCl with the following scan rate of 10, 50, 100, 150 and 200 mV s<sup>-1</sup>. (C) The cathodic and anodic current density at 0 V vs Ag/AgCl plotted as function of scan rate the C/poly1-CoO<sub>x</sub> (black) and C/CoO<sub>x</sub> (red) electrodes.

Indeed, the capacitive current measured in non-Faradaic potential region is assumed to be due to double-layer charging and can be measured from cyclic voltammograms at various scan rates (Figures 5(A,B)). As shown in Figure 4(C), C/poly1-CoO<sub>x</sub> exhibits a 1.7 fold higher capacitance (107.9 and -110.3 μF cm<sup>-2</sup> for anodic and cathodic capacitances respectively) than C/CoO<sub>x</sub> (63.1 and -63.6 μF cm<sup>-2</sup> for anodic and cathodic capacitances respectively). This confirms that the C/poly1-CoO<sub>x</sub> electrode has a higher electroactive surface area than the

C/CoO<sub>x</sub> electrode. In the previous chapter, we obtained similar values of active surface area of double-layer capacitance of 93.2 and -109.2 μF cm<sup>-2</sup> for C/poly1-NiO<sub>x</sub> and 63.6 and -79.6 μF cm<sup>-2</sup> for C/NiO<sub>x</sub>.

## ***2.2 –Characterization of Cobalt Oxide and Poly(Pyrrrole-alkilammonium) Cobalt Oxide Nanocomposite by AFM, TEM and SEM.***

Atomic force microscopy (AFM) measurements in peak force mode were performed on ITO/poly1-CoO<sub>x</sub> and ITO/CoO<sub>x</sub> in view to identify and compare the surface morphology of both electrodes (Figure 6). The ITO/poly1-CoO<sub>x</sub> and ITO/CoO<sub>x</sub> electrodes (ITO surface of 1 cm<sup>2</sup>) were prepared with a charge of 57 mC for both the poly1 and Co<sup>0</sup> deposition in view to obtain a charge density of 56 mC cm<sup>-2</sup>, similar to that used for the preparation of the C/poly1-CoO<sub>x</sub> and C/CoO<sub>x</sub> electrodes (4 mC for a C electrode surface of 0.071 cm<sup>2</sup>). From AFM 3D profiles and images, a homogenous granular topography along with well-defined grain boundaries were observed for ITO/CoO<sub>x</sub> with a root-mean square (r.m.s.) roughness of 10.2 nm (Figures 6(A, B)), while an ill-defined nodular topography (as cauliflower) was obtained with ITO/poly1-CoO<sub>x</sub> with a close r.m.s. roughness of 11.6 nm (Figures 6 (D, E)). Cauliflower topology is typical for electrodeposited polypyrrole film<sup>14, 15</sup> and, since the CoO<sub>x</sub> particles are embedded into the polymer matrix, it was difficult to measure their size within the nanocomposite from AFM measurements. Meanwhile, the CoO<sub>x</sub> particles size on the surface of the ITO/CoO<sub>x</sub> electrode was roughly estimated to be 58 ± 31 nm from the section analysis of its AFM image (Figure 6(C)).

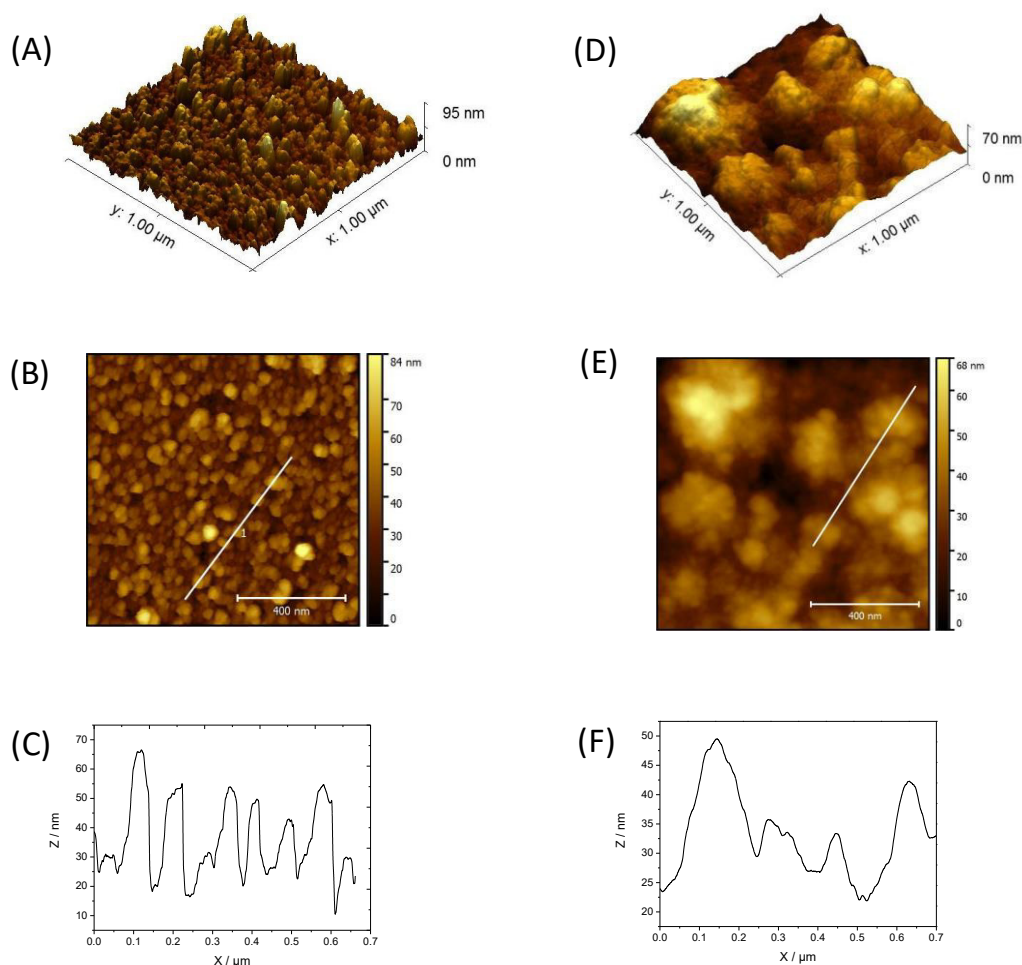


**Figure 6.** AFM 3D profiles and respective images in peak force mode of (A, B) ITO coated with  $\text{CoO}_x$  (57 mC used for deposition of  $\text{Co}^0$ ); (D, E) ITO coated with poly $\mathbf{1}$ - $\text{CoO}_x$  nanocomposite (57 mC used for deposition of poly $\mathbf{1}$  and for subsequent deposition of  $\text{Co}^0$ ); (C) and (F) exhibit section analysis of ITO/ $\text{CoO}_x$  and C/poly $\mathbf{1}$ - $\text{CoO}_x$  shown respectively in (B) and (E).

SEM pictures obtained for ITO/poly $\mathbf{1}$ - $\text{CoO}_x$  and ITO/ $\text{CoO}_x$  also confirm the AFM measurements. SEM images also revealed a granular topography and an ill-defined nodular topography for ITO/poly $\mathbf{1}$ - $\text{CoO}_x$  (Figures 7(C)) and ITO/ $\text{CoO}_x$  (Figures 8D and 8E).

In view to determine more precisely the  $\text{CoO}_x$  particles size inside the film, the poly $\mathbf{1}$ - $\text{CoO}_x$  and  $\text{CoO}_x$  materials were peeled off from the ITO plates and deposited on copper grids for transmission electron microscopy (TEM) analyses (Figure 9). TEM images revealed similar sizes for  $\text{CoO}_x$  nanoparticles on the ITO/ $\text{CoO}_x$  and ITO/poly $\mathbf{1}$ - $\text{CoO}_x$  electrodes with an average particle size of  $31 \pm 16$  and  $31 \pm 20$  nm associated (Figure 9 (A, B)). We can see also that the polymer avoids the nanoparticles agglomeration, giving better catalytic activity with the nanocomposite although the film has a smaller amount of nanoparticles incorporated (Figure 9(B)).

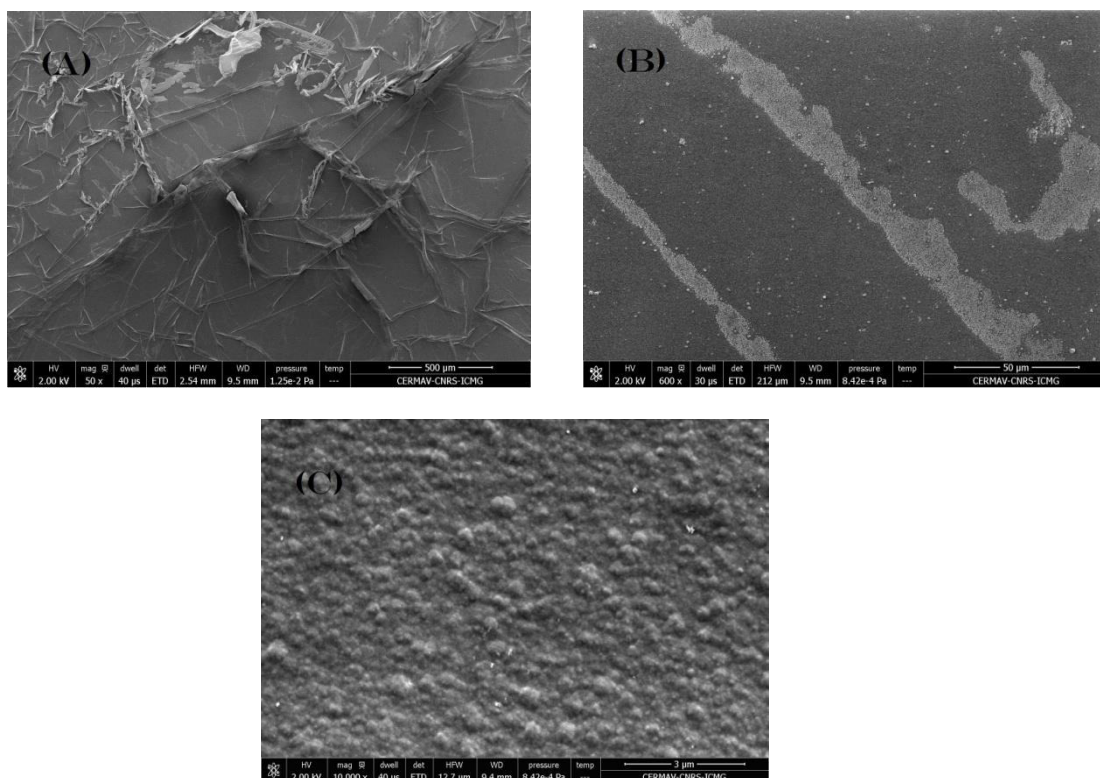


**Figure 7.** SEM images of poly1-CoO<sub>x</sub> nanocomposite, deposition of 57 mC of poly1 and Co<sup>0</sup>, respectively on ITO electrode, 1 cm<sup>-2</sup>, (A) scale 500 μm, (B) scale 50 μm, and (C) scale 3 μm.

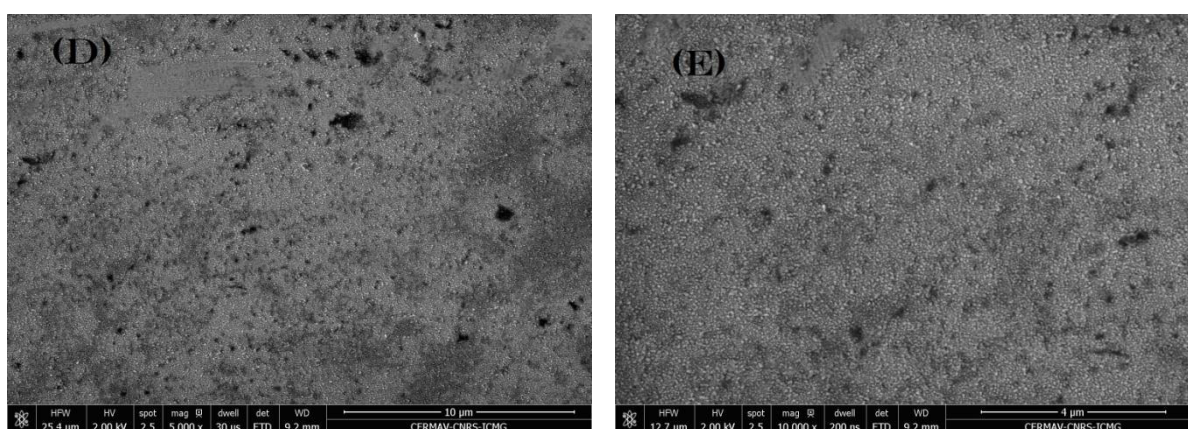


**Figure 8.** SEM images of CoO<sub>x</sub>, 57 mC of Co<sup>0</sup> deposition on ITO electrode, 1cm<sup>-2</sup>, (D) scale 10 μm, and (E) scale 4 μm.

In addition, a more or less well-resolved selected area electron diffraction (SAED) pattern was recorded with poly1-CoO<sub>x</sub> indicating that CoO<sub>x</sub> particles within polypyrrole are most probably amorphous. Zhao et. al. also obtained amorphous CoO<sub>x</sub> films of ca. 40 nm of thickness.<sup>13</sup> Others authors obtained similar cobalt particle size, as Frei et. al.<sup>20</sup> and Costentin et. al.<sup>21</sup> to mention some of them. To conclude, the use of polypyrrole films as template for cobalt deposition and CoO<sub>x</sub> formation allows obtaining nanostructured CoO<sub>x</sub> films by avoiding agglomeration of particles. A well-nanostructured poly1-CoO<sub>x</sub> composite can offer

a great electroactive surface area that is responsible of a great electrocatalytic performance towards water oxidation.

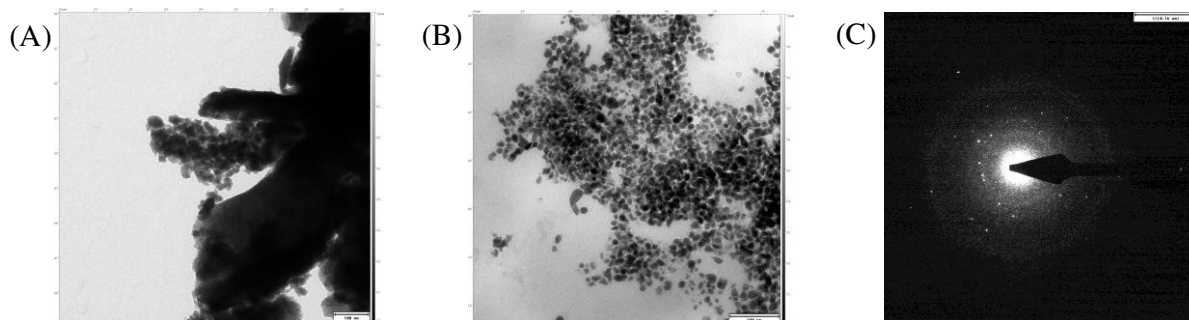


**Figure 9.** TEM images of (A) ITO/CoO<sub>x</sub>, 57 mC of Co<sup>0</sup> deposition, scale 100 nm, (B) ITO/poly1-CoO<sub>x</sub> nanocomposite, 57 mC of poly1 and Co<sup>0</sup>, respectively, scale 200 nm. (C) SAED pattern of CoO<sub>x</sub> nanoparticles within poly1-CoO<sub>x</sub> nanocomposite shown in (B).

### ***2.3 - Electrocatalytic performance of Cobalt Oxide and Poly(pyrrole-alkylammonium) Cobalt Oxide Nanocomposite Electrodes.***

The electrocatalytic activity of C/poly1-CoO<sub>x</sub> and C/CoO<sub>x</sub> electrodes have been evaluated in a conventional three-electrode cell by linear sweep voltammetry at nearly neutral pH of 9.2 as well as at more basic pHs of 13 and 14 (Figure 10). Table 1 summarized the catalytic OER performances of these electrodes and those of iridium and nickel-based electrode reported by our research group at similar pHs.<sup>14,15</sup> The architecture of catalysts able to operate at nearly neutral pH is very important<sup>22</sup> for use natural water sources but also to develop photoelectrochemical cells for light-driven water splitting<sup>10</sup> that couple a catalyst and a molecular photosensitizer, the latter is often unstable in strongly basic solution.<sup>23</sup> As we mentioned in the previous chapter, the two figures of merit usually measured for an electrocatalyst working at pH 9.2 are the catalytic current density ( $j$ ) at overpotential ( $\eta$ ) of +0.61 V (corresponding to +1.1 V vs Ag/AgCl at pH 9.2) and the overpotential to reach the catalytic current density of 1 mA cm<sup>-2</sup>. For C/poly1-CoO<sub>x</sub>, the  $j$  value at +0.61 V and the  $\eta$  value at 1 mA cm<sup>-2</sup> are respectively 3.72 mA cm<sup>-2</sup> and +0.46 V with a cobalt mass load of 1.35  $\mu\text{g cm}^{-2}$ , while for C/CoO<sub>x</sub> these values are 3.51 mA cm<sup>-2</sup> and +0.45 V with a 3.75  $\mu\text{g cm}^{-2}$ , respectively (Table 1). The C/poly1-CoO<sub>x</sub> nanocomposite electrode presents better catalytic performance than the C/CoO<sub>x</sub> direct deposition with  $\sim 2.8$  times less cobalt load, demonstrating the enhancement in catalytic activity by using a polymer film to improve the nanostructuration.

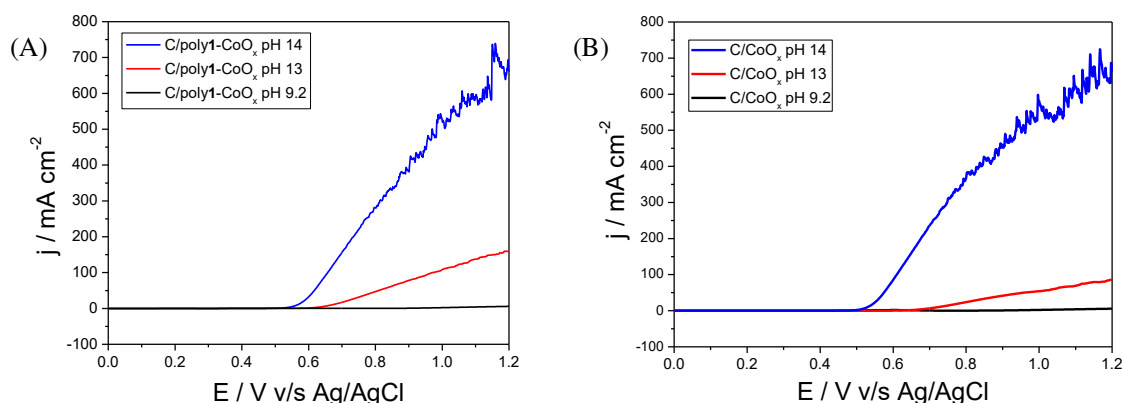


**Figure 10.** Linear sweep voltammetry recorded at (A) C/poly1-CoO<sub>x</sub> ( $\Gamma_{N^+} = 1.2 \times 10^{-7} \text{ mol cm}^{-2}$ ,  $\Gamma_{Co} = 2.29 \times 10^{-8} \text{ mol cm}^{-2}$ ) and (B) C/CoO<sub>x</sub> ( $\Gamma_{Co} = 6.33 \times 10^{-8} \text{ mol cm}^{-2}$ ) electrodes (3 mm of diameter) in an aqueous solution at pH 9.2 (0.1 M H<sub>3</sub>BO<sub>3</sub> and 0.05 M NaOH), 13 (0.1 M KOH) and 14 (1 M KOH); Scan rate of 50 mV s<sup>-1</sup>.

According to TEM analysis, both C/poly1-CoO<sub>x</sub> and C/CoO<sub>x</sub> present the same particle size (31 nm). Hence the higher catalytic activity of the C/poly1-CoO<sub>x</sub> nanocomposite in comparison with the direct deposition C/CoO<sub>x</sub> is due to the better nanostructuring of the nanocomposite that increases the active surface area of the anode and promotes a good mass transport of water and OH<sup>-</sup> ions into the nanocomposite. The value of mass activity and TOF confirm the higher OER catalytic activity of C/poly1-CoO<sub>x</sub> than that of C/CoO<sub>x</sub>, respectively with 2.75 A mg<sup>-1</sup> and 0.41 s<sup>-1</sup> for C/poly1-CoO<sub>x</sub> and 0.94 A mg<sup>-1</sup> and 0.14 s<sup>-1</sup> for C/CoO<sub>x</sub>, at pH 9.2 at an overpotential of 0.61V (Table 1). It is also interesting to note that the OER performance of C/poly1-CoO<sub>x</sub> are clearly superior to that of C/poly1-NiO<sub>x</sub> displaying lower values of mass activity and TOF of 1.12 A mg<sup>-1</sup> and 0.17 s<sup>-1</sup> respectively.

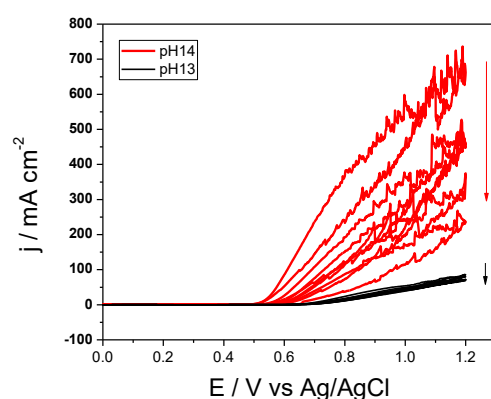
The electrocatalytic activity of the C/poly1-CoO<sub>x</sub> and C/CoO<sub>x</sub> electrodes was also investigated at basic pHs of 13 and 14 (Figures 10), since the most common commercial electrolyzers operate in strongly alkaline media and most of the metallic catalysts for OER based on non-precious and earth-abundant elements are studied in basic conditions in order to avoid the corrosion of metal. Note that, at these basic pHs, the onset potential for OER and the Co<sup>II</sup>(OH)<sub>2</sub>/Co<sup>III</sup>(O)(OH) redox process recorded at C/poly1-CoO<sub>x</sub> and C/CoO<sub>x</sub> by linear sweep voltammetry disappeared completely (Figure 10). The OER performance of C/poly1-CoO<sub>x</sub> and C/CoO<sub>x</sub> was analyzed at pH 13 and 14 in terms of catalytic current density (*j*) at an overpotential ( $\eta$ ) of 0.35 V (corresponding to 0.61 V vs Ag/AgCl at pH 13 and 0.56 V vs Ag/AgCl at pH 14) and the  $\eta$  value at *j* of 10 mA cm<sup>-2</sup>. At pH 13 (Table 1), C/poly1-CoO<sub>x</sub> displays a better catalytic performance than that of C/CoO<sub>x</sub> with current densities of 2.17 and 0.59 mA cm<sup>-2</sup> at  $\eta$  0.35 V respectively for C/poly1-CoO<sub>x</sub> and C/CoO<sub>x</sub>, and overpotentials of

0.40 and 0.46 V at  $10 \text{ mA cm}^{-2}$  respectively for C/poly1-CoO<sub>x</sub> and C/CoO<sub>x</sub>. The mass activity and TOF values of C/poly1-CoO<sub>x</sub> and C/CoO<sub>x</sub> follow the same trend with the highest values for the nanocomposite (see Table1). Our C/poly1-CoO<sub>x</sub> catalyst electrode also exhibits higher catalytic activity than our NiO<sub>x</sub><sup>15</sup> and IrO<sub>x</sub><sup>14</sup> based electrodes previously reported under basic conditions. It is interesting to mention that C/poly1-CoO<sub>x</sub> present 10 fold higher mass activity than that of C/CoO<sub>x</sub> at pH 13 with a cobalt content 3 times lower. Nevertheless, at pH 14 an opposite behaviour is observed. The performance of the simple C/CoO<sub>x</sub> electrode increase at pH 14 compared to that at pH 13 and is also bigger than C/poly1-CoO<sub>x</sub> electrode, presenting a current density of  $6.19 \text{ mA cm}^{-2}$  at  $\eta$  0.35 V and an overpotential of 0.36 V at  $10 \text{ mA cm}^{-2}$ , a mass activity of  $4.58 \text{ A mg}^{-1}$  and a TOF of  $0.69 \text{ s}^{-1}$  at  $\eta$  0.35 V, which are much lower than those of C/CoO<sub>x</sub> with a current density of  $27.7 \text{ mA cm}^{-2}$  at  $\eta$  0.35 V and a overpotential of 0.33 V at  $10 \text{ mA cm}^{-2}$ , mass activity of  $7.3 \text{ A mg}^{-1}$  and a TOF of  $1.11 \text{ s}^{-1}$  at  $\eta$  0.35 V. The OER performance of CoO<sub>x</sub> electrode are also higher than those of CoO<sub>x</sub> electrode reported by Boettcher et coll.<sup>24</sup> which displays a mass activity 85 times lower than that of our cobalt oxide electrode with a cobalt content of the same order of magnitude ( $1.32$  vs  $3.75 \text{ } \mu\text{g cm}^{-2}$ ). Basically, at pH 14 the release of O<sub>2</sub> increases drastically and then the resistance of material towards mass transport also significantly increases, which would limit the catalytic current of the anode. So, at pH 14 C/CoO<sub>x</sub> is more efficient than C/poly1-CoO<sub>x</sub> due to the fact that the polypyrrole-CoO<sub>x</sub> nanocomposite exhibit higher mass transport resistance than that of bare CoO<sub>x</sub>-film.<sup>21</sup>

At pHs 13 and 14, the C/poly1-CoO<sub>x</sub> and C/CoO<sub>x</sub> electrodes lose their activity after only few CV successive scans between 0 and 1.2 V vs Ag/AgCl (Figure 11). This poor stability in strong basic conditions can be directly correlated to the detachment of the film of poly1-CoO<sub>x</sub> or CoO<sub>x</sub> induced by the strong oxygen bubbling as the consequence of their high catalytic performances. Nevertheless, the first scan recorded at the C/poly1-CoO<sub>x</sub> and C/CoO<sub>x</sub> electrodes at pHs 13 and 14 is sufficient to evaluate their real catalytic activity and thus their potentiality towards OER in very basic conditions.

**Table 1.** OER performances of C/poly1-CoO<sub>x</sub> and C/CoO<sub>x</sub> prepared in this work compared to those of NiO<sub>x</sub> catalysts of literature at pH 9.2

Catalyst/electrode	$j$ (mA cm <sup>-2</sup> ) @ $\eta$ (V)	$\eta$ (V) @ $j$ (mA cm <sup>-2</sup> )	Metal mass loading ( $\mu\text{g cm}^{-2}$ )	mass active (A mg <sup>-1</sup> ) @ $\eta$ (V)	TOF <sub>min</sub> (s <sup>-1</sup> ) @ $\eta$ (V)	Author
pH 9.2 with 0.1M H <sub>3</sub> BO <sub>3</sub> + 0.05M NaOH						
C/poly1-CoO <sub>x</sub>	3.72@0.61	0.46@1	1.35	2.75@0.61	0.41@0.61	This work
C/CoO <sub>x</sub>	3.51@0.61	0.45@1	3.75	0.94@0.61	0.14@0.61	This work
C/poly1-NiO <sub>x</sub>	2.17@0.61	0.51@1	1.9	1.12@0.61	0.17@0.61	Morales et al
C/NiO <sub>x</sub>	0.66@0.61	0.67@1	0.7	0.95@0.61	0.14@0.61	Morales et al
pH 13 with 0.1M KOH						
C/poly1-CoO <sub>x</sub>	2.17@0.35	0.40@10	1.35	1.6@0.35	0.24@0.35	This work
C/CoO <sub>x</sub>	0.59@0.35	0.46@10	3.75	0.16@0.35	0.02@0.35	This work
C/poly1-NiO <sub>x</sub>	1.75@0.35	0.45@10	1.9	0.90@0.35	0.14@0.35	Morales et al
C/NiO <sub>x</sub>	0.39@0.35	0.57@10	0.7	0.55@0.35	0.08@0.35	Morales et al
C/poly1-IrO <sub>x</sub>	4.4@0.35	0.42@10	6.9	0.64@0.35	0.32@0.35	Moutet et al
pH 14 with 1M KOH						
C/poly1-CoO <sub>x</sub>	6.19@0.35	0.36@10	1.35	4.58@0.35	0.69@0.35	This work
C/CoO <sub>x</sub>	27.7@0.35	0.33@10	3.75	7.3@0.35	1.11@0.35	This work
C/poly1-NiO <sub>x</sub>	2.49@0.35	0.41@10	1.9	1.28@0.35	0.19@0.35	Morales et al
C/NiO <sub>x</sub>	0.30@0.35	0.51@10	0.7	0.43@0.35	0.07@0.35	Morales et al
Au-Ti/CoO <sub>x</sub>	0.020@0.30	0.381@1	1.32	0.015@0.30	0.0032@0.3	Boettcher et al <sup>24</sup>

**Figure 11.** Cyclic voltammograms recorded at a C/poly1-CoO<sub>x</sub> ( $\Gamma_{\text{N}^+} = 1.2 \times 10^{-7}$  mol cm<sup>-2</sup>,  $\Gamma_{\text{Co}} = 2.29 \times 10^{-8}$  mol cm<sup>-2</sup>) electrode (3 mm of diameter) in an aqueous solution at pH 13 (black, 0.1 M KOH) and 14 (red, 1.0 M KOH); Scan rate of 50 mV s<sup>-1</sup>.

The stability of C/poly1-CoO<sub>x</sub> and C/CoO<sub>x</sub> electrodes at pH 9.2 was evaluated by chronoamperometry measurements over a period of 2h at an applied potential of +1.2 V vs Ag/AgCl (Figure 12). The current density of the C/CoO<sub>x</sub> electrode decreases until 5.28 mA cm<sup>-2</sup> after 2 min of electrolysis and then gradually decreases to reach a pseudo plateau at 4.82 mA cm<sup>-2</sup>. Meanwhile the current density of C/poly1-CoO<sub>x</sub> increases during the first 18 s until 7.11 mA cm<sup>-2</sup> and then gradually decreases to reach a pseudo plateau at 6.35 mA cm<sup>-2</sup>. Over this time range, C/poly1-CoO<sub>x</sub> seems relatively stable and more efficient than C/CoO<sub>x</sub> with a 1.3 fold higher catalytic current, demonstrating the superiority of the nanocomposite electrode over a simple Co-based electrode. The stability of C/poly1-CoO<sub>x</sub> would be further improved following three possible manners: (i) by chemical grafting of the polymer film at the surface of the electrode, (ii) by introducing Nafion into the polymer acting as a paste, (iii) or depositing the poly1-CoO<sub>x</sub> film into a carbon sponge electrode; the film being trapped material into the reticulous carbon would not detach from the electrode during the electrolysis due to the release of oxygen bubbles.

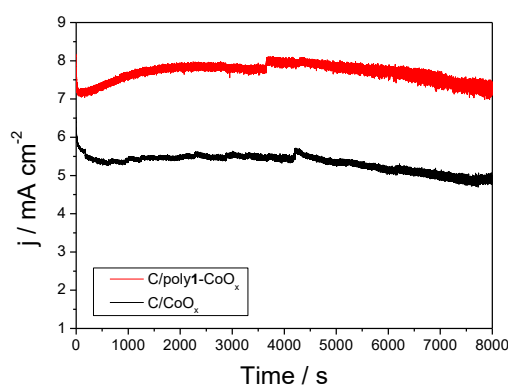


**Figure 12.** Chronoamperograms recorded at a C/poly1-CoO<sub>x</sub> ( $\Gamma_{N^+} = 1.2 \times 10^{-7} \text{ mol cm}^{-2}$ ,  $\Gamma_{Co} = 2.29 \times 10^{-8} \text{ mol cm}^{-2}$ ) and C/CoO<sub>x</sub> ( $\Gamma_{Co} = 6.33 \times 10^{-8} \text{ mol cm}^{-2}$ ) electrodes (3 mm of diameter) in an aqueous solution (pH 9.2) of 0.1 M H<sub>3</sub>BO<sub>3</sub> and 0.05 M NaOH, at constant potential of +1.2 V vs Ag/AgCl.

Tafel analysis was carried out by stepwise chronoamperometry (see experimental section) at pH 9.2 on C/poly1-CoO<sub>x</sub> and C/CoO<sub>x</sub> electrodes in order to gain some mechanistic information, through the Tafel slope, about the rate determining step for OER (Figure 13). The calculated Tafel slope values for C/poly1-CoO<sub>x</sub> and C/CoO<sub>x</sub> are 47 and 23 mV dec<sup>-1</sup> respectively. The difference in Tafel slope between the C/poly1-CoO<sub>x</sub> and C/CoO<sub>x</sub> electrodes means that the oxidation of water occurs *via* different catalytic mechanisms for both electrodes.<sup>25</sup> Sun and co-workers obtained the same a Tafel slope of 47 mV dec<sup>-1</sup> also, but with a bifunctional Co-P film in alkaline media.<sup>26</sup> The Tafel slope value of 47 mV dec<sup>-1</sup> is close the theoretical value of 40 mV dec<sup>-1</sup> usually attributed to a sequential catalytic

mechanism where the rate determining step is the second electron transfer.<sup>27</sup> Similar values were reported by other groups, Castro and co-workers obtained a Tafel slope of 40 mV dec<sup>-1</sup> for a C/Co<sub>3</sub>O<sub>4</sub> catalyst in strong alkaline media, and Boettcher et coll. obtained a Tafel slope of 42 mV dec<sup>-1</sup> for a CoO<sub>x</sub>.<sup>28,24</sup> The value of 23 mV dec<sup>-1</sup> is completely unusual and has been previously observed at once for nickel oxide based electrodes by Conway and Bourgault in 1959.<sup>19</sup> This group has proposed a plausible global mechanism for OER (Equations 1-4) and has associated this low Tafel slope value to a rate determining step corresponding to the adsorption of OH<sup>-</sup> anions at the surface of metal oxide (Equation 3).



In view of the low Tafel slope obtained with our C/poly1-CoO<sub>x</sub> anode, the mechanism of Conway and Bourgault for OER could be also envisaged. In addition, Tafel analysis confirms that C/poly1-CoO<sub>x</sub> electrode operates efficiently at a lower overpotential than C/CoO<sub>x</sub> electrodes.

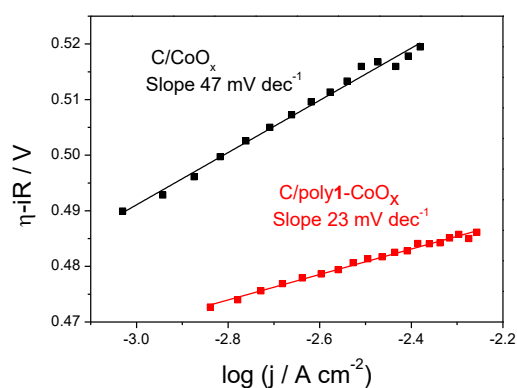


**Figure 13.** Tafel plot recorded for C/poly1-CoO<sub>x</sub> ( $\Gamma_{N^+} = 1.2 \times 10^{-7}$  mol cm<sup>-2</sup>,  $\Gamma_{Co} = 2.29 \times 10^{-8}$  mol cm<sup>-2</sup>) (red) and C/CoO<sub>x</sub> ( $\Gamma_{Co} = 6.33 \times 10^{-8}$  mol cm<sup>-2</sup>) (black) electrodes (3 mm of diameter) in an aqueous solution (pH 9.2) of 0.1 M H<sub>3</sub>BO<sub>3</sub> and 0.05 M NaOH; Scan rate of 50 mV s<sup>-1</sup>.

### 3 - Conclusion

We report a very efficient OER anode based on a cobalt oxide-poly(pyrrole-alkylammonium) nanocomposite prepared by an easy all-electrochemical synthesis. As observed by AFM and TEM, this composite features the dispersion of  $\text{CoO}_x$  particles of 31 nm into the polymer film, conferring a high electroactive surface area, an easy mass transport and thus high OER electrocatalytic performances. These cobalt oxide particles entrapped within the polypyrrole film, exhibits exceptional mass activity and TOF values for OER at mildly basic pH 9.2 of  $2.75 \text{ A mg}^{-1}$  and  $0.41 \text{ s}^{-1}$  at an overpotential of 0.61 V, and an unprecedented Tafel slope of  $23 \text{ mV dec}^{-1}$ . Under basic conditions at pH 14, the cobalt oxide-polypyrrole nanocomposite electrode, with a high mass activity and TOF values of  $4.58 \text{ A mg}^{-1}$  and  $0.69 \text{ s}^{-1}$  at an overpotential of 0.35 V, outperforms the nickel oxide-polypyrrole nanocomposite and iridium oxide based anodes previously reported by our group. In addition, at mildly basic pH, the cobalt oxide electrogenerated into polypyrrole-alkylammonium films appeared more efficient than the cobalt oxide film electrogenerated on a naked electrode surface by the same electrochemical procedure. We successfully demonstrated that our all electrochemical approach to prepare metal oxide-polymer nanocomposite can be used with cobalt metal and could be easily extended to other first-row transition metals as manganese and iron.

## References

- (1) Suzuki, O.; Takahashi, M.; Fukunaga, T.; Kuboyama, J. US Patent, 1968.
- (2) Han, L.; Dong, S.; Wang, E. *Adv. Mater.* **2016**, *28* (42), 9266–9291.
- (3) Shafirovich, V. Y.; Strelets, V. V. *Nouv. J. Chim.* **1978**, *2* (3), 199–201.
- (4) Burke, L. D.; Lyons, M. E.; Murphy, O. J. *J. Electroanal. Chem. Interfacial Electrochem.* **1982**, *132*, 247–261.
- (5) Bockris, J. O.; Otagawa, T. *J. Phys. Chem.* **1983**, *87* (15), 2960–2971.
- (6) Brockis, J. O.; Otagawa, T. *J. Electrochem. Soc.* **1984**, *131* (2), 290–302.
- (7) Chen, Y.-W. D.; Noufi, R. N. *J. Electrochem. Soc.* **1984**, *131* (6), 1447.
- (8) Rasiyah, P.; Tseung, A. C. C. *J. Electrochem. Soc.* **1983**, *130* (2), 365–368.
- (9) Rasiyah, P.; Tseung, A. C. C. *J. Electrochem. Soc.* **1984**, *131* (4), 803–808.
- (10) Kanan, M. W.; Nocera, D. G. *Science*. **2008**, *321* (5892), 1072–1075.
- (11) Lyons, M. E. G.; Brandon, M. P. *Int. J. Electrochem. Sci.* **2008**, *3*, 1386–1424.
- (12) Gardner, G.; Al-Sharab, J.; Danilovic, N.; Go, Y. B.; Ayers, K.; Greenblatt, M.; Charles Dismukes, G. *Energy Environ. Sci.* **2016**, *9* (1), 184–192.
- (13) Suryanto, B. H. R.; Lu, X.; Chan, H. M.; Zhao, C. *RSC Adv.* **2013**, *3* (43), 20936.
- (14) Lattach, Y.; Rivera, J. F.; Bamine, T.; Deronzier, A.; Moutet, J.-C. *ACS Appl. Mater. Interfaces* **2014**, *6* (15), 12852–12859.
- (15) Morales, D. V.; Lattach, Y.; Urbano, B. F.; Pereira, E.; Rivas, B. L.; Arnaud, J.; Putaux, J.-L.; Sirach, S.; Cobo, S.; Moutet, J.-C.; Fortage, J.; Collomb, M.-N. *Catal. Sci. Technol.* **2018**, Article in press. DOI: 10.1039/c7cy01949a
- (16) Surendranath, Y.; Kanan, M. W.; Nocera, D. G. *J. Am. Chem. Soc.* **2010**, *132* (46), 16501–16509.
- (17) Bloor, L. G.; Molina, P. I.; Symes, M. D.; Cronin, L. *J. Am. Chem. Soc.* **2014**, *136* (8), 3304–3311.
- (18) Zouaoui, A.; Stephan, O.; Ourari, A.; Moutet, J. C. *Electrochim. Acta* **2000**, *46* (1), 49–58.
- (19) Conway, B. E.; Bourgault, P. L. *Can. J. Chem.* **1959**, *37* (1), 292–307.
- (20) Jiao, F.; Frei, H. *Angew. Chemie-International Ed.* **2009**, *48* (10), 1841–1844.
- (21) Costentin, C.; Porter, T. R.; Savéant, J.-M. *J. Am. Chem. Soc.* **2016**, *138* (17), 5615–5622.
- (22) Zhang, N.; Fan, Y.; Fan, H.; Shao, H.; Wang, J.; Zhang, J.; Cao, C. *ECS Electrochem. Lett.* **2012**, *1* (2), H8–H10.
- (23) Kuznetsov, D. A.; Konev, D. V.; Komarova, N. S.; Ionov, A. M.; Mozhchil, R. N.; Fedyanin, I. V. *Chem. Commun.* **2016**, *52* (59), 9255–9258.
- (24) Trotochaud, L.; Ranney, J. K.; Williams, K. N.; Boettcher, S. W. *J. Am. Chem. Soc.* **2012**, *134* (41), 17253–17261.
- (25) Lehn, J. M.; Sauvage, J. P. *Nouv. J. Chim. J. Chem.* **1977**, *1* (6), 449–451.
- (26) Jiang, N.; You, B.; Sheng, M.; Sun, Y. *Angew. Chemie - Int. Ed.* **2015**, *54* (21), 6251–6254.
- (27) Doyle, R. L.; Godwin, I. J.; Brandon, M. P.; Lyons, M. E. G. *Phys. Chem. Chem. Phys.* **2013**, *15* (33), 13737–13783.
- (28) Castro, E. B.; Gervasi, C. A.; Vilche, J. R. *J. Appl. Electrochem.* **1998**, *28*, 835–841.

**HYBRID PHOTOANODES FOR WATER  
OXIDATION BASED ON A MOLECULAR  
PHOTOSENSITIZER AND A METAL OXIDE  
OXYGEN-EVOLVING CATALYST**



**Hybrid photoanodes for water oxidation: a bibliographic study**



## INDEX

1 – Introduction .....	111
2 – Hybrid Photoanodes with a Ru-tris-Bipyridine Derivative as Photosensitizer .....	113
3 – Hybrid Photoanodes with an Organic Chromophore .....	117
3.1 – Heptazine Chromophore.....	117
3.2 – Perylene Chromophore.....	118
3.3 – $\pi$ - Conjugated Polymer Naphtalene Based Chromophore.....	123
3.4 – Porphyrine Free Base Chromophore.....	124
4 – Conclusions .....	126
References .....	127



## 1 - Introduction

The construction of photo-electrochemical devices for water-splitting is a growing field of research.<sup>1</sup> Water-splitting photoelectrochemical cells (PECs) associates a photoanode for OER and a photocathode for the HER. The construction of such devices remains at the stage of exploratory research and the photoelectrodes, photoanodes and photocathodes are often optimized separately and investigated with a simple platinum counter-electrode cells, requiring the supply of electricity to operate.

Intense research are devoted to the development of photoelectrodes solely based on semiconductor materials (SCs)<sup>2</sup> but they face the difficulty of having a SC that can both effectively absorb visible light and a sufficient energy level to catalyze the OER for photoanodes and HER for photocathodes. The most investigated materials for such photoanodes are transition metal oxide SCs as TiO<sub>2</sub>, WO<sub>3</sub>, BiVO<sub>4</sub> and Fe<sub>2</sub>O<sub>3</sub>.<sup>2,3</sup> Oxynitrides photoanodes as TaON, LaTiO<sub>2</sub>N and SrNbO<sub>2</sub>N have been also used because such materials offer an alternative for visible light absorption. A strategy to improve the efficiency for these SCs based PECs is to decouple the light absorption and catalytic functions of the electrode,<sup>3</sup> by coupling to the SCs an oxygen-evolving catalyst for photoanodes (or hydrogen-evolving catalyst in the case of photocathodes), generally metal (oxide) nanoparticles.

Another strategy is to adsorb a molecular dye or photosensitizer (PS) on the surface of the semiconductor to extend the absorption in the visible, and to couple to a catalyst, generally metal-based, to promote the OER (or HER) reaction.<sup>4,5</sup> This molecular approach to the construction of PEC cells (or dye-sensitized-PEC (DS-PEC)) for water splitting, is an emerging line of research inspired by the technology of photovoltaic cells (dye-sensitized solar cells (DS-SC)).<sup>6</sup> OER or HER catalysts are either a metal oxide nanoparticles or a molecular transition metal complexes bound or co-adsorbed with the PS.<sup>1,5,7,8</sup>

At present, only about ten examples of “hybrid” photoanodes associating a molecular photosensitizer to a metal(oxide) catalyst have been published.<sup>3-5,9-19</sup> These photoanodes couple the benefit of the high stability of metal (oxide) catalysts compared to molecular catalysts and the excellent properties of visible-light absorbing molecular PS. In this bibliographic chapter, we will summarize these relatively recent studies.

As we will see, basically, these “hybrid” photoanodes consist of a transparent doped semiconductor (SC) electrode (Indium Thin Oxide (ITO) or Fluoride Thin oxide (FTO)) that can

be covered or not with another n-type semi-conductor such as  $\text{TiO}_2$ ,  $\text{SnO}_2$  or  $\text{WO}_3$  on which are co-adsorbed, generally in mono-layer, a molecular chromophore as well as metal oxide (nano)particles ( $\text{IrO}_x$ ,  $\text{CoO}_x$ ,  $\text{Ni}_{0.5}\text{Co}_{0.5}\text{O}_x$  or  $\text{Co}_3\text{O}_4$ ) deposited by a chemical way or co-adsorbed. Ru-tris-bipyridine<sup>10-13</sup> or organic dye including heptazine,<sup>14</sup> perylene,<sup>15-17</sup> naphthalen,<sup>18</sup> or porphyrin free base have been employed as PS.<sup>19</sup>

The electrochemical potential diagram of this kind of DS-PEC for water oxidation is schematized in Figure 1.

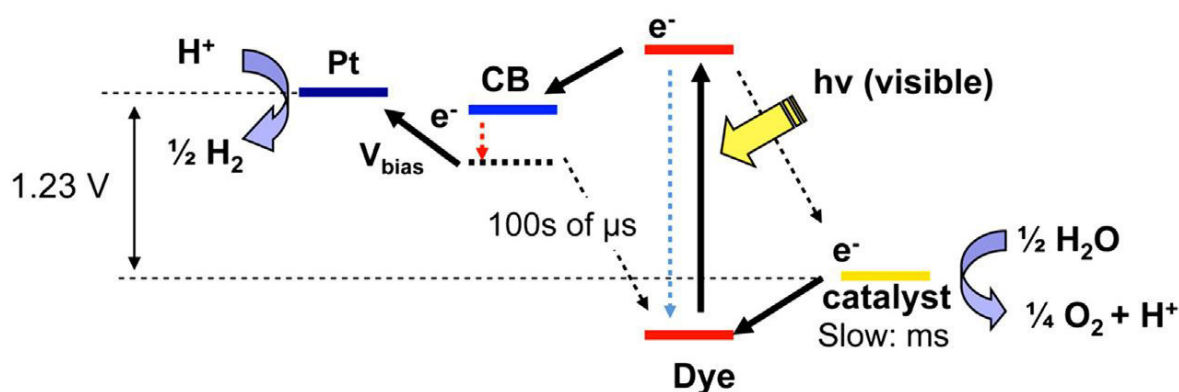


**Figure 1.** Electrochemical potential diagrams for a water-splitting dye-sensitized solar cell (DS-SC) (reproduced from ref <sup>5</sup> with the permission from Elsevier, Copyright 2017)

The light absorption by the dye molecule leads to an excited state ( $\text{dye}^*$ ), followed by a fast injection of the excited electron into the conduction band (CB) of the nanostructured semi-conductor ( $\text{TiO}_2$ ,  $\text{SnO}_2$  or  $\text{WO}_3$ ), resulting in an oxidized dye ( $\text{dye}^+$ ). In the absence of a photocathode to drive water reduction for instance, the application of a bias to the DS-PEC photoanode is required in order to take the electrons injected in the CB of the SC. If the lifetime of this charge separated state ( $\text{dye}^+/\text{e}^-$  in CB of the SC) is sufficiently long, an electron transfer from the  $\text{MO}_x$  nanoparticles catalyst to the oxidized dye occurs. Since the water oxidation required four electrons, the catalyst need to accumulate four holes in order to oxidize water. Catalytic water oxidation is typically slow (millisecond timescale), too slow to compete effectively with back electron transfer on the 100s of microseconds timescale. Thus, low quantum yields for water splitting – typically 1–2% – are a consequence of the fast kinetics of charge recombination, which competes effectively with the catalytic oxidation of water.<sup>5</sup>

In this chapter, the examples of hybride photoanodes with Ru as PS will be described first, then those with an organic chromophore.

## 2- Hybrid photoanodes with a Ru-tris-bipyridine derivative as photosensitizer

Three examples of hybrid photoanode using a ruthenium tris-bipyridine derivative as photosensitizer have been recently published.<sup>10–13</sup>

In 2009, Mallouk and coworkers<sup>10</sup> design an heteroleptic Ru tris-bipyridine complex with one bipyridine substituted by two phosphonate groups and another one substituted by a bidentate carboxylic acid (malonate) group. The phosphonate groups of the dye allows the adsorption of the dye onto porous nanocrystalline TiO<sub>2</sub> semi-conductor (SC) while the malonate links the hydrated iridium oxide nanoparticles IrO<sub>2</sub>•nH<sub>2</sub>O, that was used as efficient water oxidation catalyst<sup>20</sup> (Figure 2). Before its adsorption onto TiO<sub>2</sub>, the dye-IrO<sub>2</sub>•nH<sub>2</sub>O assembly was first chemically synthesized, the malonate acting as a stabilizer to the nanoparticles allowing to control their size and polydispersity and this results in well dispersed particles of ~ 2 nm of diameter.

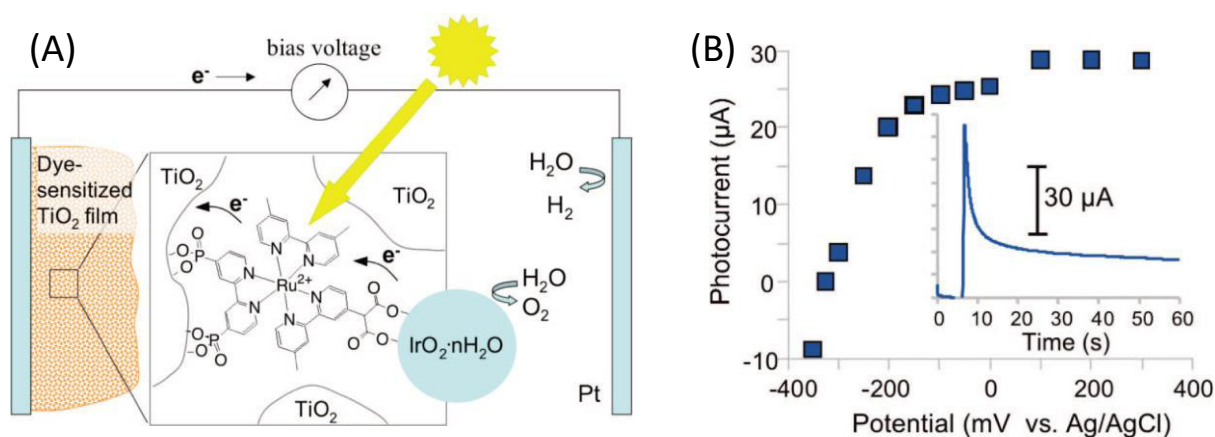


**Figure 2.** (A) Schematic representation of water splitting dye sensitized solar cell developed by Mallouk and coworkers<sup>10</sup> based on a hybrid photoanode FTO/TiO<sub>2</sub>/Ru-IrO<sub>2</sub>•nH<sub>2</sub>O nanoparticles. (B) Corresponding steady-state photocurrent in function of the applied potential and transient photocurrent recorded at 0 mV vs Ag/AgCl in function of time (inset) in an aqueous buffered solution at pH 5.75 (reproduced from ref<sup>10</sup>, with the permission from the American Chemical Society, Copyright 2009).

The measurements were carried out in a photoelectrochemical cell, composed of the working electrode of FTO/TiO<sub>2</sub> sensitized with Ru-IrO<sub>2</sub>•nH<sub>2</sub>O, a Pt wire counter electrode and an Ag/AgCl reference electrode, immersed in an aqueous buffered solution (30 mM Na<sub>2</sub>SiF<sub>6</sub> and NaHCO<sub>3</sub>) at pH 5.75. The schematic design of the water splitting dye sensitized solar cell (DSSC) is shown in Figure 2.

Irradiation of the working electrode with visible light ( $\lambda > 410$  nm) produced a measurable photocurrent at potentials more positive than -325 mV vs Ag/AgCl (Figure 2(B)). However,

once the measurement was carried out at each potential, the anodic current spike observed decayed rapidly into a steady current (typically 10 – 30  $\mu\text{A}$  vs 1 – 2  $\mu\text{A}$  with unsensitized  $\text{TiO}_2$ ). Under steady illumination, the current decayed over a period of approximately 4 hours. The decay in photocurrent is accompanied by a bleaching of the dye sensitized and visible absorbance of the film. A small bias to reach overall water splitting is needed in such system, because electrons in trap states below of the  $\text{TiO}_2$  conduction band edge are not enough reductive to generate  $\text{H}_2$  and rapidly recombine. A semiconductor with a more negative conduction band potential or the reduction of recombination rate of trapped electrons will allow achieving overall water splitting without applied bias. Finally, the photocurrent measured using 450 nm light at 7.8  $\text{mW cm}^{-2}$  intensity was of 12.7  $\mu\text{A cm}^{-2}$ , corresponding to an internal quantum yield of  $\sim 0.9\%$ . The production of hydrogen and oxygen was confirmed by gas chromatography and for oxygen also by using a pseudo-clark electrode. The current efficiency for the photoanodic oxygen generation was  $\sim 20\%$ . After approximately 4h, the total photocurrent produced corresponds to a turnover of 16 per dye molecule. The low quantum yield efficiency is the result of a slow electron transfer from the  $\text{IrO}_2 \cdot n\text{H}_2\text{O}$  nanoparticles to the oxidized dye, which was measured as six times slower than the back-electron transfer of the trapped state of the  $\text{TiO}_2$  SC to the photo-oxidized dye (from the  $\text{TiO}_2$  to the photo-oxidized dye).

The quantum yield for water splitting in dye-sensitized electrodes is low since the charge recombination reaction is faster than the catalytic four-electron oxidation of water oxidation. For this reason, in a consecutive work, Mallouk and coworkers<sup>11</sup> improved the quantum yield of the dye sensitized electrode to 2.3%, *i.e.* by more than a double, by incorporation of an electron transfer mediator, the benzimidazole-phenol (BIP), to separate the donor ( $\text{IrO}_x$  particles and the acceptor (Ru dye)), mimicking the tyrosine-histidine pair present in photosystem II (Figure 3(A)). As in the nature, for this photosynthetic system, the mediator molecule intermediates the electron transfer between a slow metal oxide catalyst that oxidizes water in milliseconds and a dye molecule that is oxidized by a fast light-induced electron transfer reaction. To achieve the structure, colloidal  $\text{IrO}_x$  particles were bound to the BIP mediator and to 2-carboxyethylphosphonic acid (CEPA) which is also used as anchoring molecule onto the  $\text{TiO}_2$  SC electrode. An extra step in the usual preparation of the nanoparticles was added to include the CEPA in view to link them easily to the  $\text{TiO}_2$ . Characterization by UV-visible spectroscopy of CEPA capped  $\text{IrO}_x$  with and without the BIP electron mediator, **1**- $\text{IrO}_x \cdot n\text{H}_2\text{O}$  (CEPA-capped  $\text{IrO}_x$  and of **2**- $\text{IrO}_x \cdot n\text{H}_2\text{O}$  (BIP- and CEPA-

capped  $\text{IrO}_x$ ), respectively showed a broad absorbance at 580 nm, typical of Ir(IV) oxide nanoparticles. TEM characterization showed irregular nanoparticles of 2 nm for both,  $1\text{-IrO}_x \cdot n\text{H}_2\text{O}$  and  $2\text{-IrO}_x \cdot n\text{H}_2\text{O}$ .

By contrast to the previous photoanode developed by this group,<sup>10</sup> the functionalized  $\text{IrO}_x$  nanoparticles are coadsorbed onto  $\text{TiO}_2$  electrode with the ruthenium polypyridyl sensitizer, that possess in this case three bipyridine ligands substituted by one phosphonate group (**3P-Ru**) (Figure 3(A)).

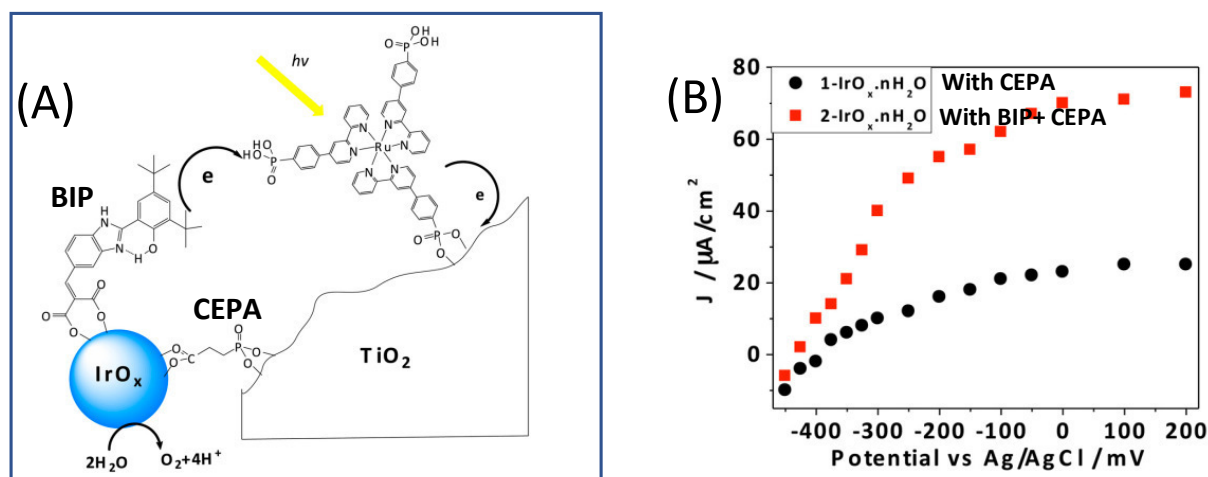


**Figure 3.** (A) Schematic representation of the electron transfer reactions in the mediator-based, dye-sensitized FTO/ $\text{TiO}_2$  photoanode developed by Mallouk and coworkers<sup>11</sup> showing the molecular structures of Benzimidazole-phenol (BIP) mediator, **3P-Ru** dye and 2-carboxyethylphosphonic acid (CEPA) anchoring group. (B) Corresponding steady-state photocurrent density in function of the anode potential for coadsorbed **3P-Ru** and  $1\text{-IrO}_x \cdot n\text{H}_2\text{O}$  or  $2\text{-IrO}_x \cdot n\text{H}_2\text{O}$  in an aqueous buffered solution at pH 5.8 (reproduced from ref <sup>11</sup>, with the permission from the National Academy of Sciences of the United states of America, Copyright 2012).

In presence of co-adsorbed **3P-Ru** on  $\text{TiO}_2$ , the comparison of the photocurrent intensity with  $\text{IrO}_x$  nanoparticles with ( $2\text{-IrO}_x \cdot n\text{H}_2\text{O}$ ) and without ( $1\text{-IrO}_x \cdot n\text{H}_2\text{O}$ ) the BIP electron mediator was made (Figure 2(B)). At pH 5.8 and for an overpotential ( $\eta$ ) of -0.69 V (0 V vs Ag/AgCl), a steady-state photocurrent density up to 80  $\mu\text{A cm}^{-2}$  is observed in the presence of the BIP mediator, with a stability over 100 s. In the absence of mediator, a photocurrent of only 25  $\mu\text{A cm}^{-2}$  was obtained (thus around three times lower), a comparable value to the previous results obtained with the heteroleptic Ru tris(bipyridyl) dye.<sup>10</sup> In addition, without BIP, the photocurrent is less stable. This result is in agreement with faster electron transfer between the  $\text{IrO}_x \cdot n\text{H}_2\text{O}$  nanoparticles with the **3P-Ru** when the catalyst nanoparticles are covered by BIP mediator. On the other hand, by using 450 nm of light at 4.5  $\text{mW cm}^{-2}$  of intensity, the steady state photocurrent densities were 29.1 and 10.1  $\mu\text{A cm}^{-2}$  for nanoparticles with and without mediator, corresponding to 2.3% and 0.8% of internal quantum yield, respectively. A

faradaic efficiency for oxygen evolution  $\geq 85\%$  was obtained by Clark electrode measurements for both  $1\text{-IrOx}\cdot n\text{H}_2\text{O}$  and  $2\text{-IrOx}\cdot n\text{H}_2\text{O}$ . One drawback of the coadsorption showed in Figure 3, is the absence of control of the juxtaposition of the sensitizer and BIP-catalyst onto the  $\text{TiO}_2$  surface. The electron transfer rate between the BIP mediator and  $3\text{P-Ru}$  dye is thus not well controlled, due to the fact that both molecules were separately adsorbed onto the  $\text{TiO}_2$  electrode surface.<sup>11</sup>

By contrast to these two reported examples of photoanodes made of ruthenium dyes and iridium oxide nanoparticles as water oxidation catalyst,<sup>10,11</sup> Na and co-workers<sup>13</sup> developed sensitized ruthenium  $\text{TiO}_2$  photoanodes using an earth abundant metal oxide as water oxidation catalyst, consisting of functionalized cobalt oxide nanoparticles ( $\text{Co}_3\text{O}_4$ ) (Figure 4(A)). In this work, a new strategy to introduce nanoparticles water oxidation catalyst within dye sensitized photoelectrochemical cell for water splitting was investigated. Indeed, nanoparticles of  $\text{Co}_3\text{O}_4$  were first synthesized and subsequently modified by 3-aminopropyltriethoxysilane (APTES). Then, the functionalized  $\text{Co}_3\text{O}_4$  were integrated to ruthenium dye sensitized (**RuP**) photoelectrode by a fast Schiff base reaction. The Ru dye was first adsorbed onto mesoporous  $\text{TiO}_2$  via two phosphonate groups of one bipyridine ligand.

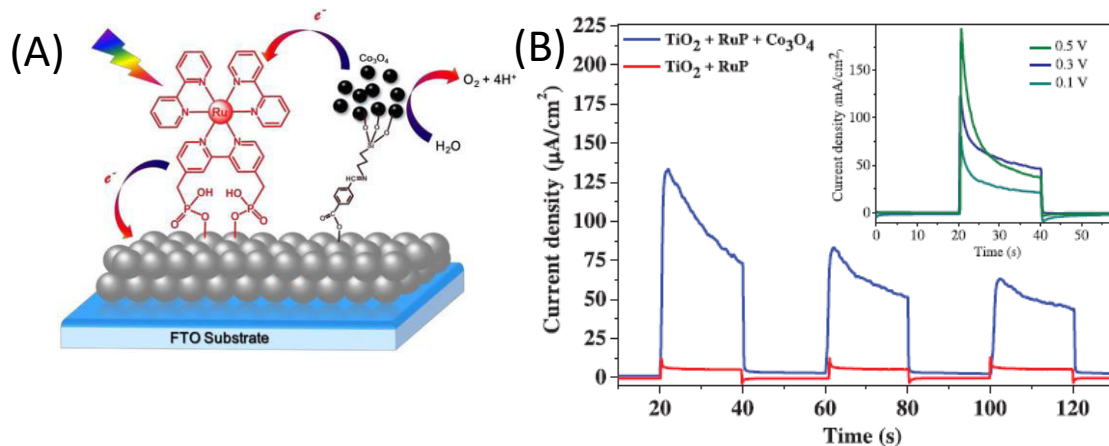


**Figure 4.** (A) Schematic representation of the hybrid photoanode developed by Na and coworkers<sup>13</sup> based on a  $\text{FTO/RuP/Co}_3\text{O}_4$ . (B) Corresponding transient photocurrent in a phosphate buffer solution at pH 6.8 at different bias vs  $\text{Ag/AgCl}$  in function of the time (reproduced from ref <sup>13</sup>, with the permission from Elsevier, Copyright 2016).

Then, the modified  $\text{Co}_3\text{O}_4$  catalyst was adsorbed onto the dye sensitized  $\text{TiO}_2$  electrode. Figure 4(B) displays the photocurrent density in function of time under visible light irradiation (400 nm) at pH 6.8 in a phosphate buffer solution. The inset shows that the optimum bias applied is +0.3 V vs  $\text{Ag/AgCl}$  ( $\eta = -0.33$  V) producing a transient photocurrent density of  $135 \mu\text{A cm}^{-2}$ , decreasing to  $50 \mu\text{A cm}^{-2}$ . Irradiation of the  $\text{TiO/RuP}$  electrode without cobalt catalyst produces a photocurrent density less than  $15 \mu\text{A cm}^{-2}$  due to a fast

charge recombination of the slow rate of reaction of the oxidized **RuP** for water oxidation. Thus,  $\text{Co}_3\text{O}_4$  modified catalyst results in an improvement of 8 times for the photocurrent density of the photoanode in comparison to the absence of  $\text{Co}_3\text{O}_4$ , due to fast electron transfer from  $\text{Co}_3\text{O}_4$  to photooxidized **RuP** dye. However, the stability of this photoanode is not promising. Indeed, the photocurrent density decreased to  $50 \mu\text{A cm}^{-2}$  (i.e. 40 % of its initial value) after 3 cycles of 20 s ON-OFF illumination of  $\sim 100$  s.<sup>13</sup> This can be due to the prepared modified  $\text{Co}_3\text{O}_4$ , which is not able to give enough reductive equivalents to the oxidized dye causing the dye's decomposition or desorption.

In conclusion, hybrid photoanodes with ruthenium photosensitizers display photocatalytic activities at negative overpotentials, but the photocurrents are weak ( $< 100 \mu\text{A cm}^{-2}$ ) and generally not stable.

### 3- Hybrid photoanodes with an organic chromophore

#### 3.1. Heptazine chromophore

In 2012, Beranek and coworkers<sup>14</sup> studied the photooxidation of water to oxygen using a hybrid photoanode of  $\text{TiO}_2$ -Polyheptazine ( $\text{TiO}_2$ -**PH**) with photodeposited Co-Pi ( $\text{CoO}_x$ ) cocatalyst under visible light irradiation (Figure 5(A)).

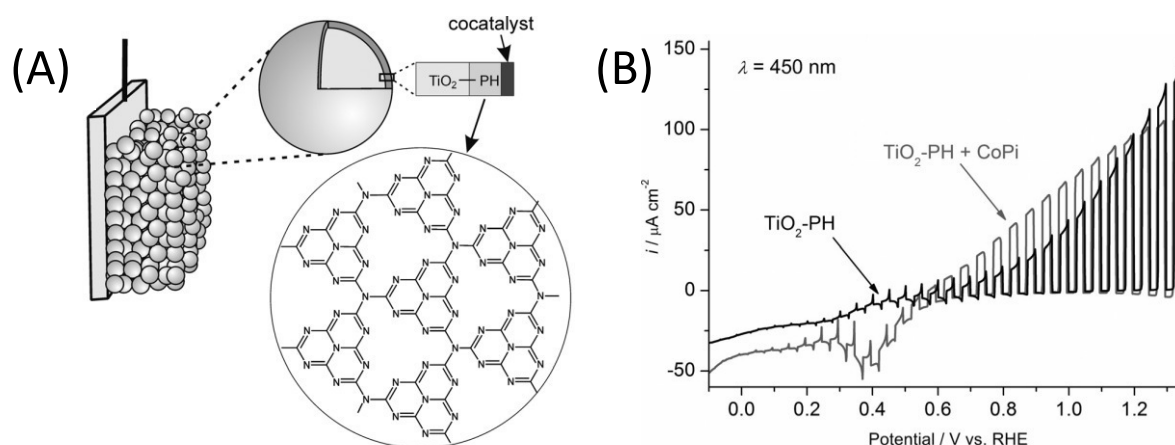


**Figure 5.** (A) Schematic representation of the hybrid photoelectrode developed by Beranek and coworkers<sup>14</sup> based on a layer of nanocrystalline  $\text{TiO}_2$  powder pressed onto an ITO electrode, sintered, with subsequent modified by polyheptazine (**PH**) and loaded with a of Co-Pi cocatalyst. (B) Corresponding transient photocurrent density measured at  $\text{TiO}_2$ -**PH** photoelectrodes with and without Co-Pi, under intermittent irradiation at  $\lambda = 450$  nm (5 s light, 5 s dark), at cathodic potential sweep of  $5 \text{ mV s}^{-1}$  in a deaerated phosphate buffer at pH 7 (reproduced from ref <sup>14</sup>, with the permission from Wiley, Copyright 2012).

The  $\text{TiO}_2$ -**PH** photoelectrodes were prepared and characterized and then loaded with Co-Pi photoelectrochemically in order to ensure that Co-Pi was formed preferentially at sites with

high concentration of photogenerated holes. The other advantage of such photoelectrochemical deposition is the control of the progress deposition by observing the photocurrent changes during the process and to fine tune the amount of Co-Pi deposited. The photoholes in the polyheptazine surface layer of TiO<sub>2</sub>-**PH** coupled effectively by Co-Pi co-catalyst. The Co-Pi also reduces the recombination of photogenerated charge at low bias potential, due to a better photooxidation kinetics that produced less holes accumulation. The latter is very important to reduce the need of external bias at hybrid photoanodes for water splitting. The photoconversion efficiency can be enhanced by increasing of effective catalytic sites for water oxidation on the surface of the hybrid photoanode. Scheme 5(B) displays the linear sweep voltammetry of the TiO<sub>2</sub>-**HP** with and without Co-Pi catalyst under on-off of visible light irradiation ( $\lambda = 450$  nm). TiO<sub>2</sub>-**HP**/Co-Pi photoanode produces a photocurrent density of  $\sim 50 \mu\text{A cm}^{-2}$  at +0.8 V vs RHE, with an  $\eta = -0.45$  V, higher than that of a simple TiO<sub>2</sub>-**PH**. TiO<sub>2</sub>-**HP**/Co-Pi photoanode shown a stability of 12 min at a potential of +0.4 V vs Ag/AgCl at neutral pH.<sup>14</sup>

### 3.2. Perylene chromophore

Three examples of hybrid photoanodes with perylene chromophores, have been recently published.<sup>15-17</sup> PDI are very interesting chromophore since they are robust with good thermal and photochemical stability, they possess a strong visible light absorption and they are relatively cheap. Many DPI exhibit also a highest occupied molecular orbital (HOMO) with a potential enough positive to oxidize water or to activate a metal oxide or a molecular water oxidation catalyst.<sup>21</sup> However, there are limited by a low oxidation potential at the excited state preventing efficient charge injection into the CB of many semi-conductors.<sup>17</sup> Thus their use in energy conversion schemes relies on the oxidative quenching of their excited state. All of these features make PDI very good candidates as sensitizer for water-splitting schemes.

The first example of an hybrid photoanode for water oxidation based on perylene dye was published Finke and co-workers<sup>15</sup> in 2014 (Figure 6(A)). To this aim, a novel perylene diimide (PDI) dye functionalized with two phosphonate groups on the imide positions (N,N'-bis(phosphonomethyl)-3,4,9,10-perylenediimide, denoted **PMPDI**) was synthesized. Thin films of **PMPDI** were deposited onto ITO electrodes by spin coating in basic aqueous solution and then the phosphonate groups were protonated by immersion in acidic solution to render the film insoluble in neutral or acidic medium. The CoO<sub>x</sub> was then photoelectrochemically deposited in view to improve water oxidation by applying a potential

of +700 mV vs Ag/AgCl during 5 min to the ITO/PMPDI immersed in a phosphate buffer at pH 7 containing 1mM of  $\text{Co}(\text{NO}_3)_2$  under illumination (Xe lamp,  $100 \text{ mWcm}^{-2}$ ). The photoelectrochemical process was chosen in view to preferentially depositing the catalyst in high concentration in photogenerated holes areas as previously described.<sup>14,22</sup>

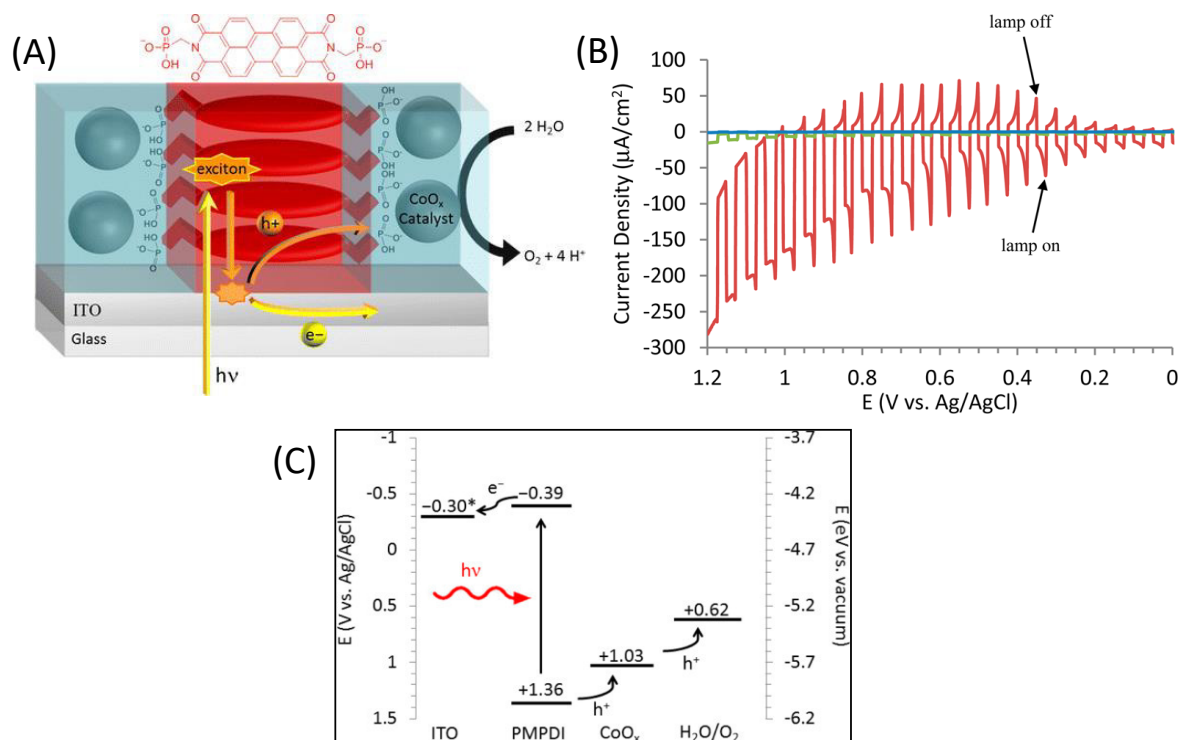


**Figure 6.** (A) Schematical representation of the hybrid photoanode developed by Finke and coworkers<sup>15</sup> based on a ITO/PMPDI/CoO<sub>x</sub> nanoparticles. (B) Corresponding transient photocurrent density in function of the applied potential measured with ITO/PMPDI/CoO<sub>x</sub> (red line), ITO/PMPDI (green line) and ITO bare (blue line) under intermittent irradiation (5 s light, 5 s dark), at cathodic potential sweep of  $5 \text{ mV s}^{-1}$  in a deaerated phosphate buffer at pH 7. Band diagram for the ITO/PMPDI/CoO<sub>x</sub> photoanode with the estimated energy levels (given vs Ag/AgCl), the actual potential \* of ITO (-0.3 V) corresponds to the bias applied in this study (C) (reproduced from ref<sup>15</sup>, with the permission from the American Chemical Society, Copyright 2014).

Visible-light assisted water oxidation was obtained with the ITO/PMPDI/CoO<sub>x</sub> electrodes with a photocurrent density  $150 \mu\text{A cm}^{-2}$  at an applied bias of +1.0 V vs Ag/AgCl in a phosphate buffer aqueous solution at pH 7 ( $\eta = 0.38 \text{ V}$ ), with a stability over 300 s. Figure 6(B) shows the linear sweep voltammetry of the ITO/PMPDI electrode with and without CoO<sub>x</sub>, and of the ITO bare, under on-off cycles of light irradiation. The oxidation of water was confirmed by the direct detection of O<sub>2</sub> obtained with a bias of +900 mV vs Ag/AgCl, which corresponds to a faradaic efficiency of  $80 \pm 15\%$ . The quantum efficiency for water oxidation was  $\sim 1\%$ . Almost none photocurrent was measured for bare ITO and relatively small photocurrents for ITO/PMPDI ( $< 10 \mu\text{A cm}^{-2}$ ) (Figure 6(B)).

When analogous photoanodes were prepared with a PDI derivative having two alkyl groups in place of the phosphonate groups of **PMPDI**, the photocurrent obtained were about one order of magnitude smaller than with the typical ITO/**PMPDI**/CoO<sub>x</sub>. This is due to the fact that, with this dye only traces of cobalt were deposited as shown by XPS measurements. These results provide evidence that the phosphonate groups of the **PMPDI** may be important for an efficient linking of the inorganic CoO<sub>x</sub> catalyst to the organic dye.

Although the ITO/**PMPDI**/CoO<sub>x</sub> anodes are capable of light-assisted water oxidation, their efficiency are limited by low light harvesting (LHE) (only about 12% of incident light is adsorbed by the thin **PMPDI** films) and low charge transfer efficiency as well as charge recombination. However, thicker films absorbed more light but showed lower photocurrents, due to the low exciton diffusion lengths of this organic material. The authors proposed that this limitation could be solved by using a dye-sensitized mesoporous semiconductor, which can absorb more light due to its higher surface area, by keeping the monolayer dye thickness. Despite the limitations, this was the first time that water oxidation can be achieved photochemically by a thin film monolayer of molecular organic semiconductor coupled to a water oxidation catalyst.

In view to improve the performance of their photoanodes, in a subsequent work, Finke and co-workers<sup>16</sup> introduced a semi-conductor, consisting of a nanostructured metal oxide of TiO<sub>2</sub>, SnO<sub>2</sub> or WO<sub>3</sub>, to design a device of the type dye sensitized photoelectrolysis cell (DS-PEC) (see Figure 1). These SCs, deposited onto FTO electrodes, were sensitized with the same **PMPDI** dye (Figure 7(A)). To increase the stability, the **PMPDI** was chemisorbed via one of the phosphonate groups onto the SCs surfaces, and not spin-coated as in their previous work.<sup>15</sup> The driving force for the electron injection from the photoexcited dye, **PMPDI\*** into the conduction band (CB) of the different SCs (the CB energies were estimated by electrochemical photocurrent method)<sup>23</sup> increases in the order TiO<sub>2</sub> < SnO<sub>2</sub> < WO<sub>3</sub> (Figure 7(C)), and thus it is expected that the photocurrent will follow the same trend. However, the adsorption of **PMPDI** dye was less efficient on SnO<sub>2</sub> than onto TiO<sub>2</sub> and not at all effective onto WO<sub>3</sub>. Anyway, when tested with a sacrificial reductant as hydroquinone (H<sub>2</sub>Q) (20 mM) in aqueous phosphate buffer at pH 7 with a bias at +0.2 V, the photocurrent produced by TiO<sub>2</sub>/**PMPDI** was much lower than that measured with SnO<sub>2</sub>/**PMPDI**, this latter reaching 1100 μA cm<sup>-2</sup> with a 99% of LHE at 490 nm.

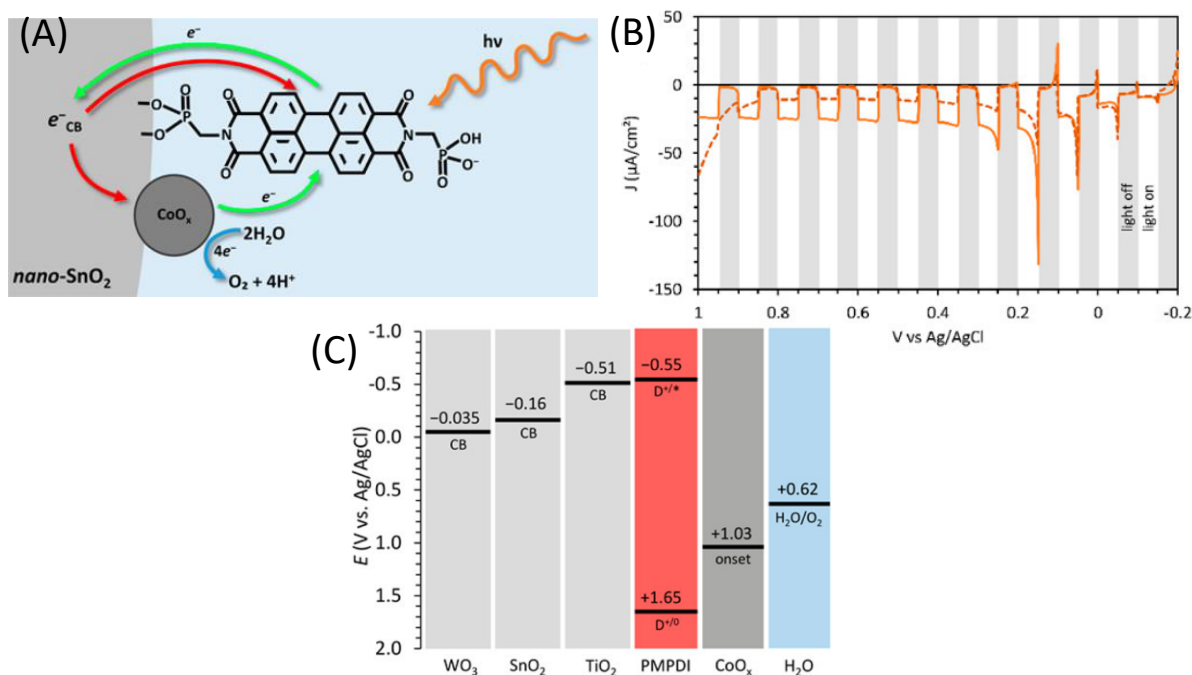


**Figure 7.** (A) Schematic representation of the hybrid photonode developed by Finke and coworkers<sup>16</sup> based on a FTO/SnO<sub>2</sub>/PMPDI/CoO<sub>x</sub> nanoparticles (red arrows correspond to recombination). (B) Corresponding transient photocurrent density in function of the applied potential for FTO/SnO<sub>2</sub>/PMPDI anode before (solid line) and after (dashed line) photoelectrochemical deposition of CoO<sub>x</sub> under intermittent irradiation (5 s white light transients), at cathodic potential sweep of 10 mV s<sup>-1</sup> in a deaerated phosphate buffer at pH 7. Estimated energy diagram for the MO<sub>x</sub>/PMPDI/CoO<sub>x</sub> system at pH 7 (C) (reproduced from ref<sup>16</sup>, with the permission from the American Chemical Society, Copyright 2017).

Thus, the CoO<sub>x</sub> water oxidation catalyst was then deposited photoelectrochemically on the SnO<sub>2</sub> substrate (Figure 7(A)), following a similar photoelectrochemical procedure used in their previous work (see above) except that a lower potential is applied in present of SnO<sub>2</sub> (+0.2 V vs Ag/AgCl). This potential is not enough positive to directly oxidize the Co(II) but sufficiently positive for the SnO<sub>2</sub>  $E_{CB}$  to collect photoinjected electrons. Unfortunately, the transient photocurrent density measured with the FTO/SnO<sub>2</sub>/PMPDI/CoO<sub>x</sub> photoanode ( $\sim 10 \mu\text{A cm}^{-2}$  (between +0.2 and +0.9 V vs Ag/AgCl ( $\eta = -0.27$  to +0.18 V)) at pH 7 decreases by a factor of 2-3 compared to that obtained without CoO<sub>x</sub> deposition ( $40 \mu\text{A cm}^{-2}$  that decreases to  $20 \mu\text{A cm}^{-2}$  over 5 min), and this corresponds to a faradaic yield of  $\sim 31\%$ . This yield is lower than of their previous ITO/PMPDI/CoO<sub>x</sub> photoanode<sup>15</sup> due to enhance charge recombination between CoO<sub>x</sub> more likely deposited directly at the SnO<sub>2</sub> surface and photoinjected electrons in SnO<sub>2</sub> (Figure 7(A)). Since O<sub>2</sub> was detected only with CoO<sub>x</sub>, the origin of photocurrent with FTO/SnO<sub>2</sub>/PMPDI could result for partial decomposition of the dye, oxidation of water to H<sub>2</sub>O<sub>2</sub> and/or of impurities species in solution.

This SnO<sub>2</sub>/PMPDI/CoO<sub>x</sub> system was the second example in the literature of a DS-PEC composed only by earth-abundant materials to successfully oxidize water (the first example was the TiO<sub>2</sub>-HP/Co-Pi published in 2012 by Beranek,<sup>14</sup> see above). From these results, the authors underline the importance of maintaining the water oxidation catalyst far away from the SC and not adsorbed on it, to prevent back recombination reactions.

In 2015, Bignozzi and coworkers<sup>17</sup> reported a water-oxidation DS-PEC consisting of a nanocrystalline WO<sub>3</sub> film sensitized with a cationic **PDI-N** dye ((N,N'-Bis(2-(trimethylammonium)-ethylene) perylene 3,4,9,10-tetracarboxylic acid bisimide)(PF<sub>6</sub>)<sub>2</sub>) and codeposited with IrO<sub>2</sub> as water oxidation catalyst (Figure 8(A)). This dye is oxidized at a potential of 1.7 V vs SCE and reduced at -0.8 V vs SCE in acetonitrile with a spectroscopic band gap of 2.36 eV resulting in an excited state oxidation potential of -0.66 V vs SCE. A spontaneous adsorption of this dye on the surface of the SC via aggregation and hydrophobic forces was observed. The IrO<sub>2</sub> nanoparticles were codeposited by different methods (Figure 8(B)), namely drop casting (b), spin coating (c), spin coating and drying in warm air (d) and soaking (e). Under irradiation by visible light at  $\lambda > 435$  nm, all electrodes exhibit a photocurrent at a bias of +0.5 V in aqueous solution at pH 3, which increases in the order, a < b < c < d < e (type a, without IrO<sub>2</sub>), consistent with electron transfer to the photogenerated oxidized state of the dye (**PDI-N**<sup>+</sup>) from IrO<sub>2</sub>, which in turn catalyzes water oxidation (Figure 8(A)). The transient photocurrent density under on-off illumination as shown in Figure 8(B) can reach  $\sim 200 \mu\text{A cm}^{-2}$ , at a potential close to +0.5 V vs SCE (0.55 V vs Ag/AgCl,  $\eta = -0.3$  V), for the best electrodes (type c and d), which corresponds to an enhancement of about 4-fold compared to without IrO<sub>2</sub> (type a). The enhancement in photoanodic current is due to a hole transfer from oxidized dye to IrO<sub>2</sub> with a rate around microsecond. As observed in Figure 8(B), the transient photocurrents rapidly decrease due to recombination processes and competition of hole transfer with the electrolyte. The charge kinetic transfer at 430 nm, was studied demonstrating that the codeposition of IrO<sub>2</sub> reduces the lifetime of the photooxidized sensitizer on WO<sub>3</sub> surface at 0.5  $\mu\text{s}$ . The latter hole transfer kinetics to IrO<sub>2</sub> occurs at the same time scale of the electron recapture by **PDI-N**<sup>+</sup>, and follows a first order with a constant rate of  $0.95 \times 10^6 \text{ s}^{-1}$ .

Other semi-conductors were tested including TiO<sub>2</sub> and SnO<sub>2</sub>, but the charge injection on WO<sub>3</sub> was found to be more efficient than on SnO<sub>2</sub>, although both SCs have similar conduction band energy.

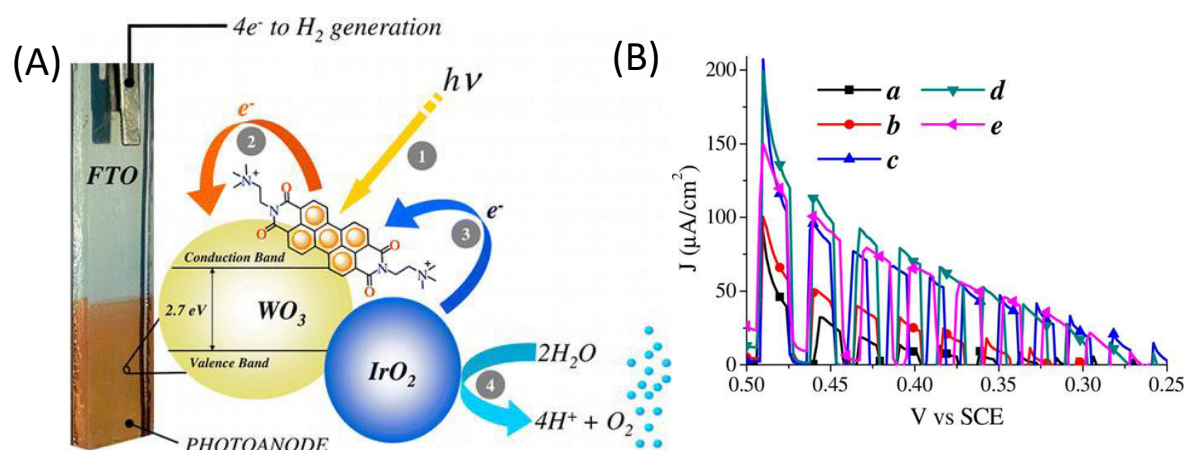


**Figure 8.** (A) Hybrid photoanodes developed by Bignozzi and coworkers<sup>17</sup> based on a FTO/ $\text{WO}_3$ /PDI-N- $\text{IrO}_x$  nanoparticles. (B) Corresponding transient photocurrent in function of the applied potential for electrodes a-e, with irradiation visible light at 435 nm cut off in aqueous 0.1M  $\text{NaClO}_4$  solution pH 3. Electrodes with different deposition method of  $\text{IrO}_2$  NPs on  $\text{WO}_3$ : a-without  $\text{IrO}_2$  NPs, b-drop casting, c-spin coating, d-spin coating and drying with warm air, and e-soaking (reproduced from ref<sup>17</sup>, with the permission from the American Chemical Society, Copyright 2015).

In general, hybrid photoanodes with perylene dyes need significant overpotentials or to be associated with a low band gap semiconductor (as  $\text{WO}_3$ ) for obtaining high photocurrents ( $> 100 \mu\text{A cm}^{-2}$ ).

### 3.3. $\pi$ -Conjugated polymer naphthalene based chromophore

In 2015, Sivula and coworkers<sup>18</sup> investigated a n-type  $\pi$ -conjugated polymer as organic dye, the poly[benzimidazobenzophenanthroline], **BBL**, to be used in a direct semi-conductor-liquid junction configuration for solar water oxidation (Figure 9(A)). **BBL** is known for its exceptional stability<sup>24</sup> and good electron mobility.<sup>25</sup> **BBL** films were prepared on FTO electrodes by a spray deposition method from an aqueous **BBL** nanofibers dispersion. Under intermittent simulated solar illumination ( $100 \text{ mW cm}^{-2}$ ) in buffered aqueous solution at pH 7, a photocurrent density up to  $230 \mu\text{A cm}^{-2}$  at 1.23 V vs RHE was obtained in the presence of a hole scavenger ( $\text{SO}_3^{2-}$ ), with an optimized nanostructured film thickness of 120 nm. The  $\text{SO}_3^{2-}$  oxidation allows the investigation of the PEC properties of the **BBL** dye with minimum kinetic limitations. The FTO/**BBL** film was also investigated without  $\text{SO}_3^{2-}$  in aqueous solution at different pH from 3.5 to 10.5. It was found that the photocurrent density increases with increasing pH (from  $\sim 10$  to  $30 \mu\text{A cm}^{-2}$  at +1.23 V vs RHE) but no  $\text{O}_2$  evolution was detected and no evidence of semi-conductor oxidation after 30 min was observed. Instead the photooxidation reaction was found to be a two-electrons oxidation of water by the bare film into  $\text{H}_2\text{O}_2$  which in turn is reduced at the anode to produce the hydroxyl radical ( $\bullet\text{OH}$ ). This later was quantified by fluorescence test.

In view to drive the four electron oxidation of water, an OER catalyst consisting of Ni-Co nanoparticles, has been directly attached to the **BBL** surface. However no  $O_2$  was produced due to the poor catalyst attachment. The successful attachment of the catalyst was obtained when the **BBL** film is pretreated with a thin layer of  $TiO_2$  ( $\sim 1\text{nm}$ ) acting as tunnel junction. Even if the application of  $TiO_2$  did not result in a significant change of the observed photocurrent density (from  $\sim 10 - 20 \mu\text{A cm}^{-2}$ ) a slight increase (up to  $\sim 30 \mu\text{A cm}^{-2}$ ) was observed upon application of the catalyst layer (Figure 9(B)). Molecular  $O_2$  was confirmed by gas chromatography during constant illumination chronoamperometry measurements ( $I \sim 10 \mu\text{A cm}^{-2}$ ) with a faradaic yield of  $82 \pm 16\%$ .

Finally, this study demonstrated for the first time that robust  $\pi$ -conjugated organic semiconductors are suitable for direct PEC water oxidation opening new perspectives for the design and optimization of photoanodes for solar water splitting.

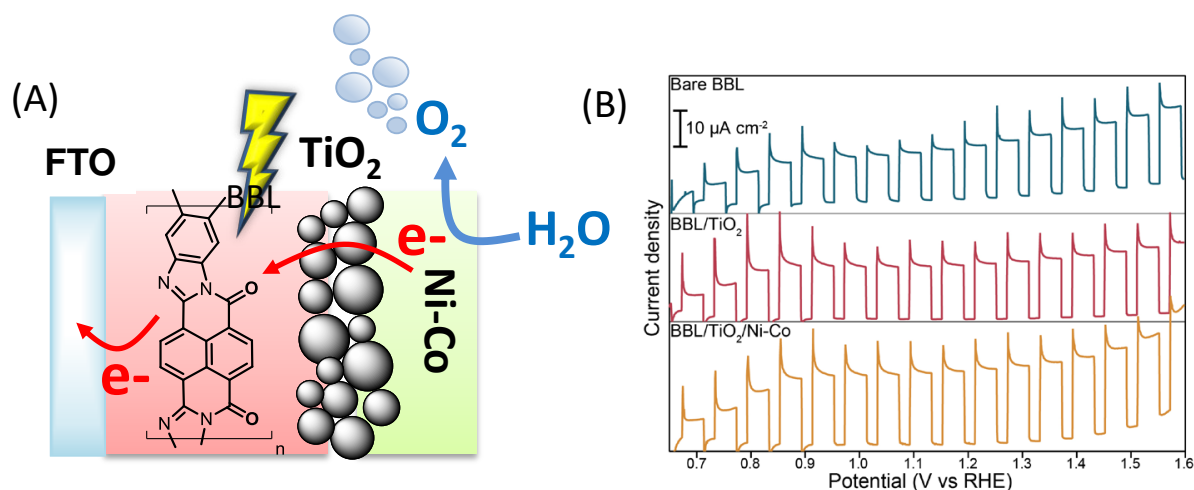


**Figure 9.** (A) Hybrid photoanodes developed by Sivula and coworkers<sup>18</sup> based on a FTO/**BBL**/ $TiO_2$ /Ni-Co nanoparticles (**BBL** = poly(benzimidazobenzophenanthroline)). (B) Corresponding transient photocurrent density in function of the applied potential for spray deposited film of **BBL** (230 nm thickness), before and after  $TiO_2$  deposition, and after catalyst codeposition in aqueous phosphate buffer at pH 7 (reproduced from ref<sup>18</sup>, with the permission from the American Chemical Society, Copyright 2015).

### 3.4. Porphyrin free base chromophore

In 2015, Mallouk and co-workers<sup>19</sup> reported the first example of a functioning water-splitting DS-PEC using organic free-base porphyrin sensitizers (Figure 10(A)). A series of metal-free porphyrins with different number and type of substituents were synthesized which exhibit Soret bands at  $\sim 410\text{ nm}$ , with high extinction coefficients ( $>10^5 \text{ M}^{-1}\text{cm}^{-1}$ ). Adsorbed on  $TiO_2$  via a carboxylate substituent, the oxidation of these sensitizers was electrochemically irreversible ( $E_{p_a}$  in the range  $+1.02$  to  $+1.29 \text{ V vs Ag/AgCl}$ ), although for some of them, presents reversible systems in nonaqueous solutions. Despite the variability of their spectral

and electrochemical properties, the majority of these porphyrins when are used to sensitize  $\text{TiO}_2$  electrodes, exhibit significant photocurrent with quite similar intensity under full visible illumination ( $>410$  nm) or red illumination ( $>590$  nm) with co-adsorbed  $\text{IrO}_2$  as water oxidation catalyst. Direct observance of  $\text{O}_2$  with a faradic yield close to 100% demonstrates that the photocurrent corresponds to water oxidation. The better results were obtained with the porphyrins substituted in meso position, **DMEP**. The photocurrent density measured at a bias of 0.1 V vs Ag/AgCl during 10 min under visible irradiation, and the corresponding integrated charge passed are shown in Figure 10(B)). Despite the poor stability of the photocurrent, UV-Vis spectra of the electrodes before and after photoelectrolysis show generally no change underlying the stability of base-free porphyrin dyes.

Finally, these free-base porphyrin sensitized electrodes generated roughly half of the photocurrent of analogous  $[\text{Ru}(\text{bpy})_2(4,4'-(\text{PO}_3\text{H}_2)(\text{bpy}))]$ , under visible irradiation ( $>410$  nm) although these latter are not active under red illumination. Although the hole transport and injection of porphyrin sensitizers are poor compared to ruthenium polypyridyl sensitizers, back electron transfer recombination are much slower with porphyrin sensitizers.

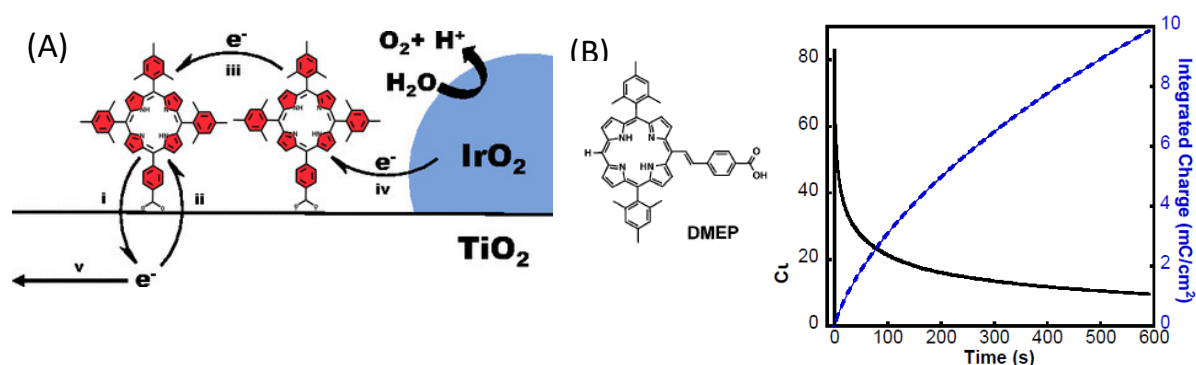


**Figure 10.** (A) Hybrid photoanode developed by Mallouk and coworkers<sup>19</sup> based on a  $\text{TiO}_2$ /porphyrin/ $\text{IrO}_2$  nanoparticles; the five steps of electron transfer process in such water-splitting DS-PEC are: (i) injection, (ii) recombination, (iii) hole transfer, (iv) regeneration of oxidized sensitizer, and (v) transport to the fluorine-doped tin oxide anode. (B) Representative photocurrent density and integrated charge in function of time for a **DMEP** sensitized electrode under illumination at  $\lambda \geq 410$  nm in phosphate buffer at pH 6.8 under an applied potential of  $E = +0.1$  V vs Ag/AgCl (reproduced from ref<sup>19</sup>, with the permission from the the National Academy of Sciences of the United states of America, Copyright 2015).

As for the  $\pi$ -conjugated polymer DS-PEC published by Sivula,<sup>18</sup> these hybrid photoanodes with **free base porphyrins** do not exhibit significant photocurrents ( $< 40 \mu\text{A cm}^{-2}$ ) and present a poor stability over time.

## 4 – Conclusion

This bibliographic chapter give an overview of the few examples of hydride photoanodes for light-driven water oxidation already published combining a molecular chromophore to a metal oxide as catalyst for water oxidation. Since the introduction of the first example published by Mallouk in 2009, much of the effort in re-design photoanodes has focused on improving the quantum yield by slowing down back electron transfer as well as to substitute the ruthenium polypyridyl sensitizers by organic sensitizers involving only earth abundant elements.

However, although these Ru- and organic dyes sensitized hybrid photoelectrodes are active in neutral or weakly acidic medium, demonstrating their potential for the OER reaction, they are poorly stable and exhibit fairly low photocurrents ( $150\text{-}200\ \mu\text{A cm}^{-2}$  for perylene derivatives and  $<20\ \mu\text{A cm}^{-2}$  for the other examples). The low photocurrent density has been mainly attributed to fast kinetics of back electron transfer (charge recombination) which competes effectively with the slow catalytic oxidation of water and the slow electron transfer kinetics between the PS and the metal oxide inorganic catalyst.

To improve the efficiency of these water-splitting PECs, the challenge is still to avoid the charge recombination reactions and also to accelerate the water oxidation reaction.

Finally, it should be stressed that in these published water-splitting PECs exemples, the amount of sensitizers and metal oxide catalysts deposited at the surface of the electrodes are weak and not well-controlled. Photosensitizers are generally adsorbed in a monolayer. To go one step further, it will be very interesting to explore novel methods of fabrication and of deposition of photosensitizers/metal oxide nanoparticles deposited at the surface of the electrodes and thus evaluate the effect of increasing the amount of materials and of the structuration of the film and their photocurrent intensity.

## REFERENCES

- (1) Yu, Z.; Li, F.; Sun, L. *Energy Environ. Sci.* **2015**, *8* (3), 760–775.
- (2) Prévot, M. S.; Sivula, K. *J. Phys. Chem. C* **2013**, *117* (35), 17879–17893.
- (3) Swierk, J. R.; Mallouk, T. E. *Chem. Soc. Rev.* **2013**, *42* (6), 2357–2387.
- (4) Youngblood, W. J.; Lee, S. A.; Maeda, K.; Mallouk, T. E. *Acc. Chem. Res.* **2009**, *42* (12), 1966–1973.
- (5) Xu, P.; McCool, N. S.; Mallouk, T. E. *Nano Today* **2017**, *14*, 42–58.
- (6) Gratzel, M. *Acc. Chem. Res.* **2009**, *42* (11), 1788–1798.
- (7) Brennaman, M. K.; Dillon, R. J.; Alibabaei, L.; Gish, M. K.; Dares, C. J.; Ashford, D. L.; House, R. L.; Meyer, G. J.; Papanikolas, J. M.; Meyer, T. J. *J. Am. Chem. Soc.* **2016**, *138* (40), 13085–13102.
- (8) Queyriaux, N.; Kaeffer, N.; Morozan, A.; Chavarot-Kerlidou, M.; Artero, V. *J. Photochem. Photobiol. C Photochem. Rev.* **2015**, *25*, 90–105.
- (9) Kirner, J. T.; Finke, R. G. *J. Mater. Chem. A* **2017**, *5*, 19560–19592.
- (10) Youngblood, W. J.; Lee, S. H. A.; Kobayashi, Y.; Hernandez-Pagan, E. A.; Hoertz, P. G.; Moore, T. A.; Moore, A. L.; Gust, D.; Mallouk, T. E. *J. Am. Chem. Soc.* **2009**, *131* (3), 926–927.
- (11) Zhao, Y.; Swierk, J. R.; Megiatto, J. D.; Sherman, B.; Youngblood, W. J.; Qin, D.; Lentz, D. M.; Moore, A. L.; Moore, T. A.; Gust, D.; Mallouk, T. E. *Proc. Natl. Acad. Sci.* **2012**, *109* (39), 15612–15616.
- (12) Swierk, J. R.; McCool, N. S.; Mallouk, T. E. *J. Phys. Chem. C* **2015**, *119* (24), 13858–13867.
- (13) Wei, P.; Hu, B.; Zhou, L.; Su, T.; Na, Y. *J. Energy Chem.* **2016**, *25* (3), 345–348.
- (14) Bledowski, M.; Wang, L.; Ramakrishnan, A.; Bétard, A.; Khavryuchenko, O. V.; Beranek, R. *ChemPhysChem* **2012**, *13* (12), 3018–3024.
- (15) Kirner, J. T.; Stracke, J. J.; Gregg, B. A.; Finke, R. G. *ACS Appl. Mater. Interfaces* **2014**, *6* (16), 13367–13377.
- (16) Kirner, J. T.; Finke, R. G. *ACS Appl. Mater. Interfaces* **2017**, *9* (33), 27625–27637.
- (17) Ronconi, F.; Syrgiannis, Z.; Bonasera, A.; Prato, M.; Argazzi, R.; Caramori, S.; Cristino, V.; Bignozzi, C. A. *J. Am. Chem. Soc.* **2015**, *137* (14), 4630–4633.
- (18) Bornoz, P.; Prévot, M. S.; Yu, X.; Guijarro, N.; Sivula, K. *J. Am. Chem. Soc.* **2015**, *137* (49), 15338–15341.
- (19) Swierk, J. R.; Méndez-Hernández, D. D.; McCool, N. S.; Liddell, P.; Terazono, Y.; Pahk, I.; Tomlin, J. J.; Oster, N. V.; Moore, T. A.; Moore, A. L.; Gust, D.; Mallouk, T. E. *Proc. Natl. Acad. Sci.* **2015**, *112* (6), 1681–1686.

- (20) Harriman, A.; Pickering, I. J.; Thomas, J. M.; Christensen, P. A. *J. Chem. Soc. Faraday Trans. 1 Phys. Chem. Condens. Phases* **1988**, 84 (8), 2795–2806.
- (21) Lee, S. K.; Zu, Y.; Hermann, A.; Geerts, Y.; Müllen, K.; Bard, A. J. *J. Am. Chem. Soc.* **1999**, 121 (14), 3513–3520.
- (22) Steinmiller, E. M. P.; Choi, K.-S. *Proc. Natl. Acad. Sci.* **2009**, 106 (49), 20633–20636.
- (23) Beranek, R. *Adv. Phys. Chem.* **2011**, 2011 (Iv), 80–83.
- (24) Arnold, F. E.; Van Deusen, R. L. *Macromolecules* **1969**, 2 (5), 497–502.
- (25) Babel, A.; Jenekhe, S. A. *J. Am. Chem. Soc.* **2003**, 125 (45), 13656–13657.

Hybrid photoanodes based on Nickel or Cobalt Oxide-  
Polypyrrole Nanocomposite Electrode Materials and a  
Perylene Organic Dye for Photocatalytic Water Oxidation



## Index

1. Introduction .....	133
2. Results and Discussion .....	134
2.1. Electrochemical and spectroscopic properties of PyrPDI.....	134
2.2. Electropolymerization of PyrPDI and electrochemical behaviour of the resulting films .....	136
2.3. Preparation of hybrid C or ITO/poly1/PyrPDI-MO <sub>x</sub> photonaodes .....	139
2.3.1. Electropolymerization of PyrPDI and 1, and the electrochemical behavior of of the corresponding poly1/PyrPDI modified electrodes .....	140
2.3.2. Electrogeneration of Nickel or Cobalt nanoparticles into poly1/PyrPDI copolymer .....	143
2.3.3. Photoelectrochemical activity for water oxidation with C/poly1/PyrPDI-MO <sub>x</sub> photoanodes (M = Ni or Co) .....	147
3. Conclusions .....	150
References .....	152

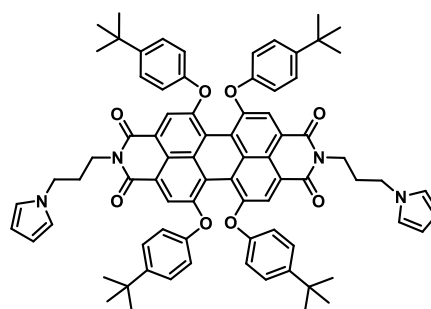


## 1- Introduction

This chapter focuses on the development and the study of new hybrid photoanodes and their use in photo-induced catalytic water oxidation. As described in the previous bibliographic chapter, only few examples of hydride photoanodes combining a molecular chromophore and an inorganic metal oxide catalyst, have been published.<sup>1-14</sup> The molecular chromophores employed were the classical ruthenium-tris-bipyridine complex<sup>5-8</sup> or organic dyes such as heptazine,<sup>9</sup> perylene,<sup>10-12</sup>  $\pi$ -conjugated naphthalen polymer<sup>13</sup> or porphyrin free base,<sup>14</sup> generally adsorbed or deposited in monolayer at the surface of a semi-conducting electrode.

Building on the results already acquired in the previous chapters, the aim of this work was to introduce a molecular chromophore within our nickel oxide/cobalt oxide-polypyrrole nanocomposite electrode materials in order to achieve photo-induced water oxidation. To ride the use of rare and expensive noble metals, we have investigated the use of a photosensitizer of the perylene diimide (PDI) family. Although still poorly explored for photocatalytic water oxidation,<sup>10-12</sup> and hydrogen production,<sup>15,16</sup> such organic molecules are very promising for water-splitting schemes. Indeed, perylene derivatives have all the properties required for such applications: i) robustness in water at both ground and excited state and high photostability, ii) strong absorption in the visible region with a very high molar extinction coefficient, iii) suitable photophysical (excited state lifetime of around 5 ns) and redox properties to allow efficient electron transfers with a catalyst such as a metal oxide or a n- or p-type semiconductor such as TiO<sub>2</sub> or NiO. Indeed, perylene show high oxidation potential, allowing the activation of many metallic oxides and molecular catalysts. In addition, there are only made of abundant elements and their structural platform is easy to functionalize by different substituents to tune their redox potentials and to introduce electropolymerizable groups such as pyrrole.

In view to introduce a PDI sensitizer, our strategy was to synthesize a derivative with electropolymerizable pyrrole substituents. The perylene diimide (PDI) derivative with two pyrrole substituents and four bulky tert-butylphenoxy groups in 3, 4, 9, and 10 positions of the perylene core (**PyrPDI** = *N,N'*-Bis(3-pyrrol-1-yl-propyl)-1,6,7,12-tetrakis(4-tert-butyl-phenoxy)perylen-



**Scheme 1.** Representation of **PyrPDI**.

3,4,9,10-tetracarboxylic acid diimine) was synthesized according to a previously published procedure of Lee and coworkers<sup>17</sup> (Scheme 1). In this previous work, the photoluminescence and electrochromism properties of the corresponding electrodeposited films have been investigated. We focused on this derivative since, in addition to the electropolymerizable pyrrole substituents, the presence of the electron donor, tert-butylphenoxy groups give an oxidation potential of about +1 V vs Ag/AgNO<sub>3</sub> (*i. e.* +1.3 V vs Ag/AgCl) sufficiently positive to oxidize the nickel or cobalt oxide nanoparticles. In addition, these later substituents enhance the solubility in organic solvents.<sup>17</sup> The synthesis and purification of the product were performed by Baptiste Dautreppe during his Master 1 training in our research group (2017). Since this perylene derivative is neutral, the strategy employed in the study described in this chapter was to co-polymerize the cationic ammonium pyrrole monomer **1** with this perylene derivative in order to have a positively charged polypyrrole film allowing the introduction of metallic nanoparticles of nickel or cobalt by the same strategy already used in the two previous chapters 2 & 3 of Part I.

In this chapter, we will first describe the electrochemical and spectroscopic properties of **PyrPDI** in acetonitrile/dichloromethane (1/1) solution, and the fabrication of the corresponding modified electrodes. We will then present the results concerning the elaboration of modified electrodes by copolymerization of **PyrPDI** and **1** as well as the incorporation of metallic nanoparticles of nickel and cobalt oxides. Finally, the photoelectrochemical activity for water oxidation of poly**1/PyrPDI**-MO<sub>x</sub> photoanodes was investigated by the measure of photocurrents under light irradiation.

## 2- Results and discussion

### 2.1. Electrochemical and spectroscopic properties of *PyrPDI*

Due to the poor solubility of the neutral organic dye **PyrPDI** in CH<sub>3</sub>CN, electrochemical studies were performed in a mixture of CH<sub>3</sub>CN/CH<sub>2</sub>Cl<sub>2</sub> (1/1 in volume) containing 0.05 M [Bu<sub>4</sub>N]ClO<sub>4</sub>. On a carbon or platinum electrode, as previously observed,<sup>17</sup> the cyclic voltammogram of **PyrPDI** exhibits, in the cathodic region, two successive reversible reduction processes, at  $E_{1/2} = -0.96$  and  $-1.11$  V vs Ag/AgNO<sub>3</sub> (Figure 1), attributed to **PyrPDI/PyrPDI<sup>•-</sup>** and **PyrPDI<sup>•-}/PyrPDI<sup>2-</sup></sup>**, respectively. In the anodic region, an intense irreversible peak at about +0.95 V is observed, corresponding to the oxidation of the two pyrrole units to form polypyrrole<sup>18</sup> and of the perylene core (**PyrPDI<sup>+</sup>/PyrPDI**).<sup>19</sup> The intensity of this peak is more than two times higher than that of the one-electron reversible reduction processes in

accordance with the exchange of more than two electrons.<sup>17</sup> A reversible one-electron wave is expected for the **PyrPDI**<sup>+</sup>/**PyrPDI** oxidation process, as observed for the parent PDI without pyrrole groups. The overall oxidation process appears irreversible here due to the superimposition of the irreversible oxidation of the pyrrole moiety.

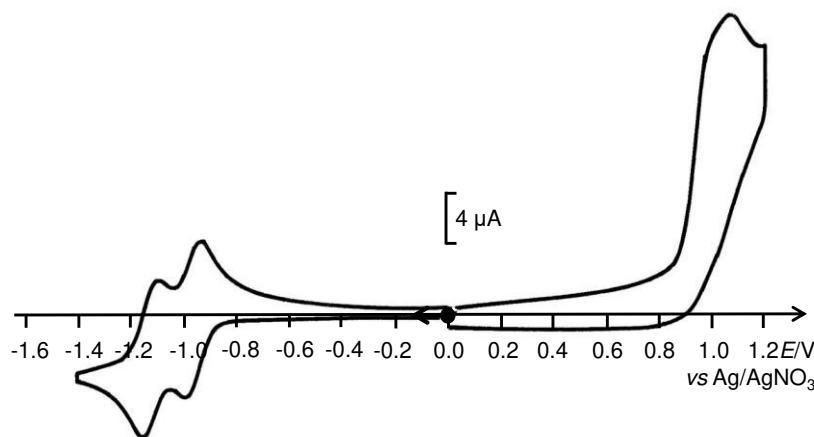


**Figure 1.** Cyclic voltammograms recorded at a C electrode (3 mm of diameter) of **PyrPDI** (0.5 mM) in a solution of CH<sub>3</sub>CN/CH<sub>2</sub>Cl<sub>2</sub> (1/1) + 0.05 M [Bu<sub>4</sub>N]ClO<sub>4</sub>; scan rate 50 mVs<sup>-1</sup>.

The absorption spectrum of **PyrPDI** exhibits two distinct bands at 453 and 576 nm ( $\epsilon \approx 36100$  M<sup>-1</sup>cm<sup>-1</sup>, shoulder at 540 nm) (Figure 2).<sup>17</sup> These absorption features are typical of PDI derivatives.<sup>20</sup>

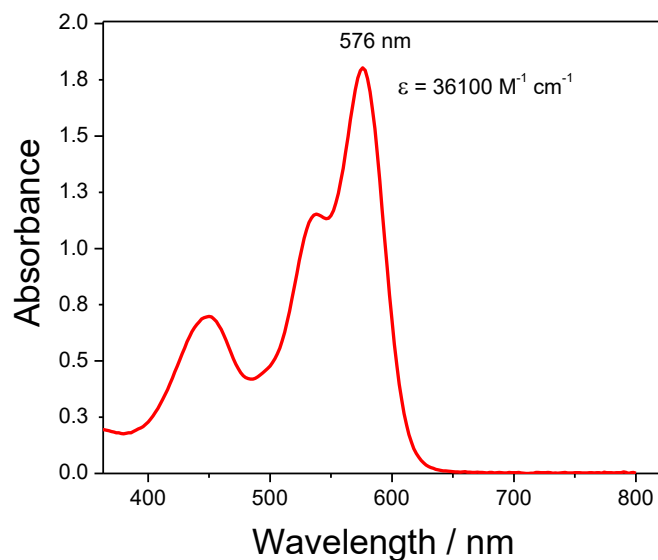


**Figure 2.** UV-Visible absorption spectrum of a solution of **PyrPDI** (0.5 mM) in CH<sub>3</sub>CN/CH<sub>2</sub>Cl<sub>2</sub> (1/1) containing 0.05 M [Bu<sub>4</sub>N]ClO<sub>4</sub>,  $l = 1$  mm.

## 2.2 – Electropolymerization of PyrPDI and electrochemical behavior of the resulting films

Lee and coworkers<sup>17</sup> have shown that **PyrPDI** could be electrodeposited by scanning at potential between 0 and +1.2 V vs Ag/AgNO<sub>3</sub> in CH<sub>2</sub>Cl<sub>2</sub>/CH<sub>3</sub>CN (1/2 in volume) containing 0.1 M M [Bu<sub>4</sub>N]PF<sub>6</sub> leading to an adherent red film at the surface of glassy carbon (C) or indium tin oxide electrodes (ITO) electrodes. The expected reversible system between 0 and about +0.7 V corresponding to the electroactivity of the polypyrrole was not observed and the resulting red film exhibited only the electroactivity of the **PyrPDI**, *i. e.* the two successive reversible reduction waves and the reversible oxidation wave. However, in contrast to the monomer **PyrPDI**, the film was found to be insoluble in CH<sub>2</sub>Cl<sub>2</sub> attesting its polymeric nature. In this work, we have performed electropolymerization of **PyrPDI** (0.5 mM) in CH<sub>3</sub>CN/CH<sub>2</sub>Cl<sub>2</sub> (1/1 in volume) containing 0.05 M [Bu<sub>4</sub>N]ClO<sub>4</sub> from a 0.5 mM solution of **PyrPDI** by applied potential of +0.95 V vs Ag/AgNO<sub>3</sub>. Typically, the anodic charge used for the polymerization is 4 and 22.1 mC for C and ITO electrodes, respectively, both corresponding to 0.056 C cm<sup>-2</sup> since the surfaces of the C and ITO electrodes are 0.071 cm<sup>2</sup> and 0.4 cm<sup>2</sup>. When the electrodes are removed from the solution, the visual examination reveals that the C and ITO surfaces are covered with a uniform dark red film. The UV-visible absorption spectrum of the poly**PyrPDI** deposited on the ITO electrode exhibits the typical absorption of the perylene unit although the higher absorption band at about 580 nm saturated due to the thickness of the film (Figure 3).

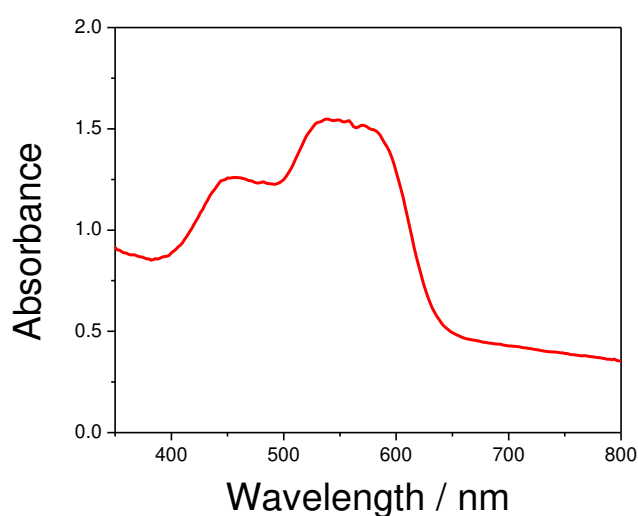


**Figure 3.** UV-Visible absorption spectrum of an poly**PyrPDI** film deposited on an ITO electrode (surface of 0.4 cm<sup>2</sup>) ( $\Gamma_{\text{PyrPDI}} = 4.34 \times 10^{-8}$  mol cm<sup>-2</sup>).

After transfer into an  $\text{CH}_3\text{CN}/\text{CH}_2\text{Cl}_2$  (1/1) solution, 0.05 M  $[\text{Bu}_4\text{N}]\text{ClO}_4$  without **PyrPDI**, these C and ITO/poly**PyrPDI** modified electrodes exhibit the typical basic redox behavior of the PDI derivative, similar to that previously observed by Lee and coworkers<sup>17</sup> from poly**PyrPDI** elaborated by repeated scans between 0 and +1.2 V (Figures 4-6). At a scan rate of  $10 \text{ mV s}^{-1}$ , the two successive one-electron reversible reduction waves are well separated and are located at about  $E_{1/2} = -1.03$  (**PyrPDI**/**PyrPDI**<sup>-</sup>) and  $-1.15 \text{ V}$  (**PyrPDI**<sup>-</sup>/**PyrPDI**<sup>2-</sup>) vs  $\text{Ag}/\text{AgNO}_3$  (Figures 4 and 5). The reversible one-electron oxidation (**PyrPDI**<sup>+</sup>/**PyrPDI**) is located at  $E_{1/2} = +1.08 \text{ V}$  vs  $\text{Ag}/\text{AgNO}_3$ . By cycling at a higher scan rate of  $50 \text{ mV s}^{-1}$ , the two reduction processes are less separated and appear as a single large wave (Figure 6). Besides, the electroactivity of the polypyrrole is not observed, despite the fact that the electropolymerization potential of  $+0.95 \text{ V}$  is less anodic than that previously used for electropolymerization by scanning.<sup>17</sup> The absence of the electroactivity of the polypyrrole probably reflects its overoxidation during the electropolymerization process. For the moment we have no explanation for this phenomenon. However, to rule out the possible implication of the excited state of the perylene in the overoxidation process, electropolymerization should be performed in the dark, to see if in this case the electroactivity of the polypyrrole is preserved.

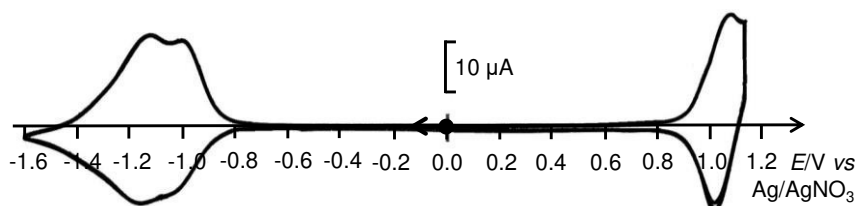


**Figure 4.** Cyclic voltammetry curves of a C/poly**PyrPDI** film (3 mm diameter) in  $\text{CH}_3\text{CN}/\text{CH}_2\text{Cl}_2$  (1/1) solution, with 0.05 M  $[\text{Bu}_4\text{N}]\text{ClO}_4$  prepared by electrolysis at  $E = +0.95 \text{ V}$  vs  $\text{Ag}/\text{AgNO}_3$  (4 mC) from a solution of **PyrPDI** (0.5 mM) in  $\text{CH}_3\text{CN}/\text{CH}_2\text{Cl}_2$ , 0.05 M  $[\text{Bu}_4\text{N}]\text{ClO}_4$  ion; scan rate of  $10 \text{ mV s}^{-1}$ . The coverage surface of **PyrPDI** units ( $\Gamma_{\text{PyrPDI}} = 4.89 \times 10^{-8} \text{ mol cm}^{-2}$ ) was calculated from the integration of the anodic and cathodic charge of the two successive reversible reduction waves of poly**PyrPDI** ( $Q_a = 6.7 \times 10^{-4} \text{ C}$  and  $Q_c = 6.7 \times 10^{-4} \text{ C}$ , respectively by scanning at  $10 \text{ mV s}^{-1}$ ). Deposition yield, 39.04%.

The surface coverage in the electroactive **PyrPDI** species immobilized,  $\Gamma_{\text{PyrPDI}}$  ( $\text{mol cm}^{-2}$ ) on the C and ITO electrodes ( $0.071 \text{ cm}^2$  and  $0.4 \text{ cm}^2$ , respectively), was quantified electrochemically by integration of the two reversible reduction waves (see Experimental Section).  $\Gamma_{\text{PyrPDI}}$  values ranging from  $3.54 \times 10^{-8} \text{ mol cm}^{-2}$  to  $4.89 \times 10^{-8} \text{ mol cm}^{-2}$  for C electrodes and  $3.76 \times 10^{-8} \text{ mol cm}^{-2}$  to  $4.34 \times 10^{-8} \text{ mol cm}^{-2}$  for ITO electrodes were obtained for anodic charges of 4 mC and 22.1 mC respectively. These values correspond to an electropolymerization yield in the range of 28 to 39% and of 30 and 35% for C and ITO electrodes, respectively.

The stability of the modified electrodes was investigated by repeated cycles through the reduction and oxidation waves of the perylene. Modified electrodes exhibited an excellent stability toward electrochemical cycling through the two reversible reduction waves (**PyrPDI**/**PyrPDI<sup>•-</sup>** and **PyrPDI<sup>•-</sup>**/**PyrPDI<sup>2-</sup>** states). Indeed, after 10 cycles at 50 mV s<sup>-1</sup> between -0.60 and -1.5 V, the intensity of the reduction processes remains constant (less than 3% loss of the integrated peaks). Poly**PyrPDI** films are less stable towards multiple oxidative scans. Typically, 10 successive scans at 50 mVs<sup>-1</sup> under the oxidation wave (0 to +1.2 V) result in the loss of about 7-10% of the electroactivity of the film, as estimated from the charge measured under the oxidation wave (Figure 6). Thus it appears that the perylene is more stable at reduced state, even in its double reduction state than in its oxidized state, although the oxidation process appears reversible at the time scale of the cyclic voltammetry.

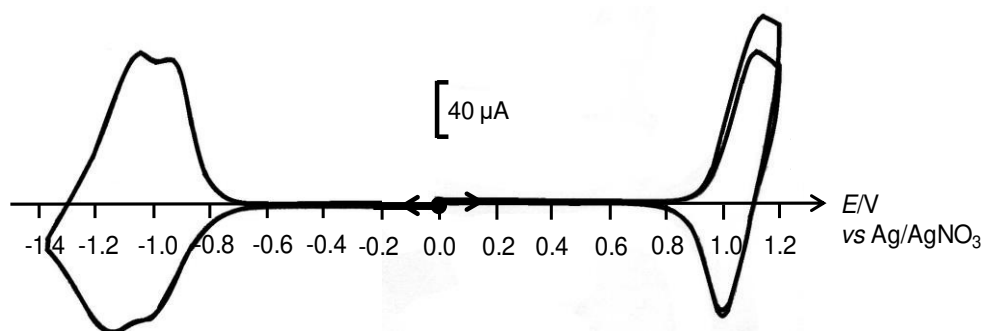


**Figure 5.** Cyclic voltammety curves of an ITO/poly**PyrPDI** film (surface of 0.4 cm<sup>2</sup>) in CH<sub>3</sub>CN/CH<sub>2</sub>Cl<sub>2</sub> (1/1) solution, with 0.05 M [Bu<sub>4</sub>N]ClO<sub>4</sub> ( $\Gamma_{\text{PyrPDI}} = 4.34 \times 10^{-8}$  mol cm<sup>-2</sup>,  $Q_a = 3.33 \times 10^{-3}$  C and  $Q_c = 3.37 \times 10^{-3}$  C, respectively by scanning at 10 mV s<sup>-1</sup>) prepared by electrolysis at  $E = +0.95$  V vs Ag/AgNO<sub>3</sub> (22.1 mC) from a solution of **PyrPDI** (0.5 mM) in CH<sub>3</sub>CN/CH<sub>2</sub>Cl<sub>2</sub>, 0.05 M [Bu<sub>4</sub>N]ClO<sub>4</sub> ion; scan rate of 10 mV s<sup>-1</sup>. Electropolymerization yield, 35%.

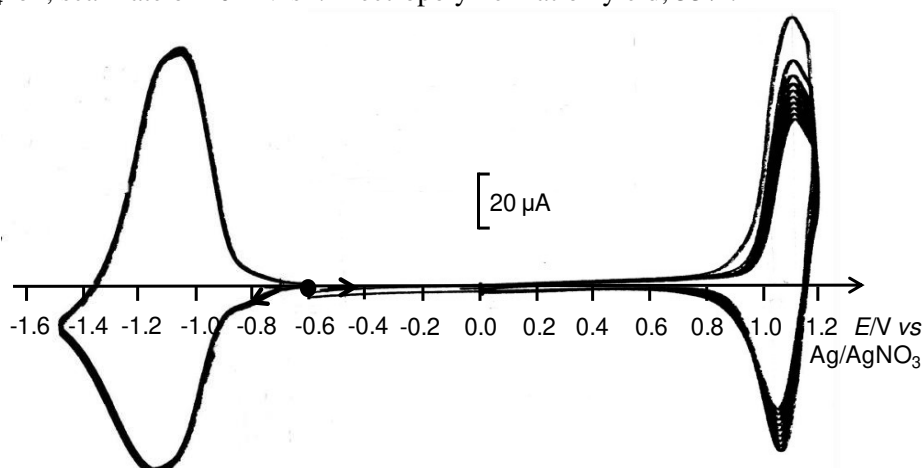


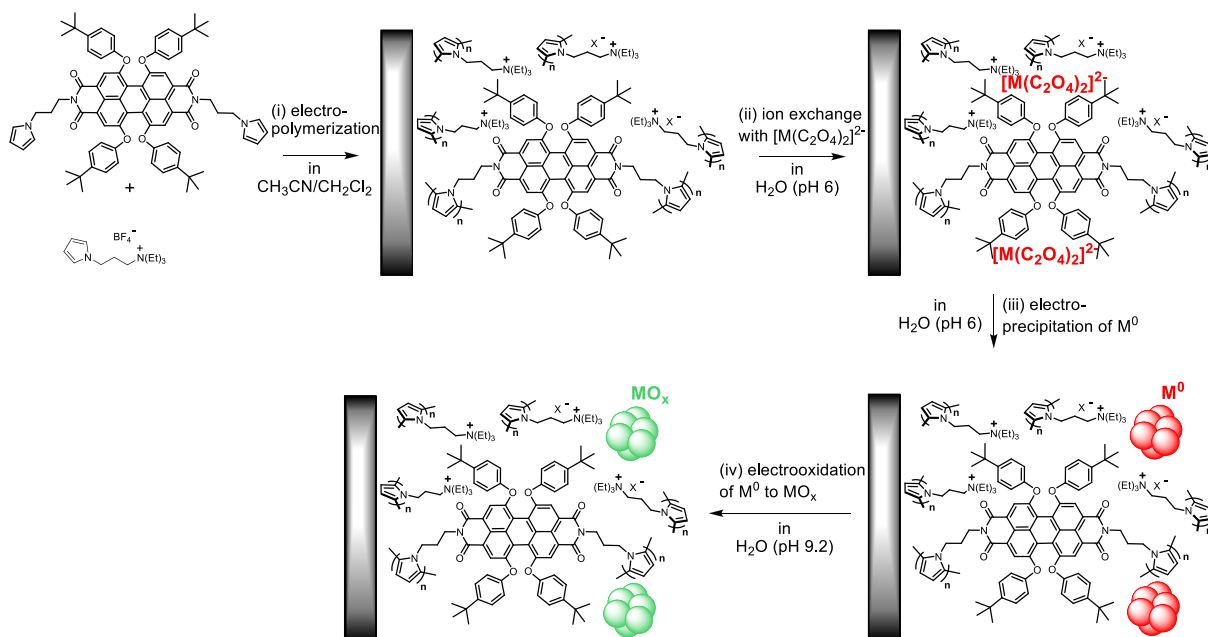
**Figure 6.** Cyclic voltammety curves of an C/poly**PyrPDI** film (3 mm diameter) in CH<sub>3</sub>CN/CH<sub>2</sub>Cl<sub>2</sub> (1/1) solution, with 0.05 M [Bu<sub>4</sub>N]ClO<sub>4</sub> ( $\Gamma_{\text{PyrPDI}} = 3.37 \times 10^{-8}$  mol cm<sup>-2</sup>,  $Q_a = 4.57 \times 10^{-4}$  C and  $Q_c = 4.68 \times 10^{-4}$  C, respectively by scanning at 50 mV s<sup>-1</sup>) prepared by electrolysis at  $E = +0.95$  V vs Ag/AgNO<sub>3</sub> (4 mC) from a solution of **PyrPDI** (0.5 mM) in CH<sub>3</sub>CN/CH<sub>2</sub>Cl<sub>2</sub>, 0.05 M [Bu<sub>4</sub>N]ClO<sub>4</sub> ion; scan rate of 50 mV s<sup>-1</sup>. Electropolymerization yield, 27%.

### 2.3. Preparation of hybrid C or ITO/poly1/PyrPDI-MO<sub>x</sub> photoanodes

Having shown that the perylene derivative **PyrPDI** readily polymerized at an applied potential of +0.95V, *i. e.* at the same potential as the ammonium pyrrole compound **1**, it should be possible to copolymerize the two entities at +0.95 V. Indeed, the positive charge provided by the ammonium units will allow for the incorporation of the metallic oxides in the film and thus the elaboration of the hybrid photoanodes.

Modified electrodes of the copolymers C or ITO/poly1-**PyrPDI**-MO<sub>x</sub> (M = Ni or Co) were thus prepared by the same four step electrochemical procedure that was already used for the preparation of C or ITO/poly1-MO<sub>x</sub> modified electrodes (Scheme 2 and see Part I, Chapters 2&3).

**Scheme 2.** General Strategy for the Electrosynthesis Poly1/PyrPDI-MO<sub>x</sub> (M = Ni or Co) on a C or ITO electrode<sup>a</sup>



<sup>a</sup>(i) Formation of a copolymer of poly1/**PyrPDI** by oxidative electropolymerization of a mixture of monomers **1** and **PyrPDI** at  $E_{app} = +0.95$  V vs Ag/AgNO<sub>3</sub> in  $\text{CH}_3\text{CN}/\text{CH}_2\text{Cl}_2$  (1/1), 0.05 M  $[\text{Bu}_4\text{N}]\text{ClO}_4$ ; (ii) incorporation of  $[\text{M}(\text{C}_2\text{O}_4)_2]^{2-}$  into poly1/**PyrPDI** upon soaking during 1h in an aqueous solution (pH 6) of  $[\text{M}(\text{C}_2\text{O}_4)_2]^{2-}$  (1 mM for M = Ni (5 mM  $\text{Na}_2\text{C}_2\text{O}_4$ ) and 4 mM for M = Co (20 mM  $\text{Na}_2\text{C}_2\text{O}_4$ )), 0.1 M  $\text{Na}_2\text{SO}_4$  and 0.1 M  $\text{H}_3\text{BO}_3$ ; (iii) electroprecipitation of  $\text{M}^0$  within poly1/**PyrPDI** at  $E_{app} = -1.4$  V vs Ag/AgCl for nickel and  $E_{app} = -1.3$  V vs Ag/AgCl for cobalt in the previously mentioned aqueous solutions of nickel or cobalt oxalate; (iv) electrooxidation of  $\text{M}^0$  to  $\text{MO}_x$  by repeated cyclic voltammetry scans between 0 and +1.1 V vs Ag/AgCl in an aqueous solution (pH 9.2) of 0.1 M  $\text{H}_3\text{BO}_3$  and 0.05 M NaOH.

The first step which consists in the co-electropolymerization of **1** and **PyrPDI** will be described first and then the three following steps corresponding to the electrogeneration of metal oxide nanoparticles for nickel and cobalt, and finally the evaluation of the photoelectrochemical activity under visible light illumination.

### 2.3.1. Electro-copolymerization of PyrPDI and **1**, and electrochemical behavior of the corresponding poly**1**/PyrPDI modified electrode

Copolymerization was performed from a mixture of the monomers **1** and **PyrPDI** in CH<sub>3</sub>CN/CH<sub>2</sub>Cl<sub>2</sub> (1/1 in volume), 0.05 M [Bu<sub>4</sub>N]ClO<sub>4</sub> at a controlled potential of +0.95 V vs Ag/AgNO<sub>3</sub> on C and ITO electrodes. The copolymerization was performed with **PyrPDI** at 0.5 mM and **1** at 1 mM (ratio 0.5:1).

Figure 7 displays the cyclic voltammogram of the resulting solution which corresponds to the superimposition of the electroactivity of both monomers in their respective proportion. In reduction, as expected, only the two reversible reduction waves of the perylene are observed. Besides, in oxidation, the very intense irreversible oxidation wave observed corresponds both to the reversible oxidation of the perylene core and of the irreversible oxidation of the pyrrole units of **PyrPDI** and of the pyrrole-alkylammonium monomer **1**, leading to the concomitant polymerization of the pyrrole units of both **1** and **PyrPDI** to form the resulting modified electrode C or ITOpoly**1**/PyrPDI.

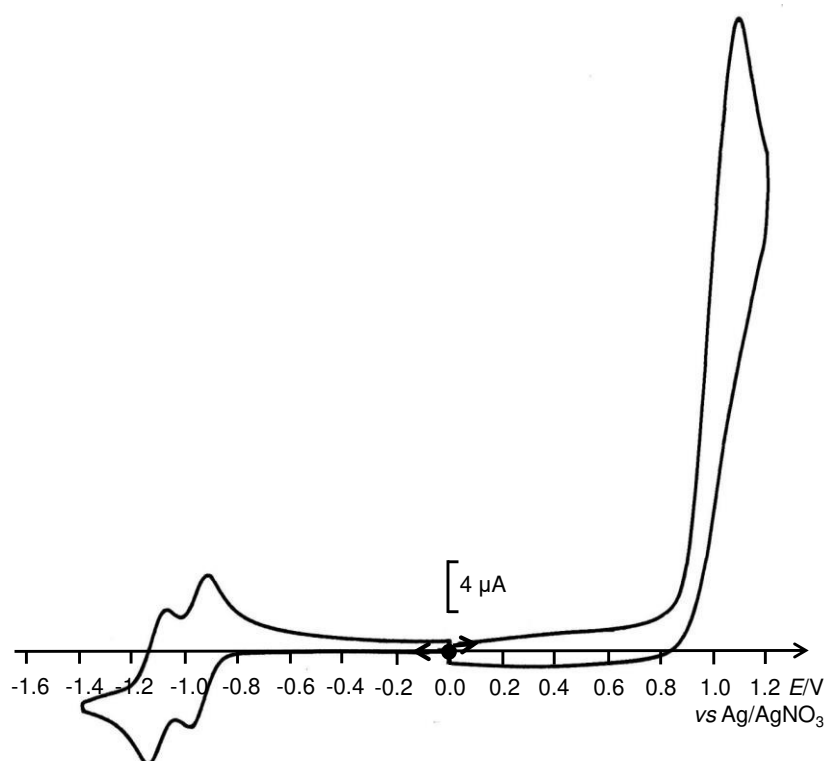


**Figure 7.** Cyclic voltammetry recorded at C electrode (3 mm of diameter) in a solution of CH<sub>3</sub>CN/CH<sub>2</sub>Cl<sub>2</sub>, 0.05 M [Bu<sub>4</sub>N]ClO<sub>4</sub> containing of **PyrPDI** (0.5 mM) and **1** (1 mM); scan rate 50 mVs<sup>-1</sup>.

Poly**1**/PyrPDI copolymer films were deposited on a series of seven glassy carbon electrodes and one ITO electrode. Figure 8 exhibits the electroactivity of the resulting poly**1**/PyrPDI

films deposited at the surface of two different C electrodes and of the ITO electrode after transfer in  $\text{CH}_3\text{CN}/\text{CH}_2\text{Cl}_2$  (1/1) solution, 0.05 M  $[\text{Bu}_4\text{N}]\text{ClO}_4$ . As expected, all the modified electrodes display the regular electroactivity of the immobilized perylene diimide in reduction with two reversible successive reduction waves located at about  $E_{1/2} = -0.96$  and  $-0.87$  V. However, even at the low scan rate of  $10 \text{ mVs}^{-1}$ , the two waves are poorly defined and are not well-separated. Interestingly, these two waves are positively shifted by a bout 150 - 200 mV compared to the same wave in polyPyrPDI.

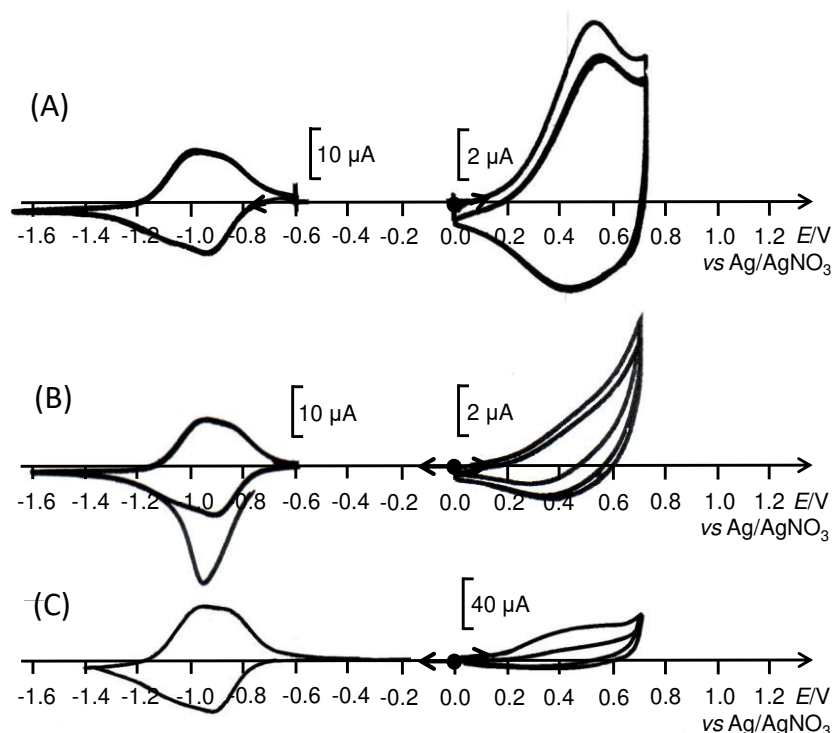


**Figure 8.** Cyclic voltammograms of (A,B) a C/poly1/PyrPDI film (3 mm diameter) and (C) of an ITO/poly1/PyrPDI film (surface of  $0.4 \text{ cm}^2$ ) in  $\text{CH}_3\text{CN}/\text{CH}_2\text{Cl}_2$  (1/1) solution, 0.05 M  $[\text{Bu}_4\text{N}]\text{ClO}_4$  prepared at an applied potential of  $E = +0.95 \text{ V vs Ag/AgNO}_3$  (4 mC for C and 22.1 mC for ITO) from a solution of PyrPDI (0.5 mM) and 1 (1 mM) in  $\text{CH}_3\text{CN}/\text{CH}_2\text{Cl}_2$ , 0.05 M  $[\text{Bu}_4\text{N}]\text{ClO}_4$ ; scan rate of  $10 \text{ mV s}^{-1}$ . The coverage surface of PyrPDI units ( $\Gamma_{\text{PyrPDI}}$ ) and deposition yield were calculated from the integration of the anodic and cathodic charge of the two successive reversible reduction waves of polyPyrPDI by scanning at  $10 \text{ mV s}^{-1}$ . The surface coverage of polypyrrole units and deposition yield was estimated by integration of the polypyrrole wave by scanning at  $10 \text{ mV s}^{-1}$ . For the C electrodes: (A)  $\Gamma_{\text{PyrPDI}} = 1.79 \times 10^{-8} \text{ mol cm}^{-2}$  ( $Q_a = 2.58 \times 10^{-4} \text{ C}$  and  $Q_c = 2.35 \times 10^{-4} \text{ C}$ ), deposition yield, 14.3%,  $\Gamma_{\text{polypyrrole}} = 7.2 \times 10^{-8} \text{ mol cm}^{-2}$ , deposition yield, 28.6%, (B)  $\Gamma_{\text{PyrPDI}} = 2.2 \times 10^{-8} \text{ mol cm}^{-2}$ , deposition yield, 17.5%;  $\Gamma_{\text{polypyrrole}} = 4.1 \times 10^{-8} \text{ mol cm}^{-2}$ , deposition yield, 16.2%. (C) For the ITO electrode,  $\Gamma_{\text{PyrPDI}} = 1.81 \times 10^{-8} \text{ mol cm}^{-2}$  ( $Q_a = 1.31 \times 10^{-3} \text{ C}$  and  $Q_c = 1.48 \times 10^{-3} \text{ C}$ ), deposition yield, 14.7%,  $\Gamma_{\text{polypyrrole}} = 1.38 \times 10^{-8} \text{ mol cm}^{-2}$ , deposition yield, 11%.

The amount of PyrPDI immobilized can be easily calculated by integration of these two waves at  $10 \text{ mVs}^{-1}$ . For C electrodes for a total charge of 4 mC, an apparent surface coverage

of perylene unit comprised between  $1.79 \times 10^{-8}$  and  $2.4 \times 10^{-8}$  mol cm<sup>-2</sup> ( $\Gamma_{\text{PyrPDI}}$ ) was obtained corresponding to a deposition yield between 14.3 and 19.3 % (Figure 8(A,B)), while for the ITO electrode, for a total charge of 22.1 mC, a  $\Gamma_{\text{PyrPDI}}$  of  $1.81 \times 10^{-8}$  mol cm<sup>-2</sup>, corresponding to a deposition yield of 14.4% was obtained (Figure 8(C)). These values are divided by more than two compared to films electrodeposition from a solution containing only the **PyrPDI** derivative at 0.5 mM, with the same deposition charge (see above, Figures 4-6). This result is consistent with the concomitant copolymerization of the monomer **1**. By scanning in the anodic potential region, a reversible wave corresponding to the electroactivity of the polypyrrole is observed but the shape is more or less intense depending on the electrodes. Anyway, we have tentatively estimated the amount of polypyrrole immobilized by integration of the polypyrrole oxidation wave by cycling between 0.0 to +0.7 V at a low scan rate (10 mV s<sup>-1</sup>) assuming that one in three pyrrole units is oxidized (Figure 8).<sup>21</sup> However, since a copolymer of **1** and **PyrPDI** is formed; it is not possible to know if the detected polypyrrole electroactivity is only related to the ammonium of **1** derivative. Although no polypyrrole electroactivity was detected for poly**PyrPDI** films (see above), we can not exclude that when copolymerized with **1**, the electroactivity of **PyrPDI** can be detected. Thus from this electrochemical method, it is not possible to estimate the amount of ammonium positive charge present in the copolymer films. Anyway, based on the integration of the polypyrrole signal, an apparent surface coverage of polypyrrole comprised between  $3.7 \times 10^{-8}$  and  $7.2 \times 10^{-8}$  mol cm<sup>-2</sup> ( $\Gamma_{\text{polypyrrole}}$ ) was obtained corresponding to a deposition yield in the range 14.9 - 28.6 % (Figure 8(A,B) which is lower than the yield of polypyrrole deposition of poly**1** (45-51 %, see Experimental Section and Part I, Chapters 2&3).

The absorption spectrum of the poly**1**/**PyrPDI** film deposited on ITO electrode is shown Figure 9. The typical absorption of the **PyrPDI** film is observed with three maximum at 572 (sh, 543 and 454 nm).<sup>17</sup> No saturation of the band at 580 nm is observed since for the same charge of 22.1 mC, the amount of **PyrPDI** deposited with the copolymer is lower than that deposited with only **PyrPDI** (respectively,  $\Gamma_{\text{PyrPDI}} = 1.81 \times 10^{-8}$  and  $4.34 \times 10^{-8}$  mol cm<sup>-2</sup>) (Figure 9).

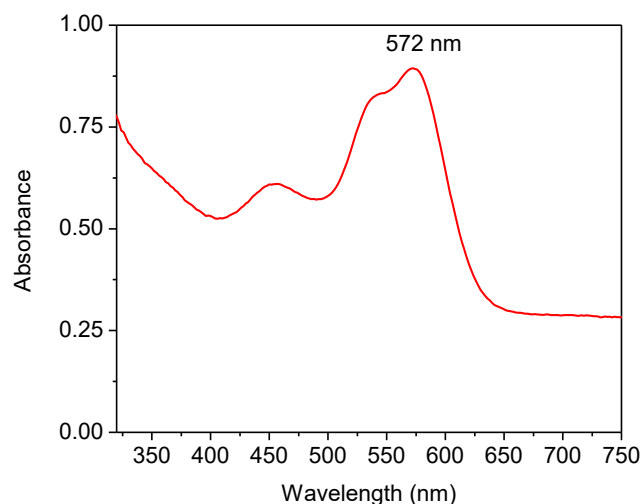


**Figure 9.** UV-Visible absorption spectrum of an poly1/PyrPDI film deposited on an ITO electrode (surface of  $0.4 \text{ cm}^2$ ) ( $\Gamma_{\text{PyrPDI}} = 1.81 \times 10^{-8} \text{ mol cm}^{-2}$ ).

### 2.3.2. Electrogeneration of Nickel or Cobalt oxide nanoparticles into poly1/PyrPDI copolymer

Before the electrogeneration of the metal oxides in the poly1/PyrPDI deposited on glassy carbon electrodes, the electroactivity of the films has been recorded in aqueous borate buffer solution at pH 9.2. In  $\text{CH}_3\text{CN}$ , the electroactivity of the perylene in poly1/PyrPDI appears at about  $-0.98$ ,  $-0.87 \text{ V}$  and  $+1.08 \text{ V}$  vs  $\text{Ag}/\text{AgNO}_3$  (Figures 4-6 and 8). Thus, in water, the corresponding waves should be located at about  $-0.65$ ,  $-0.54$  and  $+1.41 \text{ V}$  vs  $\text{Ag}/\text{AgCl}$ . By scanning in reduction up to  $-1.0$  or  $-1.2 \text{ V}$  vs  $\text{Ag}/\text{AgCl}$ , the electroactivity of the perylene diimine immobilized appears, at a scan rate of  $50 \text{ mVs}^{-1}$  as a single reversible wave in the range  $E_{1/2} = -0.43$  to  $-0.47 \text{ V}$  vs  $\text{Ag}/\text{AgCl}$  ( $\Delta E_p = 220$  to  $245 \text{ mV}$ ), so again a potential positively shifted to the expected one (Figure 10(c) and Figure 11(c)). To avoid the deterioration of the film, we did not cycle in this aqueous medium in the positive region up to  $+1.4 \text{ V}$  in view to observe the oxidation wave of the perylene. Anyway, since the oxidation process to transform  $\text{M}^0$  nanoparticles into metal oxide  $\text{MO}_x$  nanoparticles requires cycling between  $0$  to  $+1.2 \text{ V}$  vs  $\text{Ag}/\text{AgCl}$ , in principle this potential is lower than the oxidation wave of the perylene and will not lead to its deterioration. As we will see below, the potential for the oxidation process of  $\text{M}^0$  into  $\text{MO}_x$  has limited to  $+1.1 \text{ V}$  vs  $\text{Ag}/\text{AgCl}$ , as a precautionary measure.

The electrochemical procedures used for the deposition of nickel and cobalt oxide nanoparticles with the poly1/PyrPDI cationic films are similar to those previously employed for the deposition within poly1 films without the perylene derivative (see Part 1, Chapters

2&3). Because of time constraints, only two C/poly1/PyrPDI electrodes were used for this study, for which the electroactivity is shown in Figures 8(A) and Figure 8(B), before nickel and cobalt deposition, respectively.

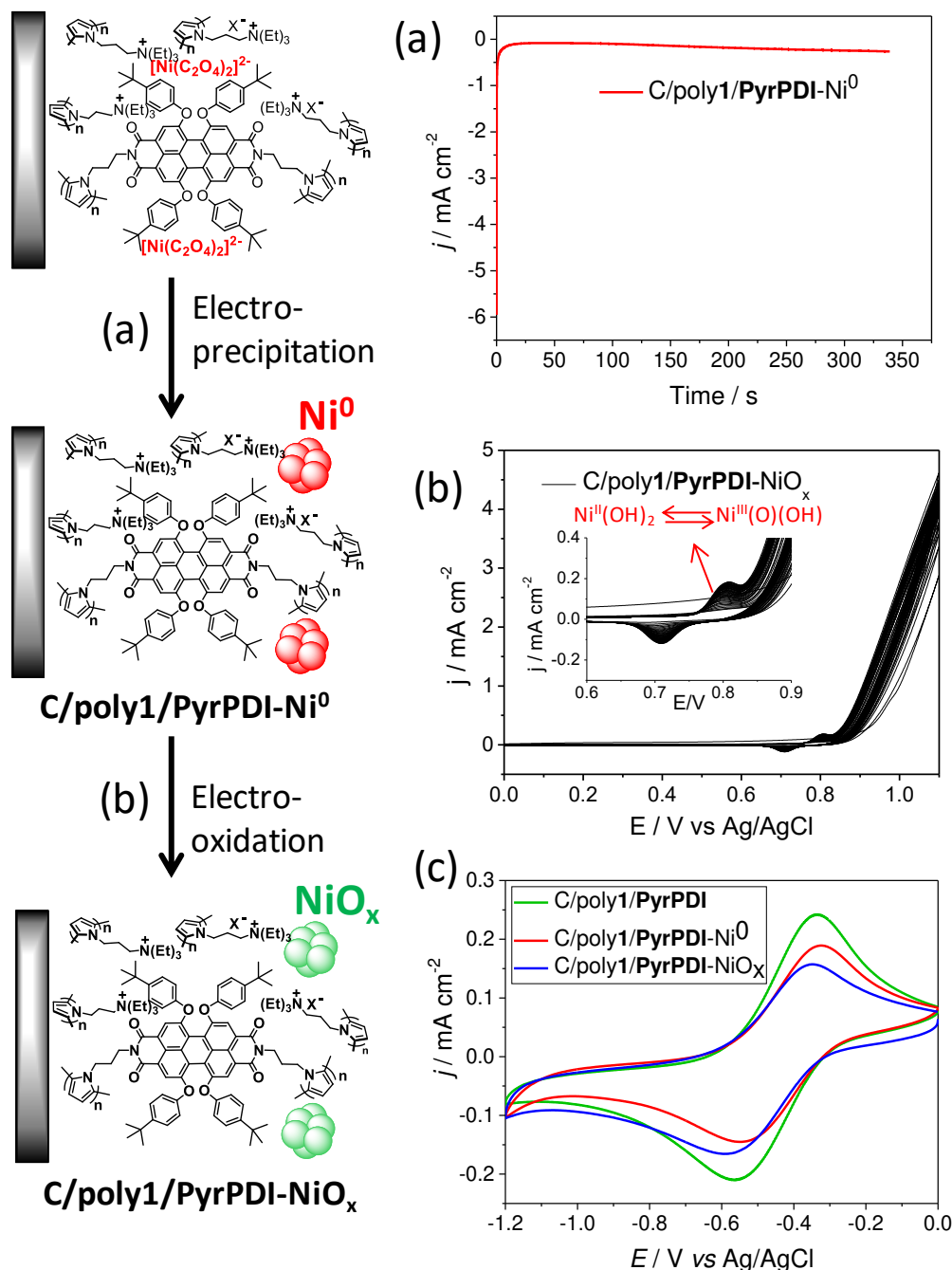


**Figure 10.** (a) Electrogeneration of Ni<sup>0</sup> nanoparticles by reduction at  $E_{\text{appl}} = -1.4$  V vs Ag/AgCl ( $Q = 4$  mC) in a C/poly1/PyrPDI film ( $\Gamma_{\text{PyrPDI}} = 1.79 \times 10^{-8}$  mol cm<sup>-2</sup>,  $\Gamma_{\text{polypyrrole}} = 7.2 \times 10^{-8}$  mol cm<sup>-2</sup>) (3 mm of diameter) in an aqueous borate solution (pH 6) of 1 mM NiSO<sub>4</sub>, 5 mM Na<sub>2</sub>C<sub>2</sub>O<sub>4</sub>, 0.1 M Na<sub>2</sub>SO<sub>4</sub>, 0.1 M H<sub>3</sub>BO<sub>3</sub> (the electrode was soaked for 1 hour in the solution before the reduction process). (b) Electrochemical generation of NiO<sub>x</sub> from Ni<sup>0</sup> by 50 consecutive scans in an aqueous borate buffer solution (pH 9.2), 0.1 M H<sub>3</sub>BO<sub>3</sub>, 0.1M Na<sub>2</sub>SO<sub>4</sub> and 0.05M NaOH solution. (c) Cyclic voltammograms between 0 and -1.0 V showing the electroactivity of the perylene of the corresponding modified

electrode, C/poly1/PyrPDI (green), after electrogeneration of  $\text{Ni}^0$  (red) and after oxidation of  $\text{Ni}^0$  into  $\text{NiO}_x$ , in the 0.1 M borate solution (pH 9.2), scan rate  $50 \text{ mV s}^{-1}$ .

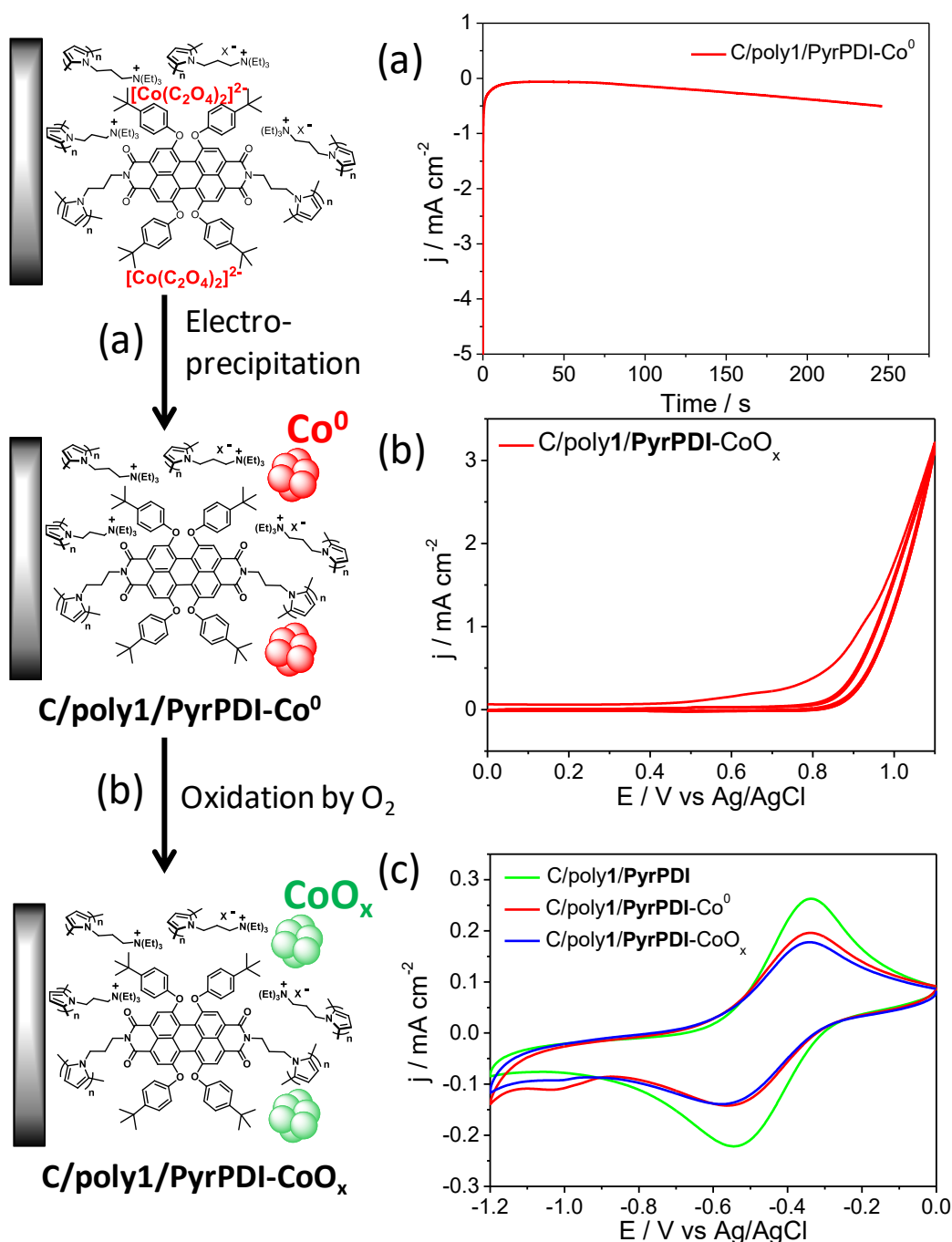


**Figure 11.** (a) Electrogeneration of  $\text{Co}^0$  nanoparticles by reduction at  $E_{\text{appl}} = -1.3 \text{ V vs Ag/AgCl}$  ( $Q = 4 \text{ mC}$ ) in a C/poly1/PyrPDI film ( $\Gamma_{\text{PyrPDI}} = 2.2 \times 10^{-8} \text{ mol cm}^{-2}$ ,  $\Gamma_{\text{polypyrrole}} = 4.1 \times 10^{-8} \text{ mol cm}^{-2}$ ) (3 mm of diameter) in an aqueous borate solution (pH 6) of 4 mM  $\text{CoSO}_4$ , 20 mM  $\text{Na}_2\text{C}_2\text{O}_4$ , 0.1 M  $\text{Na}_2\text{SO}_4$ , 0.1 M  $\text{H}_3\text{BO}_3$ , (the electrode was soaked for 1 hour in the solution before the reduction process). (b) Electrochemical generation of  $\text{CoO}_x$  from  $\text{Co}^0$  by 5 consecutive scans in an aqueous borate buffer solution (pH 9.2), 0.1 M  $\text{H}_3\text{BO}_3$ , 0.1M  $\text{Na}_2\text{SO}_4$  and 0.05M  $\text{NaOH}$  solution. (c) Cyclic voltammograms between 0 and -1.2 V showing the electroactivity of perylene of the corresponding modified electrode, C/poly1/PyrPDI (green), after electrogeneration of  $\text{Co}^0$  (red) and after oxidation of  $\text{Co}^0$  into  $\text{CoO}_x$ , in the 0.1 M borate solution (pH 9.2), scan rate  $50 \text{ mV s}^{-1}$ .

For the nickel, the procedure consists in loading the cationic film of poly1/PyrPDI with the anionic the nickel oxalate complex,  $[\text{Ni}(\text{C}_2\text{O}_4)_2]^{2-}$ , by soaking in the C/poly1/PyrPDI electrodes in an aqueous 0.1 M borate buffer solution at pH 6.0 containing a mixture of the  $\text{NiSO}_4$  (1 mM) and  $\text{Na}_2\text{C}_2\text{O}_4$  (5 mM) and  $\text{Na}_2\text{SO}_4$  (0.1 M) (Scheme 2).  $\text{Ni}^0$  nanoparticles were then electrogenerated with the poly1/PyrPDI film by applying a potential of -1.4 V vs Ag/AgCl by maintaining the electrode in the nickel oxalate solution (Figure 10(a)). For the cobalt, the borate solution is more concentrated in cobalt oxalate ( $\text{CoSO}_4$  (4 mM) and  $\text{Na}_2\text{C}_2\text{O}_4$  (20 mM)) and the deposition is performed at -1.3 V vs Ag/AgCl (Figure 11(a)).

The  $\text{NiO}_x$  was then generated by electrochemical oxidation of  $\text{Ni}^0$  upon scanning the poly1/PyrPDI- $\text{Ni}^0$  modified electrodes in a borate buffer solution at pH 9.2 for 50 consecutive scans at  $50 \text{ mVs}^{-1}$  between 0 and +1.1 V (Figure 10(b)). The formation of  $\text{NiO}_x$  is confirmed by the progressive growth of the  $\text{Ni}^{\text{II}}(\text{OH})_2/\text{Ni}^{\text{III}}(\text{O})(\text{OH})$  redox process as shown in Figure 10(b). For the cobalt, only 5 consecutive cycles over the 0 to +1.1 V potential range are required to fully generate the  $\text{CoO}_x$  (Figure 11(b)) (see Part I, Chapter 3). Even if the formation of  $\text{CoO}_x$  is not clearly visible because of the  $\text{Co}^{\text{II}}(\text{OH})_2/\text{Co}^{\text{III}}(\text{O})(\text{OH})$  redox system is difficult to observe, the catalytic current density up to  $\sim 3 \text{ mA cm}^{-2}$  at +1.1 V confirms the presence of the  $\text{CoO}_x$  as water oxidation catalyst.

The amount of nickel and cobalt loaded for these two electrodes was estimated by ICP-MS experiments after complete dissolution of the poly1/PyrPDI- $\text{MO}_x$  films in acidic conditions (see Experimental Section). It should be noted that the dissolution of the films was performed after the study of the evaluation of the photocatalytical activity of these electrodes under light irradiation (see below, section 2.3.3). Ni and Co loadings were estimated to be  $2.66 \times 10^{-8} \text{ mol cm}^{-2}$  and  $1.92 \times 10^{-8} \text{ mol cm}^{-2}$ , respectively. For a similar charge of 4 mC for Ni and Co deposition in C/poly1 films, loading were  $3.32 \times 10^{-8} \text{ mol cm}^{-2}$  and  $2.29 \times 10^{-8} \text{ mol cm}^{-2}$ , respectively (see Part 1, Chapters 2&3). Thus, for the same quantity of charge (4 mC), even if the amount of ammonium units is lower in the case of the poly1/PyrPDI copolymer, the amount of deposited Ni and Co corresponds to about 80-83% of that deposited into C/poly1 films.

Finally, we also verified that the reduction and oxidation processes accompanying the generation of the  $\text{MO}_x$  nanoparticles (Figures 10(a,b) and 11(a,b)) do not alter significantly the perylene by checking its electroactivity between 0 and -1.2 V vs Ag/AgCl. It appears that the first step reduction to electrogenerate the  $\text{Ni}^0$  nanoparticles by reduction at -1.4 V induces a slight decrease of the electroactivity of the reversible system by about 25%, and the second

oxidation step, no further decrease is observed (Figures 10(c)). Rather similar values of 23 and 5% have been obtained for the cobalt (Figures (Figure 11(c)). Since a large amount of the perylene dye is maintained after the deposition of the  $\text{MO}_x$  nanoparticles within the poly1/PyrPDI copolymer films, we have investigated the photoelectrochemical activity of these electrodes under light irradiation.

### 2.3.3. Photoelectrochemical activity for water oxidation with C/poly1/PyrPDI- $\text{MO}_x$ photoanodes ( $M = \text{Ni}$ and $\text{Co}$ )

The photoelectrocatalytic performances of the C/poly1/PyrPDI- $\text{MO}_x$  photonanodes were first investigated by slow linear sweep voltammetry from 0 to +1.1 V vs Ag/AgCl under visible light ( $\lambda = 400 - 700$  nm) in 0.1 M borate buffer at pH 9.2 (Figures 12(a) and 13(a), for  $M = \text{Ni}$  and  $\text{Co}$ , respectively). These performances were also compared with the same electrodes before the deposition of  $\text{MO}_x$ . A positive photocurrent starts to be produced at potential more positive than +0.6 V vs Ag/AgCl for the C/poly1/PyrPDI- $\text{MO}_x$  electrodes and drastically increases to reach very high value at +1.1 V. Indeed, at this potential, a photocurrent density high as  $7400 \mu\text{A cm}^{-2}$  is measured for the poly1/PyrPDI- $\text{NiO}_x$  electrode when the same electrode without  $\text{MO}_x$  produces only  $280 \mu\text{A cm}^{-2}$  (Figure 12(a)). For the poly1/PyrPDI- $\text{CoO}_x$  electrode, although lower, the photocurrent reaches  $1650 \mu\text{A cm}^{-2}$  to be compared to  $290 \mu\text{A cm}^{-2}$  for the same electrode without  $\text{CoO}_x$  nanoparticles (Figure 13(a)).

For comparison with a similar photoanode without SC, a photocurrent density of about  $200 \mu\text{A cm}^{-2}$  was obtained at +1.1 V vs Ag/AgCl for the ITO/PMPDI/ $\text{CoO}_x$  photoanode developed by Finke and coworkers<sup>10</sup> while ITO/PMPDI produces a photocurrent density of about  $10 \mu\text{A cm}^{-2}$  (see Part II, Chapter 1). The larger photocurrents obtained in our case for C/poly1/PyrPDI with and without  $\text{MO}_x$  loading is probably the result of the higher nanostructuration and higher amount of active materials deposited on the electrode surface, the PyrPDI dye as well as the  $\text{MO}_x$  water oxidation catalyst.

A measure of the photocurrent density was also performed with the C/poly1/PyrPDI- $\text{MO}_x$  electrodes and the corresponding electrodes without  $\text{MO}_x$  using 100 s transient illumination at three different applied bias of +0.49 V vs Ag/AgCl ( $\eta = 0$  V), +0.69 V ( $\eta = 0.2$  V) and +0.8 V ( $\eta = 0.3$  V) before and after loading of  $\text{MO}_x$  (Figures 12 and 13(b-d)). We chose to limit the anodic potential to +0.8 V, since at higher potential, a direct electrocatalytic water oxidation by the  $\text{MO}_x$  catalysts can occur (see Part I, Chapter 2).

At +0.49 V, an identical photocurrent density of  $14 \mu\text{A cm}^{-2}$  was measured for both anodes, with and without  $\text{NiO}_x$  (Figure 12(b)). At higher bias of 0.69 V, the poly1/PyrPDI and

poly1/PyrPDI-NiO<sub>x</sub> anodes showed photocurrent density of ~42 and 82  $\mu\text{A cm}^{-2}$ , respectively (Figure 12(c)). Interestingly, when the applied potential further increases to +0.80 V, a large increase of the photocurrent density is observed with the poly1/PyrPDI-NiO<sub>x</sub> anode reaching 750  $\mu\text{A cm}^{-2}$  while at this potential the photocurrent with poly1/PyrPDI remains close to that obtained at +0.69 V (56  $\mu\text{A cm}^{-2}$ ) (Figure 12(d)). The significantly higher photocurrent density obtained with poly1/PyrPDI-NiO<sub>x</sub> (about 13-fold enhancement) is consistent with a catalytic reaction of water oxidation occurring in presence of the NiO<sub>x</sub> water oxidation catalyst. However, the production of oxygen should be confirmed by oxygen detection experiments.

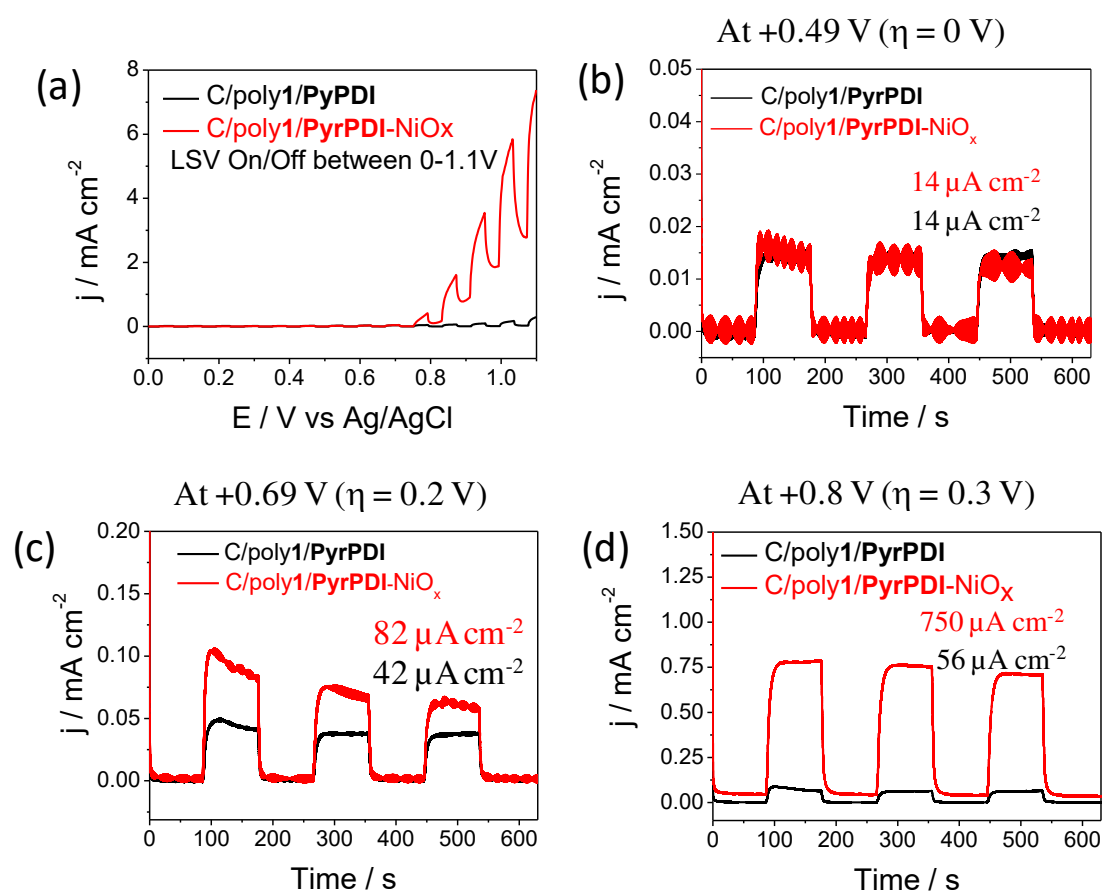


**Figure 12.** (a) Linear sweep voltammograms from 0.0 to +1.1 V after ON-OFF cycles of visible-light irradiation ( $\lambda = 400 - 700$  nm) in an aqueous borate buffer, 0.1M Na<sub>2</sub>SO<sub>4</sub>, 0.05 M NaOH, 0.1 M H<sub>3</sub>BO<sub>3</sub> (pH 9.2) of a C/poly1/PyrPDI electrode ( $\Gamma_{\text{PyrPDI}} = 1.79 \times 10^{-8}$  mol cm<sup>-2</sup>,  $\Gamma_{\text{polypyrrole}} = 7.2 \times 10^{-8}$  mol cm<sup>-2</sup>) (black), and under the same conditions after introduction of the nickel oxide, C/poly1/PyrPDI-NiO<sub>x</sub> (red) electrode. The scan rate is 2 mV s<sup>-1</sup>, lighting ON/OFF cycles of 40 sec each were applied. (b-d) Chronoamperograms after ON-OFF cycles of visible-light irradiation ( $\lambda = 400 - 700$  nm) of the same modified electrode under an applied potential of +0.49 V (b), +0.69 V (c) and +0.8 V vs Ag/AgCl (d), lighting ON/OFF cycles of 100 sec.

Similar results have been obtained for the anodes with cobalt (Figure 13(b-d)), although at +0.80 V, the photocurrent density measured of  $375 \mu\text{A cm}^{-2}$  remains lower than that obtained with poly1/PyrPDI-NiO<sub>x</sub> at the same potential (Figure 12(d)).

Regarding the stability, as shown in Figure 12(d) for C/poly1/PyrPDI-NiO<sub>x</sub> and C/poly1/PyrPDI, photocurrents at +0.8 V ( $\eta = 0.3$  V) remain relatively stable after several ON-OFF cycles of illumination of 40 sec. For the C/poly1/PyrPDI-CoO<sub>x</sub>, during the same period of time, an increase from 290 to  $374 \mu\text{A cm}^{-2}$  was measured that can be due to the generation of higher amount of CoO<sub>x</sub> from Co<sup>0</sup> oxidation concomitant with the water oxidation catalysis (Figure 13(d)).

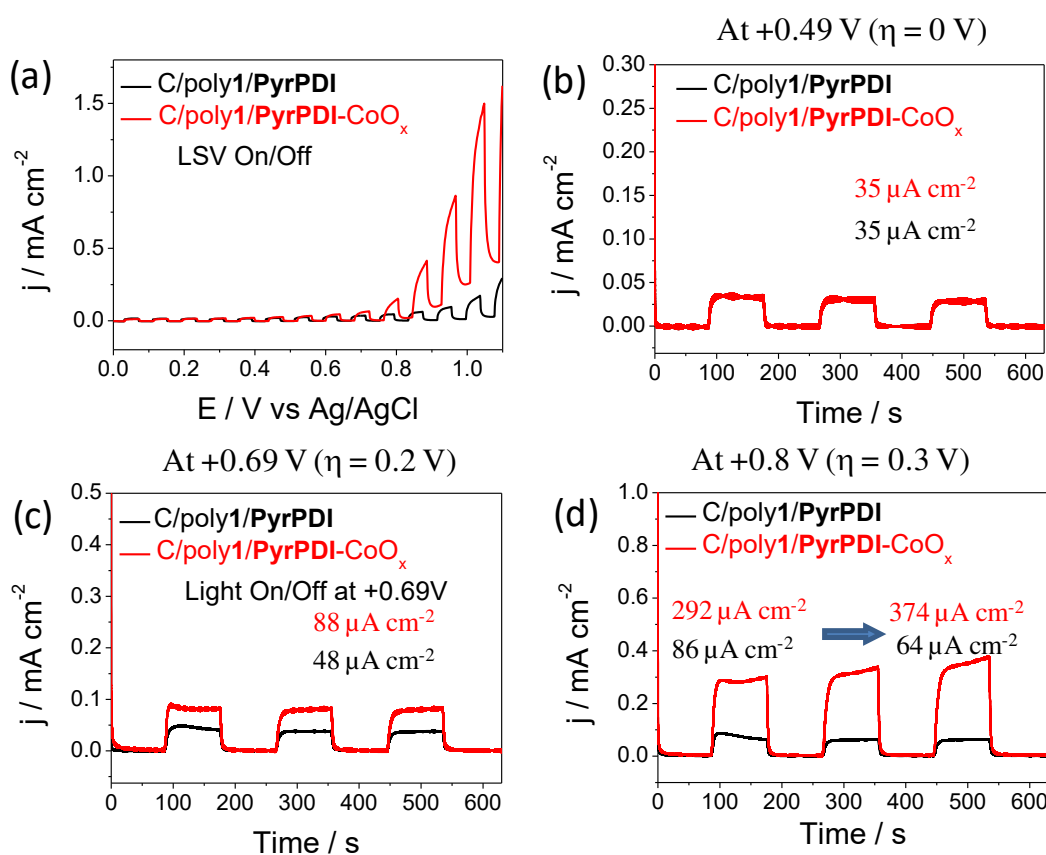


**Figure 13.** (a) Linear sweep voltammograms from 0.0 to +1.1 V after ON-OFF cycles of visible-light irradiation ( $\lambda = 400 - 700$  nm) in an aqueous borate buffer, 0.1M Na<sub>2</sub>SO<sub>4</sub>, 0.05 M NaOH, 0.1M H<sub>3</sub>BO<sub>3</sub> (pH 9.2) of a C/poly1/PyrPDI electrode ( $\Gamma_{\text{PyrPDI}} = 2.2 \times 10^{-8}$  mol cm<sup>-2</sup>,  $\Gamma_{\text{polypyrrole}} = 4.1 \times 10^{-8}$  mol cm<sup>-2</sup>) (black), and under the same conditions after introduction of the cobalt oxide, C/poly1/PyrPDI-CoO<sub>x</sub> (red) electrode. The scan rate is  $2 \text{ mV s}^{-1}$ , lighting ON/OFF cycles of 40 sec each were applied. (b-d) Chronoamperograms after ON-OFF cycles of visible-light irradiation ( $\lambda = 400 - 700$  nm) of the same modified electrode under an applied potential of +0.49 V (b), +0.69 V (c) and +0.8 V vs Ag/AgCl (d), lighting ON/OFF cycles of 100 sec.

### 3 – Conclusions

In this chapter hybrid photoanodes associating a perylene chromophore and a nickel or cobalt oxide as water oxidation catalysts have been elaborated. A neutral perylene diimine derivative having a high oxidation potential (+1.3 V *vs* Ag/AgCl) and two electropolymerizable pyrrole groups (**PyrPDI**) has been copolymerized with the cationic alkylammonium pyrrole monomer 1 already employed in the first part of this thesis (Part I, Chapters 2&3) to elaborate NiO<sub>x</sub> and CoO<sub>x</sub> anodes for water oxidation. The positive charge brought by the ammonium units have allowed the successful incorporation of NiO<sub>x</sub> and CoO<sub>x</sub> in the poly1/**PyrPDI** films deposited at the surface of carbon electrodes without significant deterioration of the perylene dye. The presence of MO<sub>x</sub> within the films has been confirmed by electrochemical measurements. Ni and Co loadings were also estimated by ICP-MS experiments and for the same charge of deposition (4 mC), the amount of deposited Ni and Co corresponds to about 80-83 % of that deposited into C/poly1 films without perylene dye (see part I, Chapters 2&3).

With these C/poly1/**PyrPDI**-MO<sub>x</sub> photoanodes, very high photocurrent up to 750 μA cm<sup>-2</sup> with nickel oxide and up to 375 μA cm<sup>-2</sup> with cobalt oxide have been measured under visible light illumination (λ = 400 - 700 nm) at a moderate overpotential of η = +0.3 V (E = +0.8 V *vs* Ag/AgCl) along with a relatively good stability over time. These photocurrent density values largely exceed those reached by similar “hybrid” photoanodes combining an organic dye and a metal oxide as catalyst (see Part I, Chapter 1). This can be due to larger amount of dye and catalyst deposited at the electrode surface (not limited to a single monolayer). Besides, the nanostructuring of our materials can also lead to a larger photocurrent. In addition the polymer matrix (polypyrrole film) can play a favorable role for maintaining the integrity of the MO<sub>x</sub> nanoparticles precluding their corrosion and thus improve the stability of the photoanodes.

Anyway, further experiments have to be performed to confirm the catalytic activity toward water oxidation by the detection of oxygen by gas chromatography and Clark electrode. Longer term photolysis will also be necessary to evaluate the stability and to measure the faradic yield of oxygen formation. Besides additional characterizations of the new photoactive nanocomposite materials have to be completed through deposition on ITO electrodes by different and complementary methods, such as Atomic Force Microscopy (AFM), Scanning Electron Microscopy (SEM), Energy-Dispersive X-Ray Spectroscopy

(EDX), X-ray Photoelectron Spectroscopy (XPS), Inductively Coupled Plasma Mass spectrometry (ICP-MS), and High-Resolution Transmission Electron Microscopy (HR-TEM) in order to evaluate the morphology, chemical composition, oxidation state of the metals and the size of the nanoparticles.

Finally, the photoanodes described in this chapter need further optimization for instance by the study the effect of the film thickness and dye loading (ratio **PyrPDI/1**) as well as the amount of  $\text{MO}_x$  loading on the photocatalytic activity. The introduction of a semi-conductor such as  $\text{TiO}_2$  deposited onto the ITO (or FTO) surface will be also of important to design DS-PEC that will required lower bias to operate.

## References

- (1) Youngblood, W. J.; Lee, S. A.; Maeda, K.; Mallouk, T. E. *Acc. Chem. Res.* **2009**, *42* (12), 1966–1973.
- (2) Swierk, J. R.; Mallouk, T. E. *Chem. Soc. Rev.* **2013**, *42* (6), 2357–2387.
- (3) Xu, P.; McCool, N. S.; Mallouk, T. E. *Nano Today* **2017**, *14*, 42–58.
- (4) Kirner, J. T.; Finke, R. G. *J. Mater. Chem. A* **2017**, *5*, 19560–19592.
- (5) Youngblood, W. J.; Lee, S. H. A.; Kobayashi, Y.; Hernandez-Pagan, E. A.; Hoertz, P. G.; Moore, T. A.; Moore, A. L.; Gust, D.; Mallouk, T. E. *J. Am. Chem. Soc.* **2009**, *131* (3), 926–927.
- (6) Zhao, Y.; Swierk, J. R.; Megiatto, J. D.; Sherman, B.; Youngblood, W. J.; Qin, D.; Lentz, D. M.; Moore, A. L.; Moore, T. A.; Gust, D.; Mallouk, T. E. *Proc. Natl. Acad. Sci.* **2012**, *109* (39), 15612–15616.
- (7) Swierk, J. R.; McCool, N. S.; Mallouk, T. E. *J. Phys. Chem. C* **2015**, *119* (24), 13858–13867.
- (8) Wei, P.; Hu, B.; Zhou, L.; Su, T.; Na, Y. *J. Energy Chem.* **2016**, *25* (3), 345–348.
- (9) Bledowski, M.; Wang, L.; Ramakrishnan, A.; Bétard, A.; Khavryuchenko, O. V.; Beranek, R. *ChemPhysChem* **2012**, *13* (12), 3018–3024.
- (10) Kirner, J. T.; Stracke, J. J.; Gregg, B. A.; Finke, R. G. *ACS Appl. Mater. Interfaces* **2014**, *6* (16), 13367–13377.
- (11) Kirner, J. T.; Finke, R. G. *ACS Appl. Mater. Interfaces* **2017**, *9* (33), 27625–27637.
- (12) Ronconi, F.; Syrgiannis, Z.; Bonasera, A.; Prato, M.; Argazzi, R.; Caramori, S.; Cristino, V.; Bignozzi, C. A. *J. Am. Chem. Soc.* **2015**, *137* (14), 4630–4633.
- (13) Bornoz, P.; Prévot, M. S.; Yu, X.; Guijarro, N.; Sivula, K. *J. Am. Chem. Soc.* **2015**, *137* (49), 15338–15341.
- (14) Swierk, J. R.; Méndez-Hernández, D. D.; McCool, N. S.; Liddell, P.; Terazono, Y.; Pahk, I.; Tomlin, J. J.; Oster, N. V.; Moore, T. A.; Moore, A. L.; Gust, D.; Mallouk, T. E. *Proc. Natl. Acad. Sci.* **2015**, *112* (6), 1681–1686.
- (15) Weingarten, A. S.; Kazantsev, R. V.; Palmer, L. C.; McClendon, M.; Koltonow, A. R.; Samuel, A. P. S.; Kiebal, D. J.; Wasielewski, M. R.; Stupp, S. I. *Nat Chem* **2014**, *6* (11), 964–970.
- (16) Weingarten, A. S.; Kazantsev, R. V.; Palmer, L. C.; Fairfield, D. J.; Koltonow, A. R.; Stupp, S. I. *J. Am. Chem. Soc.* **2015**, *137* (48), 15241–15246.
- (17) Choi, W.; Ko, H. C.; Moon, B.; Lee, H. *J. Electrochem. Soc.* **2004**, *151* (2), E80.
- (18) Deronzier, A.; Moutet, J. C. *Acc. Chem. Res.* **1989**, *22* (7), 249–255.
- (19) Lee, S. K.; Zu, Y.; Hermann, A.; Geerts, Y.; Müllen, K.; Bard, A. J. *J. Am. Chem. Soc.* **1999**, *121* (14), 3513–3520.
- (20) Würthner, F.; Thalacker, C.; Sautter, A.; Schärfl, W.; Ibach, W.; Hollricher, O. *Chem. - Eur. J.* **2000**, *6* (21), 3871–3886.
- (21) Genies, E. M.; Bidan, G.; Diaz, A. F. *J. Electroanal. Chem. Interfacial Electrochem.* **1983**, *149* (1), 101–113.

## General conclusion and perspectives

This thesis work has been devoted to the development of efficient anodes for electrocatalytic water oxidation based on nanocomposite materials in which nickel oxide ( $\text{NiO}_x$ ) or cobalt oxide ( $\text{CoO}_x$ ) nanoparticles have been inserted in a positively charged poly(pyrrole-alkylammonium) film (denoted poly**1**). These nanocomposite materials have been prepared by an easy all-electrochemical synthesis at the surface of an electrode. These nanocomposite anodes (poly**1**- $\text{NiO}_x$  and poly**1**- $\text{CoO}_x$ ) and their analogues, in which  $\text{NiO}_x$  or  $\text{CoO}_x$  has been deposited on electrode without poly**1** film, have been characterized by various electrochemical, physico-chemical and microscopic techniques.

As observed by TEM, the simple deposit of  $\text{NiO}_x$  on electrode exhibited quite big agglomerated nanoparticles of *ca.* 100 nm with a large size distribution ( $\pm 42$  nm), while the poly**1**- $\text{NiO}_x$  composite featured small crystalline  $\text{NiO}_x$  particles of 21 nm dispersed in the polymer film with a small size distribution ( $\pm 4$  nm), which confers a great nanostructuration, a high electroactive surface area and thus high electrocatalytic performance. These nickel oxide particles entrapped within the polypyrrole film, whose nature has been determined by coulometric titration to be  $\beta\text{-Ni}^{\text{III}}(\text{O})(\text{OH})$ , exhibits very high mass activity and TOF values for OER at pH 9.2 of  $1.12 \text{ A mg}^{-1}$  and  $0.17 \text{ s}^{-1}$  at an overpotential of 0.61 V. Under basic conditions at pH 14, the poly**1**- $\text{NiO}_x$  nanocomposite anode presents high mass activity and TOF values of  $1.28 \text{ A mg}^{-1}$  and  $0.19 \text{ s}^{-1}$  at an overpotential of 0.35 V, outperforms the nickel-based anodes of the literature (undoped by Fe) and those using precious metal oxides, such as  $\text{RuO}_2$  and  $\text{IrO}_2$ .

In contrast to the nickel-based anodes, TEM images revealed similar nanometric sizes of amorphous  $\text{CoO}_x$  particles (31 nm) for the simple deposit and the composite, even if particles within poly**1**- $\text{CoO}_x$  are not agglomerated and are well dispersed into the polymer film as previously observed within poly**1**- $\text{NiO}_x$ , conferring a high electroactive surface area and thus high OER electrocatalytic performances. These poly**1**- $\text{CoO}_x$  displays exceptional mass activity and TOF values for OER at mildly basic pH 9.2 of  $2.75 \text{ A mg}^{-1}$  and  $0.41 \text{ s}^{-1}$  at an overpotential of 0.61 V, and an unprecedented Tafel slope of  $23 \text{ mV dec}^{-1}$ . Under basic conditions at pH 14, the cobalt oxide-polypyrrole nanocomposite electrode, with a high mass activity and TOF values of  $4.58 \text{ A mg}^{-1}$  and  $0.69 \text{ s}^{-1}$  at an overpotential of 0.35 V, outperforms the poly**1**- $\text{NiO}_x$  nanocomposite and the poly**1**- $\text{IrO}_x$  anode previously reported by our group. Otherwise, at mildly basic pH, the cobalt and nickel oxides electrogenerated into polypyrrole-

alkylammonium films appeared also more efficient than the cobalt and nickel oxide films electrogenerated on a naked electrode surface (without poly1) by the same electrochemical procedure, highlighting the beneficial role of the polypyrrole matrix in generating small and non-agglomerated metal oxide particles with high OER activity.

This very promising way to elaborate nanocomposite material paves the way for the design of new anodes very active for OER by using other earth abundant metals, and also mixed metal oxide nanoparticles such as NiFeO<sub>x</sub>, known to be highly efficient and stable towards water oxidation (see the perspectives below).

Our strategy has been successfully extended to the design of photoanodes for photocatalytic water oxidation by combining these nanocomposite materials containing a nickel or cobalt oxide with a robust organic dye of the perylene diimine family. Even if further experiments have to be performed in view to optimize these photoanodes, the results already obtained in terms of photocurrents under visible light irradiation are very promising. Indeed, photocurrent as high as 750  $\mu\text{A cm}^{-2}$  with nickel oxide and 375  $\mu\text{A cm}^{-2}$  with cobalt oxide have been measured at a moderate overpotential of  $\eta = +0.3 \text{ V}$  ( $E = +0.8 \text{ V vs Ag/AgCl}$ ) along with a relatively good stability over time. These values largely exceed those reached by similar “hybrid” photoanodes combining an organic dye and a metal oxide as catalyst already published. This can be due to a completely different approach that we use to prepare the dye/catalyst assembly than those generally used in literature, leading to a larger amount of dye and catalyst deposited at the electrode surface. In addition, the probable good distribution of the catalyst and dye in the nanocomposite material can promote the electron transfers between both entities. Further experiments have to be performed to characterize this new photoactive nanocomposite material and to confirm the catalytic activity toward water oxidation by the quantification of the oxygen produced.

Perspectives of this thesis work will be to develop and characterize new nanostructured electrode materials for the design of more efficient anodes and photoanodes for the catalytic oxidation of water.

An objective will be to improve the efficiency of the poly(pyrrole-alkylammonium)/MO<sub>x</sub> (M = Ni or Co) anodes developed by doping the metal oxide with a second metal M'. Indeed, as discussed in the first chapter of this thesis, the catalytic performances of certain metal oxides are significantly increased (*i.e.* decrease of the overpotential and increase of the catalytic current) by the introduction of a second metal or alkaline earth metal in certain proportions,

for example 40% of Fe in Ni oxide. The mixed metal oxide active nanoparticles ( $M(M')O_x$ ) could be electrogenerated *in situ* following the same strategy used for monometallic  $MO_x$  from a mixture of anionic metal complexes of the respective metal salt in the positively charged ammonium pyrrole films. With this method, it will be easy to test increasing amounts of  $M'$  anionic complex in order to determine the best  $M/M'$  ratio leading to the most efficient anodes for water oxidation (overpotential and catalytic current).

Another objective will be to develop a new, even simpler and more versatile strategy for the development of these nanomaterials, allowing the direct incorporation of metal cations ( $Co^{2+}$ ,  $Ni^{2+}$ ,  $Fe^{2+}$ ,  $Mn^{2+}$  ...) without having to generate in solution negatively charged complexes  $[M(L)_x]^{n-}$  which can be difficult with some metallic salts. This can be achieved thanks to the use of a negatively charged polymer matrix. In that case, metal oxide active nanoparticles ( $M(M')O_x$ ) can be electrogenerated *in situ* by simple oxidation of the metallic cations  $M^{n+}$  dispersed in the negatively charged polymeric matrix, or, if this method is not effective, by reduction in  $M^0(M')^0$  and then oxidation to  $M(M')O_x$ .

Regarding the elaboration of photoanode, to go one step further, it will be important to introduce in the platform of the perylene dye, in addition to the electropolymerizable groups, additional positively or negatively charged substituents. Thus direct incorporation of anionic metal complexes in a positively charged perylene or cationic metal salt in the case of a negatively charged perylene will be possible without resorting to the more complex elaboration of copolymers.

The electroactive materials for photoanodes will be first deposited in a carbon or ITO electrode similarly that for the elaboration of the anode. In a second stage, in view to improve the photocatalytic performances of the photoanodes, DS-PEC will be designed by electrodeposition of a thin layer of a *n*-type semiconductor like  $TiO_2$  at the surface of the ITO or FTO electrode before the electrogeneration of the nanocomposite materials.

Finally, similar strategies are also envisaged to elaborate (photo)cathodes for hydrogen production (HER reaction). Nickel and cobalt metallic nanoparticles are indeed well-known to be efficient  $H_2$ -evolution catalysts. Other effective HER catalysts like  $MoS_x$  could be also introduced within a perylene nanocomposite in view to construct a photocathode  $H_2$  production with only earth abundant elements.



## Experimental Section



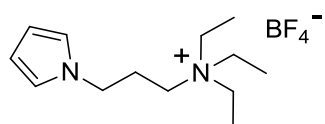
## Index

1- Chemicals and Reagents.....	160
2- Electrodes, Electrochemical Cells and Instrumentation .....	160
3- Preparation of the Nanocomposite Film Modified Electrodes .....	161
3.1- Electrosynthesis of Poly(pyrrole-alkylammonium) Film Modified Electrodes .....	161
3.2- Electrodeposition of Metallic Nanoparticles ( $M^0$ ) and Electrooxidation into Metal Oxide $MO_x$ (M= Ni or Co).....	163
3.3- Electrodeposition of poly1/PyrDPI- $MO_x$ Nanocomposite.....	164
4- Determination of M contents (q) on Electrodes by Inductively Coupled Plasma Mass Spectrometry (ICP-MS).....	164
5- Determination of the Average Number of Electron Consumed per Nickel Deposited on Electrodes.....	165
6- Capacitance Measurement.....	165
7- Calculation of Mass Activity and Turnover Frequency (TOF).....	166
8- Tafel Plot.....	167
9- Atomic Force Microscopy (AFM) Observation.....	167
10- Transmission Electron Microscopy (TEM) Observation and Selected Area Electron Diffraction (SAED).....	168
11- Selected Area Electron Diffraction (SAED) Analysis for Nickel.....	168
12- Scanning Electron Microscopy (SEM) Analysis for Cobalt.....	169
13- Irradiation Lamp for Photoelectrolysis.....	170
References.....	171

## 1 – Chemicals and Reagents

The monomer (3-pyrrole-1-yl-propyl)-triethylammonium tetrafluoroborate, denoted **1** (Scheme S1), was prepared as previously reported.<sup>1</sup> Nickel(II) sulfate hexahydrate ( $\text{NiSO}_4 \cdot 6\text{H}_2\text{O}$ , 99% Acros), Cobalt(II) Sulfate ( $\text{CoSO}_4$ , Prolabo), sodium oxalate ( $\text{NaC}_2\text{O}_4$ , 99% Prolabo), boric acid ( $\text{H}_3\text{BO}_3$ , 99.5% Normapur), acetonitrile (Fisher, HPLC grade), sodium sulfate ( $\text{Na}_2\text{SO}_4$ , 99% Laurylab), sodium hydroxide ( $\text{NaOH}$ , 99% Laurylab), potassium hydroxide ( $\text{KOH}$ ,  $\geq 85\%$  Prolabo) and tetra-*n*-butylammonium perchlorate ( $[\text{Bu}_4\text{N}]\text{ClO}_4$ , Fluka puriss) were purchased from commercial suppliers. All reagents and solvents were used as received. Distilled water was obtained from an Elga water purification system (milli-Q system, Purelab option, 15.0 M $\Omega$ .cm, 24 °C).

### Scheme S1. Pyrrole-based monomer (1).



## 2 – Electrodes, Electrochemical Cells and Instrumentation.

The electrochemical experiments were performed using a conventional three-electrode system. Electroanalytical experiments were performed using a CHI 660B Electrochemical analyser (CH Instruments). Electrosynthesis of nanocomposites and bulk electrolysis were carried out using an EGG PAR Model 273 potentiostat. Potentials were referred to Ag/AgCl (3 M KCl in water) or Ag/AgNO<sub>3</sub> (10 mM AgNO<sub>3</sub> in CH<sub>3</sub>CN + 0.1 M  $[\text{Bu}_4\text{N}]\text{ClO}_4$ ) references electrodes in aqueous and acetonitrile solutions, respectively. Potentials referred to the Ag/AgCl (3 M KCl) system can be converted to the reversible hydrogen electrode (RHE)<sup>2</sup> according to the Nernst equation S1:

$$E_{\text{RHE}} = E_{\text{Ag/AgCl}} + 0.059 \times \text{pH} + E_{\text{Ag/AgCl}}^{\circ} \quad (\text{S1})$$

where  $E_{\text{Ag/AgCl}}^{\circ} = 0.199 \text{ V vs NHE}$  at 25°C and NHE is the normal hydrogen electrode.

Potentials referred to the Ag/AgNO<sub>3</sub> reference electrode can be converted to Ag/AgCl (3 M KCl) by adding 330 mV.

For analytical experiments and films deposition of poly $\mathbf{1}$ - $M^0$  ( $M = \text{Ni}$  or  $\text{Co}$ ), or for direct deposition of  $M^0$ , glassy carbon working electrodes (denoted C, 3 mm in diameter corresponding to a surface of  $0.071 \text{ cm}^2$ ) were used. These electrodes were polished with  $1 \mu\text{m}$  diamond paste before coating. Films of poly $\mathbf{1}$ - $M^0$ , or direct deposition of  $\text{Ni}^0$  or  $\text{Co}^0$  were also deposited onto indium tin oxide-coated glass electrodes (ITO of 0.4, 0.5 and  $1 \text{ cm}^2$ , 30 Ohms, from Solems) for microscopy characterization. For electrodeposition of poly $\mathbf{1}$ - $\text{Ni}^0$  or poly $\mathbf{1}$ - $\text{Co}^0$ , or direct deposition of  $\text{Ni}^0$  or  $\text{Co}^0$  and the subsequent oxidation of  $\text{Ni}^0$  to  $\text{NiO}_x$  or  $\text{Co}^0$  to  $\text{CoO}_x$ , the auxiliary electrode was either a platinum plate ( $\approx 2 \text{ cm}^2$ ) for the C working electrode or a circular platinum grid in the case of the ITO working electrode. All experiments were performed at room temperature under argon atmosphere. The overpotential ( $\eta$ ) applied to the working electrode for performing water oxidation was calculated from the following equation S2:

$$\eta = E_{\text{RHE}} - 1.23 \text{ V} \quad (\text{S2})$$

where 1.23 V is standard potential of water oxidation reaction at pH 0.

### 3. Preparation of the Nanocomposite Film Modified Electrodes.

#### 3.1. Electrosynthesis of Poly(pyrrole-alkylammonium) Film Modified Electrodes.

Polymer films (denoted poly $\mathbf{1}$ ) were deposited either on C or ITO electrodes, by potentiostatic oxidative electropolymerization at  $E_{\text{app}} = +0.95 \text{ V vs Ag/AgNO}_3$  for C and  $+1.1 \text{ V}$  for ITO from a 4 mM solution of  $\mathbf{1}$  in  $\text{CH}_3\text{CN}$  containing  $[\text{Bu}_4\text{N}]\text{ClO}_4$  (0.1 M) as supporting electrolyte, without stirring. The polymerization of  $\mathbf{1}$  was monitored through the anodic charge recorded during electrolysis (see figure 1, chapter II). Typically, the anodic charge used for polymerization of  $\mathbf{1}$  is 4 and 28 mC, for nickel experiments and 4 and 57 mC for cobalt, for C and ITO electrodes, respectively, both corresponding to  $0.056 \text{ C cm}^{-2}$ . The amount of pyrrole units in the films and thus, the apparent surface coverage in ammonium units  $\Gamma_{\text{N}^+}$  ( $\text{mol cm}^{-2}$ ) were determined by the integration of the polypyrrole oxidation wave by cycling between 0.0 to  $+0.7 \text{ V}$  ( $\text{vs Ag/AgNO}_3$ ) at a low scan rate ( $10 \text{ mV s}^{-1}$ ) assuming that one in three pyrrole units is oxidized,<sup>3</sup> after transfer of the poly $\mathbf{1}$  modified electrodes into a  $\text{CH}_3\text{CN}$  solution containing only 0.1 M  $[\text{Bu}_4\text{N}]\text{ClO}_4$  (see figure 2, chapter II). The charge obtained from this integration (denoted  $Q_{\text{exp}}$ ), is used to calculate the quantity of poly $\mathbf{1}$  ( $q_{\text{exp}}$  expressed in mol) deposited on C electrode following the equation S3:

$$q_{exp} = \frac{Q_{exp}}{n_{e^-} \times F} \quad (S3)$$

Where F is the Faraday constant (96500 C mol<sup>-1</sup>) and n<sub>e<sup>-</sup></sub> is the number of electron involved in the oxidation of polypyrrole which is equal to 0.33.

Γ<sub>N<sup>+</sup></sub> values ranging from 1.1 × 10<sup>-7</sup> to 1.2 × 10<sup>-7</sup> mol cm<sup>-2</sup> for nickel and cobalt experiments were obtained for deposition of poly1 films onto C electrode (surface of 0.071 cm<sup>2</sup>), denoted C/poly1 using a polymerization charge of 4 mC which correspond to an electropolymerization yield in the range of 45 to 51% for nickel and cobalt experiments. Γ<sub>N<sup>+</sup></sub> values ranging from 4.5 × 10<sup>-7</sup> to 5.5 × 10<sup>-7</sup> mol cm<sup>-2</sup> for nickel and cobalt experiments were obtained for deposition of poly1 films onto ITO electrode (surface of 0.5 cm<sup>2</sup> for nickel and 1.0 cm<sup>2</sup> for cobalt), denoted ITO/poly1 using a polymerization charge of 28 mC for nickel and 57 mC for cobalt which correspond to an electropolymerization yield in the range of 26 to 32%. The electropolymerization yield was determined from the equation S4:

$$Yield(\%) = \frac{q_{exp}}{q_{theo}} \times 100 \quad (S4)$$

The theoretical quantity of polypyrrole deposited on C electrode (q<sub>theo</sub> expressed in mol) was determined from the equation S5:

$$q_{theo} = \frac{Q_{appl}}{n_{e^-} \times F} \quad (S5)$$

Where Q<sub>appl</sub> is the charge used for poly1 electrodeposition (4 or 28 or 57 mC), F is the Faraday constant and n<sub>e<sup>-</sup></sub> is number of electron involved in the electropolymerization of pyrrole unit, which is equal to 2.33.<sup>3</sup> Indeed, the electropolymerization requires that two pyrroles are oxidized, thus two electrons are needed to promote the propagation of the pyrrole chain. In addition, the potential applied (e.g. +0.95 V vs Ag/AgNO<sub>3</sub> for C electrode) for the oxidation of pyrrole monomer is higher than the oxidation potential of the polypyrrole film, thus 0.33 electron is also necessary (*vide supra*). The theoretical quantity of polypyrrole (q<sub>theo</sub>) for 4 and 28 mC of charge were determined to be 1.78 × 10<sup>-8</sup> mol and 1.25 × 10<sup>-7</sup> mol, respectively for nickel experiment, and 1.78 × 10<sup>-8</sup> mol and 2.55 × 10<sup>-7</sup> mol for 4 and 57 mC for cobalt experiment, respectively.

### 3.2. Electrodeposition of Metallic Nanoparticles ( $M^0$ ) and Electrooxidation into Metal Oxide $MO_x$ ( $M = Ni$ or $Co$ )

Before the electrodeposition of nickel or cobalt, in order to have an optimum incorporation of the anionic nickel or cobalt oxalate complex,  $[Ni(C_2O_4)_2]^{2-}$  or  $[Co(C_2O_4)_2]^{2-}$ , within the poly1 film, the C/poly1 and ITO/poly1 working electrodes were soaked during 1 h in an aqueous solution 0.1 M  $H_3BO_3$  and 0.1 M  $Na_2SO_4$  (pH 6.0) of 1 mM  $NiSO_4$  and 5mM  $Na_2C_2O_4$  for nickel, and 4 mM  $CoSO_4$  and 20 mM  $Na_2C_2O_4$  for cobalt (under stirring for C electrodes and without stirring for ITO electrodes).<sup>4</sup> The electrodeposition of nickel(0) or cobalt(0) within poly1 films was then performed by a controlled-potential reduction of the C/poly1 modified electrode at  $E_{app} = -1.4$  or  $-1.3$  V vs Ag/AgCl ( $-1.6$  or  $-1.5$  V for ITO/poly1) in this nickel or cobalt oxalate solution under an argon atmosphere. Similarly to the poly1 deposition described above, the charge used for nickel and cobalt electrodeposition is 4 mC for C/poly1 and 28 mC (57 mC for cobalt) for ITO/poly1, both corresponding to  $0.056$  C  $cm^{-2}$ . For comparative studies, an electrodeposition of  $Ni^0$  or  $Co^0$  on naked C and ITO electrodes was also performed following the same electrochemical procedure, but without prior soaking the electrode in the nickel or cobalt oxalate solution. The *in-situ* electrochemical oxidation (anodization) of  $Ni^0$  to  $NiO_x$  or  $Co^0$  to  $CoO_x$  was carried out *via* 50 and 5 repeated cyclic voltammetry scans of the poly1- $Ni^0$  or poly1- $Co^0$  modified electrodes (or  $Ni^0$  or  $Co^0$  modified electrodes) from 0 to +1.2 V vs Ag/AgCl (scan rate  $50$  mV  $s^{-1}$ ) in aqueous solution (pH 9.2) of 0.1 M  $H_3BO_3$  and 0.05 M NaOH. It is worthnoting that in the case of poly1- $Co^0$ , the oxidations of  $Co^0$  to  $CoO_x$  is mainly operated by  $O_2$  present in air or in solution and the 5 repeated cycles are performed to ensure the complete oxidation of cobalt on the electrode. The loading of nickel or cobalt deposited on C electrodes (denoted  $\Gamma_{Ni}$  or  $\Gamma_{Co}$ ) was estimated by ICP-MS (see below). Typically, the  $\Gamma_{Ni}$  values range from  $3.13 \times 10^{-8}$  to  $3.51 \times 10^{-8}$  mol  $cm^{-2}$  for C/poly1- $NiO_x$  electrodes and from  $1.16 \times 10^{-8}$  to  $1.21 \times 10^{-8}$  mol  $cm^{-2}$  respectively for C/ $NiO_x$  electrodes. Meanwhile the  $\Gamma_{Co}$  values range from  $1.02 \times 10^{-8}$  to  $3.56 \times 10^{-8}$  mol  $cm^{-2}$  for C/poly1- $CoO_x$  electrodes and from  $3.96 \times 10^{-8}$  to  $8.70 \times 10^{-8}$  mol  $cm^{-2}$  for C/ $CoO_x$  electrodes.

### 3.3. Electrodeposition of poly1/PyrDPI-MO<sub>x</sub> Nanocomposite.

The synthesis of the perylene diimine, **PyrDPI**, was prepared according to the publication of Lee et. al.<sup>5</sup> Copolymerization of poly1/PyrDPI were obtained by electropolymerization of 4 mC 0.5 mM **PyrDPI** with 1 mM **1** on C electrodes in CH<sub>3</sub>CN/ CH<sub>2</sub>Cl<sub>2</sub> (1/1) solution with 0.05 M of [Bu<sub>4</sub>N]ClO<sub>4</sub> by chronoamperometry at applied potential of 0.95 V vs Ag/AgCl. Electrodeposition of MO<sub>x</sub> (M = Ni or Co) into the poly1/PyrDPI films were performed according to section 3.2.

### 4. Determination of M Contents (q) on Electrode by Inductively Coupled Plasma Mass Spectrometry (ICP-MS).

The C/poly1-NiO<sub>x</sub> and C/poly1-CoO<sub>x</sub> ( $\Gamma_N^+ = 1.2 (\pm 0.1) \times 10^{-7}$  mol cm<sup>-2</sup>), and C/NiO<sub>x</sub> or C/CoO<sub>x</sub> films on C electrodes (3 mm diameter), prepared with a charge of 4 mC for poly1 and for Ni<sup>0</sup> or Co<sup>0</sup>, were dried in air and dissolved in 5 mL of an acidic aqueous solution containing 2 and 4 % HNO<sub>3</sub> for nickel and cobalt, respectively. 15 min in this acidic solution is needed to entirely dissolve the poly1/NiO<sub>x</sub> and NiO<sub>x</sub> films, meanwhile is needed of 6h to complete dissolution of the poly1/CoO<sub>x</sub> and CoO<sub>x</sub> films. The complete films dissolution was then verified by the absence of the Ni<sup>II</sup>(OH)<sub>2</sub>/Ni<sup>III</sup>(O)(OH) or Co<sup>II</sup>(OH)<sub>2</sub>/Co<sup>III</sup>(O)(OH) redox process and of the catalytic current of water oxidation in the cyclic voltammogram. The concentration of nickel or cobalt within the acidic solutions was analyzed by inductively coupled plasma-mass spectrometry (ICP-MS) using a Thermo X serie II spectrometer (Thermo Electron, Bremen, Germany) equipped with an impact bead spray chamber and a standard nebulizer (1 mL min<sup>-1</sup>).

<sup>60</sup>Ni and <sup>59</sup>Co isotopes were selected for the measurement and <sup>103</sup>Rh isotope was used as internal standard. Polyatomic interferences were eliminated using the collision cell mode. The concentrations were obtained using an external calibration curve. Thus, the Ni content (q) was estimated to be c.a.  $2.35 \pm 0.14$  and  $0.84 \pm 0.18$  nmol respectively for C/poly1-NiO<sub>x</sub> and C/NiO<sub>x</sub> electrodes which correspond respectively to Ni loading of  $33.2 \pm 1.9$  and  $11.9 \pm 0.2$  nmol cm<sup>-2</sup>. Meanwhile Co content (q) was estimated to be  $1.63 \pm 0.9$  and  $4.5 \pm 1.68$  nmol respectively for C/poly1-CoO<sub>x</sub> and C/CoO<sub>x</sub> electrodes which correspond respectively to Co loading of  $22.95 \pm 12.72$  and  $63.36 \pm 23.71$  nmol cm<sup>-2</sup>.

## 5. Determination of the Average Number of Electron Consumed per Nickel Deposited on Electrodes.

The mean number of electron consumed per nickel site (denoted  $n_{e^-/Ni}$ ) present on C/poly1-NiO<sub>x</sub> ( $\Gamma_{Ni^{+}} = 1.2 \times 10^{-7} \text{ mol cm}^{-2}$ ,  $\Gamma_{Ni} = 3.3 \times 10^{-8} \text{ mol cm}^{-2}$ ) and C/NiO<sub>x</sub> ( $\Gamma_{Ni} = 1.2 \times 10^{-8} \text{ mol cm}^{-2}$ ) electrodes was calculated from the experimental charge ( $Q_{exp}$ ) used for the reduction of Ni<sup>III</sup>(O)(OH) to Ni<sup>II</sup>(OH)<sub>2</sub> and from the Ni content ( $q$ , determined from ICP-MS) on these electrodes using the following equation S6:

$$n_{e^-/Ni} = \frac{Q_{exp}}{q \times F} \quad (S6)$$

Where  $F$  is the Faraday constant ( $96500 \text{ C mol}^{-1}$ ),  $Q_{exp}$  and  $q$  are respectively expressed in C and mol.

Basically, after the anodization process in the aqueous borate buffer solution at pH 9.2 (see above), the C/poly1-NiO<sub>x</sub> and C/NiO<sub>x</sub> electrodes were maintained at a potential of  $E = + 0.90 \text{ V vs Ag/AgCl}$  for 200 s in order to oxidize all the Ni<sup>II</sup>(OH) into Ni<sup>III</sup>(O)(OH), and then swept from +0.90 to 0 V and back to +1.2 V at a scan rate  $50 \text{ mV s}^{-1}$ . The experimental charge ( $Q_{exp}$ ) was obtained from the integration of the cathodic peak of the Ni<sup>II</sup>(OH)<sub>2</sub>/Ni<sup>III</sup>(O)(OH) redox process in the cyclic voltammogram, the anodic peak being ruled out for the determination of the  $n_{e^-/Ni}$  value since it should contain OER process. A  $n_{e^-/Ni}$  value equal or superior to 1 indicates that all nickel sites are electrochemically accessible, and thus this value allows estimating the average oxidation state of nickel deposited on electrode.<sup>6-11</sup> Conversely, a  $n_{e^-/Ni}$  value inferior to 1 allows only estimating the ratio of the number of effective catalytically active sites to the theoretical number of active sites.<sup>12</sup> Indeed, a  $n_{e^-/Ni}$  value  $< 1$  could be due to the fact that only a part of NiO<sub>x</sub> film exhibits the  $\beta$ -Ni<sup>III</sup>(O)(OH) or  $\gamma$ -Ni<sup>IV</sup>(O)(OH) phases (the rest being most probably Ni<sup>II</sup>(OH)<sub>2</sub> or Ni<sup>II</sup>O) and/or that only the surface of the NiO<sub>x</sub> film is catalytically active towards water oxidation.<sup>12</sup>

This calculation was not performed for cobalt due to the fact that the Co<sup>II</sup>(OH)<sub>2</sub>/Co<sup>III</sup>(O)(OH) redox system is present just in the direct deposition.

## 6. Capacitance Measurement.

The double-layer capacitance ( $C_{DL}$  expressed in  $\text{F cm}^{-2}$ ) of C/poly1-NiO<sub>x</sub> ( $\Gamma_{Ni^{+}} = 1.2 \times 10^{-7} \text{ mol cm}^{-2}$ ,  $\Gamma_{Ni} = 3.3 \times 10^{-8} \text{ mol cm}^{-2}$ ) or C/poly1-CoO<sub>x</sub> ( $\Gamma_{Ni^{+}} = 1.2 \times 10^{-7} \text{ mol cm}^{-2}$ ,  $\Gamma_{Co} = 2.01 \times$

$10^{-8} \text{ mol cm}^{-2}$ ), and C/NiO<sub>x</sub> ( $\Gamma_{\text{Ni}} = 1.2 \times 10^{-8} \text{ mol cm}^{-2}$ ) or C/CoO<sub>x</sub> ( $\Gamma_{\text{Co}} = 6.10 \times 10^{-8} \text{ mol cm}^{-2}$ ) electrodes was determined from non-faradaic capacitive current densities ( $j_c$ ) measured at 0 V vs Ag/AgCl by cyclic voltammetry under scanning at various scan rates (from 10 to 200 mV s<sup>-1</sup>) between -0.1 and +0.1 V in aqueous solution (pH 9.2) of 0.1 M H<sub>3</sub>BO<sub>3</sub> and 0.05 M NaOH. The  $j_c$  value is related to the double-layer capacitance ( $C_{\text{DL}}$ ) and the scan rate ( $\nu$ ) following the equation S7:

$$j_c = C_{\text{DL}} \times \nu \quad (\text{S7})$$

where  $j_c$ ,  $C_{\text{DL}}$  and  $\nu$  values are expressed respectively in A cm<sup>-2</sup>, F cm<sup>-2</sup> and V s<sup>-1</sup>.

Consequently, the  $C_{\text{DL}}$  value corresponds to the slope obtained from the plot of  $j_c$  in function of  $\nu$ .

## 7. Calculation of Mass Activity and Turnover Frequency (TOF).

The TOF value (expressed in s<sup>-1</sup>) at a given overpotential is usually defined as mole of O<sub>2</sub> produced per mole of Ni per second, O<sub>2</sub> produced being measured by gas chromatography. The TOF values for each Ni based electrode could be also calculated from electrochemical experiments following the equation S8:

$$TOF = \frac{j \times S}{4 \times F \times n} \quad (\text{S8})$$

Where  $j$  is the catalytic current density (A cm<sup>-2</sup>) at a given overpotential,  $S$  is the surface of the electrode (0.071 cm<sup>2</sup>),  $F$  is the Faraday constant (*vide supra*) and  $n$  is the molar number of nickel deposited on electrode. This TOF value corresponds to its lower limit (TOF<sub>min</sub>) since it was considered that all nickel or cobalt sites deposited on the electrode are active for water oxidation. The quantity of Ni or Co deposited was estimated by ICPMS (*vide supra*).

The mass activity (expressed in A mg<sup>-1</sup>) at a given overpotential is calculated from the equation S9:

$$\text{Mass activity} = \frac{i}{m} \quad (\text{S9})$$

Where  $i$  is the catalytic current at a given overpotential (A) and  $m$  is the mass of nickel deposited on electrode (mg).

## 8. Tafel Plot.

The Tafel curves were plotted as the overpotential ( $\eta$ ) in function of the current density in logarithm form and should be linear following the equation S10:

$$\eta = a + b \log j \quad (\text{S10})$$

Where  $j$  ( $\text{A cm}^{-2}$ ) is the current density at a given overpotential ( $\eta$  (V)) and  $b$  is the Tafel slope ( $\text{V dec}^{-1}$ ). The current-overpotential data collected for Tafel plot were obtained by carrying out electrolyses with C/poly1-MO<sub>x</sub> or C/MO<sub>x</sub> (M = Ni or Co) rotating disc electrodes (1000 rpm) in aqueous borate buffer solution (pH 9.2) at various overpotentials between +0.42 V and +0.51 V (*i.e.* between +0.91 and +1.0 V *vs* Ag/AgCl). For each imposed potential, the current data were collected during electrolysis when the latter reaches a steady state after *c.a.* 600 s. The rotation of the electrode for the Tafel plot data collection allows reducing the mass transport effect on the catalytic current. High and low overpotentials (respectively above 0.51 V and below 0.41 V) were ruled out for Tafel analysis in order to avoid respectively a strong oxygen evolution inducing mass transport limitations, and the Ni<sup>II</sup>(OH)<sub>2</sub>/Ni<sup>III</sup>OOH or Co<sup>II</sup>(OH)<sub>2</sub>/Co<sup>III</sup>OOH redox couple, that could lead to erroneous interpretations of the Tafel slope. The  $\eta$  overpotentials were corrected by subtracting the ohmic potential drop ( $iR$ ). The solution resistance ( $R$ ) was estimated to be 568 and 557  $\Omega$  respectively for C/poly1-NiO<sub>x</sub> and C/NiO<sub>x</sub>, and 574 and 481  $\Omega$  for C/poly1-CoO<sub>x</sub> and C/CoO<sub>x</sub>, respectively. The Tafel analyses were obtained with C/poly1-NiO<sub>x</sub> ( $\Gamma_{\text{N}^+} = 1.2 \times 10^{-7}$  mol cm<sup>-2</sup>,  $\Gamma_{\text{Ni}} = 3.3 \times 10^{-8}$  mol cm<sup>-2</sup>) and C/NiO<sub>x</sub> ( $\Gamma_{\text{Ni}} = 1.2 \times 10^{-8}$  mol cm<sup>-2</sup>), and C/poly1-CoO<sub>x</sub> ( $\Gamma_{\text{N}^+} = 1.2 \times 10^{-7}$  mol cm<sup>-2</sup>,  $\Gamma_{\text{Co}} = 2.01 \times 10^{-8}$  mol cm<sup>-2</sup>), and C/CoO<sub>x</sub> ( $\Gamma_{\text{Co}} = 6.10 \times 10^{-8}$  mol cm<sup>-2</sup>) for electrodes that have been prepared with 4 mC of Ni, Co and poly1 as described above.

## 9. Atomic Force Microscopy (AFM) Observation.

The NiO<sub>x</sub>, CoO<sub>x</sub>, poly1-NiO<sub>x</sub> and poly1-CoO<sub>x</sub> nanocomposites samples were prepared by electrodeposition on ITO electrodes (0.5 cm<sup>2</sup> for Ni<sup>0</sup> and 1 cm<sup>2</sup> for Co<sup>0</sup>) (a charge of 28 mC was used for the deposition of Ni<sup>0</sup> from the nickel oxalate solution, and 57 mC for Co<sup>0</sup> deposition, see above section 3). The samples were observed with a Bruker instrument (Dimension Icon with ScanAsyst) equipped with a Bruker Stage controller and a Nanoscope® V Bruker control box. The topography images were recorded by peak force mode with different scanning ranges and a tapping nose was used for imaging. AFM cantilevers with a

silicon tip on nitride lever (Bruker scanasyst-air) with a nominal spring constant of  $77.6 \text{ mN m}^{-1}$  were used. The peak force frequency and amplitude were set to 2 kHz and 150 nm, respectively. The images were displayed and processed using the Gwyddion program.

## 10. Transmission Electron Microscopy (TEM) Observation and Selected Area Electron Diffraction (SAED).

TEM images and SAED patterns for poly1-NiO<sub>x</sub> and NiO<sub>x</sub> materials were recorded with a JEOL JEM 1200 EX II instrument, performed in Chile. Meanwhile TEM images and SAED patterns for poly1-CoO<sub>x</sub> and CoO<sub>x</sub> materials were studied in Grenoble, recorded on a Philips CM200 microscope (FEI Company, Hillsboro, OR, USA) operating at 80 kV. For TEM measurements, the poly1-MO<sub>x</sub> and MO<sub>x</sub> (M = Ni or Co) were separated from the ITO/poly1-MO<sub>x</sub> and ITO/MO<sub>x</sub> electrodes (previously prepared for AFM, see above) by peeling off with a blade. The resulting powdered fragments were collected in water and a droplet of the dispersion suspension was deposited onto carbon-coated copper grids. The images of poly1-NiO<sub>x</sub> and NiO<sub>x</sub> were recorded with a digital camera and processed using the ImageJ software. Meanwhile the images of poly1-CoO<sub>x</sub> and CoO<sub>x</sub> were treated using Gwyddion program.

## 11. Selected Area Electron Diffraction (SAED) Analysis for Nickel.

The SAED analysis was carried out using the software ImageJ (version 1.50i). For calibration and indexing, several circles were drawn on the diffraction pattern of poly1-NiO<sub>x</sub> (Figure S1). Five circles were identified, analyzed and the calculated distances (1/nm) are presented in Table S1. The results are consistent with the nickel oxide structure.<sup>13,14</sup>

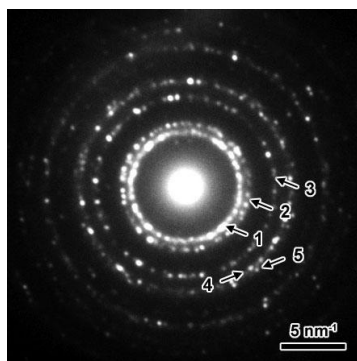


**Figure S1.** SAED pattern recorded from NiO<sub>x</sub> nanoparticles within poly1-NiO<sub>x</sub> nanocomposite. The numbers (*n*) correspond to the rings that have been calibrated in Table 1.

**Table S1.** Indexation of crystallographic plans of NiO<sub>x</sub> electrogenerated within poly1 film from the SAED pattern. *n* is the number of the diffraction ring, starting from the smallest ring; *r* is the reciprocal distance measured from the rings and calibrated using the diffraction scale bar; *d* is the interplanar spacing in the crystal equal to 1/*r*. *hkl* are the Miller indices of the corresponding crystallographic planes .

<i>n</i>	<i>r</i> (nm <sup>-1</sup> ) <sup>a</sup>	<i>d</i> (nm) <sup>b</sup>	<i>hkl</i> <sup>c</sup>
1	4.272	0.234	111
2	5.032	0.199	200
3	6.972	0.143	220
4	8.127	0.123	311
5	8.470	0.118	222

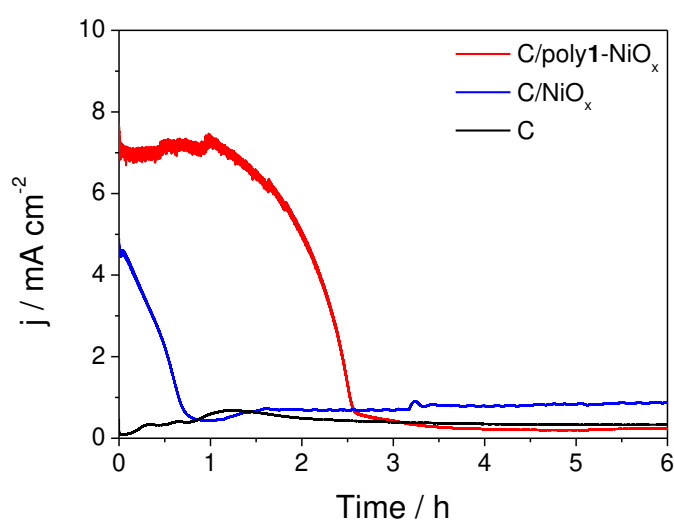


**Figure S2.** Chronoamperograms recorded at C/poly1-NiO<sub>x</sub> ( $\Gamma_{\text{N}^+} = 1.1 \times 10^{-7} \text{ mol cm}^{-2}$ ,  $\Gamma_{\text{Ni}} = 3.3 \times 10^{-8} \text{ mol cm}^{-2}$ ) (red), C/NiO<sub>x</sub> ( $\Gamma_{\text{Ni}} = 1.2 \times 10^{-8} \text{ mol cm}^{-2}$ ) (blue) and bare C (black) electrodes (3 mm of diameter) in a stirred aqueous solution (pH 9.2) of 0.1 M H<sub>3</sub>BO<sub>3</sub> and 0.05 M NaOH, at constant potential of +1.2 V vs Ag/AgCl.

## 12. Scanning Electron Microscopy (SEM) analysis for Cobalt.

SEM analysis was performed only for cobalt, due to the SEM equipment of Chile do not was enough strong to observe the low conductivity of poly1-NiO<sub>x</sub> and NiO<sub>x</sub> materials. SEM analysis was perfoemd in Grenoble using a Zeiss Ultra 55 (Carl Zeiss Co., Ltd., Oberkochen,

Germany) operating at an accelerating voltage of 2 kV. The samples of poly**1**-CoO<sub>x</sub> and CoO<sub>x</sub> were taken from ITO/poly**1**-CoO<sub>x</sub> and ITO/CoO<sub>x</sub> electrodes (previously prepared for AFM, see above). The ITO electrode was placed directly under the microscope.

### **13. Irradiation Lamp for Photoelectrocatalysis.**

The poly**1**/**PyrPDI**-MO<sub>x</sub> electrodes were illuminated at 3 cm of distance with a Xenon lamp (150 W, Hamamatsu L8253, type LC8-03) equipped with cut/off filter or high pass filter (< 400 nm).<sup>15</sup>

## REFERENCES

- (1) Cosnier, S.; Deronzier, A.; Moutet, J. C.; Roland, J. F. *J. Electroanal. Chem.* **1989**, *271* (1–2), 69–81.
- (2) Zhong, M.; Hisatomi, T.; Kuang, Y.; Zhao, J.; Liu, M.; Iwase, A.; Jia, Q.; Nishiyama, H.; Minegishi, T.; Nakabayashi, M.; Shibata, N.; Niishiro, R.; Katayama, C.; Shibano, H.; Katayama, M.; Kudo, A.; Yamada, T.; Domen, K. *J. Am. Chem. Soc.* **2015**, *137* (15), 5053–5060.
- (3) Genies, E. M.; Bidan, G.; Diaz, A. F. *J. Electroanal. Chem. Interfacial Electrochem.* **1983**, *149* (1), 101–113.
- (4) Zouaoui, A.; Stephan, O.; Ourari, A.; Moutet, J. C. *Electrochim. Acta* **2000**, *46* (1), 49–58.
- (5) Choi, W.; Ko, H. C.; Moon, B.; Lee, H. *J. Electrochem. Soc.* **2004**, *151* (2), E80.
- (6) Desilvestro, J.; Corrigan, D. A.; Weaver, M. J. *J. Electrochem. Soc.* **1988**, *135*, 885.
- (7) Corrigan, D. A.; Knight, S. L. *J. Electrochem. Soc.* **1989**, *136*, 613.
- (8) Cordoba-Torresi, S. I.; Gabrielli, C.; Hugot-le goff, A.; Torresi, R. *J. Electrochem. Soc.* **1991**, *138*, 1548.
- (9) Fu, X.-Z.; Zhu, Y.-J.; Xu, Q.-C.; Li, J.; Pan, J.-H.; Xu, J.-Q.; Lin, J.-D.; Liao, D.-W. *Solid State Ionics* **2007**, *178*, 987.
- (10) Bediako, D. K.; Lassalle-Kaiser, B.; Surendranath, Y.; Yano, J.; Yachandra, V. K.; Nocera, D. G. *J. Am. Chem. Soc.* **2012**, *134*, 6801.
- (11) Trotochaud, L.; Ranney, J. K.; Williams, K. N.; Boettcher, S. W. *J. Am. Chem. Soc.* **2012**, *134*, 17253.
- (12) Fominykh, K.; Chernev, P.; Zaharieva, I.; Sicklinger, J.; Stefanic, G.; Döblinger, M.; Müller, A.; Pokharel, A.; Böcklein, S.; Scheu, C.; Bein, T.; Fattakhova-Rohlfing, D. *ACS Nano* **2015**, *9*, 5180.
- (13) Wang, Z.; Kale, G. M.; Yuan, Q.; Ghadiri, M. *RSC Advances* **2012**, *2*, 9993.
- (14) Long, H.; Shi, T.; Hu, H.; Jiang, S.; Xi, S.; Tang, Z. *Scientific reports* **2014**, *4*, 7413.
- (15) Castillo, C. E.; Gennari, M.; Stoll, T.; Fortage, J.; Deronzier, A.; Collomb, M. N.; Sandroni, M.; Légalité, F.; Blart, E.; Pellegrin, Y.; Delacote, C.; Boujtita, M.; Odobel, F.; Rannou, P.; Sadki, S. *J. Phys. Chem. C* **2015**, *119* (11), 5806–5818.

## **Abstract:**

This thesis is focused on the development of efficient anodes and photonanodes for electrocatalytic and photocatalytic water oxidation based on nanocomposite materials in which nickel or cobalt oxide nanoparticles have been inserted in a positively charged poly(pyrrole-alkylammonium) film.

The nanocomposite anodes exhibit small nanoparticles of nickel or cobalt oxides and high nanostructuration induced by the polypyrrole matrix leading to very high catalytic performance in comparison with bare anodes on which nickel and cobalt oxides have been deposited without polypyrrole. These nanocomposite electrodes outperform the nickel-based anodes of the literature (undoped by iron) and those using precious metal oxides, such as RuO<sub>2</sub> and IrO<sub>2</sub>.

This strategy has been successfully extended to the design of hybrid photoanodes by introducing a perylene diimine chromophore in these nickel or cobalt oxide nanocomposite materials. These photoanodes display very high photocurrent density with nickel oxide and cobalt oxide under visible light illumination along with a relatively good stability over time. These photocurrent density values largely exceed those reached by similar hybrid photoanodes of literature combining an organic dye and a metal oxide as catalyst, demonstrating the great potentialities of our approach to implement (photo)electrochemical cells devoted to water splitting into H<sub>2</sub> and O<sub>2</sub>.

**Titre:** Matériaux nanocomposites polypyrrole-oxyde métallique pour l'oxydation de l'eau en oxygène par voie électrocatalytique et photocatalytique

## **Résumé :**

Ce mémoire de thèse est consacré au développement d'anodes et de photonanodes efficaces pour l'oxydation électrocatalytique et photocatalytique de l'eau à base de nanocomposites dans lesquels des nanoparticules d'oxyde de nickel ou de cobalt ont été insérées dans un film de poly(pyrrole-alkylammonium) chargé positivement. Les anodes nanocomposites renferment des petites nanoparticules d'oxydes de nickel ou de cobalt avec une excellente nanostructuration induite par le film polypyrrole, et des performances catalytiques très élevées par rapport à des anodes sur lesquelles des oxydes de nickel et de cobalt ont été directement déposés sans polypyrrole. Ces électrodes nanocomposites surpassent les anodes à base de nickel de la littérature (non dopées par du fer) et celles utilisant des oxydes de métaux précieux, tels que RuO<sub>2</sub> et IrO<sub>2</sub>.

Cette stratégie a été étendue avec succès à la conception de photoanodes hybrides en introduisant un chromophore de pérylène diimine dans ces nanocomposites d'oxydes de nickel ou de cobalt. Ces photoanodes présentent une densité de photocourant très élevé avec l'oxyde de nickel et l'oxyde de cobalt sous irradiation dans le visible avec une stabilité relativement bonne dans le temps. Ces valeurs de photocourant dépassent largement celles obtenues par des photoanodes hybrides similaires de la littérature combinant un colorant organique et un oxyde métallique comme catalyseur, démontrant les grandes potentialités de notre approche pour élaborer des cellules (photo)électrochimiques dédiées à la dissociation de l'eau en H<sub>2</sub> et O<sub>2</sub>.